

# The vascular properties of the BOLD signal

by

Ian Driver, MSci.

Thesis submitted to the University of Nottingham  
for the degree of Doctor of Philosophy

September 2011

# Contents

<b>Abstract</b>	<b>vi</b>
<b>Acknowledgements</b>	<b>viii</b>
<b>1 Introduction</b>	<b>1</b>
1.1 Thesis outline . . . . .	2
<b>2 Theory</b>	<b>4</b>
2.1 Introduction . . . . .	4
2.2 Nuclear Magnetic Resonance . . . . .	4
2.2.1 Spin angular momentum . . . . .	5
2.2.2 Ensemble of $^1\text{H}$ nuclear spins at thermal equilibrium . . . . .	7
2.2.3 Excitation of the spin ensemble . . . . .	8
2.2.4 Bloch equations . . . . .	10
2.2.5 Transverse relaxation and spin echoes . . . . .	11
2.3 Magnetic Resonance Imaging . . . . .	15
2.3.1 Hardware . . . . .	15
2.3.2 Spatial encoding . . . . .	18
2.3.3 Pulse sequences . . . . .	25
2.3.4 Parallel imaging . . . . .	38
2.3.5 Safety considerations . . . . .	38
2.4 functional Magnetic Resonance Imaging . . . . .	40
2.4.1 Physiology underlying fMRI . . . . .	41
2.4.2 Blood Oxygenation Level Dependent signal contrast . . . . .	43
2.4.3 BOLD experiment design and analysis . . . . .	49
2.4.4 Other fMRI techniques . . . . .	51

2.4.5	BOLD calibration . . . . .	54
2.5	Conclusion . . . . .	58
<b>3</b>	<b>Modulation of blood gases</b>	<b>59</b>
3.1	Introduction . . . . .	59
3.2	Theory . . . . .	60
3.3	The Respiract™ and its use in a 7 Tesla scanner environment . . . . .	62
3.4	Safety . . . . .	69
3.5	Other approaches to modulating $P_{ET}CO_2$ and $P_{ET}O_2$ . . . . .	71
3.6	Conclusion . . . . .	72
<b>4</b>	<b>Effect of field strength on the temporal characteristics of the BOLD response</b>	<b>73</b>
4.1	Introduction . . . . .	73
4.2	Method . . . . .	76
4.3	Results . . . . .	84
4.4	Discussion . . . . .	95
4.5	Conclusion . . . . .	100
<b>5</b>	<b>Investigating cerebral haemodynamics using hypercapnia</b>	<b>101</b>
5.1	Introduction . . . . .	101
5.2	The effect of hypercapnia on the vasculature . . . . .	102
5.3	Applications of hypercapnia in MRI . . . . .	104
5.4	Cerebrovascular reactivity at 3 and 7 Tesla . . . . .	109
5.4.1	Introduction . . . . .	109
5.4.2	Echo time optimisation . . . . .	109
5.4.3	Development of paradigm . . . . .	111
5.4.4	Method . . . . .	114
5.4.5	Results . . . . .	119
5.4.6	Discussion . . . . .	122
5.5	Assessing vascular asymmetry in the primary motor cortex . . . . .	127
5.5.1	Introduction . . . . .	127
5.5.2	Method . . . . .	128
5.5.3	Results . . . . .	132

5.5.4	Discussion . . . . .	134
5.6	Conclusion . . . . .	138
<b>6</b>	<b>Improved BOLD calibration using hyperoxia</b>	<b>140</b>
6.1	Introduction . . . . .	140
6.2	Uses of hyperoxia in MRI . . . . .	141
6.3	A new approach to BOLD calibration using hyperoxia . . . . .	145
6.4	The effect of hyperoxia on the vasculature . . . . .	147
6.5	Magnetic Properties of $O_2$ . . . . .	149
6.6	Image artefacts caused by hyperoxic challenges and their effect on $R_2^*$ quantification . . . . .	152
6.6.1	Introduction . . . . .	152
6.6.2	Method . . . . .	153
6.6.3	Results . . . . .	155
6.6.4	Discussion . . . . .	157
6.7	Venous blood oxygenation and calibrated BOLD measurements	158
6.7.1	Introduction . . . . .	158
6.7.2	Method . . . . .	158
6.7.3	Results . . . . .	163
6.7.4	Discussion . . . . .	165
6.8	Conclusion . . . . .	174
<b>7</b>	<b>Conclusions</b>	<b>175</b>
	<b>Bibliography</b>	<b>177</b>

# Glossary

<b>ASL</b>	Arterial Spin Labelling
<b>BOLD</b>	Blood Oxygenation Level Dependent
<b>CBF</b>	Cerebral Blood Flow
<b>CBV</b>	Cerebral Blood Volume
<b>CMRO<sub>2</sub></b>	Rate of Cerebral Oxygen Metabolism
<b>CSF</b>	Cerebral Spinal Fluid
<b>CVR</b>	Cerebrovascular Reactivity
<b>dHb</b>	Deoxygenated Haemoglobin
<b>EPI</b>	Echo Planar Imaging
<b>F<sub>i</sub>O<sub>2</sub></b>	Inspired Fraction of Oxygen
<b>FWHM</b>	Full Width at Half Maximum
<b>GE</b>	Gradient Echo Magnetic Resonance Imaging
<b>Hb</b>	Oxygenated Haemoglobin
<b>HRF</b>	Haemodynamic Response Function
<b>NMR</b>	Nuclear Magnetic Resonance
<b>MRI</b>	Magnetic Resonance Imaging
<b>OEF</b>	Oxygen Extraction Fraction
<b>P<sub>a</sub>CO<sub>2</sub></b>	Arterial Partial Pressure of Carbon dioxide
<b>P<sub>a</sub>O<sub>2</sub></b>	Arterial Partial Pressure of Oxygen
<b>PET</b>	Positron Emission Tomography
<b>P<sub>ET</sub>CO<sub>2</sub></b>	End-Tidal Partial Pressure of Carbon dioxide
<b>P<sub>ET</sub>O<sub>2</sub></b>	End-Tidal Partial Pressure of Oxygen
<b>ROI</b>	Region Of Interest
<b>S<sub>a</sub>O<sub>2</sub></b>	Arterial haemoglobin Oxygen Saturation

<b>SE</b>	Spin Echo Magnetic Resonance Imaging
<b>SGD</b>	Sequential Gas Delivery breathing circuit
<b>SNR</b>	Signal-to-Noise Ratio
<b>TE</b>	Echo Time
<b>TI</b>	Inversion Time
<b>TR</b>	Repetition Time
<b>TTP</b>	Time-To-Peak
<b>VERVE</b>	Venous Refocussing for Volume Estimation
<b><math>Y_v</math></b>	Venous cerebral blood oxygenation

# Abstract

The work presented in this thesis is intended to contribute towards the understanding of the cerebral vascular behaviour in response to changes in neuronal activation. The blood oxygenation-level dependent (BOLD) functional magnetic resonance imaging (fMRI) signal provides an indirect measure of neuronal activation, arising from a combination of metabolic and vascular (blood flow and blood volume) changes local to the activation. Therefore the BOLD signal is dependent on local vascular properties as well as on the neuronal activation, leading to a variability of the BOLD signal, based on the underlying vascular structure. It has become an important goal to improve understanding of the mechanisms underlying the BOLD signal in order to separate out this vascular variability from the underlying correspondence with the neuronal activation.

The effect of field strength on the temporal characteristics of the BOLD haemodynamic response function is investigated. An earlier BOLD response onset has been measured with increasing static magnetic field strength, consistent with an earlier microvascular (compared with macrovascular) signal response. This result can be used to improve haemodynamic models of the BOLD signal.

Hypercapnia, a vasodilator, has been used both to assess the relationship between transverse relaxation and blood oxygenation at 3 and 7 Tesla and to identify vascular heterogeneity between two equivalent brain regions. A tight, linear relationship was found between the level of hypercapnia and transverse relaxation at both 3 and 7 Tesla, whilst the change in transverse relaxation due to hypercapnia increased  $2.1 \pm 0.5$  fold from 3 to 7 Tesla, indicating an approximately linear relationship across field strength. In a separate experi-

ment, a vascular asymmetry was found between the left and right precentral gyri using hypercapnia. This result highlights the need to account for the vascular contribution to the BOLD signal before using this BOLD signal to make comparisons of neuronal activity across brain regions.

Finally, an improved model for calibrated BOLD has been proposed and implemented, which requires fewer assumptions than existing approaches. This uses the BOLD response to some task, repeated both at normoxia and hyperoxia. To assess the validity of this model, the effects of paramagnetic oxygen molecules are considered, both dissolved in blood plasma and in airspaces adjacent to the brain. These effects were found to be small, except for in the frontal cortex.

# Acknowledgements

I would like to take this opportunity to thank everyone who has helped and supported me during the course of my PhD studies. First of all, I would like to express my greatest appreciation to my two excellent supervisors, Professor Penny Gowland and Dr Susan Francis, who provided invaluable advice and assistance in performing this work. I would also especially like to thank Nicholas Blockley for providing much early help to allow me to find my feet in the field. For many useful and interesting discussions, I would like to thank Emma Hall and Paula Croal. For his assistance and software for performing dynamic field mapping, I would like to thank Jack Harmer. I would like to extend a general thanks to everyone at the Sir Peter Mansfield Magnetic Resonance Centre, for being a very sociable group of people, creating a very friendly work environment.

Finally, I would like to express my gratitude for the Sir Peter Mansfield Scholarship and the United Kingdom Medical Research Council grant which supported this work.

# Chapter 1

## Introduction

Blood oxygenation-level dependent (BOLD) functional magnetic resonance imaging (fMRI) is a very promising tool for studying brain function. Since the first implementation of the BOLD signal to detect changes in neuronal activation in response to visual and motor stimuli [1, 2], this technique has been widely adopted for psychology and neuroscience research. However some of its limitations are restricting its use in a clinical environment. BOLD fMRI measures the local vascular response to neuronal activity (typically within several mm of the neuronal activity [3]). This vascular response acts as a filter to blur the detected signal change both spatially and temporally compared with the underlying neuronal activity. Also, comparison of the neuronal activity across subjects and across brain regions using BOLD is confounded by the amplitude of the BOLD response depending on local vascular properties as well as the underlying neuronal activity. This is of particular importance for patient groups who have compromised cerebrovascular or cardiovascular function. Also, some drugs (for example caffeine) will influence the basal cerebrovascular state, leading to an altered BOLD signal in response to neuronal activation. This work aims to develop techniques for improving the understanding of the BOLD signal response to changes in brain function.

## 1.1 Thesis outline

Chapter 2 introduces the physics behind NMR, the concepts underlying MRI and the physics and physiology which provide contrast in fMRI. This chapter introduces a range of MRI pulse sequences, of use for fMRI experiments. Various fMRI acquisition techniques are introduced, along with some of the current limitations of fMRI, which aim to be addressed in subsequent chapters.

Chapter 3 describes the theory behind modulating a subject's blood gas levels of oxygen and carbon dioxide. These can be used to provide a global perturbation to the cerebral vasculature, which can be used to investigate the vascular dependence of the BOLD signal. A system is described for modulating blood gas levels of oxygen and carbon dioxide, which is used in the subsequent chapters. Details of the application of this method to an MRI experiment are also provided.

Chapter 4 presents results from a study which investigated the dependence of the BOLD temporal characteristics on field strength. The relative contributions to the BOLD signal of different sources (such as from large and small blood vessels, or from blood and the surrounding tissue) depends on field strength. Therefore this work aimed to investigate temporal differences in the BOLD signal from these different sources through the perturbation of field strength.

Chapter 5 is concerned with how hypercapnia perturbs cerebral vasculature and how this can be used to investigate the BOLD signal mechanism. This chapter presents results from two experiments. The first used hypercapnia to investigate the relationship between transverse relaxation rate and the blood gas level of carbon dioxide at 3 Tesla and 7 Tesla. This is of use for improving the application of a technique for calibrating the BOLD signal at these field strengths. The second experiment used the BOLD response to hypercapnia to demonstrate a difference in the underlying vascular response between two equivalent brain regions, the left and right precentral gyrus.

Chapter 6 considers the effect of hyperoxia on both vascular and magnetic properties, to assess the viability of hyperoxia as a tool to investigate the BOLD signal mechanism. Results are presented from an experiment to determine whether a field inhomogeneity created by increased oxygen in the nasal cavity and frontal sinuses will cause a significant effect on the MRI signal, which would confound BOLD analysis. A new approach for calibration of the BOLD response to a task repeated both an normoxia and hyperoxia was proposed and results presented for an experiment demonstrating implementation of this approach.

Chapter 7 summarises the work presented in this thesis.

# Chapter 2

## Theory

### 2.1 Introduction

This chapter aims to introduce the major concepts of a magnetic resonance imaging (MRI) experiment. The basic theory behind nuclear magnetic resonance *NMR* is described, leading to a description of the behaviour of an ensemble of hydrogen nuclei in the presence of time-varying magnetic fields. Basic principles of magnetic resonance imaging *MRI* are discussed, including a brief introduction to the hardware used for MRI acquisition in this thesis. Finally a description of the principles of using MRI to study brain function is presented, highlighting some of the issues that will be addressed in the following chapters of this thesis.

### 2.2 Nuclear Magnetic Resonance

Nuclear magnetic resonance *NMR* arises from spin angular momentum, which is an intrinsic property of nuclei. This section introduces some basic principles of the behaviour of nuclear spin angular momentum in the presence of a static magnetic field. The magnetic properties of an ensemble of many hydrogen nuclei is considered at thermal equilibrium, in perturbed states and the recovery from a perturbed state back to thermal equilibrium.

### 2.2.1 Spin angular momentum

Spin angular momentum is an intrinsic quantum mechanical property of a particle, without a classical macroscopic analogue. Unlike conventional angular momentum, spin angular momentum does not relate to rotation. Spin angular momentum ( $L_s$ ) of a particle is described by:

$$L_s = \hbar\sqrt{S(S+1)}, \quad (2.1)$$

where  $\hbar = 1.054 \times 10^{-34}$  Js is Planck's constant divided by  $2\pi$  and  $S$  is the spin quantum number.  $S$  can either take a integer or half-integer value and is either positive or zero. A particle with spin quantum number  $S$  has  $2S + 1$  energy level states, associated with another quantum number  $m_s$ . Here,  $m_s$  takes a range of values, from  $-S$  to  $+S$ , in integer steps. The separation between these  $m_s$  states depends on the magnetic field experienced by the particle. In the absence of a magnetic field, these states are degenerate (all having the same energy). The splitting of these levels in a magnetic field is known as the *Zee-man effect* [4].

Spin angular momentum is associated with a magnetic moment, such that magnetic moment is proportional to spin angular momentum. The constant of proportionality is known as the *gyromagnetic ratio*  $\gamma$ . Magnetic moment is parallel to spin angular momentum when  $\gamma > 0$  and is anti-parallel to spin angular momentum when  $\gamma < 0$ . In the absence of a magnetic field the spin angular momentum vector and hence the magnetic moment vector can be oriented in any direction. When a magnetic field is applied the spin angular momentum vector precesses about the field, at a constant angle with respect to the field. This precession is due to the magnetic field exerting a torque on the magnetic moment, such that torque is the cross product of magnetic moment and field. The frequency of this precession is known as the *Larmor frequency*  $\omega_0$ :

$$\omega_0 = -\gamma B_0, \quad (2.2)$$

where  $\gamma$  is the gyromagnetic ratio and  $B_0$  is the magnetic field experienced by the particle. The precession direction is dependent on the sign of  $\gamma$ , as shown

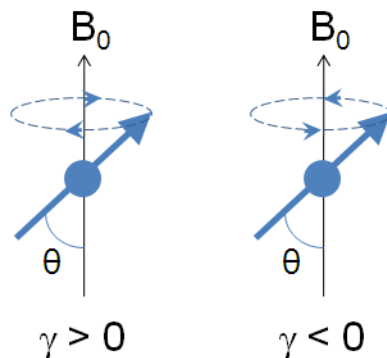


Figure 2.1: Diagram showing the precession of the spin angular momentum vector about a magnetic field  $B_0$ , for the cases of positive and negative gyromagnetic ratios  $\gamma$ .

in *figure 2.1*.

For the specific case of nuclear spin, the convention is to replace  $S$  and  $m_s$  with  $I$  and  $m_I$ . The nuclear spin quantum number depends on the number of protons and neutrons in the nucleus. If the number of protons and neutrons are both even, then the nucleus will have  $I = 0$ , whereas if the nucleus has odd numbers of both protons and neutrons, then  $I$  will be a positive integer [4]. If there are an odd number of either protons or neutrons and an even number of the other nucleon, then  $I$  will have a half-integer value. Examples of biologically interesting nuclei with  $I = 1/2$  are  $^{13}\text{C}$ ,  $^{19}\text{F}$  and  $^{31}\text{P}$ .

This thesis will only deal with NMR of hydrogen nuclei, specifically the  $^1\text{H}$  isotope. NMR of hydrogen ( $^1\text{H}$ ) atoms is widely used to study organic tissue, due to a high concentration of hydrogen atoms in tissue and a high natural abundance ( $\sim 100\%$  [4]) of  $^1\text{H}$ . The majority of hydrogen atoms in tissue are contained in water ( $\text{H}_2\text{O}$ ) molecules.  $^1\text{H}$  nuclei have  $I = 1/2$ , so  $m_I = -1/2, 1/2$ , through Zeeman splitting. The gyromagnetic ratio of hydrogen nuclei  $\gamma_{^1\text{H}}$  is  $267.522 \times 10^6 \text{ rad s}^{-1} \text{ T}^{-1}$  [4]. The separation between  $m_I = 1/2$  and  $m_I = -1/2$  spin states is  $\Delta E = \hbar \cdot \gamma_{^1\text{H}} \cdot B_0$ , where  $m_I = 1/2$  is the lower energy state, since the associated magnetic moment is parallel to the applied magnetic field.

## 2.2.2 Ensemble of $^1\text{H}$ nuclear spins at thermal equilibrium

An ensemble of many  $^1\text{H}$  nuclear spins will have a distribution of spin angular momentum vectors, with the spin state of each being a superposition of the  $m_I = 1/2$  and  $m_I = -1/2$  spin states. For this many spin,  $I = 1/2$  system, a spin density operator  $\hat{\rho}$  can be used to describe the quantum state of the whole spin ensemble [4].

$$\hat{\rho} = \begin{bmatrix} \rho_{\frac{1}{2},\frac{1}{2}} & \rho_{\frac{1}{2},-\frac{1}{2}} \\ \rho_{-\frac{1}{2},\frac{1}{2}} & \rho_{-\frac{1}{2},-\frac{1}{2}} \end{bmatrix} \quad (2.3)$$

This spin density operator contains terms for the fractional populations of both spin states ( $\rho_{\frac{1}{2},\frac{1}{2}}, \rho_{-\frac{1}{2},-\frac{1}{2}}$ ) and the coherence between both spin states ( $\rho_{\frac{1}{2},-\frac{1}{2}}, \rho_{-\frac{1}{2},\frac{1}{2}}$ ). The population terms are fractions of the total spin ensemble, such that  $\rho_{\frac{1}{2},\frac{1}{2}} + \rho_{-\frac{1}{2},-\frac{1}{2}} = 1$ . They can be used to determine the net magnetisation of the spin ensemble in the direction of the applied magnetic field (the *longitudinal* direction). Non-zero coherence terms indicate some net magnetisation in the plane perpendicular to the applied magnetic field (the *transverse* plane). This transverse component of net magnetisation arises from phase coherence in the precession of the spin ensemble.

In the absence of an applied magnetic field, the spin angular momentum vectors will have an isotropic distribution, so will have no net magnetic moment across the spin ensemble. In this case, the coherence terms of the spin density operator will equal zero and both population terms will be equal ( $\rho_{\frac{1}{2},\frac{1}{2}} = \rho_{-\frac{1}{2},-\frac{1}{2}} = 0.5$ ). If a magnetic field (amplitude  $B_0$ ) were then applied to this system, spin precession would occur with a frequency  $\omega_0$  (equation 2.2) and at a constant angle from the applied field (figure 2.1), determined by the initial orientation to the applied field. This precession alone will not change net magnetisation. However, random molecular motion causes microscopic perturbations to the field experienced by the spins, causing a shift in the axis about which precession occurs. This gradually changes the precession angle about  $B_0$ , leading to changes in the spin density operator population terms and a change in net longitudinal magnetisation, until the spin ensemble

reaches thermal equilibrium for the new  $B_0$ . At thermal equilibrium, the spin density operator can be calculated as follows. There is no coherence between states at thermal equilibrium, so  $\rho_{\frac{1}{2},-\frac{1}{2}} = \rho_{-\frac{1}{2},\frac{1}{2}} = 0$ . The population terms depend on magnetic field strength  $B_0$  and temperature ( $T$  (K)), following the *Boltzmann distribution*:

$$\rho_{\pm\frac{1}{2},\pm\frac{1}{2}} = \frac{\exp(\frac{\pm\frac{1}{2}\hbar\cdot\gamma_{\text{H}}\cdot B_0}{k_B T})}{\exp(\frac{+\frac{1}{2}\hbar\cdot\gamma_{\text{H}}\cdot B_0}{k_B T}) + \exp(\frac{-\frac{1}{2}\hbar\cdot\gamma_{\text{H}}\cdot B_0}{k_B T})}, \quad (2.4)$$

where  $k_B = 1.38066 \times 10^{-23} \text{ JK}^{-1}$  is the Boltzmann constant. At room temperature ( $T = 298 \text{ K}$ ), the difference in populations is  $5 \times 10^{-6}$  at 1.5 T,  $10 \times 10^{-6}$  at 3 T and  $24 \times 10^{-6}$  at 7 T, so the net magnetisation is of the order of  $10^{-5}$  that of the total magnetisation if all magnetic moments aligned with  $B_0$ . In the limit where  $(\frac{1}{2}\hbar \cdot \gamma_{\text{H}} \cdot B_0) \ll k_B T$ , *equation 2.4* reduces to a linear dependence of population difference on  $B_0$ . At room temperature, this limit holds for a  $B_0$  up to several orders of magnitude higher than 7 T. The rate at which the spin ensemble reaches thermal equilibrium is the *longitudinal relaxation rate*. In this case, from an isotropic distribution to thermal equilibrium at the applied field  $B_0$ , the net longitudinal magnetisation obeys an exponential recovery curve, with time constant  $T_1$ .

### 2.2.3 Excitation of the spin ensemble

The longitudinal nuclear spin magnetisation resulting from this population difference cannot be directly detected during an NMR experiment, due to large electron spin magnetisation in the longitudinal direction (several orders of magnitude greater than nuclear spin magnetisation). Instead, the nuclear spin magnetisation is measured in the transverse plane. This is achieved using magnetic field perturbations, which oscillate in time at a frequency approximating  $\omega \sim \omega_0$  [5, 6]. This field perturbation is known as the *radio-frequency pulse*, since this frequency is on the order of radio waves in the electromagnetic spectrum. The effect of the radio-frequency pulse is to convert the population difference into coherence, so the net magnetisation vector gains a component

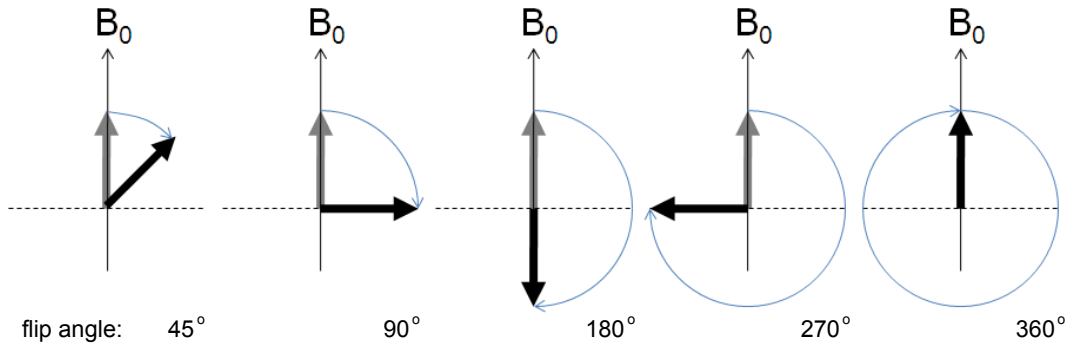


Figure 2.2: Classical illustration showing examples of the effect of a radio-frequency pulse, with various durations, on the net magnetisation vector. The vertical axis is the direction of the static magnetic field  $B_0$ . The transverse plane is collapsed down to the horizontal dashed line in this plot.

in the transverse plane and the net longitudinal component is reduced.

The radio-frequency pulse can be separated into two circularly rotating magnetic field components, rotating in opposite directions, with angular frequency  $\omega$  and  $-\omega$ . The first component rotates at approximately the same frequency as spin precession, whereas the second component rotates at a frequency approximately  $2\omega_0$  from spin precession. In the limit that the amplitude of the radio-frequency pulse ( $B_1$ ) is much less than the static magnetic field (so  $B_1 \ll B_0$ ) the second component has a negligible effect on the spin ensemble. The first component causes the net magnetisation vector to rotate orthogonally to the static magnetic field (as shown in *figure 2.2*), with the amount of rotation depending on the duration of the radio-frequency pulse. The radio-frequency pulse duration and amplitude product is typically described by the angle of rotation it causes on the net magnetisation vector, relative to the static magnetic field direction, called the *flip angle*.

The effect on the spin density operator is initially to decrease the difference in population terms and create non-zero coherence terms. The population difference decreases and the coherence increases with increasing flip angle, until the flip angle =  $90^\circ$ , at which point the populations of both spin states are equal and the coherence is at a maximum. Between  $90^\circ < \text{flip angle} < 180^\circ$

the population difference increases again and coherence decreases, but with the higher energy spin state ( $m_I = -1/2$ ) having a higher population. When the flip angle =  $180^\circ$ , the coherence equals zero and the spin state populations are inverted (so there is the same population difference as for before the radio-frequency pulse). For  $180^\circ < \text{flip angle} < 360^\circ$  the spin state populations return to their initial values and coherence increases up to a maximum at flip angle =  $270^\circ$  and then decreases to zero at flip angle =  $360^\circ$ , in a mirror of  $0^\circ < \text{flip angle} < 180^\circ$ . Therefore the spin density operator is the same before and after a  $360^\circ$  flip angle radio-frequency pulse.

The radio-frequency pulse perturbs the spin density operator such that the spin ensemble will not be in a state of thermal equilibrium. After the radio-frequency pulse, microscopic perturbations to the field caused by random molecular motion causes both the population terms and coherence terms to return to thermal equilibrium values, through longitudinal relaxation and transverse relaxation respectively. The rate at which the coherence terms reach their thermal equilibrium values (zero) is known as the *transverse relaxation rate*, described by a time constant  $T_2$ .

As well as transverse and longitudinal relaxation, after the radio-frequency pulse the net magnetisation vector rotates in the transverse plane, with the same frequency as spin precession ( $\omega_0$ ). The transverse component of the net magnetisation vector can be detected through a receive coil, by the transverse magnetic field caused by the magnetisation vector inducing a current in the coil. This will be described in more detail in *section 2.3.1*.

#### **2.2.4 Bloch equations**

Felix Bloch proposed a set of empirical differential equations to describe the relaxation of the net magnetisation vector to thermal equilibrium, known as the *Bloch equations* [7]. Defining a Cartesian coordinate system (such that x-, y- and z-axes are perpendicular to one another), where the static magnetic field lies parallel to the z-axis and the x- and y-axes are parallel to the transverse

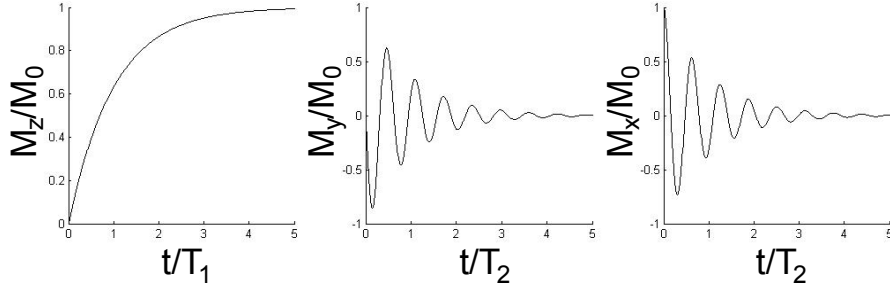


Figure 2.3: A solution to the Bloch equations (equation 2.6) following a  $90^\circ$  radio-frequency pulse. Note that the choice of  $\omega_0$  (of  $10/T_2$ ) is for illustration only. Typical values of  $\omega_0$  are of the order  $10^6/T_2$ .

plane, then:

$$\begin{aligned}
 \frac{dM_z}{dt} &= \frac{1}{T_1}(M_0 - M_z) \\
 \frac{dM_y}{dt} &= -\omega_0 M_x - \frac{M_y}{T_2} \\
 \frac{dM_x}{dt} &= \omega_0 M_y - \frac{M_x}{T_2}
 \end{aligned} \tag{2.5}$$

such that  $M_0$  is the longitudinal magnetisation at thermal equilibrium,  $M_x$ ,  $M_y$  and  $M_z$  are the net magnetisation components in each respective direction.

One possible solution of the Bloch equations for a time  $t$  after a  $90^\circ$  radio-frequency pulse is

$$\begin{aligned}
 M_z(t) &= M_0(1 - e^{-t/T_1}) \\
 M_y(t) &= -M_0 e^{-t/T_2} \sin(\omega_0 t) \\
 M_x(t) &= M_0 e^{-t/T_2} \cos(\omega_0 t).
 \end{aligned} \tag{2.6}$$

An illustration of these equations is shown in *figure 2.3*. The sinusoidal oscillation terms describe the rotation of the net magnetisation vector about the static magnetic field, reflecting spin precession.

### 2.2.5 Transverse relaxation and spin echoes

So far, this description assumes a homogeneous background magnetic field, which is not the case in reality. Macroscopic field inhomogeneities are generally

present across any sample. These field inhomogeneities are of the order of a millionth of the magnitude of the static magnetic field, but are sufficient to increase the rate of transverse relaxation. The extra component of transverse relaxation due to macroscopic field inhomogeneities is described by a time constant  $T'_2$ . The total transverse relaxation is described by another time constant  $T_2^*$ , such that

$$\frac{1}{T_2^*} = \frac{1}{T_2} + \frac{1}{T'_2}. \quad (2.7)$$

As an aside, it is worth noting that sometimes a rate constant is used instead of a time constant, such that

$$R_1 = \frac{1}{T_1}, R_2 = \frac{1}{T_2}, R'_2 = \frac{1}{T'_2} \text{ and } R_2^* = \frac{1}{T_2^*}. \quad (2.8)$$

For a spin ensemble in the presence of macroscopic field homogeneities the net magnetisation can be calculated by replacing  $T_2$  with  $T_2^*$  in *equations 2.5 and 2.6*.

Therefore transverse relaxation is caused by a combination of microscopic field fluctuations ( $T_2$  decay) that are rapidly varying and macroscopic field inhomogeneities ( $T'_2$  decay) that are considered to be static over short time-scales. Transverse relaxation due to  $T_2$  decay is considered unrecoverable due to the random nature of molecular motion causing the microscopic field fluctuations. However it is possible to reverse the relaxation due to macroscopic field inhomogeneities, through the application of a  $180^\circ$  radio-frequency pulse.

If a  $180^\circ$  radio-frequency pulse is applied at time  $TE/2$  after the  $90^\circ$  radio-frequency pulse, then the transverse relaxation due to macroscopic field inhomogeneities is refocussed. This is seen as an echo of transverse magnetisation, centred on a time  $TE/2$  after the  $180^\circ$  radio-frequency pulse (see *figure 2.4*). This will be designated as a *spin echo*, centred at a time  $TE$  after the  $90^\circ$  radio-frequency pulse, where  $TE$  is the *echo time*. To consider the origins of this spin echo, it is appropriate to move to a non-inertial reference frame, rotating around the axis of the static magnetic field with frequency  $\omega_0$ . In this reference frame, spin precession at  $\omega_0$  can be neglected, so the transverse component of the net magnetisation vector can be considered purely in terms

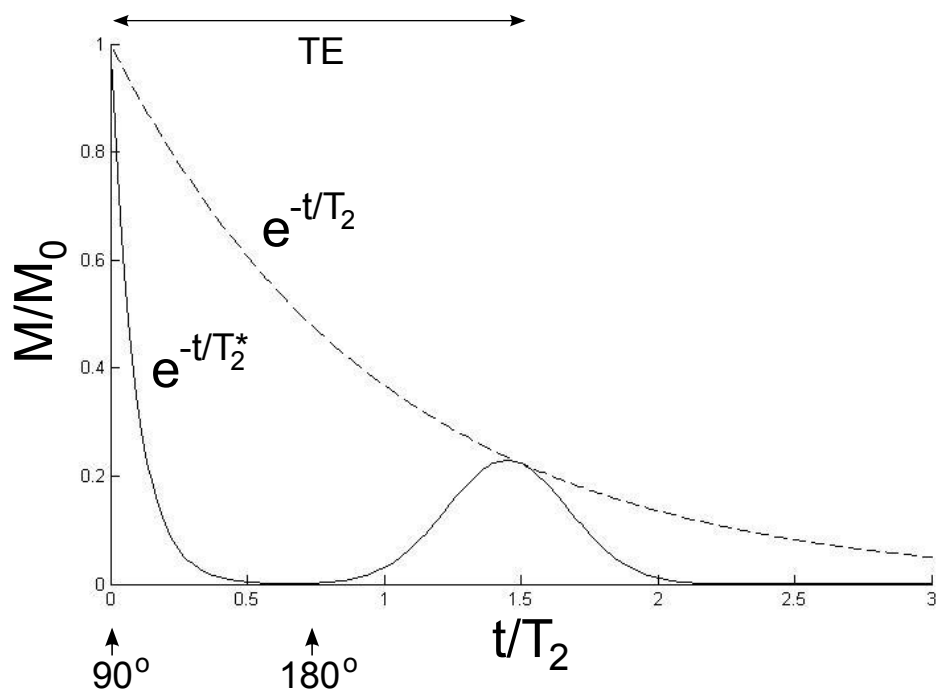


Figure 2.4: Plot illustrating the effect on transverse magnetisation of a  $90^\circ$  radio-frequency pulse, followed a time  $TE/2$  later by a  $180^\circ$  radio-frequency pulse. The  $T_2'$  decay is fully refocussed after a time  $TE$  after the initial  $90^\circ$  radio-frequency pulse, causing a spin echo, however the amplitude of the spin echo is attenuated by the  $T_2$  decay. This plot is formed in a reference frame rotating in phase with spins precessing with frequency  $\omega_0$ , so there is no oscillation at  $\omega_0$ , as there would be in the laboratory reference frame.

of relaxation.

The spin ensemble can be separated into groups of nuclei which experience the same field, such that all nuclei in a group have a common spin density operator. Each group is called an *isochromat*, which can be considered to have its own net magnetisation vector.  $T_2'$  decay can be illustrated by considering the relative phase of the transverse component of each isochromat magnetisation vector (see *figure 2.5*, referring to stages A–E). Prior to the  $90^\circ$  radio-frequency pulse (A), each isochromat has no net transverse magnetisation, as the whole spin ensemble is at thermal equilibrium. The  $90^\circ$  radio-frequency pulse (at  $t = 0$ ) converts the net longitudinal magnetisation of each isochromat into a transverse phase coherence, such that immediately after the  $90^\circ$  radio-frequency pulse (B), the transverse component of the net magnetisation vector of all isochromats precess in phase with one another. However, since each isochromat experiences a different local field, their net magnetisation vectors precess at different frequencies, such that faster precessing isochromats lead slower precessing isochromats, causing  $T_2'$  decay (C). The effect of the  $180^\circ$  radio-frequency pulse (at  $t = TE/2$ ) is to rotate the net magnetisation vector of each isochromat by  $180^\circ$ , both inverting the net longitudinal magnetisation (as will be discussed in *section 2.3*) and net transverse magnetisation (see *figure 2.5*). Therefore, immediately after the  $180^\circ$  radio-frequency pulse slower precessing isochromats lead faster precessing isochromats (D) and at time  $t = TE$  the transverse magnetisation of all isochromats are in phase again (E). This leads to a net transverse magnetisation of the whole spin ensemble at  $t = TE$  which is only attenuated by  $T_2$  decay and not  $T_2'$  decay.

In summary, the time constants  $T_1$  and  $T_2$  characterise the return of longitudinal and transverse magnetisation, respectively to thermal equilibrium of a spin ensemble. These values will depend on molecular environment, temperature and field strength, according to *Bloembergen-Purcell-Pound theory* [8]. According to this theory, both  $T_1$  and  $T_2$  should increase with field strength, which is the case for  $T_1$ , for example in human grey matter [9]. For  $T_2$  however, a decrease is observed with increasing field strength when assessed on clini-

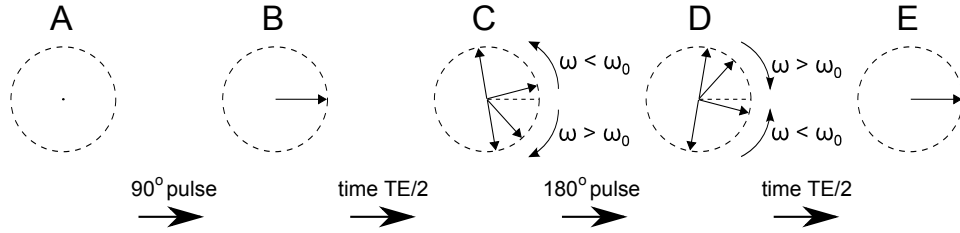


Figure 2.5: Diagram illustrating the relative phases of isochromat magnetisation vectors through a spin echo, as shown in *figure 2.4*. Each arrow represents the transverse magnetisation vector of an isochromat, each precessing at slightly different frequencies due to macroscopic field inhomogeneities. This diagram shows the transverse plane in a reference frame rotating in phase with spins precessing with frequency  $\omega_0$  and ignores  $T_2$  decay, which would affect each isochromat equally.

cal scanners, for example in human grey matter [10]. This can be attributed to increased effects of diffusion, as field inhomogeneities increase with field strength. The effect of diffusion on measured  $T_2$  will be discussed in *section 2.3.3*. Increasing field inhomogeneities with field strength will also lead to a decrease in  $T_2'$  with field strength, whilst  $T_2^*$  decreases with field strength as a combination of  $T_2$  and  $T_2'$ .

## 2.3 Magnetic Resonance Imaging

The concepts required for performing magnetic resonance imaging *MRI* are outlined in this section. A brief introduction to the hardware is presented, followed by a description of spatial encoding and slice selection; some relevant pulse sequences are introduced and the safety considerations associated with an MRI experiment are addressed.

### 2.3.1 Hardware

The major components present in an MRI scanner are the static magnet, shimming gradient sets, imaging gradient coils and radio-frequency transmit and receive coils. Static magnetic fields of 1.5 T or greater are typically used for MRI, to make use of a greater signal available from the higher net magnetisation at higher field strengths (*equation 2.4*). The large currents used to induce

these magnetic fields require superconducting coils, to avoid the high power dissipation that would result from passing the large currents through resistive wires. Superconducting coils are less susceptible than their resistive equivalents to external voltage and temperature fluctuations causing fluctuations in the induced magnetic field. The static magnetic field  $B_0$  needs to be homogeneous over the imaging region, known as the magnet's iso-centre. When the magnet is positioned in the magnet hall, field inhomogeneities from the local surroundings need to be corrected through a process known as *shimming*. Shimming involves placing ferromagnetic material (usually iron) at locations suitable to correct the inhomogeneities (*passive shimming*), followed by the addition of shimming coil sets (*active shimming*), to refine the field homogeneity. Field inhomogeneities are also caused by the sample or subject to be imaged, so additional corrective shimming gradient sets are also used on an individual scan basis.

In this thesis, work is presented which uses three MRI systems, Philips Achieva 1.5 T, 3 T and 7 T whole body scanners. These are horizontal, cylindrical scanners, such that the static magnet coils, shimming set and imaging gradient coils surround a cylindrical bore of approximately 90 cm diameter. A bed can be moved into and out of the bore, to manoeuvre the sample or subject into and out of the magnet iso-centre.

Imaging gradient coils induce spatially linearly varying magnetic field gradients and are used for spatial encoding, as will be shown in *section 2.3.2*. These gradient coils are designed so that they can be rapidly switched during an imaging experiment. Gradient sets (gradient coil and amplifier combinations) are specified by the field gradient they can produce (*maximum amplitude*) and the switching rate (*maximum slew rate*). *Table 2.1* lists these specifications for the three MRI systems used in this thesis. The 7 T gradient set was upgraded in between projects, such that data from *chapter 5* was acquired with the lower values whilst other data at 7 T was acquired with the higher values.

Both transmit and receive coils are radio-frequency coils, which are tuned (us-

Gradient parameter	1.5 T	3 T	7 T
Maximum amplitude (mT/m)	66	40	30 / 33
Maximum slew rate (mT/m/ms)	160	200	100 / 166

Table 2.1: Imaging gradient specifications. The two values at 7 T are before and after an upgrade.

ing capacitors) to approximately  $\omega_0$  of the nuclei of interest, which in this case is  $^1\text{H}$ . Transmit coils are generally designed to generate a radio-frequency pulse that is as spatially homogeneous as possible over the volume of interest. Receive coils have sensitivity profiles that drop off with distance from the volume of interest, so are positioned as close as possible to the volume of interest. For the case of performing MRI of the brain, typically receive coils are made up of multiple coils, positioned around the head to maximise the sensitivity to the whole brain. Smaller coils generally have a smaller region of sensitivity, so there is a compromise between having many small channels, closely fitting the shape of the head, and having large enough coils to be sensitive to medial parts of the brain, furthest from the surface. Net transverse magnetisation of the sample will induce a current in the receive coil, forming the measured signal from the sample. Each receive coil is attached to a different receive channel.

The signal detected by the receive coil is combined (multiplied) with a sinusoidal reference waveform which has a reference frequency approximately equal to  $\omega_0$ . This removes the component of the signal that oscillates at exactly the reference frequency (de-modulation), analogous to viewing the signal from a reference frame which rotates at the reference frequency, in the direction of spin precession. This highlights both transverse relaxation and any component of the signal which oscillates at different frequencies from the reference frequency. This approach cannot distinguish whether components are oscillating at higher or lower frequencies than the reference frequency. Therefore the solution is to produce two reference waveforms, both oscillating at the same reference frequency, but separated by a  $\pi/2$  phase difference. When the detected signal is compared with both of these reference waveforms, the two resulting components can be used to determine whether components are oscillating at higher

or lower frequencies than the reference frequency. This technique is known as *quadrature detection*.

### 2.3.2 Spatial encoding

The concept of using spatially varying magnetic field gradients to encode spatial information about an object in the NMR signal was originally proposed by Paul Lauterbur [11]. An outline of using linear spatial gradients for spatial encoding in MRI is provided here. The effect of a magnetic field gradient that varies linearly in one dimension on a spin ensemble is to create a spatial dependence of the spin precession frequency.

For example, consider two spin isochromats positioned along a magnetic field gradient such that the first experiences field  $B_0 + \Delta B$  and the second experiences field  $B_0 - \Delta B$ . Therefore the two isochromats will precess at  $\omega_0 + \Delta\omega$  and  $\omega_0 - \Delta\omega$  respectively (where  $\Delta\omega = \gamma_0\Delta B$ ). Where the gradient is applied following a  $90^\circ$  radio-frequency pulse the measured signal would be related to a summation of the transverse magnetisation from both isochromats, such that the signal would include components with frequencies of  $\omega_0 + \Delta\omega$  and  $\omega_0 - \Delta\omega$ . Therefore the positions of the isochromats can be measured with respect to the magnetic field gradient.

#### Gradient echoes

Gradients are applied to encode spatial information, however these gradients are field inhomogeneities that lead to additional transverse dephasing. This can be recovered by applying a gradient of opposite sign, of equal duration ( $\tau$ ) and amplitude (G) to the original gradient (*figure 2.6*). This will lead to an echo (at TE =  $2\tau$ ) in the net transverse relaxation, known as a *gradient echo*, through a similar mechanism as for a spin echo as shown in *figures 2.4 and 2.5*, except that only dephasing due to the gradient field inhomogeneities is refocussed. The transverse magnetisation (and therefore measured signal) at time TE will be attenuated by  $T_2$  and  $T_2'$  decay, but not by the gradients.

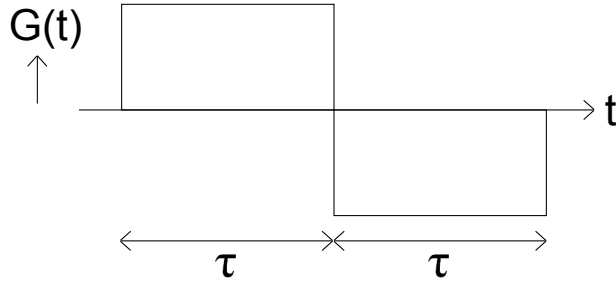


Figure 2.6: Gradients required to form a gradient echo

### **k-space**

The linear gradients create a well-defined relationship between the precession frequency ( $\omega$ ) and position ( $\mathbf{r}$ ). The same is also true for their reciprocal values of time ( $t$ ) and spatial frequency ( $\mathbf{k}$ ) [12]. To that end, spatial frequency  $\mathbf{k}$  can be defined as

$$\mathbf{k}(t) = \gamma \int_0^t G(t') dt', \quad (2.9)$$

where bold typeface denotes a three dimensional vector,  $G$  is the gradient amplitude (such that  $B(\mathbf{r}) = B_0 + \Delta B(\mathbf{r}) = B_0 + G \cdot \mathbf{r}$ ). The integral is over time, from the start of the applied gradient, up to time  $t$  and this accounts for phase accumulation due to the gradient. The effect of applying a linear gradient in a particular direction across an object is to sample the object's spatial frequency distribution across that direction. The range of spatial frequencies sampled depends on both the gradient amplitude  $G$  and on the sampling time  $t$ . Position and spatial frequency can be related (much like time and temporal frequency) by a Fourier transform.

The spatial encoded quantity is defined as the *spin density*  $\rho(\mathbf{r})$ , such that  $\rho(\mathbf{r})$  is proportional to the concentration of  $^1\text{H}$  nuclei and the polarisation of the system (so is dependant on  $B_0$  and temperature, see *equation 2.4*). The constant of proportionality is determined by a scaling factor related to the receiver amplification and can also be weighted by  $T_1$ ,  $T_2$  or  $T_2^*$ , depending on the

method for generating net transverse magnetisation. The signal  $s(\mathbf{k})$  (where  $\mathbf{k}$  is related to  $t$  by *equation 2.9*) is a three dimensional Fourier transform of  $\rho(\mathbf{r})$  [13, 14], such that

$$s(\mathbf{k}) = \iiint \rho(\mathbf{r}) \cdot e^{-i2\pi\mathbf{k}\cdot\mathbf{r}} d\mathbf{r}. \quad (2.10)$$

Therefore an inverse Fourier transform can be used to calculate  $\rho(\mathbf{r})$  from the measured signal  $s(\mathbf{k})$ .

If a gradient is applied which varies in only one dimension, then this integral can be evaluated in that dimension alone. Defining a Cartesian coordinate system such that the z-axis is parallel to the longitudinal direction and the x- and y-axes are in the transverse plane, then a gradient is applied which only varies along the x-axis, such that the magnetic field in the longitudinal (z) direction varies as a function of x ( $B_z(x)$ ). In this case, the three dimensional  $\rho(\mathbf{r})$  collapses down into a one-dimensional function  $\rho(x)$ , where each point along the x-dimension is formed by an integration of  $\rho(\mathbf{r})$  along the y- and z-dimensions such that

$$\rho(x) = \iint \rho(\mathbf{r}) dydz. \quad (2.11)$$

The inverse Fourier transform of the resulting signal will provide a projection of the spin density  $\rho$  along the x-axis. An example of this is shown in *figure 2.7*.

The effect of a linear gradient is to sample part of the spatial frequency distribution. This spatial frequency distribution can be mapped in inverse space, or *k-space*. Gradients can be applied which vary in space across any arbitrary direction, across *k-space trajectories*. Where the component of  $B_z$  which varies spatially in the x dimension is defined as  $G_x$ ,  $G_y$  in the y dimension and  $G_z$  in the z dimension, the effect on k-space trajectory due to various combinations of  $G_x$  and  $G_y$  is shown in *figure 2.8*. This example is not particularly useful as transverse magnetisation is not refocussed, however it demonstrates how gradients in multiple dimensions can be used separately or simultaneously to sweep across any k-space trajectory. Also, real gradients will have a trapezium shape and not a perfect box-car shape, taking time to reach the desired

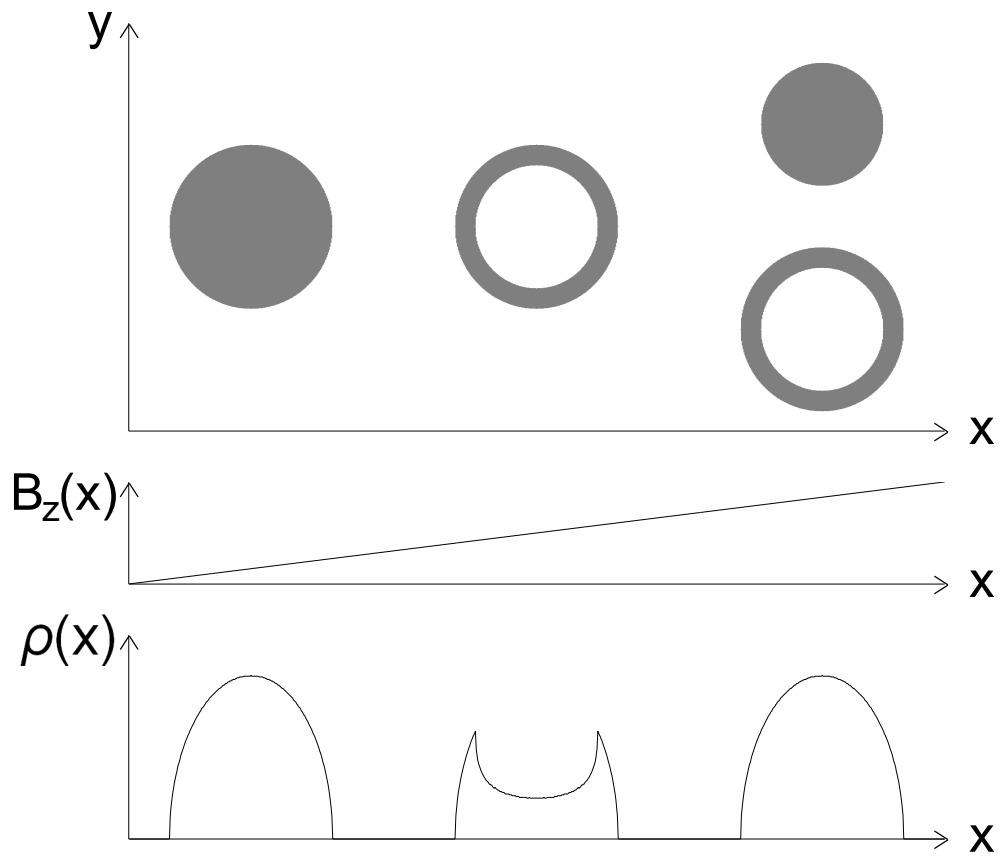


Figure 2.7: Example of using a one dimensional linear gradient  $B_z(x)$  to perform spatial encoding on the objects shown at the top of the plot. An inverse Fourier transform of the measured signal would result in the projection of  $\rho(x)$  shown at the bottom of the plot. Note that all information about the  $\rho(y)$  distribution is lost, as shown by the right hand objects.

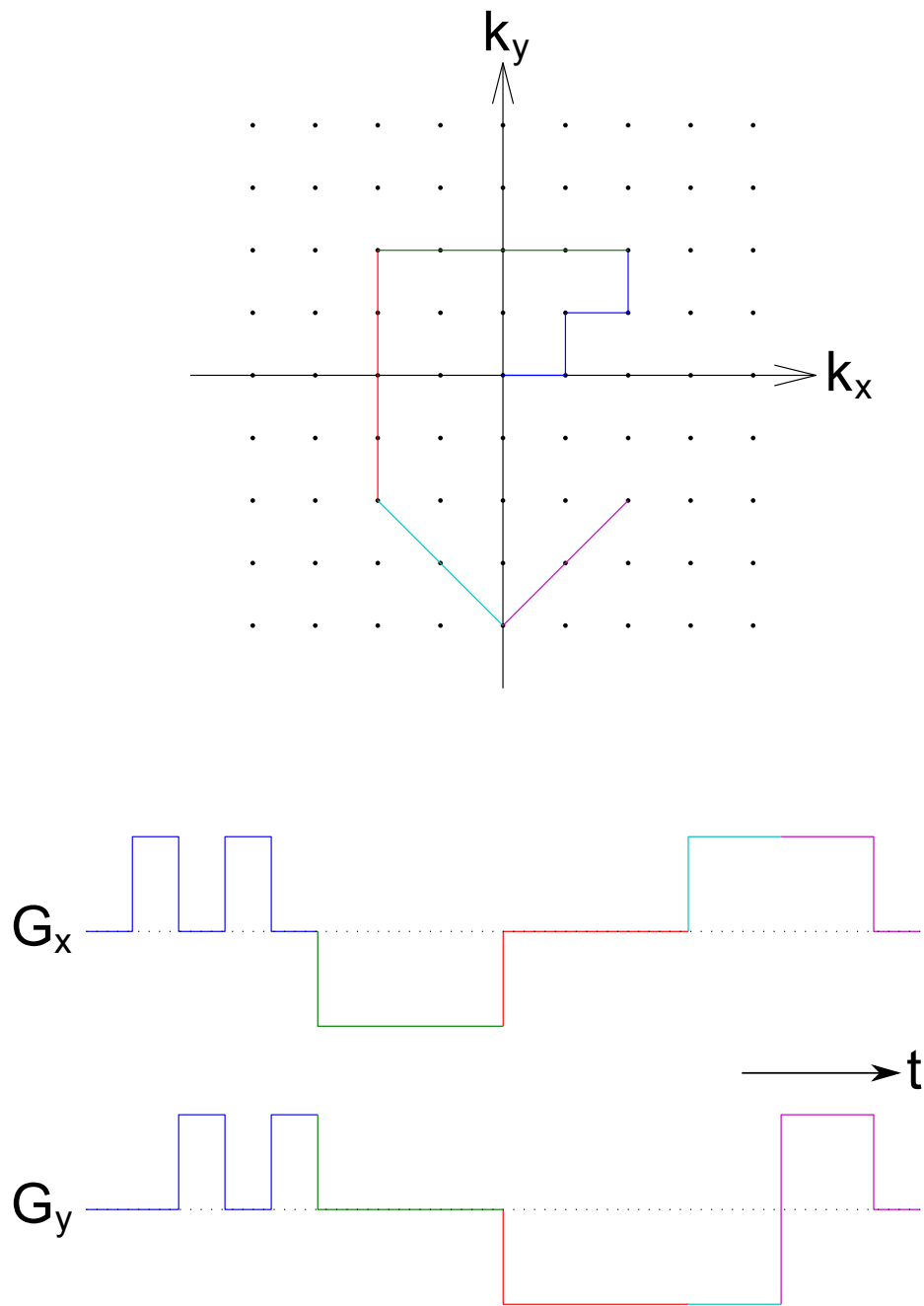


Figure 2.8: Plot illustrating the effect of linear gradient ( $G_x$ ,  $G_y$ ) combinations in two dimensions on k-space trajectory. Each stage is colour coded, such that the effect of gradients (bottom) can be seen on the k-space trajectory (top).

amplitude. The box-car shape is used here as it is easier to display and does not have a significant impact on the subsequent theory.

### Slice selection

The examples shown so far have involved mapping k-space in one or two dimensions. This effectively gives a two-dimensional projection of  $\rho$ , where each point includes all associated points from the third dimension. It is often desirable to only excite a finite volume of the sample, for example to select a discrete slice and spatially encode across only two dimensions.

A slice of the sample can be selectively excited by applying a field gradient  $G_{\text{slice}}$  at the same time as the radio-frequency pulse  $B_1(t)$ , which varies in a direction perpendicular to the slice (referred to as the *slice direction*). The gradient causes a spatial dependence of precession frequency in the slice direction. The radio-frequency pulse can be designed to only excite spins precessing over a limited range of frequencies, selecting a specific slice of the sample. A radio-frequency pulse taking the form of a sinc function in time will excite spins with a well-defined range of precession frequencies  $\Delta\omega$ . The reason for this is that the Fourier transform of a sinc function is a box-car (*figure 2.9a*), which is non-zero over a distinct range of frequencies ( $\Delta\omega$ ). This range of selected frequencies depends on the shape of the sinc function. The thickness of the slice selected will therefore depend on both the gradient amplitude  $G_{\text{slice}}$  and on  $\Delta\omega$ . Real radio-frequency pulses have a finite duration, so the sinc function is truncated. The Fourier transform resulting from this truncated sinc function has less well-defined edges, but is a good approximation of a box-car.

*Figure 2.9b* shows an example pulse sequence diagram of slice selection. The radio-frequency pulse is centred halfway along the slice-selection gradient. Following the radio-frequency pulse the gradient will cause phase to accumulate in the slice direction. This is corrected by a negative gradient lobe, half the duration of the positive lobe.

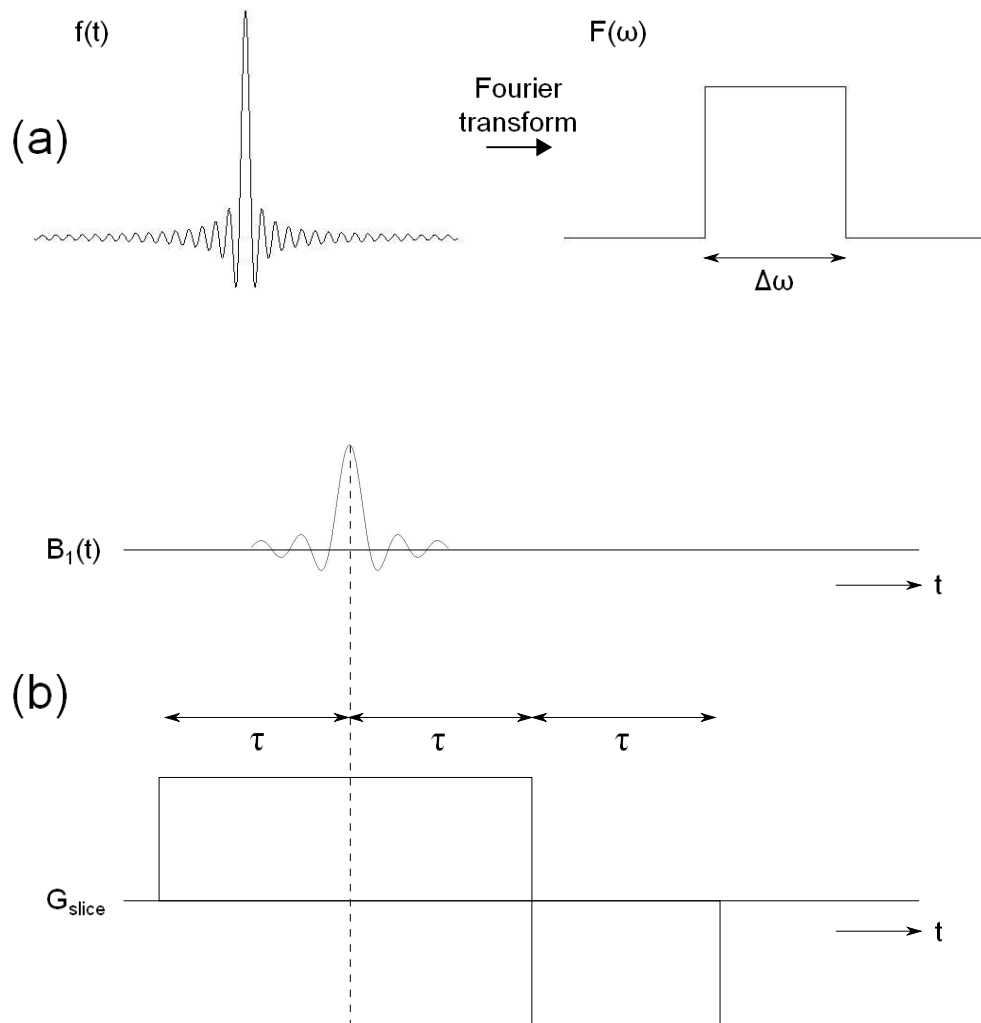


Figure 2.9: Demonstrating the principles of slice selection. (a) A sinc function has a box-car Fourier transform, so is a good choice for the slice selective radio-frequency pulse shape since it has a well defined frequency distribution. (b) Pulse sequence diagram of slice selection. A radio-frequency pulse is applied, centred a time  $\tau$  after the start of the slice selective gradient. The gradient has a positive lobe for slice selection (duration  $2\tau$ ) and a negative lobe (duration  $\tau$ ) to refocus phase accumulated during slice selection.

### 2.3.3 Pulse sequences

This section describes a selection of common pulse sequences. Although other k-space trajectories may be used (such as radial and spiral trajectories), only Cartesian k-space trajectories are used here. A Cartesian coordinate system is defined, with three orthogonal dimensions of  $k_{\text{slice}}$ ,  $k_{\text{read}}$  and  $k_{\text{phase}}$ . The  $k_{\text{slice}}$  dimension is the slice selection dimension as defined in the previous section. The  $k_{\text{read}}$  dimension is the *readout* or *frequency-encoded* dimension and the  $k_{\text{phase}}$  dimension is the *phase-encoded dimension*.

#### $T_2^*$ -weighted sequences: Basic gradient echo

The frequency-encoded and phase-encoded dimensions are illustrated using the example in *figure 2.10*. Following slice selection, gradients are applied in both the frequency-encoded dimension ( $G_{\text{read}}$ ) and phase-encoded dimension ( $G_{\text{phase}}$ ), selecting a k-space coordinate ( $k_{\text{read}}$ ,  $k_{\text{phase}}$ ). Following these gradients, a frequency-encoding gradient is applied of opposite amplitude and twice the duration of the previous gradients. This subsequent gradient causes transverse relaxation to refocus in a gradient echo (as described in the previous section), with a peak at the mid-point of the gradient lobe. Signal is detected during this subsequent gradient, sampling k-space along the  $k_{\text{read}}$  direction, with a constant  $k_{\text{phase}}$ . Therefore the phase-encoding gradient selects the  $k_{\text{phase}}$  value to be sampled. In a basic gradient echo pulse sequence, as shown in *figure 2.10*, only one line of k-space (with one  $k_{\text{phase}}$  value) is sampled from each radio-frequency pulse. Multiple repeats are performed, each with a different  $G_{\text{phase}}$  amplitude, to fully sample k-space. This takes a significant length of time ( $\sim 5T_2$ ) as transverse magnetisation needs to return to thermal equilibrium steady state (through  $T_2$  decay) in between radio-frequency pulses. The time between the radio-frequency pulse and the mid-point of the  $G_{\text{read}}$  lobe is defined as the TE.

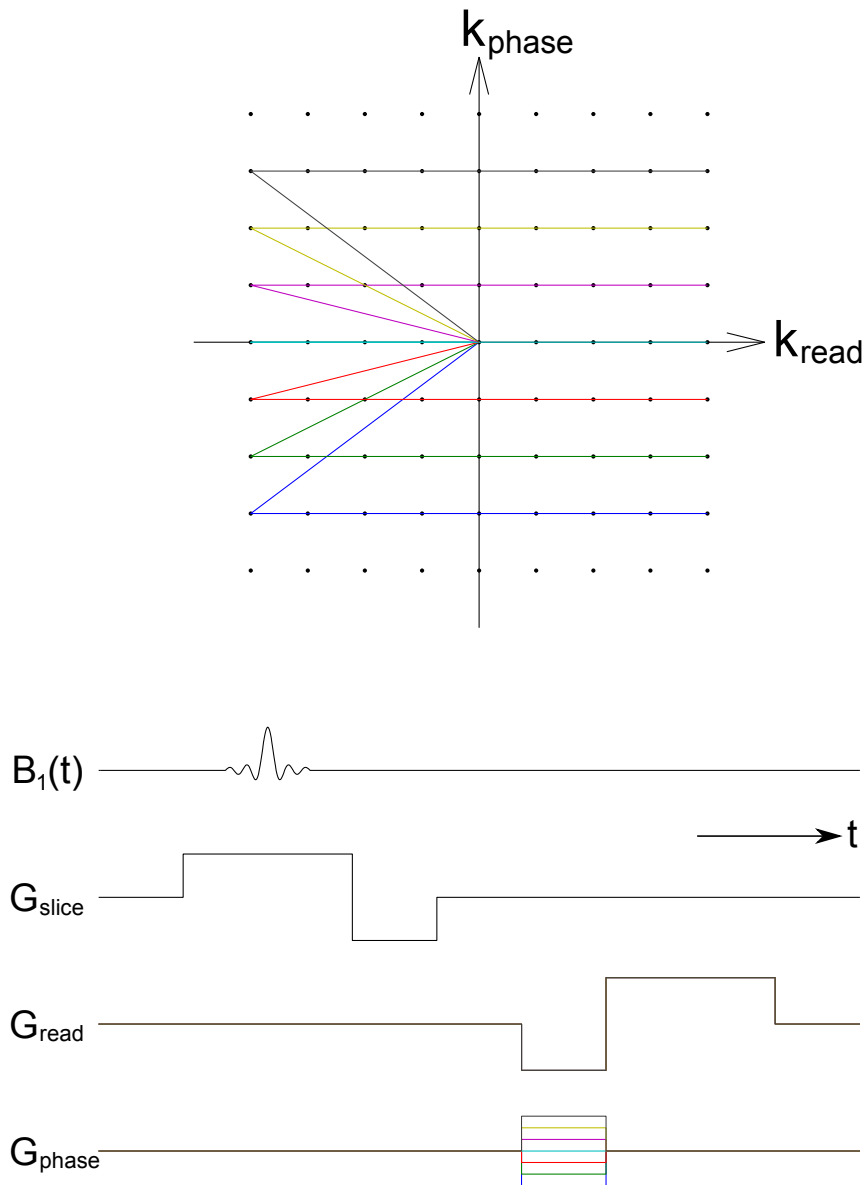


Figure 2.10: The k-space trajectories and pulse sequence diagram for a simple gradient echo imaging sequence. Multiple repeats (corresponding to different colours) are required to sample k-space in both dimensions.

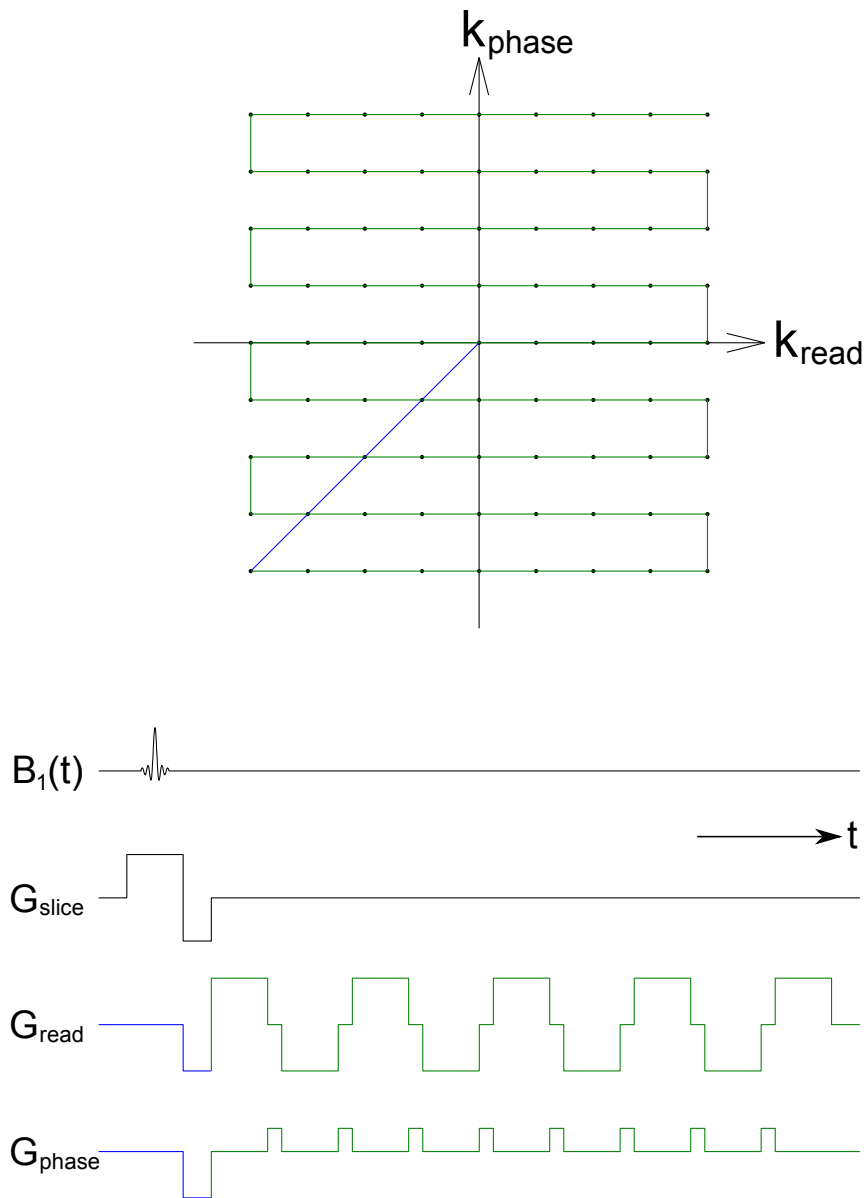


Figure 2.11: *Echo-planar imaging* (EPI) k-space trajectory and pulse sequence diagram. The blue gradient lobes select the initial k-space coordinates, whilst a train of  $G_{\text{read}}$  lobes, alternating between positive and negative gradients, cause a series of gradient echoes to form.  $G_{\text{phase}}$  lobes positioned between  $G_{\text{read}}$  lobes selects the  $k_{\text{phase}}$  coordinate to be sampled with each echo.

## $T_2^*$ -weighted sequences: Echo-planar imaging

There are a variety of sequences which sample more than one line of k-space following a single radio-frequency pulse. The most extreme example is single shot *echo-planar imaging* (EPI). This is where a series of gradient echoes (an *echo train*) are formed following a single radio-frequency pulse, with each echo sweeping  $k_{\text{read}}$  at a different  $k_{\text{phase}}$  coordinate. EPI is the most commonly used pulse sequence in this thesis, so is described in detail here. It is possible to acquire all (single shot) or part (interleaved) of k-space following a single radio-frequency pulse. An example k-space trajectory and pulse sequence diagram is shown in *figure 2.11*. Each gradient echo is formed by reversing the  $G_{\text{read}}$  amplitude, alternating between positive and negative gradient lobes. In between  $G_{\text{read}}$  (frequency encoding) lobes, short  $G_{\text{phase}}$  lobes sweep across  $k_{\text{phase}}$  for phase encoding. To save time, the initial gradients for selecting the starting k-space position (blue in *figure 2.11*) overlap with the refocussing lobe of the slice select gradient. The series of gradient echoes are represented by a single TE, located at the center of k-space, so at the midpoint of the  $G_{\text{read}}$  lobe where  $k_{\text{phase}} = 0$ .

Short acquisition times make EPI a popular choice for studying dynamic changes, however this technique has several problems associated with its fast nature. The effect of acquiring a series of echoes within a single  $T_2^*$  decay is that each echo (and so different  $k_{\text{phase}}$  coordinates) will have different amplitudes. This will act as a filter causing spatial blurring.

Imperfections in the spatial encoding gradients lead to offsets in the gradient echo position relative to the  $G_{\text{read}}$  lobes. The result of this is to introduce a ghost image displaced from the original image by half of the field of view in the phase-encoded direction, called a Nyquist ghost. This can be corrected for prospectively by correcting for these imperfections in the sequence design.

Reversal of  $G_{\text{read}}$  amplitude between echoes means that this technique is susceptible to any imperfection which will have opposite effects on the positive and negative spatial gradients (termed phase errors), resulting in offsets in

adjacent lines of k-space that build up across echoes. This can be corrected for by taking an initial reference image, which is identical to the EPI, except in that it lacks phase-encoding gradients. This reference image can be used to measure and remove these offsets due to switching the frequency encoding direction in adjacent echoes.

The acquisition bandwidth for EPI is low and the sampling time is long in the phase-encoded direction compared to a basic gradient echo. Macroscopic field inhomogeneities will cause particularly large distortions for EPI due to this low bandwidth. The effect of a field inhomogeneity is to cause a frequency shift (*equation 2.2*), so spatial encoding will give a shifted position for regions experiencing this inhomogeneity. The magnitude of this shift will depend on the field inhomogeneity frequency shift as a fraction of the bandwidth. Therefore the image will either be stretched or compressed due to the field inhomogeneity. These distortions can be corrected retrospectively by using maps of the field inhomogeneities [15], or prospectively by applying shim gradients to partially cancel with the inhomogeneities. Field inhomogeneities within a voxel (a volume element, the volume equivalent to a pixel) will also cause intra-voxel dephasing, which is where dephasing due to the field inhomogeneity is not refocussed with the gradient echo, causing signal loss which is unrecoverable without using a spin echo.

EPI is particularly affected by chemical shift of the signal from fat. Hydrogen nuclei in fat molecules experience a different molecular environment from water, so microscopic field variations due to their molecular environment lead to a shift in their precession frequency. Therefore spatial encoding gradients will cause the fat signal to appear slightly displaced from its actual location. This displacement is cumulative across the phase-encoding gradients [14], leading to large displacements of the fat signal along the phase-encoding direction, with larger displacement from smaller amplitude gradients. The resulting fat signal appears shifted with respect to the brain and can appear to overlap the brain. Several methods exist to reduce the fat signal, such as selective saturation of the fat signal.

After the first EPI echo train, it is possible to apply another set of refocussing gradients and sample k-space again, at a later TE (see *figure 2.12*). Repeated samplings of k-space can be performed following a single radio-frequency pulse, within the constraint of sufficient signal within the  $T_2^*$  decay. This can be used to form two or more images, each at a different TE (defined as the center of k-space for each echo train, as for the single echo train). These are referred to as a *double echo* EPI acquisition for the case of two images and *multi-echo* for more than two echoes. The number of images that can be acquired during a single  $T_2^*$  decay depends on the duration of each echo train and on the  $T_2^*$  of the sample of interest. This type of sequence can be used to map  $T_2^*$  [16].

### $T_2^*$ -weighted sequences: Ernst angle

Following the initial radio-frequency pulse, the recovery of longitudinal magnetisation to thermal equilibrium values obeys the Bloch equations (*equations 2.5*), taking several multiples of  $T_1$  to do so. Ideally, to maximise signal and minimise  $T_1$ -weighting of the resulting images, the *repetition time* (TR) between acquiring consecutive images should also be several multiples of  $T_1$ . However, to measure dynamic changes, or to shorten the experiment time when repeated measurements are required, it may be desirable to acquire images at faster intervals, increasing temporal resolution. When the longitudinal magnetisation has not fully recovered between consecutive radio-frequency pulses, following several such pulses the longitudinal magnetisation reaches a steady state of less than the thermal equilibrium value. This is demonstrated for a series of  $90^\circ$  radio-frequency pulse, each separated by a time TR equal to  $T_1$ , in *figure 2.13*.

For long TR experiments, where longitudinal magnetisation is almost at thermal equilibrium values,  $90^\circ$  radio-frequency pulses give the maximum signal. However, for shorter TR experiments, a smaller flip angle will preserve more longitudinal magnetisation for the next radio-frequency pulses. Although a smaller proportion of the total magnetisation is available in the transverse

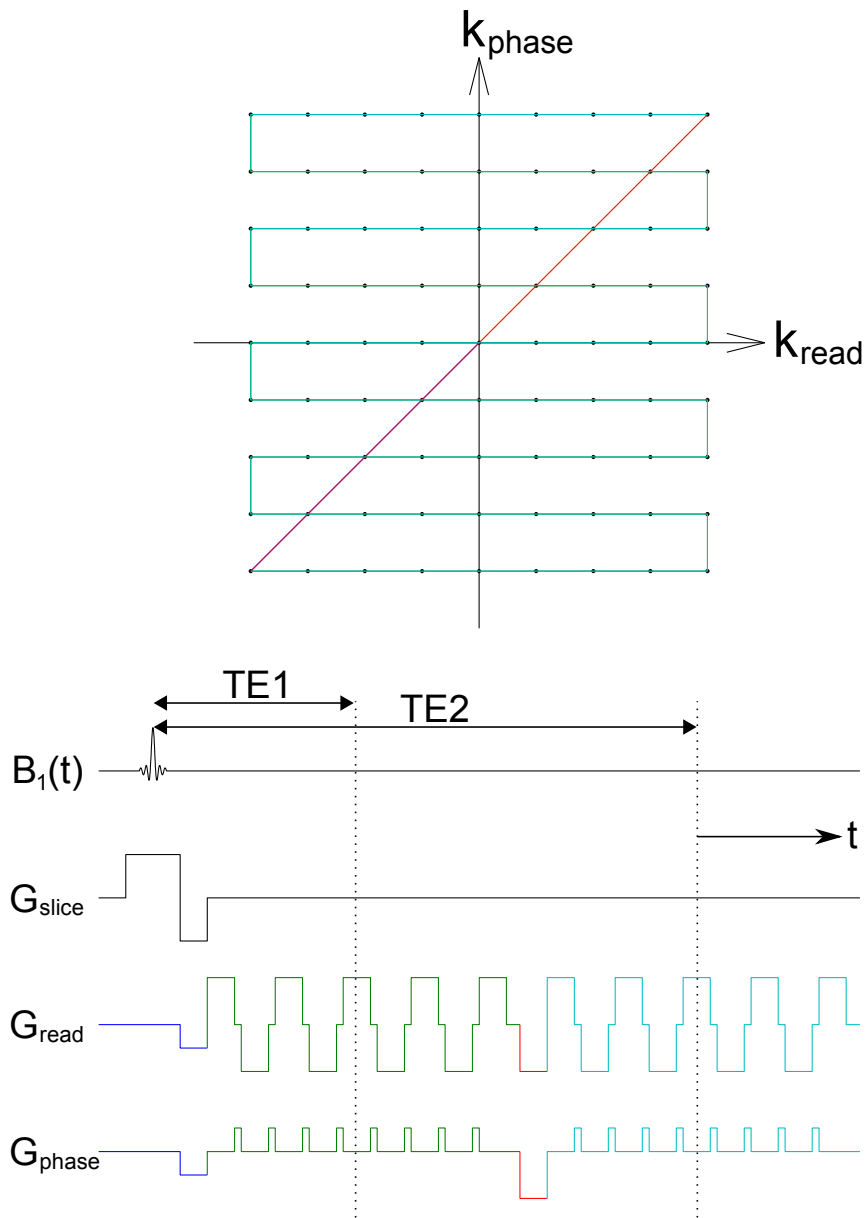


Figure 2.12: Double echo EPI k-space trajectory and pulse sequence diagram. The first echo train (identical to *figure 2.11*) is followed by a set of refocussing gradients (red), followed by an additional echo train, to sample k-space for a second time, at a later TE ( $TE_2$ ). The echo times for both echo trains ( $TE_1$  and  $TE_2$ ) are the time from the radio-frequency pulse to the center of k-space for each.

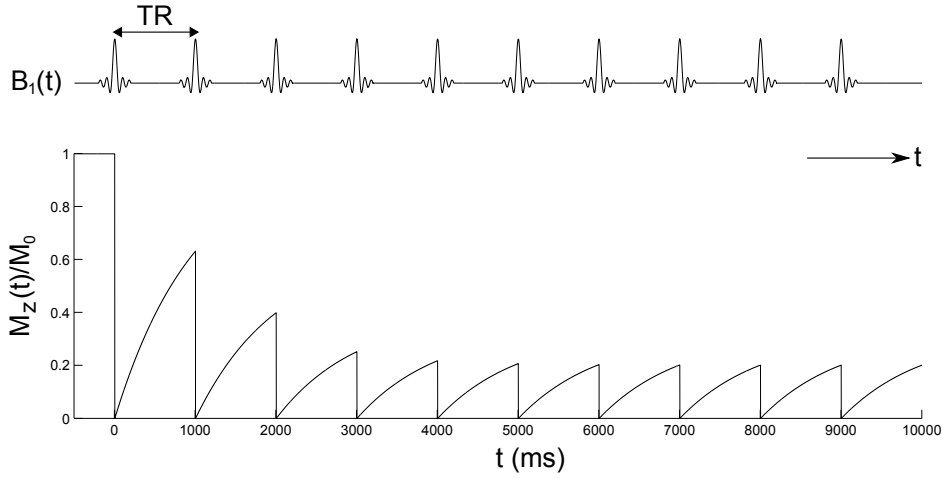


Figure 2.13: Example of the effect of a series of radio-frequency pulses on longitudinal magnetisation. In this case  $90^\circ$  radio-frequency pulses were used and  $TR = T_1 = 1000$  ms. Longitudinal magnetisation (immediately before the next radio-frequency pulse) reaches a steady state after approximately 5 TRs in this case.

plane, more is preserved for later repeats, resulting in higher transverse magnetisation once a steady state is reached. There is a compromise between a smaller flip angle preserving more longitudinal magnetisation when steady state is reached and a larger flip angle leading to a larger fraction of longitudinal magnetisation converted into transverse magnetisation for detection. The optimum angle, providing the highest transverse magnetisation for a given TR and  $T_1$  (once a steady state is reached) is known as the *Ernst angle* ( $\theta_E$ ), such that

$$\theta_E = \cos^{-1} \left( e^{-TR/T_1} \right) \quad (2.12)$$

$\theta_E$  (in degrees) is plotted as a function of the ratio TR to  $T_1$  in *figure 2.14*.

### $T_2^*$ -weighted sequences: FLASH (Spoiled gradient echo)

When high spatial resolution images are required, EPI is not the best choice of gradient echo acquisition, as the echo train length increases with finer spatial resolution and compounds the above issues. An alternative is to use a series of low flip angle radio-frequency pulses and a short TR to acquire multiple

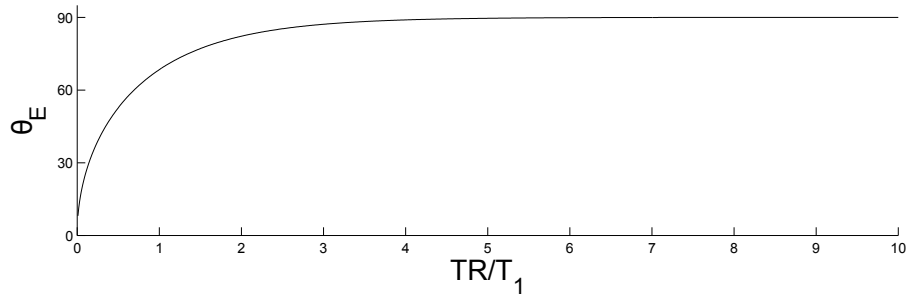


Figure 2.14: Dependence of  $\theta_E$  (in degrees) on the ratio between TR and  $T_1$ .

lines of k-space in a short space of time. This approach acquires a single line of k-space following each radio-frequency pulse, so is far less susceptible to distortions than an EPI acquisition. It is able to sample k-space in a short amount of time compared to a basic gradient echo due to the short TR, so is less susceptible to subject motion. The TR values can be so short that transverse magnetisation has not decayed to zero between radio-frequency pulses. Spoiler gradients can be applied to dephase transverse magnetisation before the next radio-frequency pulse. The resulting image can be weighted by  $T_1$  and/or by  $T_2^*$ , based on the TR and TE values chosen relative to the sample's  $T_1$  and  $T_2^*$ , respectively. Names for this low angle, short TR, spoilt sequence include *fast low angle shot imaging* (FLASH) and *spoiled gradient echo*. The pulse sequence is shown in *figure 2.15*.

### **$T_2$ -weighted sequences**

A  $T_2$ -weighted image can be formed by using a  $90^\circ$  radio-frequency pulse, followed by a  $180^\circ$  radio-frequency pulse a time TE/2 later. A spin echo will form a time TE after the  $90^\circ$  radio-frequency pulse, as shown in *figures 2.4 and 2.5*. The  $90^\circ$  radio-frequency pulse can be tailored for slice selection, with the associated gradients (*figure 2.9*). Spatial encoding gradients can be applied so that a gradient echo forms at the same time as the spin echo, so the resulting image will only depend on  $T_2$  and not  $T_2^*$ . A long TR is required, to prevent  $T_1$ -weighting. For the case of an ideal, static sample,  $T_2$  could be measured by repeating this sequence for various TE values and fitting the resultant signal

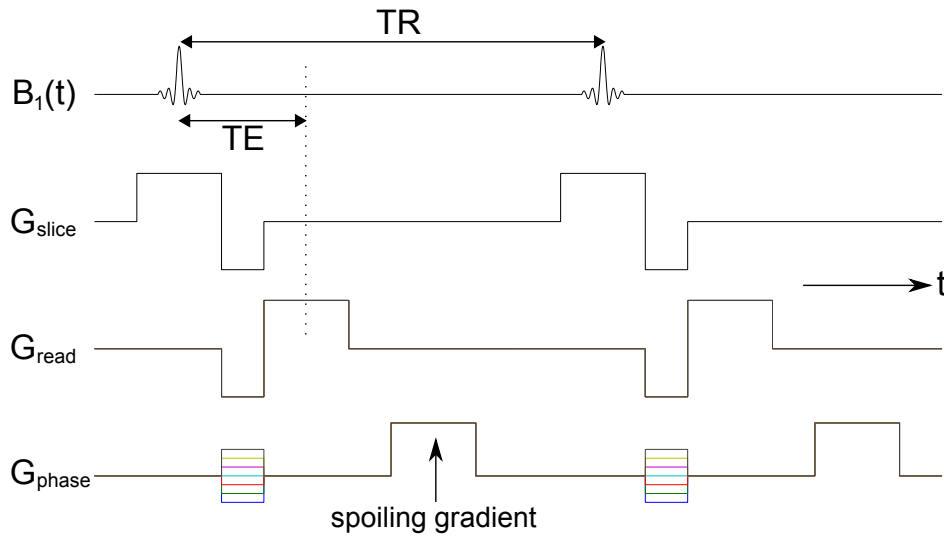


Figure 2.15: Example of a FLASH (spoiled gradient echo) pulse sequence. Due to the short TR, spoiler gradients are required to dephase any remaining transverse magnetisation before the subsequent low angle radio-frequency pulse. These spoiler gradients are shown in the phase-encoded direction, but may be applied in multiple dimensions.

to an exponential decay curve.

Water molecules undergo diffusion, so if there are any field inhomogeneities across the sample, diffusing  $^1\text{H}$  spins will accumulate phase as they move across the field homogeneity in a random walk. This phase will not be refocussed by the  $180^\circ$  radio-frequency pulse, resulting in reduced net transverse magnetisation and an attenuation of the measured signal. This phase accumulation (and hence signal attenuation) will be dependent on the amount of molecular motion (described by a *diffusion coefficient*  $D$ ), the field homogeneity amplitude and on the TE. A  $T_2$  measurement of a sample undergoing diffusion using the method described in the previous paragraph will therefore underestimate  $T_2$ , due to diffusion-based signal attenuation having a TE dependence.

A method for reducing the effects of diffusion on  $T_2$  measurements is to apply a series of  $180^\circ$  radio-frequency pulses following the initial  $90^\circ$  radio-frequency pulse, known as a *Carr-Purcell Meiboom Gill* (CPMG) sequence [17, 18]. The first  $180^\circ$  radio-frequency pulse is applied a time  $TE/2$  after the  $90^\circ$  radio-

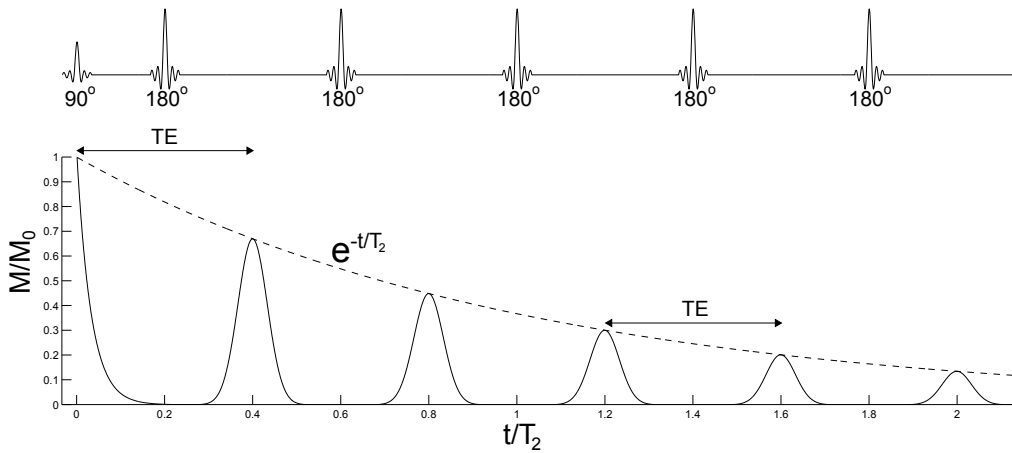


Figure 2.16: Net transverse magnetisation during a CPMG pulse sequence

frequency pulse and the separation between  $180^\circ$  radio-frequency pulses is TE. An echo train will form with each echo occurring at integer multiples of TE after the initial  $90^\circ$  radio-frequency pulse (as shown in *figure 2.16*). The effects of diffusion on the  $T_2$  measurement is reduced by using short echo separation times (TE), limiting diffusion-based phase accumulation.

### $T_1$ -weighted sequences

Any short TR (TR of the order of  $T_1$  or shorter) sequence will have some  $T_1$ -weighting, however it is possible to control the  $T_1$ -weighting using a  $180^\circ$  radio-frequency pulse, applied before the  $90^\circ$  radio-frequency pulse. The time between these two pulses is known as the *inversion time* (TI). This arrangement can be applied preceding imaging gradients, such as EPI as shown in *figure 2.17*. Following a  $180^\circ$  radio-frequency pulse, net longitudinal magnetisation is inverted and it recovers back to thermal equilibrium values based on a solution to the Bloch equations, as shown in *figure 2.18*. This sequence can be used to measure  $T_1$  by repeating the sequence several times, with different TI values. The TR needs to be long compared with  $T_1$ , so that longitudinal magnetisation fully recovers between repeats. This type of sequence is known as an *inversion recovery* (IR) sequence.

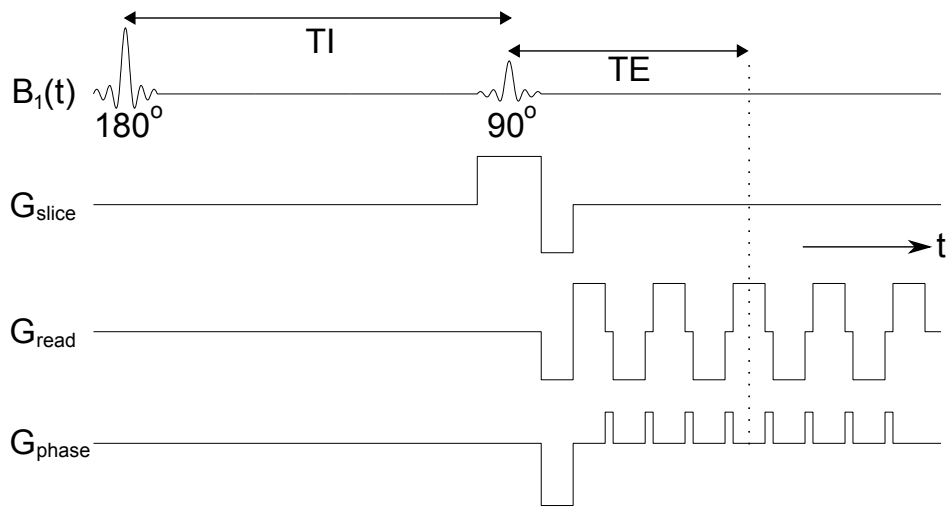


Figure 2.17: *Inversion recovery* (IR) EPI pulse sequence diagram. The TI is the time between  $180^\circ$  and  $90^\circ$  radio-frequency pulses and the TE is the time from the  $90^\circ$  radio-frequency pulse to the center of k-space, as with other EPI sequences.

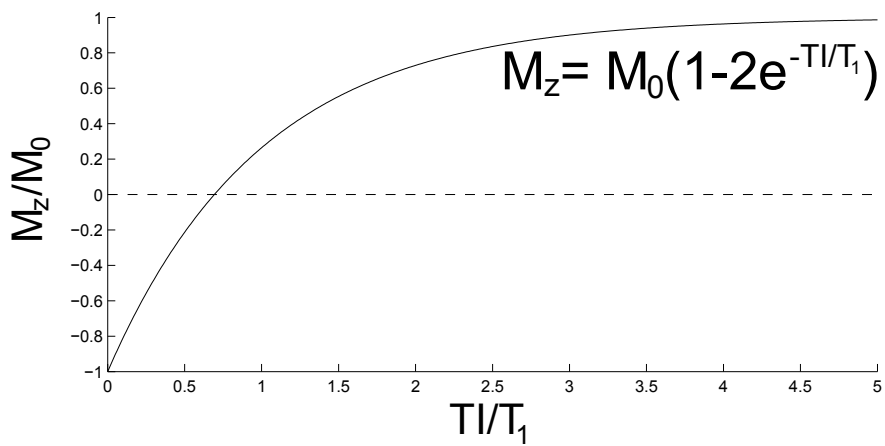


Figure 2.18: A plot of the behaviour of net longitudinal magnetisation following a  $180^\circ$  radio-frequency pulse.

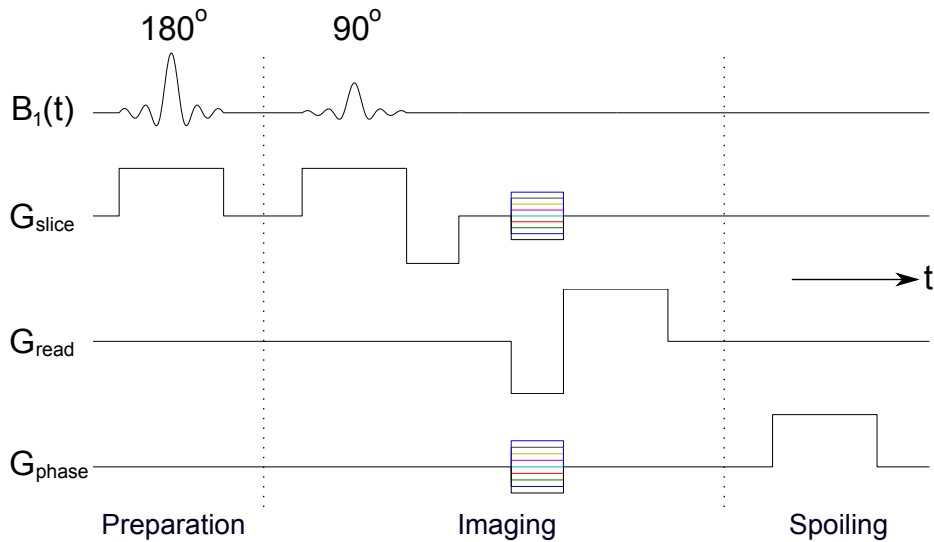


Figure 2.19: Example of an MPRAGE pulse sequence. This consists of three stages; preparation, imaging and spoiling; as separated by vertical dotted lines. Multiple repeats of the imaging and spoiling stages can be performed for a single preparation stage, to measure multiple  $k_{\text{phase}}$  and  $k_{\text{slice}}$  lines. In this case, the k-space center is positioned to be at the appropriate TI.

Finally, a  $T_1$ -weighted pulse sequence will be described, which is widely used to acquire high spatial resolution anatomical images. This is a *magnetisation-prepared rapid gradient echo* (MPRAGE) acquisition. An MPRAGE sequence (as shown in figure 2.19) consists of three stages; preparation, imaging and spoiling. The magnetisation preparation stage includes a  $180^\circ$  radio-frequency pulse, to control the  $T_1$ -weighting. The imaging stage can be three-dimensional, by the use of spatial encoding blips in the slice selection direction. In this case, slice selection will excite a wide volume, instead of a single slice and the spatial encoding blips cycle through the slice dimension in k-space ( $k_{\text{slice}}$ ). Short TR values are typically used, such that spoiler gradients are required to dephase any remaining net transverse magnetisation before subsequent radio-frequency pulses. Due to the short TR, the radio-frequency pulses are usually a lot less than  $180^\circ$  and  $90^\circ$ , respectively, to preserve longitudinal magnetisation for the next radio-frequency pulse.

### 2.3.4 Parallel imaging

It is possible to reduce the time required to acquire an image by reducing the number of k-space lines acquired. This will effectively reduce the field of view in the phase encoded direction, so the image will wrap around, leading to the signal from multiple points in space occupying the same point in the spatially encoded signal (aliasing). Where multiple receive coils are used, this aliasing can be resolved by using the spatial sensitivity profiles of each coil, combined with the wrapped around image from that coil [19]. The relative intensities measured for each position from each coil can be used to separate out the aliased signal from multiple positions, using the different sensitivity profiles of each coil to that spatial position. This technique is known generically as parallel imaging, but when implemented on the Philips scanners used in this work, it is known as SENSE. One advantage to this method is for EPI, where the low bandwidth in the phase encoded direction leads to large image distortions from field inhomogeneities, especially at higher field strengths. Acquiring less lines of k-space will lead to an increased bandwidth, reducing these distortions.

### 2.3.5 Safety considerations

The safety issues arising from working around an MRI scanner are briefly summarised in this section. The static field can disrupt electronic medical equipment, such as pace-makers, so people with such a device fitted are not allowed within the 0.5 mT field line surrounding each magnet. For the scanners used in this work, access to these areas is restricted by key-coded doors. Ferromagnetic objects could become projectiles when brought into proximity with the strong static magnetic field, so careful consideration is made to ensure that no one brings such objects into the magnet hall. This especially involves reminding anyone going into the magnet hall to remove keys, coins and jewellery before entering the magnet hall. In the event of an extreme situation, the static magnetic field can be ramped down by pressing one of several red buttons, located in the magnet hall and the control room. This heats up part of the coil to make it resistive, dissipating the current and quickly reducing the induced magnetic field. It is likely that this will damage the scanner and

it will take a significant amount of time to ramp the scanner back up to the desired field. One reason for this safety precaution would be if a person was pinned to the magnet by a large piece of ferromagnetic equipment such that they were in danger of serious harm.

Cryogenic liquids (commonly helium) are used to cool the superconducting coils. The commercial scanners are designed in such a way that the cryogenic liquid is vented out through the roof of the scanner, so should not enter the magnet hall, reducing the risk of a person being exposed to the cryogenic liquid. Also, the static coils and shimming and imaging gradient coils experience very high voltages. The scanners are designed to be well insulated, such that the risk of electrocution is negligible so long as this insulation remains intact. Imaging gradient coils can heat up during use, so water cooling is used to dissipate this heat.

Fast switching imaging gradients exert mechanical forces on the magnet bore, which causes it to vibrate, causing a loud noise. This is especially so for EPI acquisition. Therefore anyone present in the magnet hall, especially the volunteer in the bore, requires ear protection. Ear plugs and headphones are routinely provided for this purpose. For the 7 T scanner, there is a local head transmit coil, which prevents the use of headphones through spatial constraints, so foam padding is used to cover the ears and attenuate the sound. The walls of the magnet hall attenuate sound sufficiently such that anyone present outside of the magnet hall, for example in the control room, does not require ear protection. Another problem with the fast switching imaging gradients is that they can induce currents in nerves peripheral to the imaging region (an effect known as *peripheral nerve stimulation* (PNS)). This problem is increased with increasing static field strength, maximum gradient strength and gradient slew rate. For experiments imaging the head, this can stimulate peripheral nerves in the shoulders. Typically gradients are limited so that only a mild form is experienced, such that the subject feels a slight muscle twitch across the shoulders.

The radio-frequency time-varying fields can cause some energy absorption by tissue, which will result in a mild heating of the tissue. The *signal attenuation ratio* (SAR) is used to determine whether the energy absorption due to a set of radio-frequency pulses is safe. Metallic objects will absorb much more energy than tissue, so any metallic objects, such as jewellery should be removed before scanning. Some tattoos contain metal pigment, which can heat up under radio-frequency pulses, therefore care must be taken when scanning subjects with tattoos. If equipment is required in the bore which uses conducting wires, then these wires must not touch the subject's skin. Also, these wires should not cross over each other.

## 2.4 functional Magnetic Resonance Imaging

The practice of using MRI to dynamically monitor changes in physiology associated with neuronal activity is known as *functional magnetic resonance imaging* (fMRI). A direct measurement of neuronal activity would be to measure neuronal firing rate. This can be done using non-invasive methods, by measuring the small electric or magnetic field perturbations arising from neuronal currents (electroencephalography and magnetoencephalography, respectively). However, although these methods have high (sub millisecond) temporal resolution, they have low spatial resolution and they are much more sensitive to signals close to the surface of the head, rather than deep in the brain. The main advantage of using fMRI to measure cerebral activity is the high spatial resolution available with MRI. Current fMRI methods measure localised changes in vascular properties, focussed around changes in neuronal activity. It is worth noting the different categories of neuronal activity, such as neuronal firing rate, local field potentials, multi-unit activity and single-unit activity, however local field potentials are thought to be most closely correlated to fMRI measures [20].

This section introduces the connection between cerebral activity and the associated vasculature. The principles underlying  $T_2^*$ -weighted blood oxygenation level dependent (BOLD) contrast are described, followed by a comparison with

other fMRI techniques. The concept of calibrated BOLD fMRI is introduced and some of its limitations are discussed, which will be addressed in the following chapters.

### 2.4.1 Physiology underlying fMRI

The human brain has a constant energy demand, which is met through the aerobic metabolism of oxygen ( $O_2$ ) and glucose. Blood vessels supply oxygen and glucose to brain tissue and remove carbon dioxide ( $CO_2$ ) and water ( $H_2O$ ), which are the products of this aerobic metabolism. Local increases in neuronal activation will lead to an increased energy demand, which is met by a local increase in oxygen and glucose metabolism [21, 22]. A local increase in the supply of oxygen and glucose per unit time to the active tissue is achieved by a local increase in *cerebral blood flow* (CBF).

CBF is a measure of perfusion, the volume of blood feeding a unit of tissue per unit time. Commonly used units for CBF are ml/100g/min (millilitres of blood supplying 100 grams of tissue per minute). CBF in human grey matter is of the order of 60 ml/100g/min and approximately three times higher than in white matter [23]. Another vascular property, which is of importance for fMRI, is the *cerebral blood volume* (CBV), which is the volume occupied by blood vessels, often expressed as a fraction of tissue volume. In an MRI context, it is useful to consider CBV as the volume fraction of a voxel which is occupied by blood vessels.

The vascular network consists of artery, arteriole, capillary, venule and vein blood vessels, as shown in *figure 2.20a*. Large arteries supply blood to cerebral tissue, branching out into smaller arterioles, which themselves branch into capillaries. Oxygen and glucose pass into neuronal cells from capillaries and the products of aerobic metabolism ( $CO_2$  and  $H_2O$ ) pass into the capillaries. Capillaries feed into venules, which in turn feed into veins which drain the cerebral tissue. Arterioles, venules and capillaries are defined as *microvasculature*, whereas arteries and veins are defined as *macrovasculature*.

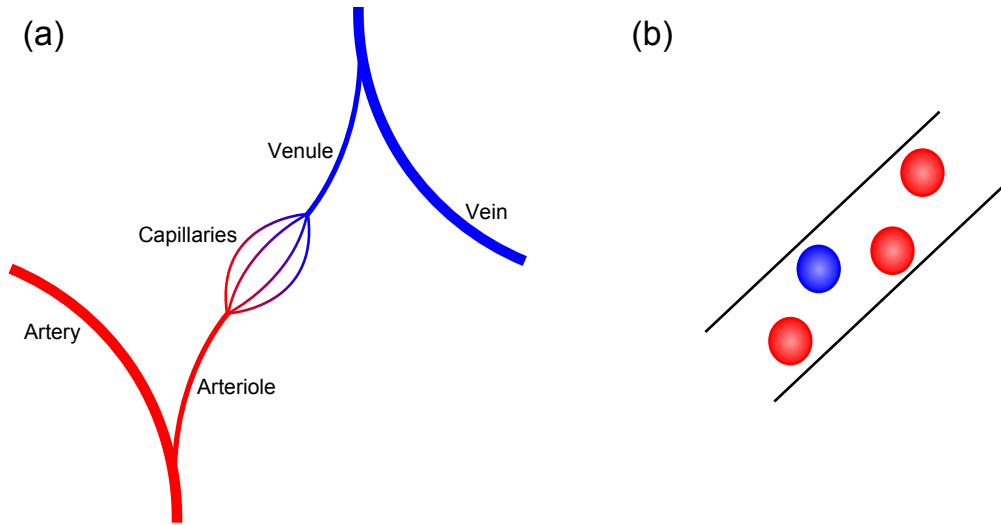


Figure 2.20: (a) A simple illustration of different types of blood vessels. (b) Blood vessels contain haemoglobin, which is either bound to oxygen (oxygenated haemoglobin, red circle) or not (deoxygenated haemoglobin, blue).

Oxygen is transported in blood through being bound to haemoglobin molecules in red blood cells. Haemoglobin has a high affinity to oxygen, so the majority of oxygen in blood is bound to haemoglobin. In this case the molecule is described as *oxygenated haemoglobin* (Hb), whereas without oxygen the molecule is described as *deoxygenated haemoglobin* (dHb). The oxygen saturation of haemoglobin in blood is referred to as *blood oxygenation* ( $Y$ ), here defined as the fraction of total haemoglobin molecules that are bound to oxygen

$$Y = \frac{\sum \text{Hb}}{\sum \text{Hb} + \sum \text{dHb}}. \quad (2.13)$$

For arteries and arterioles, almost all haemoglobin molecules are bound to oxygen ( $Y \sim 1$ ), shown in red in *figure 2.20a*. Blood oxygenation decreases through the capillary bed, such that approximately 40 % of haemoglobin is not bound to oxygen in the venules and veins ( $Y \sim 0.6$ ), shown in blue in *figure 2.20a*.

Accompanying a period of increased neural activity, local CBF increases and blood vessels dilate causing an increase in local CBV. The increase in CBF leads to more oxygen being supplied to the active tissue. The increased *rate of cerebral oxygen metabolism* ( $\text{CMRO}_2$ ) in the active tissue means that more

oxygen is used. However, upon neuronal activation, local CBF increases exceed the  $\text{CMRO}_2$  increases [24], such that although more oxygen is being used by the active tissue, even more is supplied, so the fraction of total supplied oxygen that is extracted by the active tissue (the *oxygen extraction fraction*, OEF) is reduced upon neuronal activation. Therefore during neuronal activation the blood oxygenation of venules and veins draining the active tissue increases.

### 2.4.2 Blood Oxygenation Level Dependent signal contrast

The most commonly used form of fMRI is gradient echo *blood oxygenation level dependent* (BOLD) signal contrast. The gradient echo BOLD signal is due to the dependence of  $T_2^*$  on deoxygenated haemoglobin (dHb) [1, 2], providing a non-invasive method of monitoring neuronal activation, whilst having the highest *signal to noise ratio* (SNR) and *contrast to noise ratio* (CNR) of any current fMRI method, with the possible exception of contrast agent enhanced fMRI methods. This section presents the theory of the BOLD signal change in  $T_2^*$ -weighted images.

#### BOLD signal models and simulations

Magnetic susceptibility is a property of an object which determines the magnetisation of an object in the presence of a magnetic field. The volume susceptibility ( $\chi_v$ ) of dHb has been measured as  $\chi_v = (-0.483 \pm 0.013) \times 10^{-6}$  [25], whereas oxygenated haemoglobin (Hb) has a volume susceptibility  $\chi_v = (-0.749 \pm 0.010) \times 10^{-6}$  which is very close to blood plasma  $\chi_v = (-0.714 \pm 0.007) \times 10^{-6}$  and water  $\chi_v = -0.719 \times 10^{-6}$  [25]. Therefore tissue (which is predominantly water), blood plasma and Hb can be considered magnetically similar, whereas the presence of dHb will cause a field perturbation. Note that  $\chi_v$  is presented in *cgs units*, for consistency with the literature. These values can be converted to *SI units* through multiplication by  $4\pi$ .

The effect of dHb on  $T_2^*$  can be separated into two components, one from

tissue adjacent to the blood vessel (termed *extravascular*) and one from the signal within the blood vessel (termed *intravascular*). The extravascular signal contribution has been the subject of many simulations and models [26, 27, 28, 29, 30, 31, 32, 33]. The source of the extravascular BOLD signal is the field inhomogeneity arising from blood vessels containing dHb. An example of this field inhomogeneity is shown in *figure 2.21*, which is based on an infinite cylinder model of a blood vessel [31] and with the main magnetic field ( $B_0$ ) perpendicular to the cylinder axis. The field inhomogeneity (and hence the extravascular BOLD signal) depends on the orientation of the blood vessel to the main magnetic field. If the blood vessel is near parallel to the main magnetic field, then the field inhomogeneity due to the vessel will be minimal, whereas if the blood vessel is perpendicular to the main magnetic field, then the field inhomogeneity is at a maximum.

There are two mechanisms by which the field inhomogeneity will affect extravascular  $T_2^*$ . The first is static dephasing, where different spin isochromats experience different fields due to the inhomogeneity and precess at different frequencies, resulting in signal attenuation. The second is diffusive dephasing, where water molecules move across the field inhomogeneity in a random walk, accumulating phase based on the field experienced. Where static dephasing dominates, the transverse relaxation rate  $R_2^*$  will vary linearly with the susceptibility difference between the blood vessel and tissue ( $\Delta\chi_v$ ). However, where diffusive dephasing dominates, there will be a quadratic relationship between extravascular  $R_2^*$  and  $\Delta\chi_v$  [27]. Intermediate regimes are also possible, where both mechanisms contribute, leading to a relationship between  $R_2^*$  and  $\Delta\chi_v$  of somewhere between linear and quadratic. Whether the static or diffusive dephasing mechanism dominates depends on the amount of diffusion and the size of the gradient of the field inhomogeneity. Simulations have shown that the dominant mechanism depends on the frequency shift created by  $\Delta\chi_v$  and on vessel size [31], with larger vessels and a larger  $\Delta\chi_v$  leading to the static dephasing mechanism dominating. This is expanded on in *chapters 4 and 5*.  $\Delta\chi_v$  is linearly related to the dHb fraction  $(1 - Y)$  [25], so similar linear or quadratic relationships will hold between  $R_2^*$  and  $(1 - Y)$ . Extravascular  $R_2^*$  is

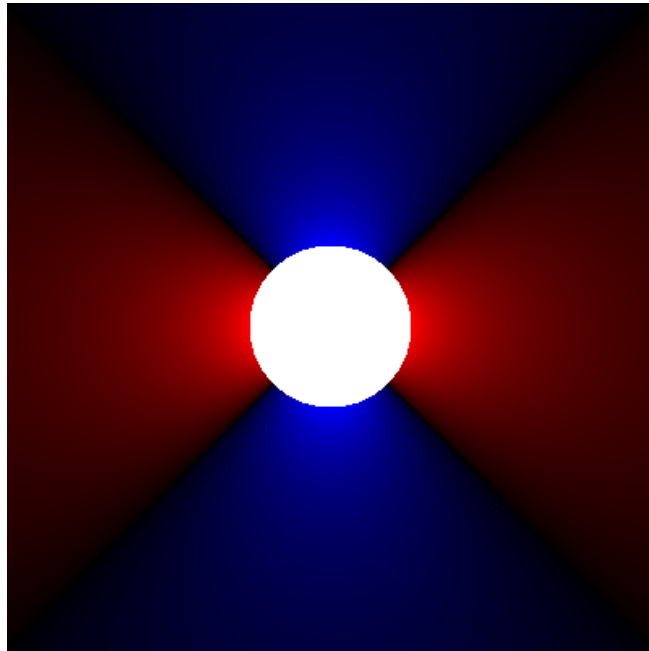


Figure 2.21: Image illustrating the extravascular field perturbations resulting from a cylindrical blood vessel with a susceptibility difference from the surrounding tissue. Positive field perturbations are shown in red and negative field perturbations in blue, with lighter colours showing a larger magnitude perturbation. In this example, the background field is in a horizontal direction and is perpendicular to the cylindrical vessel.

also linearly dependent on CBV, as will be further discussed in *chapter 6*.

The intravascular BOLD signal arises from water molecules in blood plasma. The gradient echo signal from these water molecules is both affected by field inhomogeneities and also by  $T_2$  shortening due to nearby dHb molecules. The relationship between intravascular  $R_2^*$  and  $(1 - Y)$  is quadratic [34].

The total BOLD signal for a voxel will depend on a combination of extravascular and intravascular components, weighted by their relative volume contributions (so  $(1 - \text{CBV})$  and  $\text{CBV}$ , respectively). In summary, the BOLD signal will depend on  $Y$  and  $\text{CBV}$ .  $Y$  will depend on both  $\text{CBF}$  and  $\text{CMRO}_2$ , so the BOLD signal can be considered as being dependent on  $\text{CBF}$ ,  $\text{CBV}$  and  $\text{CMRO}_2$ . The BOLD signal is therefore not a direct measure of neuronal activity, also depending on local vascular structure, causing a haemodynamic variability in the BOLD signal which is independent of the neuronal activity. The compartment which provides the dominant contribution to the BOLD signal contains a significant amount of dHb, and as such arterial and arteriolar blood vessels can be ignored and the  $\text{CBV}$  contributions from capillaries, venules and veins can be considered in isolation. Finally, it is worth noting that the BOLD signal contribution from large veins draining the active tissue will mean that the BOLD signal has a wider spatial extent than the actual active tissue spatial extent [3].

### **BOLD temporal characteristics**

The temporal characteristics of the BOLD signal are dependent on the temporal characteristics of the underlying  $\text{CBF}$ ,  $\text{CBV}$  and  $\text{CMRO}_2$  changes in response to the neuronal activation. The dynamic nature of the vascular properties, such as  $\text{CBF}$ ,  $\text{CBV}$  and  $\text{CMRO}_2$ , are referred to as *haemodynamic* properties. The temporal characteristics of the BOLD signal following an event can be separated into three features, as shown in *figure 2.22*. Following the onset of a task which increases neural activity, there is an initial reduction in BOLD signal called the *initial dip*, with typical duration of approximately  $\sim 2$  seconds. There is then a large increase in BOLD signal, sometimes known as

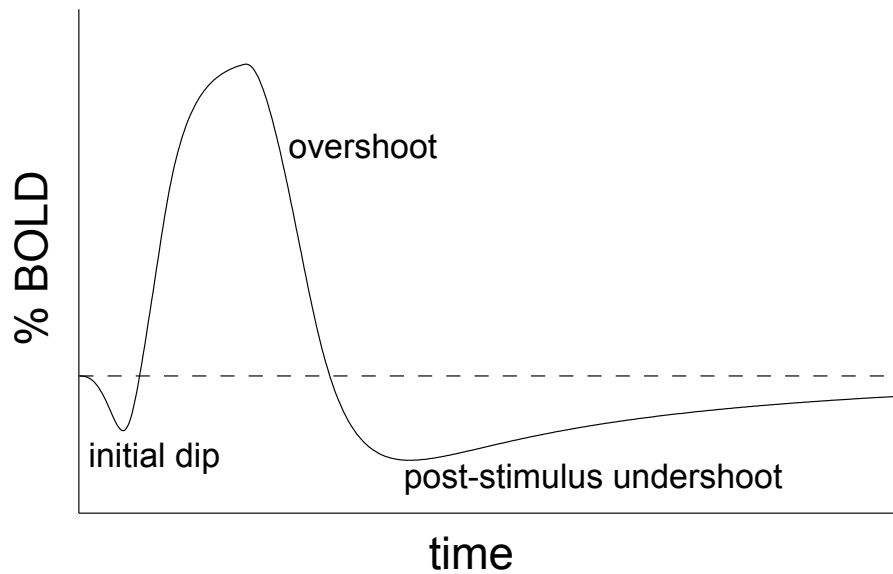


Figure 2.22: A simulated BOLD signal curve, illustrating the three main features of the BOLD response to a single event. The dashed line indicates the baseline signal level.

the positive BOLD response or *overshoot*, occurring  $\sim 6$ – $8$  seconds after the task onset. This is followed by a subsequent decrease in BOLD signal, such that it drops below the baseline value, called the *post-stimulus undershoot*, before slowly recovering back to the baseline value, up to a minute after the task ended. Here, the baseline value is defined as the signal before the period of increased neural activity. Note this is not an absolute baseline, which might imply no neuronal activity or oxygen extraction.

The initial dip is an elusive feature, with a short duration and small amplitude (of the order of 1 % [35, 36]). It is not well understood since most fMRI paradigms are not sensitive enough to detect it. The source of the initial dip is thought to be due to an increase in  $CMRO_2$  before a CBF increase. This causes an increase in dHb, leading to a decrease in BOLD signal. One of the reasons the initial dip is of interest is that it may have better spatial localisation to the active tissue [35] and might show potential for measuring the relative change in  $CMRO_2$  on activation, due to not being confounded by changes in CBF and CBV [36].

The positive BOLD signal may be referred to as an overshoot since it is caused by a CBF increase which exceeds the CMRO<sub>2</sub> increase, causing an increase in Y, despite an increased oxygen consumption. The amplitude of this feature depends on the task, local vasculature, field strength and TE, but a typical value of 3–4 % might be expected at 3 T, with TE = 45 ms. Although the main feature of the BOLD response is most commonly the positive signal change, negative BOLD responses have been observed, for example in the motor cortex ipsilateral to hand motion [37, 38] and in the medial occipital cortex [39]. There is interest in identifying whether this negative BOLD signal is neuronal or vascular in origin [37].

The post-stimulus undershoot occurs several seconds after the end of the task and has a typical amplitude of approximately half that of the positive BOLD overshoot. It is the subject of extensive research and the mechanism behind it is the subject of some debate. One theory is that the negative signal arises from a delayed recovery of CBV after CMRO<sub>2</sub> and CBF have returned to baseline [40, 41]. Other studies suggest that the negative signal is due to a sustained CMRO<sub>2</sub> increase after CBF and CBV have recovered to baseline [42, 43, 44, 45]. The post-stimulus undershoot appears to be dependent on the type of task performed and the task duration, for example static and flashing chequerboards result in similar positive BOLD responses, but different post-stimulus undershoot amplitudes [46]. The undershoot may provide better spatial localisation to the active tissue, compared with the positive BOLD response [47].

The BOLD signal response can be considered as a convolution of the neuronal activity with the *haemodynamic response function* (HRF) acting as a temporal filter, such that the observed BOLD response is blurred in time compared to the neuronal activity. Without knowing the underlying haemodynamics, it is possible to approximate this HRF to a summation of gamma variate functions [48, 49, 50]. The gamma variate parameters have been optimised experimentally to form a *canonical HRF* [49, 50]. The canonical HRF can

be convolved with the task design to form a model timecourse for statistical analysis of fMRI datasets, to identify regions of an image whose timecourse has a significant correlation with this model timecourse.

### 2.4.3 BOLD experiment design and analysis

This section introduces the concepts behind BOLD experimental design and typical analysis steps commonly performed. The stimulus or task that will lead to a change in neuronal activation can be presented continuously over a long period (called a *block paradigm*), or for a single instance or short period on the order of a second or less (called an *event-related paradigm*). Periods of stimulus are referred to as the *active period*. These periods are typically interspersed with periods with no stimulus, which are referred to as the *rest period*. For a block paradigm, the active period typically has a duration of between a few seconds to a minute, with the rest period duration being of a similar length or slightly longer. The durations of active and rest periods depend on the type of stimulus and the experimental objectives.

Typically for gradient echo BOLD fMRI, a fast imaging sequence is used, which can image a large volume in a short amount of time and as such EPI is a popular sequence for fMRI. The acquisition parameters are very important in optimising the SNR and BOLD contrast between active and rest states. A short TR will lead to a reduced signal, as discussed in *section 2.3.3*, whilst a longer TR will limit the dynamic changes that can be monitored. This compromise between signal and temporal resolution will depend on the experimental objectives, for example as to whether fast dynamic changes are being monitored or changes between steady states. For gradient echo BOLD contrast the optimal TE is close to the  $T_2^*$  of the tissue of interest (cortical grey matter), as illustrated in *figure 2.23*.

Before statistical analysis is performed on the BOLD dataset to locate regions of significant stimulus-related signal changes, several processing steps are commonly performed. These include motion correction or realignment, temporal filtering, physiological noise correction and spatial smoothing. Motion correc-

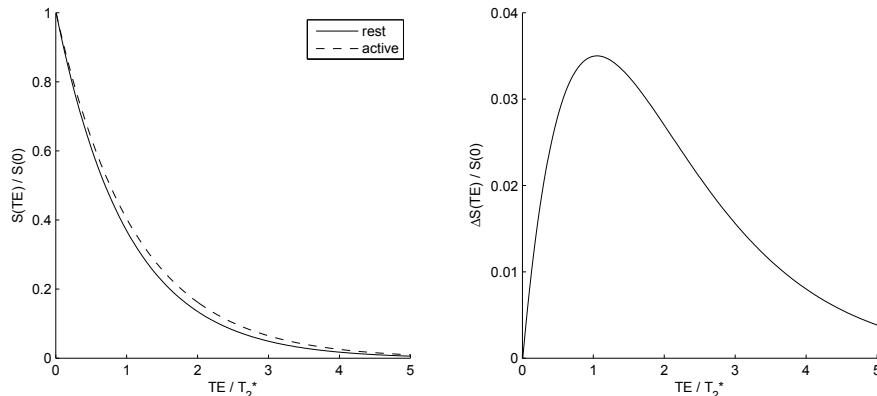


Figure 2.23: Plot illustrating the effect of TE on the signal change due to a change in  $T_2^*$ . The left hand plot shows a  $T_2^*$  decay at rest (solid line), compared to a  $T_2^*$  decay during an active condition (dashed line), simulated by a 10 % increase in  $T_2^*$ . The resulting signal difference is shown in the right hand plot, with a maximum when  $TE \sim T_2^*$ .

tion can be used to partially correct for subject motion through the paradigm. This works by realigning all dynamic images to a common reference image, using a 6 parameter rigid body algorithm based on intensity matching. High-pass temporal filtering will remove low frequency components in the timecourse of each voxel, thus removing low frequency signal drift. The cut-off frequency for this filter should be less than the repetition frequency of the stimulus paradigm, to minimise the effect of the filter on the BOLD response to the task. Low-pass temporal filtering smooths the dataset in the temporal dimension, improving temporal SNR at the expense of temporal resolution. Physiological noise correction corrects for signal intensity changes due to the respiratory and cardiac cycles. This correction uses data on these cycles recorded during the scan [51], using respiratory bellows and either a pulse oximeter, or a vector cardiogram (VCG) to monitor the respiratory and cardiac cycles, respectively. One particular method of physiological correction used in this thesis is known as RETROICOR [51]. Spatial smoothing is often used to sacrifice spatial resolution for increased SNR. This is applied by convolving the image with a smoothing kernel, where a gaussian kernel is typically used. Typical gaussian smoothing functions have a full width at half maximum of  $1.5 \times$  the voxel size.

Typical statistical analysis performed on the BOLD dataset involves forming a model timecourse through convolution of the task design with a canonical HRF. The BOLD dataset is compared to the model timecourse and a statistical test is performed as follows. Firstly, voxels with significant correlation to the model timecourse are defined by a Z-score threshold corresponding to a particular uncorrected P-value. For example, typically a threshold of  $Z > 2.3$  corresponds to an uncorrected  $P < 0.01$ , so 1 out of every 100 voxels will be a false positive result. The second step is to select clusters of voxels passed by the first test, by considering the *familywise error* (FWE) to test each cluster of voxels against a corrected P-value, typically using  $P < 0.05$ .

#### 2.4.4 Other fMRI techniques

This section outlines other fMRI techniques, the vascular origin of these signals used to monitor neuronal activation and compares them to gradient echo BOLD. The main focus of this section is spin echo BOLD and *arterial spin labelling* (ASL) methods for measuring CBF changes, but a number of other methods are also mentioned to provide an overview of fMRI techniques.

So far, only gradient echo (GE) BOLD has been discussed, BOLD contrast can also be obtained from spin echo images. The intravascular component of spin echo (SE) BOLD signal is primarily due to dHb shortening intravascular  $T_2$ . Extravascular spin echo BOLD signal arises from the same mechanisms as extravascular gradient echo BOLD signal, described above. However, the spin echo refocusses static dephasing, but not diffusive dephasing. Therefore extravascular spin echo BOLD contrast is based on the diffusive dephasing mechanism, meaning that extravascular spin echo BOLD signal is restricted to smaller diameter vessels than gradient echo [31]. The extravascular spin echo BOLD signal contrast is thus spatially restricted to closer to the active tissue, rather than including large contributions from large draining veins, as happens with gradient echo BOLD contrast. As well as being spatially closer to the neuronal activation than gradient echo, the spin echo BOLD response has also been shown to be temporally closer to the underlying neuronal activa-

tion, exhibiting a faster time to peak signal following the onset of a task [52]. Spin echo BOLD is also less susceptible than gradient echo BOLD to large field inhomogeneities, so can be used in regions where such an inhomogeneity is present, such as in the orbitofrontal cortex [53]. However, spin echo BOLD contrast is much lower than for gradient echo BOLD due to an insensitivity to static dephasing [31]. Therefore the SNR is much lower compared with gradient echo BOLD. For this reason, gradient echo BOLD is mostly used in preference to spin echo BOLD in regions without large field inhomogeneities, especially at lower field strengths where the total available signal is already low (*equation 2.4*).

The direct change in CBF due to increased neuronal activation can be measured using *arterial spin labelling* (ASL) [54]. The basic principle of ASL is to label water molecules in a slab of tissue adjacent to the region of interest, wait some time (the post-label delay) for arterial labelled water to flow into the region of interest and enter tissue through perfusion, then image that region. The *flow-sensitive alternating inversion recovery* (FAIR) labelling method will be described here as an example ASL scheme (since it is used in this work), however a wide variety of labelling methods have been proposed and are widely used [55, 56, 57, 58, 59]. The FAIR pulse sequence is similar to that of an inversion recovery pulse sequence (see *figure 2.17*), with an inversion  $180^\circ$  radio-frequency pulse a time TI before the  $90^\circ$  readout radio-frequency pulse. In FAIR, alternate dynamics are acquired with the inversion being non-selective and with the inversion being selective to a slab centred on, but slightly larger than the imaging volume to be imaged (since a real inversion spatial profile will not have discrete edges). All spins in the imaging region are inverted in both non-selective and selective dynamics, so the only difference will be from water molecules which enter the imaging region from outside the inversion slab in the time TI. The non-selective dynamic is referred to as the *tag* image and the selective dynamic is referred to as the *control* image, whilst adjacent non-selective and selective dynamics are grouped as a *tag/control pair*. Subtracting the tag image from the control image will remove all signal except from inflowing water molecules, giving the ASL signal.

One advantage of CBF fMRI over BOLD fMRI is that changes in CBF occur primarily in the microvasculature and not in large draining veins, so the active region measured by CBF fMRI will be more localised to the active tissue [60]. However, due to the limited signal from inflowing arterial water molecules, ASL has an intrinsically lower SNR than BOLD.

The first human fMRI experiments for mapping neuronal activity were performed using a gadolinium compound (Gd-DTPA), an exogenous contrast agent [61]. This method is sensitive to the change in total CBV local to active tissue. When in blood the gadolinium compound does not pass into tissue, but reduces the  $T_1$  of blood plasma and has a susceptibility difference from tissue. Extravascular  $R_2^*$  is increased with the same mechanisms as for dHb, dependent on the total blood volume (CBV) and on the concentration of the gadolinium compound in blood. Therefore changes in total CBV can be measured using the change in signal intensity, assuming a constant concentration of the gadolinium compound. This method has better SNR than gradient echo BOLD for a single trial, but due to subject safety (due to the risk of NSF (nephrogenic systemic fibrosis)) and due to the gadolinium compound taking a long time to washout, this method is not repeatable, unlike BOLD. This combined with the invasive delivery nature of the gadolinium compound (through intravenous injection) means that BOLD fMRI is preferred to contrast agent enhanced fMRI.

An alternative non-invasive measurement for total CBV fMRI has been proposed [62], which exploits the difference in  $T_1$  relaxation time between blood and tissue. This method is called *vascular space occupancy* (VASO). An inversion recovery type sequence is used where the TI is set to be at the nullpoint of blood, where the longitudinal magnetisation of blood is zero. Therefore only tissue signal remains. CBV increases related to neuronal activation are measured by the decrease in signal associated with tissue being displaced by increased blood volume. However, cerebral spinal fluid (CSF) can have a similar  $T_1$  to blood, so can confound CBV measurements. This method also has a

low SNR compared with BOLD fMRI measurements and is also strongly dependent on the inversion being homogeneous across the image, so longitudinal magnetisation from blood across the image is zero at the same TI.

The venous blood volume compartment CBV has been exploited as a source of fMRI contrast using a technique termed *venous refocussing for volume estimation* (VERVE) [63]. This technique makes use of the attenuation of a spin echo by diffusion. It uses two CPMG sequences, one with a very short echo spacing and one with a longer echo spacing. The difference in signal between the shorter and longer echo spacing datasets will depend on the volume of the dHb compartment (venous CBV). However, this technique has a very low SNR.

An fMRI technique which is not entirely vascular in origin is diffusion fMRI [64, 65]. This is where strong diffusion gradients are applied to suppress the signal from water with a large diffusion coefficient. It was found that the % BOLD signal in response to increased neuronal activation was enhanced when large diffusion gradients were applied. This was attributed to neuronal cells swelling on increased activation, where cells have a lower diffusion coefficient than the surroundings. Cell swelling would provide a measure of neuronal activation that was more direct than vascular measures. However, a recent study found a similar % BOLD enhancement using diffusion fMRI with hypercapnia [66], suggesting that diffusion fMRI has at least some vascular component.

#### **2.4.5 BOLD calibration**

The specific local vascular structure will affect the magnitude of the BOLD signal change, so the BOLD signal magnitude alone cannot be used as a direct indicator of neuronal activation magnitude. This is especially true in patient groups with compromised cerebrovascular function, such as stroke [67], or some cases of cancer [68], diabetes and sickle-cell disease. One method for accounting for the haemodynamic variability in the BOLD signal is to calibrate the BOLD signal [69]. This involves measuring some constant which represents the vascular contribution to the BOLD magnitude, so the neuronal contribution

can be separated out.

The method of calibrated BOLD proposed by Davis and co-workers [69] was to perform an additional hypercapnia stimulus, which can be used to calculate a calibration parameter. Hypercapnia will be discussed in more detail in *chapter 5*, but it provides a vasodilatory stimulus (increased CBF and CBV) whilst assuming that  $\text{CMRO}_2$  is unchanged by hypercapnia. This allows a probe of vascular properties independent of  $\text{CMRO}_2$ .

The model theory for calibrated BOLD is detailed here. This uses the simplified assumption that  $R_2^*$  is linearly proportional to CBV and is also proportional to the magnetic susceptibility difference ( $\Delta\chi$ ) between blood vessels and surrounding tissue, raised to a power  $\beta$ :

$$R_2^* \propto \text{CBV}(\Delta\chi)^\beta \quad (2.14)$$

The value of  $\beta$  depends on vessel size and on the vessel-tissue frequency shift, such that it takes a value between 1 and 2 as described in *section 2.4.2*. In the literature, it is commonly assumed that  $\beta = 1.5$ , a value calculated for 1.5 T [27, 31]. This relationship only describes the extravascular contribution to  $R_2^*$ . Total CBV is commonly used here, but since arterial blood is close to fully oxygenated, the arterial CBV contribution to  $R_2^*$  will be small compared to the venous CBV contribution, so using total CBV may not be appropriate here.

As mentioned in *section 2.4.2*,  $\Delta\chi$  is linearly proportional to the concentration of dHb ( $[\text{dHb}]$ ). Fick's principle of mass conservation is used such that  $[\text{dHb}]$  is linearly proportional to  $\text{CMRO}_2$  and inversely proportional to CBF [69]. The resulting change in  $R_2^*$  from a rest steady state (subscript *rest*), to an active steady state (subscript *act*), is:

$$\Delta R_2^* \propto \text{CBV}_{\text{act}} \left( \frac{\text{CMRO}_{2,\text{act}}}{\text{CBF}_{\text{act}}} \right)^\beta - \text{CBV}_{\text{rest}} \left( \frac{\text{CMRO}_{2,\text{rest}}}{\text{CBF}_{\text{rest}}} \right)^\beta \quad (2.15)$$

For a BOLD signal acquired with an echo time TE, assuming that  $\text{TE}\Delta R_2^* \ll 1$ , a linear approximation can be made relating BOLD and  $\Delta R_2^*$ , such that:

$$\frac{\Delta \text{BOLD}}{\text{BOLD}_{\text{rest}}} \propto \text{CBV}_{\text{rest}} \left( \frac{\text{CMRO}_{2,\text{rest}}}{\text{CBF}_{\text{rest}}} \right)^\beta \left[ 1 - \text{CBV} \left( \frac{\text{CMRO}_2}{\text{CBF}} \right)^\beta \right], \quad (2.16)$$

where  $\Delta\text{BOLD} = \text{BOLD}_{\text{act}} - \text{BOLD}_{\text{rest}}$ ,  $\text{CMRO}_2 = \frac{\text{CMRO}_{2,\text{act}}}{\text{CMRO}_{2,\text{rest}}}$ ,  $\text{CBF} = \frac{\text{CBF}_{\text{act}}}{\text{CBF}_{\text{rest}}}$  and  $\text{CBV} = \frac{\text{CBV}_{\text{act}}}{\text{CBV}_{\text{rest}}}$ .

The constants of proportionality and resting steady state terms can be grouped into a single parameter  $M$ :

$$\frac{\Delta\text{BOLD}}{\text{BOLD}} = M \left[ 1 - \text{CBV} \left( \frac{\text{CMRO}_2}{\text{CBF}} \right)^\beta \right] \quad (2.17)$$

The parameter  $M$  is the maximum possible BOLD signal change, corresponding to a condition where no dHb is present. This is the calibration parameter, which can be used as a measure of haemodynamic variability. This parameter can be measured using hypercapnia, as will be described in *chapter 5*.

A calibrated BOLD experiment is performed by acquiring  $T_2^*$ -weighted BOLD data and ASL CBF data during both a task and for a period of hypercapnia. Typically CBV is not measured directly, but the change in CBV is estimated assuming a coupling relationship between the change in CBV and the change in CBF [70], which will be discussed in detail in *chapter 6*. This assumed coupling relationship only holds for steady state conditions, whereas there is a more complicated relationship during dynamic changes in CBV [71, 72]. *Equation 2.17* can be rearranged, such that the relative change in  $\text{CMRO}_2$  (normalised by the resting steady state value) can be calculated based on the measured relative changes in BOLD and CBF during the task and the value of  $M$  calculated during hypercapnia. This relative change in  $\text{CMRO}_2$  provides an indication of neuronal activity which is independent of local vascular properties.

Three main issues are associated with this calibrated BOLD approach. Firstly, the signal model relating  $R_2^*$  to [dHb] only applies to the extravascular compartment, however this approach was originally applied at 1.5 T where the intravascular compartment is expected to provide the dominant signal contribution (as will be discussed in more detail in *chapter 4*). The extravascular signal model also assumes a supralinear power law relationship between  $R_2^*$  and [dHb] with  $\beta = 1.5$ , which was derived for 1.5 T. The frequency shift

( $\Delta\omega = \gamma \cdot \Delta B$ ) around a dHb containing blood vessel increases with field strength, such that there will be a higher relative contribution of static dephasing compared to diffusive dephasing for field strengths above 1.5 T (as described in *section 2.4.2*). Therefore the value of  $\beta$  will be closer to 1 at higher field strengths [31]. This is discussed in more detail in *chapter 5*.

Secondly, the assumed coupling relationship between CBV and CBF is based on total CBV measurements [70], whereas the BOLD signal is more sensitive to the venous compartment, which contains the majority of dHb. Venous CBV has been shown to increase by less than total CBV due to a large arterial CBV increase, in response to hypercapnia [73] and forepaw stimulation [74] in rats, whilst the coupling relationship between venous CBV and CBF in humans [75, 76] has been shown to be smaller than for total CBV. Therefore using the total CBV coupling relationship will lead to an overestimation in  $\text{CMRO}_2$  [75]. The flow-volume coupling relationship will be addressed in more detail in *chapter 6*.

Thirdly,  $\text{CMRO}_2$  calculations are very sensitive to errors in  $M$  [77, 78]. Using hypercapnia to measure  $M$  requires a measurement of the relative change in CBF due to hypercapnia. There is a large error associated with measuring the CBF response to mild hypercapnia with ASL, due to a small change in CBF associated with mild hypercapnia in comparison to that from neuronal activation in response to the task. This error propagates through to an error in  $M$ , which in turn leads to a large error in the calculation of  $\text{CMRO}_2$ . One solution for reducing the error associated with measuring  $M$  is to use hyperoxia instead of hypercapnia. This approach is described in *chapter 6*. The hyperoxia approach does not require a CBF measurement, as it is assumed that CBF is unchanged during hyperoxia (an assumption that will be discussed in *chapter 6*).

## 2.5 Conclusion

The underlying physics of NMR has been introduced, followed by the application of NMR to imaging using spatially varying magnetic field gradients. A description of the haemodynamic physiology underpinning fMRI techniques has been presented and the origin of gradient echo BOLD. Finally, the vascular variability associated with fMRI techniques was presented and how this can be overcome by a calibration experiment to measure changes in oxygen metabolism.

The issues with fMRI that will be dealt with in this work are listed here. The BOLD response is delayed with respect to the temporal characteristics of the underlying neuronal activation. *Chapter 4* investigates how this delay is affected by field strength. The vascular nature of the BOLD response means that differences in vascular structure and reactivity across brain regions will lead to different BOLD responses from what may be equivalent changes in neuronal activity. *Chapter 5* illustrates this vascular source of BOLD variability by using hypercapnia to measure the inter-hemispheric difference in vascular reactivity between two equivalent brain regions, the left and right precentral gyri. The calibrated BOLD approach presented in *section 2.4.5* uses a model for relating  $R_2^*$  to blood oxygenation which is derived at 1.5 T and may not apply at higher field strengths. *Chapter 5* measures this relationship at higher field strengths, using a graded hypercapnia paradigm performed both at 3 T and 7 T. An assumed coupling relationship between CBV and CBF is required for this calibrated BOLD approach, which is poorly characterised. This is addressed in *chapter 6*, where the task causing increased neuronal activity is repeated at both normoxia and hyperoxia to account for changes in CBV without requiring a coupling relationship.

# Chapter 3

## Modulation of blood gases

### 3.1 Introduction

This chapter describes methods for modulating arterial CO<sub>2</sub> and O<sub>2</sub> content. The technique used in this work to deliver controlled levels of CO<sub>2</sub> and O<sub>2</sub> is discussed, with consideration to implementing this method in an MRI environment. Other methods of modulated inspired gases are discussed along with safety considerations associated with modulating arterial CO<sub>2</sub> and O<sub>2</sub> content.

Blood CO<sub>2</sub> and O<sub>2</sub> content are measured in terms of gas partial pressure (PCO<sub>2</sub> and PO<sub>2</sub> respectively). Since arterial blood gas measurements are invasive, it is commonly accepted to sample exhaled (end-tidal) gas content, as a close correlate of arterial gas content. The end-tidal partial pressures of CO<sub>2</sub> and O<sub>2</sub> ( $P_{ETCO_2}$  and  $P_{ETO_2}$  respectively) best reflect alveolar gas content, which is in equilibrium with arterial gas content. The standard SI unit of pressure is the Pascal (Pa), where the approximate atmospheric pressure at sea level is 10<sup>5</sup> Pa. However, a non-SI unit system is commonly used when measuring PCO<sub>2</sub> and PO<sub>2</sub>; mmHg. In this unit system, atmospheric pressure at sea level is 760 mmHg and approximately 133 Pa corresponds to 1 mmHg. The work presented here uses mmHg units, the units used by the apparatus, and for comparison with the literature.

## 3.2 Theory

The technique used to control and modulate  $P_{ET}CO_2$  and  $P_{ET}O_2$  in this work is a *feed-forward low gas flow* method. This technique was implemented using a Respiract™ system (Thornhill Research Inc., Toronto, Canada). This section provides an overview of the principles underlying the feed-forward low gas flow method of controlling  $P_{ET}CO_2$  and  $P_{ET}O_2$ .

The basis for this method is a rebreathing sequential gas delivery (SGD) circuit, which can be used to hold  $P_{ET}CO_2$  and  $P_{ET}O_2$  fairly constant, independent of changes in ventilation (breathing depth and pace) [79]. This uses fresh gas, supplemented by a reserve gas, which has approximately the same composition as alveolar gas, so only the fresh gas supplied affects arterial blood gas composition. In this case the reserve gas is previously exhaled gas, which is assumed to have the same composition as alveolar gas.

The rebreathing SGD circuit used in this work is shown in *figure 3.1*. A continuous supply of fresh gas flows into the inspiratory gas reservoir and gas flows from the inspiratory gas reservoir to the mask upon inspiration. Once the inspiratory gas reservoir is collapsed, the remainder of the inspiratory demand is met by reserve gas from the exhaled gas reservoir. The valve system works to ensure that fresh gas is inspired first before being supplemented by the reserve gas and the valve system prevents exhaled gas from entering the inspiratory gas reservoir. Slits in the bottom corners of the exhaled gas reservoir vent excess reserve gas and these close as the reservoir collapses to prevent entraining room air.

A simple model of the lungs is used, consisting of two compartments, alveoli and anatomical dead space. Only gas entering the alveolar compartment can pass into the bloodstream, and alveolar gas exchanges with blood gas such that alveolar and arterial  $PCO_2$  and  $PO_2$  are in equilibrium. The anatomical dead space includes the trachea, bronchi and bronchioles. The fresh gas composition can be modulated to control arterial  $PCO_2$  and  $PO_2$  ( $P_aCO_2$  and  $P_aO_2$

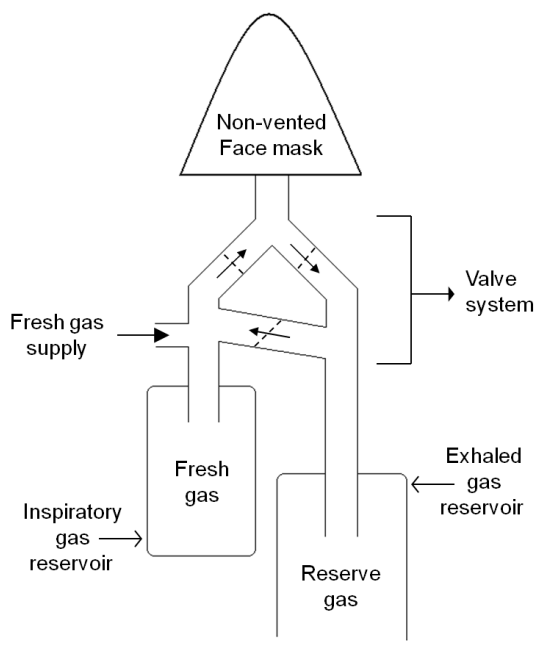


Figure 3.1: Schematic (left) and photograph (right) of the SGD breathing circuit used. Dashed lines represent valves. Slits in the exhaled gas reservoir are shown by gaps in the bottom corners.

respectively). For optimal control of  $P_{ET}CO_2$ , the volume of fresh gas delivered should be equal to alveolar ventilation (volume inspired into alveoli) [80]. The fresh gas is delivered first, filling the alveoli and the subsequent reserve gas fills the anatomical dead space. This approach has been shown to control  $P_{ET}CO_2$  for up to five times the resting ventilation [80]. For this approach to work, the participant must avoid shallow breathing, where the inspired gas does not reach the alveoli before exhalation. If approximate resting metabolic  $CO_2$  production and  $O_2$  consumption rates are known, then a model [81] can be used to modulate the fresh gas composition to target  $P_{ET}CO_2$  and  $P_{ET}O_2$  levels on a breath-by-breath basis.

### **3.3 The Respiract™ and its use in a 7 Tesla scanner environment**

#### **Apparatus**

The use of the feed forward low gas flow method in the environment of an MRI scanner is described here. The apparatus required to implement this method included four large gas cylinders of different gas mixtures, a small gas cylinder of a calibration gas, the Respiract™ device and laptop computer, a fresh gas line, two sample gas lines and the SGD circuit. A pulse oximeter was also used to monitor arterial  $O_2$  saturation during early experiments. However, after some experience was gained in using this set-up, confidence was gained in using the exhaled gas sampling to monitor the participant instead of a pulse oximeter.

Each of the large gas cylinders contains a different gas mixture. These mixtures are medical air (21%  $O_2$ , 79%  $N_2$ ), medical oxygen (100%  $O_2$ ) and two special mixtures (10%  $O_2$ , 90%  $N_2$ ) and (20%  $CO_2$ , 10%  $O_2$ , 70%  $N_2$ ). Each of these cylinders has an assigned regulator. The regulators are clearly labelled with which gas to connect to and pin index valves mean that the medical air and medical oxygen regulators can only be connected to their respective cylinder. The regulators are each connected to a pipe ending with a gas connector, which

will open when connected to the Respiract™. Each pipe is colour-coded at the gas connector end, indicating which fitting to connect to the Respiract™ device.

The small gas cylinder contains a calibration gas, consisting of  $\sim 9\%$  CO<sub>2</sub>, 91% N<sub>2</sub>. This cylinder contains no oxygen, so several steps have been taken to ensure that this gas is not connected whilst a participant is breathing gas supplied by the Respiract™. Unlike the other cylinders, the calibration gas regulator is not medical grade, so it has a distinctly different connector and connecting pipe (*figure 3.2a*), with a distinctly different connection to the Respiract™ device. This gas is only connected during the calibration procedure, as described later. The calibration gas cylinder is removed from the room before the participant is given the SGD circuit.

The Respiract™ device (*figure 3.2c*) is a computer controlled gas mixer, which also includes total pressure, CO<sub>2</sub> and O<sub>2</sub> partial pressure sensors. This device is kept outside the 3 mT field line. For the 7 T magnet, the majority of the control room is inside this line (*figure 3.3*), so the Respiract™ device is positioned with the cylinders in a corridor at the edge of the room (*figure 3.2b*), just outside the 3 mT line. The 3 T magnet is actively shielded, meaning that the 3 mT area is much smaller than for the 7 T magnet, as a result the Respiract™ device can be positioned next to the waveguides giving access to the magnet hall.

Each participant was assigned their own SGD breathing circuit, which is connected to the Respiract™ device by three gas lines. Fresh gas is supplied to the circuit through a reinforced (blue) gas line (*figure 3.2c*). This line can withstand being stepped on without becoming occluded. The other two gas lines sample the gas at the nose (*figure 3.1 to figure 3.2c*), with one line used to measure the total pressure trace through the breathing cycle, to detect inspiration and exhalation, whilst the other line is connected to the CO<sub>2</sub> and O<sub>2</sub> partial pressure sensors. All three gas lines are approximately 10 metres, which is the length needed to cover the distance from the device, through waveguides

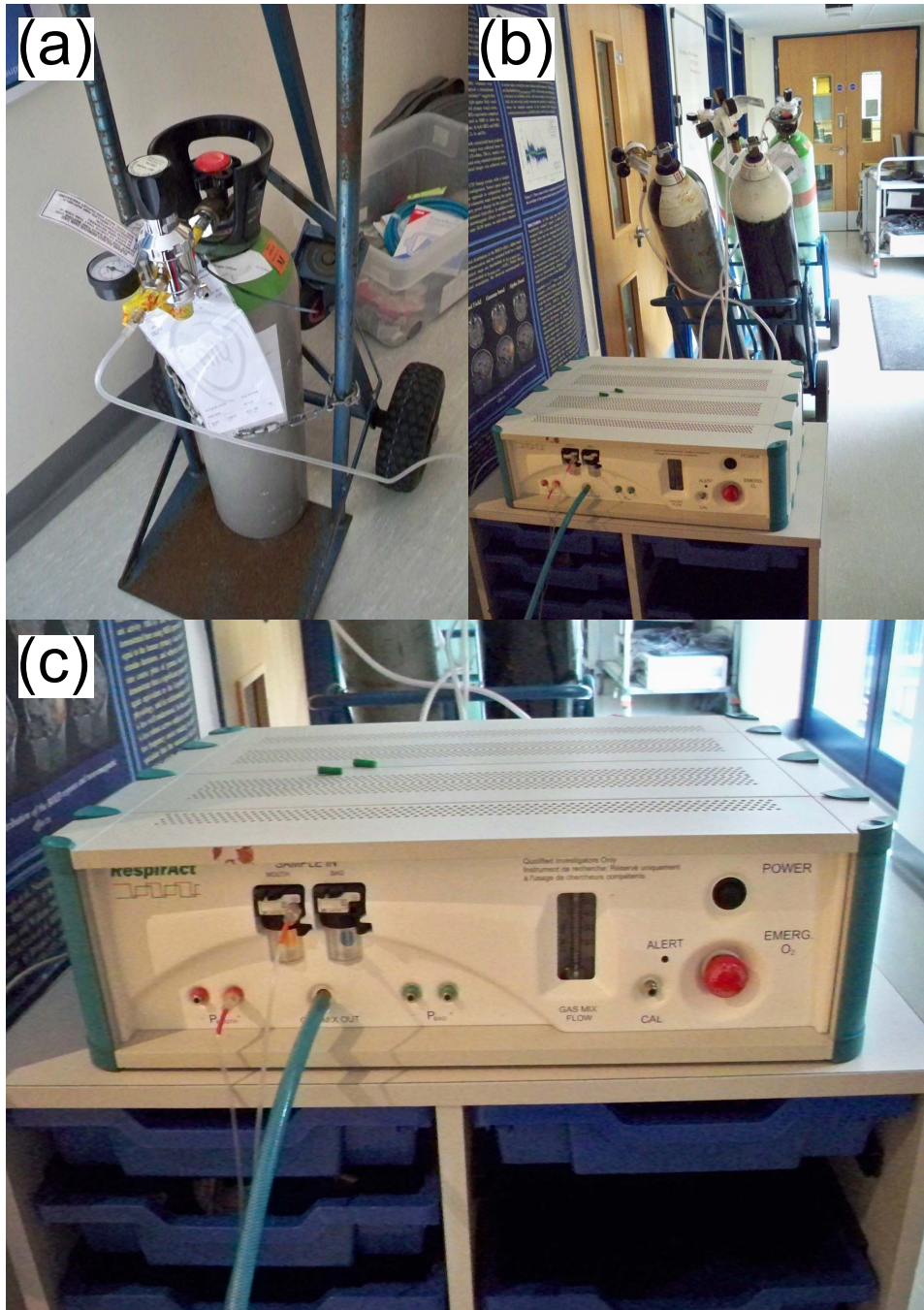


Figure 3.2: (a) Calibration gas cylinder and regulator. (b) Positioning of the Respiract™ device and cylinders during a 7 T experiment (see *figure 3.3* for schematic of this positioning). (c) The Respiract™ device, with three gas lines which connect to the breathing circuit. N.B. the gas cylinders connect to the opposite side of the device.

and to the 7 T magnet bore (*figure 3.3*). These long gas lines introduce delays of several seconds in gas sampling. The SGD breathing circuit is compatible with an MR environment, as it does not have any metal components.

The system is operated using software installed on a dedicated laptop computer (*figure 3.4*). The software displays  $PCO_2$  and  $PO_2$  traces, includes the model for prospectively targeting  $P_{ET}CO_2$  and  $P_{ET}O_2$  and a simple program for picking end-tidal points in the breathing cycle, using the pressure trace.

## Calibration

The  $CO_2$  and  $O_2$  partial pressure sensors need to be calibrated every session. This was done by alternating gas flow between 100%  $O_2$  (0%  $CO_2$ ) and the calibration gas ( $\sim 9\%$   $CO_2$ , 0%  $O_2$ ). The calibration procedure was performed using the software, but required the calibration gas to be connected.  $PCO_2$  and  $PO_2$  sensors and the delay associated with the gas line were calibrated. Once the calibration was complete, the calibration gas was removed from the room and the gas line reconnected to the breathing circuit.

## Sequence for controlling $P_{ET}CO_2$ and $P_{ET}O_2$

During a sequence, medical air is replaced by a mixture of the other three gases to form the fresh gas flow. The composition of the fresh gas is varied by changing the individual flow rates of these three gases. Therefore the amount of  $CO_2$  and  $O_2$  delivered in the fresh gas can be used to target  $P_{ET}CO_2$  and  $P_{ET}O_2$  levels on a breath-by-breath basis. The model used to calculate the delivered gas mixtures requires approximate values for the participant's resting metabolic  $CO_2$  production and  $O_2$  consumption rates. The software can then calculate the fresh gas mixtures required to target  $P_{ET}CO_2$  and  $P_{ET}O_2$  levels, within user-defined constraints, such as the fresh gas flow rate and breathing rate.

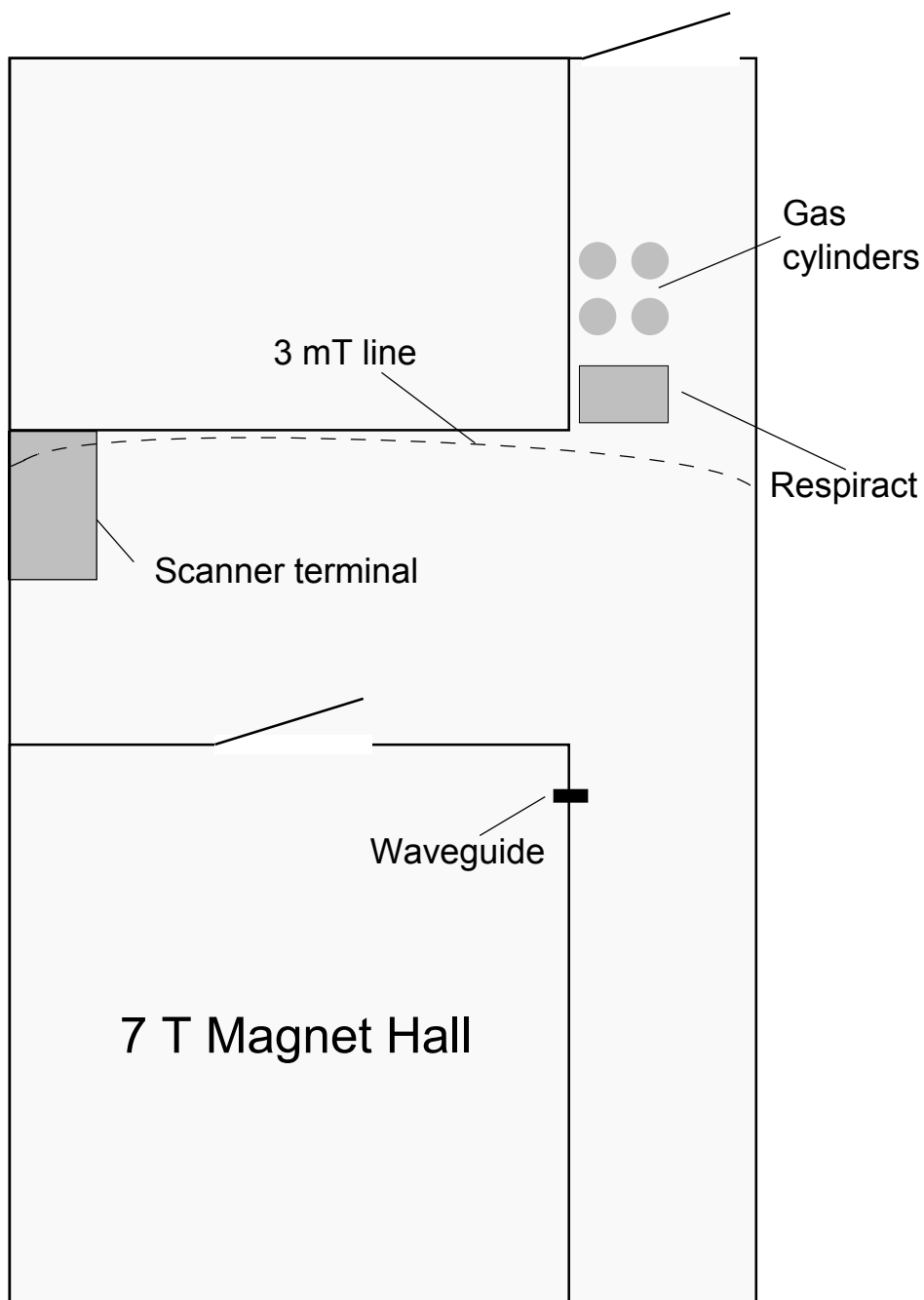


Figure 3.3: Schematic demonstrating the position of the Respiract™ device and gas cylinders in the scanner room (not to scale). These need to be kept outside of the 3 mT line, marked by a dashed line.

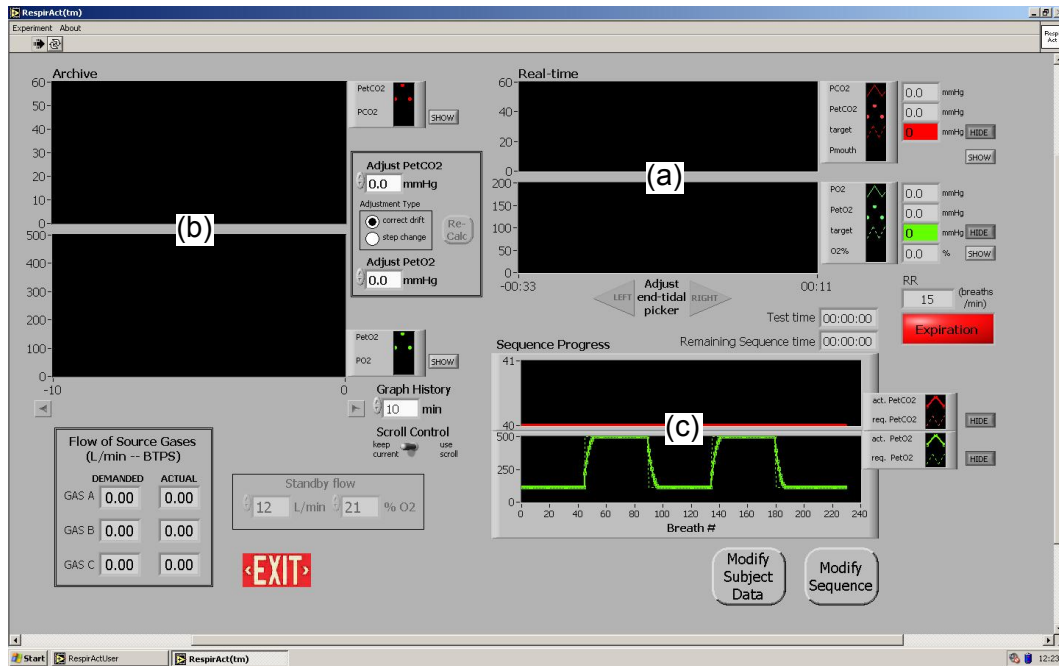


Figure 3.4: The Respiract™ software display, including (a) continuous monitoring of  $PCO_2$  and  $PO_2$  traces, (b) end-tidal values and (c) the ability to prospectively target a breath-by-breath sequence of  $P_{ET}CO_2$  and  $P_{ET}O_2$  levels.

The participant was instructed to pace their breathing using visual cues and attempt to empty the inspiratory gas reservoir with every breath during a sequence. A green ‘IN’ and a red ‘OUT’ on a black background was projected onto a screen at the end of the magnet bore. When in the 7 T head coil, prism glasses were used to see the screen. In the 3 T scanner the use of a whole body transmit coil means that a mirror can be positioned over the receive coil, which is open between elements, removing the need for prism glasses. Some participants could detect when the inspiratory gas reservoir collapsed through a noticeable change in pressure as the valve switched over, or through the contrast between the dry fresh gas and humid reserve gas. The operator could use the  $PCO_2$  trace to identify whether the inspiratory gas reservoir was collapsing with every breath (figure 3.5).

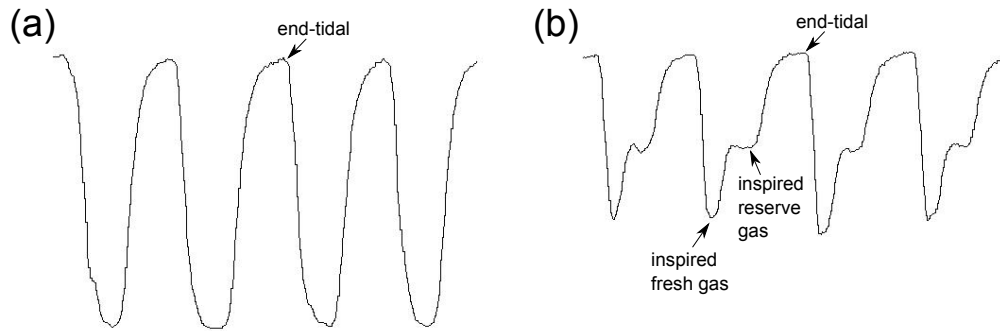


Figure 3.5: Example PCO<sub>2</sub> traces. (a) Trace where the inspiratory gas reservoir is not fully emptied. (b) Trace where the inspiratory gas reservoir fully collapses and fresh gas is supplemented by some reserve gas. The distinction between (a) and (b) is a shoulder in trace (b), indicating when reserve gas is being inhaled.

## Setting up the subject

After the calibration was completed, medical air was supplied as the fresh gas unless a sequence was running. With the participant sitting upright on the scanner bed, they were instructed to place the mask comfortably on their face, covering both nose and mouth, then skin tape (Tegederm, 3M Healthcare, St. Paul, USA) was used to create an air-tight seal to the face. The participant then lay on the bed, out of the scanner bore, for several minutes whilst they became accustomed to the mask. During this time, some set-up sequences were run to determine a comfortable flow rate (typically in the range 6–10 Lmin<sup>-1</sup>) and breathing frequency and to estimate resting metabolic CO<sub>2</sub> production and O<sub>2</sub> consumption rates.

The software can provide estimates of these resting metabolic CO<sub>2</sub> production and O<sub>2</sub> consumption rates using the participant's height, weight, age and sex. These values are then refined by running a sequence where resting  $P_{ET}CO_2$  and  $P_{ET}O_2$  levels are targeted. If the values are correct then the resulting  $P_{ET}CO_2$  and  $P_{ET}O_2$  levels will be maintained at the correct level. If either drifts, then the estimated value can be changed and the sequence recalculated until the correct values are found. The participant was then given ear protection and a patient alarm, positioned comfortably in the head coil and the scanner bed

manoeuvred so that the head coil was centred in the magnet's iso-centre.

### 3.4 Safety

Prolonged hypercapnia (for several hours) causes respiratory acidosis, increases in blood pressure and heart rate [82, 83] and can cause increased anxiety and other behavioural changes [84]. However, mild hypercapnia ( $\leq 5\%$ ) is widely used for short periods of time without adverse effects (see *section 5.3* for some examples). Prolonged hyperoxia can lead to oxygen toxicity, due to increased tissue oxygenation leading to the formation of oxygen free radicals [85, 86]. For normobaric hyperoxia, it takes at least four hours for symptoms to develop. In this work, only mild hypercapnia and normobaric hyperoxia were used, for periods of less than 6 minutes. These short, mild steps are considered safe for healthy participants.

For the feed forward low flow gas delivery system, all of the gas blends contains at least 10% O<sub>2</sub>. Therefore even if the software crashed in such a way that it just delivered one of the gas blends, at least 10% O<sub>2</sub> would still be provided. Hypoxia induced by breathing in a 10% gas mixture at sea level (760 mmHg air pressure) is less severe than the hypoxia experienced due to high altitude (5400 metres) at the Everest base camp [87]. For this work however, care was taken to ensure that participant's arterial  $PO_2$  did not go much below 100 mmHg, which is the low end of normoxia. Exhaled gas  $PCO_2$  and  $PO_2$  traces were continuously monitored whilst the participant was breathing through the SGD circuit, to ensure that safe arterial gas levels were maintained throughout.

The Respiract™ device has some built in fail-safes. If at any time communication is interrupted between the gas mixer and the computer software, then 100% O<sub>2</sub> is supplied to the breathing circuit, at a high flow rate. There is also a large red button on the front of the gas mixer (*figure 3.2c*), which can be pressed at any time to supply 100% O<sub>2</sub> at a high flow rate. In general, this is a useful safety precaution, however in an MRI environment, this can be problematic. Although efficient gradient coils should not do so, there is a

chance that during gradient switching, sparks could be generated. High flow rates of 100% O<sub>2</sub> could significantly increase the oxygen content of the magnet, causing a fire risk. Therefore, if at any stage this emergency 100% O<sub>2</sub> is activated, scanning is stopped immediately and the participant is removed from the bore. During standard hyperoxia experiments, this is not a problem, since low flow rates (6–8 Lmin<sup>-1</sup>) are presented, whilst the circuit design ensures that only exhaled air enters the bore.

The main risk associated with the SGD method is that the delivered fresh gas flow rate drops to zero. This could happen if the gas line supplying fresh gas to the breathing circuit became occluded or if the required flow rate were set to zero (possible with the software). If the fresh gas flow rate were to stop, the participant would only breath the rebreathed gas, leading to an increase in  $P_{ET}CO_2$  and a decrease in  $P_{ET}O_2$ . Continuous monitoring of these values means that if this were to happen, the operator can quickly identify this as a problem and the participant can breath room air through the removal of a blue plug in the front of the mask (*figure 3.1*). The fresh gas line is reinforced, to minimise the risk of it becoming occluded.

Much care was required in handling compressed gas cylinders. There is a risk of cylinders falling over, which could both cause crush injuries and a possible risk of the cylinder becoming a projectile, through release of the compressed gas. To minimise this risk, the cylinders were stored outside in a cage and restrained using chains. Cylinder trolleys were used to move the cylinders and to provide a stable place to hold the cylinders during experiments. Appropriate footwear (with reinforced toecaps) was used when moving the cylinders. The cylinders are ferromagnetic, so were never placed near the magnet hall.

### 3.5 Other approaches to modulating $P_{ET}CO_2$ and $P_{ET}O_2$

The simplest method for modulating blood gases is to change respiratory pace and depth. Breath holding causes an increase in  $P_aCO_2$  and a decrease in  $P_aO_2$ , in a sigmoidal relationship with the breath hold duration [88]. Hyperventilation causes  $P_aCO_2$  to decrease and  $P_aO_2$  to increase. A controlled form of hyperventilation has been proposed recently [89], where breathing is paced at an increased rate for just a couple of breaths. This method has been used to look at the cerebrovascular response delay across brain regions. Both breath holding and hyperventilation require no equipment, so are simple to implement. These tasks cannot separate changes in  $P_aCO_2$  and  $P_aO_2$  and have a large inter-subject variation in response [90, 91].

The most commonly used method for increasing either  $P_{ET}CO_2$  or  $P_{ET}O_2$  above resting values is to supply a fixed inspired gas mixture with enhanced  $CO_2$  or  $O_2$  content compared to air ( $\sim 0\% CO_2$ ,  $21\% O_2$ ). For example, a typical hypercapnic challenge is to present a gas mixture of  $5\% CO_2$ ,  $21\% O_2$ , balanced  $N_2$ . A typical hyperoxic challenge is to present  $100\% O_2$ . The resulting change in  $P_{ET}CO_2$  and  $P_{ET}O_2$  will vary across subjects, depending on oxygen metabolism rate, breathing rate and depth. Also,  $P_{ET}CO_2$  and  $P_{ET}O_2$  changes are not independent of one another with this method. There is an increased ventilatory response to hypercapnia, so increased  $P_{ET}CO_2$  will be accompanied by an increase in  $P_{ET}O_2$  [92, 93]. During hyperoxia, the  $CO_2$  carrying capacity of blood is reduced (the Haldane effect) [94], resulting in a decrease in  $P_{ET}CO_2$  and an associated drop in CBF.

The *dynamic end-tidal forcing* method [95, 96, 92] allows independent control of  $P_{ET}CO_2$  and  $P_{ET}O_2$ . This method achieves targeted  $P_{ET}CO_2$  and  $P_{ET}O_2$  values by iteratively changing the gas mixture delivered to the subject. A computer controlled feedback loop is used to monitor current  $P_{ET}CO_2$  and  $P_{ET}O_2$  values, compare with targeted values and adjust the delivered gas  $CO_2$  and  $O_2$  composition such that  $P_{ET}CO_2$  and  $P_{ET}O_2$  converge on the targeted

values. Good independent control of  $P_{ET}CO_2$  and  $P_{ET}O_2$  values are achieved as long as respiratory pace and depth are approximately constant. Very high flow rates are required ( $70 \text{ Lmin}^{-1}$  [92]) to ensure that the subject does not re-breathe exhaled gas. The main problem with using this method in an MR environment is that the gas sensors need to be positioned at low magnetic field, far from the subject. Long sample gas lines introduce a measurement delay which hinders the feedback mechanism. This would be especially problematic with our 7 T set-up, where the gas lines need to be approximately 10 metres from the subject. An advantage of the dynamic end-tidal forcing method over the feed-forward low gas flow method is that changes in the subject's metabolism will not cause slow drifts in end-tidal values.

### 3.6 Conclusion

This chapter has discussed independent modulation of  $P_aCO_2$  and  $P_aO_2$  in an MRI environment. The SGD technique used in this work has been introduced, with a brief overview of the underlying theory. A description of the implementation of this technique in both 3 T and 7 T scanners has been presented, along with safety considerations. Finally, alternative methods for modulating  $P_aCO_2$  and  $P_aO_2$  have been discussed.

# Chapter 4

## Effect of field strength on the temporal characteristics of the BOLD response

### 4.1 Introduction

The motivation for this work was to use the main magnetic field strength as a perturbation to assist understanding of the BOLD effect and to investigate changes in the haemodynamic response function (*HRF*) across field strength. It has been observed that the spin-echo BOLD response time to peak (*TTP*) to a task occurs earlier than the gradient-echo BOLD response *TTP* to the same task at 3 T [52] (spin-echo BOLD has been introduced in *section 2.4.4*). This was attributed to the spin-echo BOLD signal originating from a larger venous microvascular (relative to macrovascular) component compared to the gradient-echo signal. A subsequent study (also at 3 T) modelled the dispersion of blood oxygenation changes through the venous vasculature, in response to neuronal activation [97]. That study predicted, and showed experimentally, an increase in both the *TTP* and full-width at half-maximum (*FWHM*) of the BOLD signal response with the vessel's distance downstream from the capillary bed supplying the active neurons. Therefore, the BOLD signal contribution from capillaries and venules will generally be earlier and the *HRF* narrower in time than that from large draining veins.

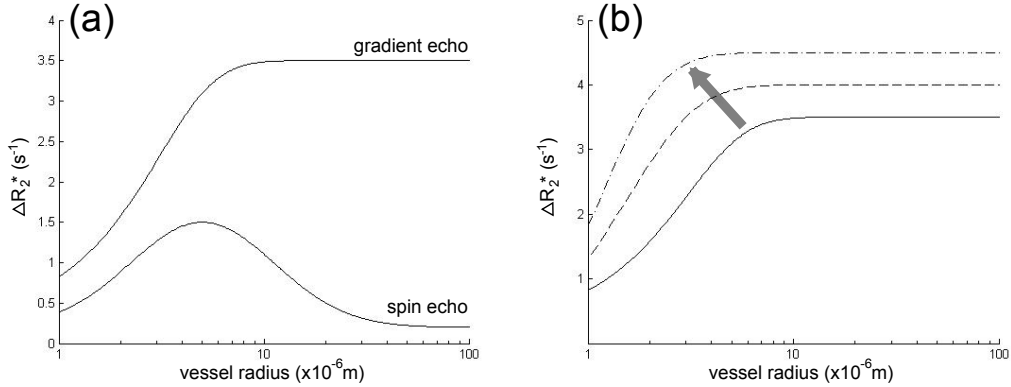


Figure 4.1: (a) Plot reproducing *Figure 1* of [31]. This plot shows the  $\Delta R_2^*$  (or  $\Delta R_2$  for spin echo) dependence on vessel radius for gradient echo (hyperbolic tangent function) and spin echo (gaussian function) signal, in response to a 0.1 ppm change in the vessel susceptibility with respect to the surrounding tissue at 1.5 T. (b) Illustrative plot demonstrating the effect of increasing frequency shift (following the arrow; due to contrast agent or field strength) on the  $\Delta R_2^*$  dependence on vessel radius for gradient echo BOLD.

Monte Carlo simulations of extravascular BOLD signal have found a sensitivity dependence on vessel size [31]. This is demonstrated in *figure 4.1*, for gradient echo and spin echo BOLD contrast for blood vessels with a 0.1 ppm susceptibility shift from surrounding tissue at 1.5 T. *Figure 4.1a* directly demonstrates that the spin echo BOLD signal is more sensitive to smaller vessel sizes than larger vessel sizes, whereas gradient echo BOLD signal has a large component from larger vessels. The predicted consequence of increasing field strength is to shift the curves to lower vessel radii and increase the amplitude of signal changes (due to increased  $\Delta R_2^*$ ) resulting in increased sensitivity to smaller vessels, as shown in *figure 4.1b*. This results from the vessel-tissue susceptibility difference causing an increased frequency shift at higher field strengths. Note that in [31] the frequency shift was changed by increasing contrast agent concentration, but would equally apply to a field strength induced increase in frequency shift. Therefore the gradient-echo BOLD signal will have a larger microvascular contribution at higher field strengths. By combining the prediction of an increased microvasculature component at higher field strength [31] with the observation of an earlier BOLD response from smaller veins, the pre-

diction can be made that the BOLD response is earlier at higher field strengths. This may take the form of a faster leading edge (onset) of the BOLD response.

Several studies have investigated the relationship between field strength and BOLD signal characteristics. The spatial extent of statistically significant activation was shown to be greater at 3 T than at 1.5 T for visual and working memory tasks [98] and a motor task [99]. In the latter study this trend existed over a wide range of echo times, up to 130 ms. Single-echo %BOLD measurements in response to visual stimulation have been shown to be higher at 4 T than 1.5 T [100] for an echo-time chosen to approximate grey matter  $T_2^*$  at each field strength. Multi-echo acquisitions have been used to show that  $\Delta R_2^*$  in response to a task increases with field strength from 0.5 T to 7 T [101, 102, 103, 104]. In a study conducted at 1.5 T, 3 T and 7 T,  $\Delta R_2^*$  has been shown to increase linearly with field strength in response to motor [103] and visual [104] tasks. These studies also confirm that the maximum %BOLD is found for an echo-time approximately equal to grey matter  $T_2^*$ . All of these previous cross-field studies employ a block design for task presentation, no previous studies have considered the effect of field strength on the BOLD signal temporal characteristics (HRF shape).

Venous blood has a  $T_2^*$  of approximately 60/17/5 ms at 1.5/3/7 T respectively [105]. Therefore with typical echo-times (TEs) approximately equal to the  $T_2^*$  of grey matter (66/48/28 ms respectively) [106], the intravascular signal component will have a much larger contribution to the total BOLD signal at 1.5 T than at 7 T. The relative extravascular and intravascular BOLD signal components can be separated by adding flow suppression bipolar gradients to the gradient-echo sequence. These gradients dephase the signal from spins moving above a critical velocity in the direction of the applied gradients, thus removing the majority of the intravascular signal and providing an upper estimate of the extravascular BOLD signal. Several studies have used this technique to estimate the extravascular fraction of gradient-echo BOLD signal at various field strengths. At 1.5 T, the BOLD signal has been shown to be dominated by the intravascular component [107, 108], with the extravascular component

contributing between 0 and 30 % to the total BOLD signal. At 4 and 7 T an extravascular component of greater than 90 % and approximately 100 % were measured respectively, although these were measured at long TEs (80 ms and 55 ms respectively) compared with grey matter  $T_2^*$ , thus further reducing the intravascular effect. A multiple echo approach was used to measure the total and extravascular  $\Delta R_2^*$  BOLD signal contributions in response to a visual stimulus at 1.5 T, 3 T and 7 T [104], finding 45–70 %, 70–91 % and 91–98 % extravascular contributions respectively (the range of values reflecting two choices of ROI). Since the ratio of intravascular to extravascular BOLD signal contributions primarily depends on the difference in venous and grey matter  $T_2^*$ , then this ratio will strongly depend on the choice of TE.

The aim of this work is to investigate how the temporal characteristics of the BOLD haemodynamic response function change with field strength. With the same controlled task performed at each field strength, neuronal and haemodynamic responses can be assumed to be the same, and so any differences in shape provide information on the different BOLD signal compartments (microvascular and macrovascular compartments (see *figure 4.1*), or intravascular and extravascular compartments). In this work fMRI data was collected both without and with flow suppression bipolar gradients to suppress the intravascular signal component. This allows separation of the intravascular and extravascular components whose relative BOLD signal contributions will change with field strength.

## 4.2 Method

Seven healthy volunteers (5 female, 2 male) participated in this study. All subjects gave informed written consent prior to participating and ethical approval was given by the University of Nottingham Medical School Ethics Committee. Each subject was scanned on three separate occasions over a three week period, once at each field strength of 1.5, 3 and 7 T. Within the constraints of volunteer and scanner availability, the field strength order was varied across volunteers to prevent a systematic bias due to adapting to the task across ses-

Parameter	1.5 T	3 T	7 T
TE (ms)	55	45	32
SENSE factor	2	2	3
# slices acquired	8	10	10
flip angle (°)	66	66	60
# dynamics	240	360	360
TR (s)	1	1	1

Table 4.1: Scan parameters

sions.

## Data acquisition

Scanning was performed on Philips Achieva 1.5 T and 3 T systems, with whole body volume transmit and 8 channel SENSE head receive coils, and a Philips Achieva 7 T system, with head volume transmit and 16 channel SENSE head receive coil. Scanning consisted of an initial localiser scan to identify the visual cortex, followed by multiple blocks of the main visual fMRI experiment, which is described in later paragraphs. Alternate fMRI scans were run without and with flow suppression bipolar gradients in an order which was randomised across subjects. The scanner operator spoke to the subject between scans to ensure that the subject maintained attention throughout. Respiratory bellows and a pulse oximeter were used at 7 T to monitor the subject’s breathing and cardiac trace respectively. Only respiratory bellows were used at 3 T, since the pulse oximeter in that scanner did not work at the time of the study; neither were used at 1.5 T. Physiological noise is lower at lower field strengths [109] and for the relatively fine spatial resolution used here (2 mm isotropic) can be considered insignificant at 1.5 T for the purpose of this experiment.

For both the localiser scan and main fMRI scans, axial gradient-echo EPI data were acquired with a 2 mm isotropic spatial resolution over a reduced field-of-view (128×192 mm) centred on the occipital lobe. For the localiser scan, 20

contiguous slices were acquired in a TR of 2 s and with a flip angle of 80°, 80° and 75° (the Ernst angle), at 1.5, 3 and 7 T respectively, 120 dynamics were collected. Acquisition parameters for the fMRI scans at each field strength are shown in *table 4.1*. The reduced slice coverage and number of dynamics at 1.5 T were due to limitations of the gradient set combined with the demands of applying the bipolar gradients.

The flow suppression bipolar gradients were not applied in the slice direction, as this was found to cause eddy currents, generating large image intensity artefacts. Bipolar gradients were applied in both the phase and readout directions with the parameters shown in *table 4.2*. The gradient amplitudes ( $A$ ) used were the maximum achievable with each respective gradient set, and the shorter duration at 7 T was to allow for the shorter optimal TE. The 1 ms linear ramp-up and ramp-down slope for each gradient lobe is longer than the minimum available, but was found to significantly reduce eddy current artefacts. The equations for calculating  $b$  and  $v_{enc}$  were taken from [108], which specify for bipolar gradients

$$b = \frac{2}{3}\delta^3(2\pi\gamma A)^2 \quad (4.1)$$

$$v_{enc} = (2\gamma A\delta^2)^{-1} \quad (4.2)$$

where  $\gamma$  is the proton gyromagnetic ratio,  $A$  is the gradient lobe amplitude and  $\delta$  is the gradient lobe duration plus half the sum of the rise and fall times. These bipolar gradients resulted in a diffusion weighting of  $b = 72.9$  s/mm<sup>2</sup> at 1.5 and 3 T, and  $b = 44.3$  s/mm<sup>2</sup> at 7 T. The bipolar gradients will cause an attenuation of the signal from moving protons, such that there will be a distribution of attenuation values across flow velocities. The velocity value of  $v_{enc}$  gives an indication as to the lower end of this distribution. In this case,  $v_{enc} = 3.26$  mm/s at 1.5 and 3 T, and  $v_{enc} = 4.83$  mm/s at 7 T corresponds to vessels larger than capillaries and small microvasculature [110].

A visual stimulus (red LED goggles, flashing at 8 Hz) was used, for reproducible stimulus presentation across trials and field strength. All lights in the magnet hall and bore were switched off throughout the functional experiment.

Gradient parameters	1.5 T	3 T	7 T
Amplitude $A$ (mT/m)	25	25	30
Duration (ms)	11	11	8
Rise/fall time (ms)	1	1	1
$b$ (s/mm <sup>2</sup> )	72.9	72.9	44.3
$v_{enc}$ (mm/s)	3.26	3.26	4.83

Table 4.2: Properties of the flow suppression bipolar gradients

The stimulus was presented in short blocks to maintain attention, 4 minutes at 1.5 T, 6 minutes at 3 T and 7 T (the shorter block duration at 1.5 T was due to the hardware limitation on the number of dynamics). Each block comprised an initial 60 s OFF period to identify a clear baseline period, followed by repeats of 5 s ON and 55 s OFF.

A short TR was required to adequately sample the BOLD HRF temporal characteristics, which restricted the number of slices acquired. Therefore, to position the image slab to cover the primary visual cortex, a localiser scan was performed initially. This localiser had a longer TR allowing wider slice coverage, a visual stimulus of four cycles of 10s ON and 20s OFF was used and an online analysis program (inbuilt in the scanner software) was used to generate real-time BOLD activation maps to identify the primary visual cortex. To ensure that the same slice coverage was acquired across all three field strengths, screenshots were taken for comparison (for example see *figure 4.2*). When planning the slice coverage for the second and third sessions, a combination of the screenshots from previous sessions and the localiser scan from the current session were used to position the imaging slab.

## Analysis

Data analysis consisted of motion correction, high-pass temporal filtering, physiological noise correction and voxelwise intensity normalisation. These steps will be described in detail in the next few paragraphs.

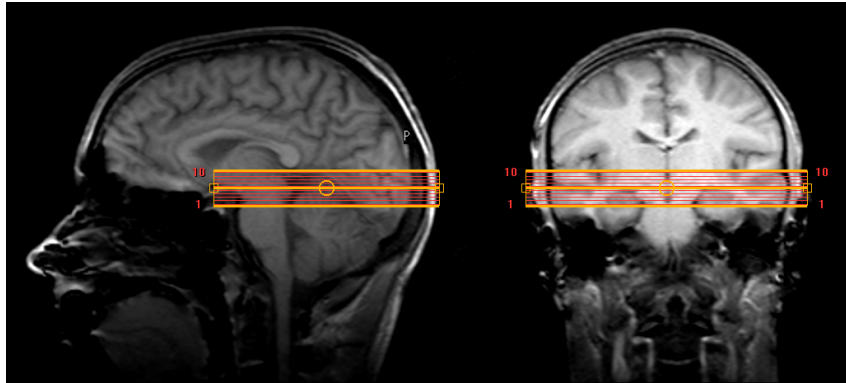


Figure 4.2: Example of a screenshot taken at 3 T, showing the slice orientation for the main scan blocks. This was used for reference in slice positioning at the other field strengths.

Motion correction of this data proved problematic, due to the reduced field-of-view, low SNR associated with a 1 s TR and the use of diffusion gradients. The use of motion correction algorithms from FSL (fMRIB, Oxford, UK), SPM (UCL, London, UK) and AFNI (NIH, Bethesda, USA) were assessed, but these appeared to add spurious motion to the datasets. The effectiveness of the motion correction algorithms were judged by manual inspection of the motion parameter estimates and movies comparing the motion corrected and original datasets using FSLview (FSL). Using these methods of inspection, it was decided to not motion correct those datasets which featured no sudden jumps in the original dataset and had less than 1 mm (half the voxel size) motion throughout the dataset. From these criteria, 5 datasets (of 84) required motion correction. These datasets were motion corrected using MRTTools, a Matlab-based toolbox designed for processing fMRI data. This toolbox led to less spurious motion than the other algorithms, and for these five datasets, the spurious motion added was less than the actual, corrected motion. This method of motion correction required a lot of user input and would not have improved the other datasets, and so was only performed on these 5 datasets.

All datasets were high-pass temporal filtered with a 120 s cut-off period. Physiological noise correction was performed using RETROICOR [51], implemented

using in-house Matlab code (written by Emma Hall). Both respiratory and cardiac cycles were used for correction at 7 T, whilst only respiratory cycle related noise was corrected at 3 T (see *data acquisition section*). For each subject, all datasets acquired at a given field strength were first realigned to the same space, using FLIRT (FSL). This corrected for any small motion between scans. These transformations were carefully checked using FSLview to overlay one dataset on another. Spatial smoothing was performed, with a 3 mm FWHM gaussian kernel using SUSAN (FSL). All datasets were intensity normalised to the OFF periods on a voxel-by-voxel basis, by dividing each dynamic image by the mean image over the initial 60 s OFF period. For each subject, all repeated scans were concatenated into a *combined dataset*. This resulted in six combined datasets for each subject. Average trials were formed for each combined dataset by averaging over all trials (60 s periods, starting from the visual stimulus onset).

Statistical analysis was performed on each combined dataset, using FEAT (FSL). Clusters of significant activation were chosen using a voxelwise  $Z$ -score threshold of  $Z > 2.3$  and cluster corrected  $P_{corr} < 0.05$ . A single region of interest (*ROI*) was then defined for each subject as follows: the binary cluster masks ( $P_{corr} < 0.05$ ) from the 1.5 T and 3 T combined datasets without bipolar gradients were moved into 7 T space. This was performed by first registering an average 1.5 T and 3 T image to a 7 T average image, then applying the realignment parameters to the binary masks. The registrations were checked manually using FSLview and no significant differences in distortions were observed across field strengths. A *common ROI* was then formed from the intersection of masks from all three field strengths, so only including voxels with a significant response at all three field strengths. The common ROI was then transformed back into 1.5 T and 3 T space, so the same region could be studied at all three field strengths.

Four parameters were measured in order to characterise the temporal characteristics of the average trials; TTP, FWHM, BOLD amplitude and the onset time (delay between the start of the stimulus presentation and the BOLD re-

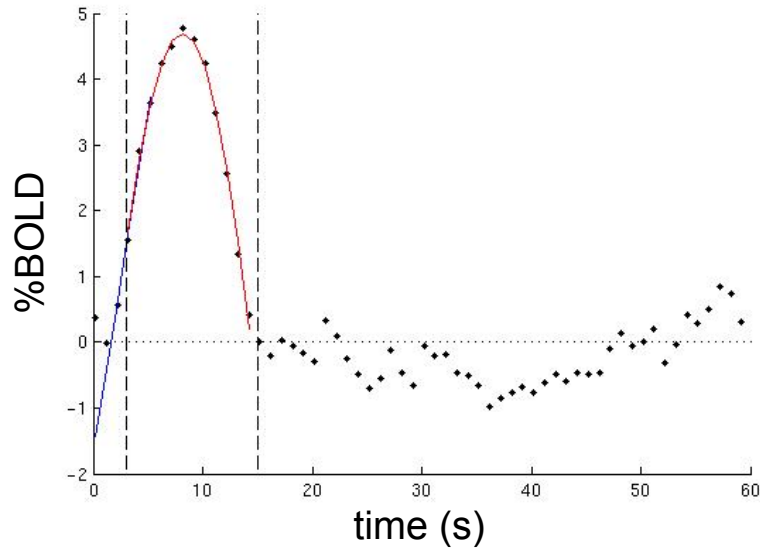


Figure 4.3: Example of the gaussian (red curve) and linear (blue line) fits to an average trial %BOLD timecourse (black dots). This demonstration timecourse is averaged over the common ROI for a single slice of one subject at 7 T. The vertical dashed lines indicate the window for the gaussian fit (3–15 s). The linear fit was windowed between 3–6 s and the blue line is extended back to 0 s to illustrate the %BOLD = 0 intercept (horizontal dotted line), in this case at 1.6 s.

sponse onset). A least-squares fit was performed of a gaussian function to the average trial %BOLD timecourse over timepoints 3 to 15 s after the start of the visual stimulus. From this fit TTP, FWHM and peak BOLD amplitude were measured. To measure the onset time, a linear regression was performed to the timepoints between 3 and 6 s and the fitted line then interpolated back to the %BOLD = 0 intercept. This analysis of temporal characteristics was performed on a voxelwise basis, for all voxels included in the common ROI. To demonstrate the gaussian and linear fits, an average trial %BOLD timecourse is shown for a single slice in one subject at 7 T in *figure 4.3*. When measuring these parameters, slice timing needs to be accounted for. Each slice in the volume was acquired at a different point in time, spaced evenly across the TR (equidistant, 0.125 s between slices at 1.5 T and 0.1 s at 3 T and 7 T). To account for this, the time vector was shifted appropriately when considering each slice.

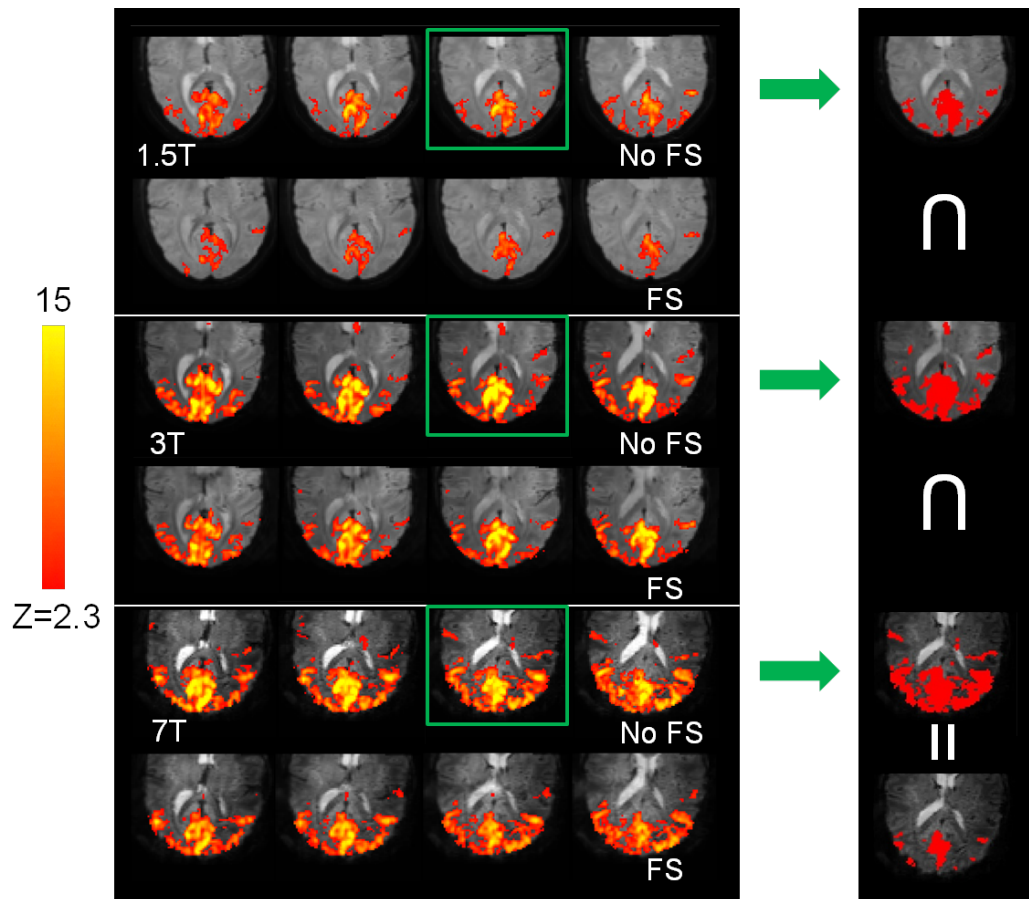


Figure 4.4: Single-subject example of Z-statistic maps, showing the  $Z > 2.3$ ,  $P_{corr} < 0.05$  clusters at all three field strengths for the cases of without (No FS) and with (FS) flow-suppression bipolar gradients. The images on the right demonstrate how the common ROI was formed (from the outlined slice) from the No FS binary cluster masks ( $Z > 2.3, P_{corr} < 0.05$ ), as described in the *analysis section* text.

Volume (mm <sup>3</sup> )	1.5 T	3 T	7 T
NoFS	16407 ± 8653	45923 ± 18635	62400 ± 24274
FS	11145 ± 5145	36816 ± 23127	58049 ± 26305
100×FS/NoFS (%)	68	80	93

Table 4.3: Volume of activation for each field strength (mean±standard deviation over subjects) for the NoFS and FS case. Also shown is the FS activation volume as a percentage of NoFS activation volume.

### 4.3 Results

One subject was discarded, as they reported loss of attention during the 1.5 T scan, this was supported by there being no clusters of significant activation for this dataset. Example results for the statistical analysis and the formation of a common ROI are shown in *figure 4.4*, for a single subject. From this point onwards, datasets acquired without the flow-suppression bipolar gradients will be referred to as the no flow-suppression (*NoFS*) case, whilst datasets with flow-suppression bipolar gradients will be referred to as the with flow-suppression (*FS*) case. For the six subjects for which a complete set of data was available at all three field strengths, the average volume of activation at each field strength is shown for the NoFS and FS case together with the FS activation volume as a percentage of the NoFS activation volume (*table 4.3*).

TTP maps for a single slice in a single subject are shown in *figure 4.5a*, whilst TTP histograms of all common ROI voxels in all subjects are shown in *figure 4.5b*. The equivalent maps and histograms are shown for FWHM in *figure 4.6*, for peak BOLD amplitude maps in *figure 4.7* and for onset time in *figure 4.8*. The histograms indicate the voxel-level variation of each parameter.

To consider any differences in TTP, FWHM and onset time across field strength and between the NoFS and FS case, a 2-way ANOVA was used on the subject mean values of each parameter, with post-hoc t-tests between NoFS and FS cases at each field strength with Bonferroni correction. The crude fitting technique for measuring the onset time led to some erroneous fits, such as

negative or very long onset times. The erroneous fit values, including outliers with magnitude on the order of 100 s, dominate subject average values if a mean is taken over all common ROI voxels. Therefore a trimmed mean was calculated only using values of onset time between 0–6 s, to generate average values which better represent the peak of the histogram. TTP and FWHM mean values and trimmed mean onset time values for each subject are shown in *figure 4.9*. Also shown in this figure are results for the statistical analysis, which show that the onset time decreases with increasing field strength and that TTP and onset time were affected by flow suppression at low field (1.5 T), but not at higher field (3 and 7 T).

Voxelwise scatter plots comparing peak BOLD amplitude versus onset time are shown in *figure 4.10*. They might be expected to show some correlation of later onset times for higher peak BOLD amplitude, since voxels containing large draining veins would be expected to have a large peak BOLD amplitude and a later onset time compared with tissue voxels. However, the scatter plots actually show an approximately normal distribution, centred on the mean values reported in *figure 4.9c*. Voxels with high peak BOLD amplitude, which may be expected to have a more accurate onset time fit, are also situated close to the mean onset time value. Monte Carlo simulations and improved fitting functions may help to determine whether this lack of a positive correlation between peak BOLD amplitude and onset time is due to limitations of the sensitivity of this method or the choice of ROI.

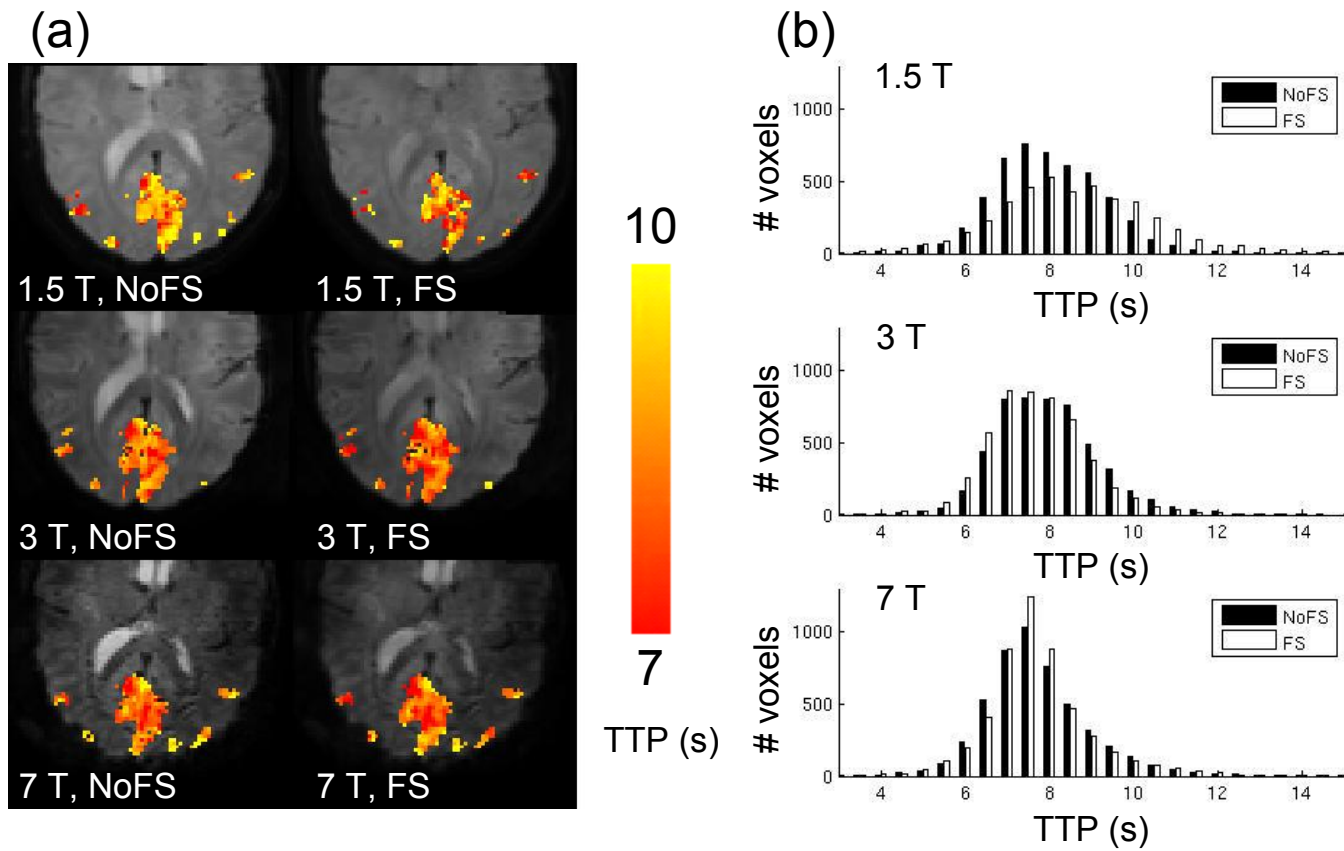


Figure 4.5: Voxelwise time-to-peak (TTP) results. (a) Single-subject example of the voxelwise TTP maps for the NoFS and FS case at each field strength. (b) Histograms of the voxelwise TTP maps, formed from common ROI voxels for all subjects.

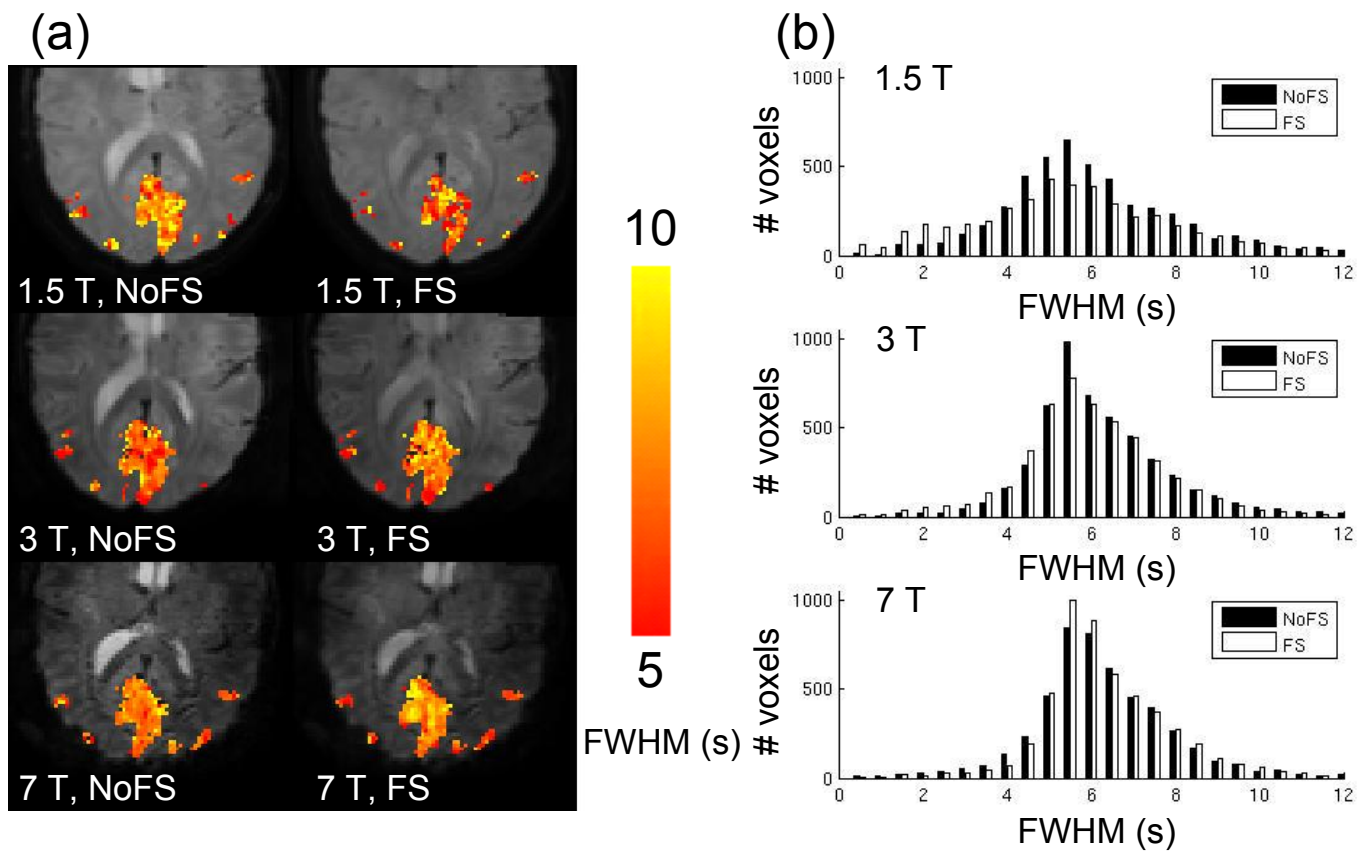


Figure 4.6: Voxelwise full-width-half-maximum (FWHM) results. (a) Single-subject example of the voxelwise FWHM maps for the NoFS and FS case at each field strength. (b) Histograms of the voxelwise FWHM maps, formed from common ROI voxels for all subjects.

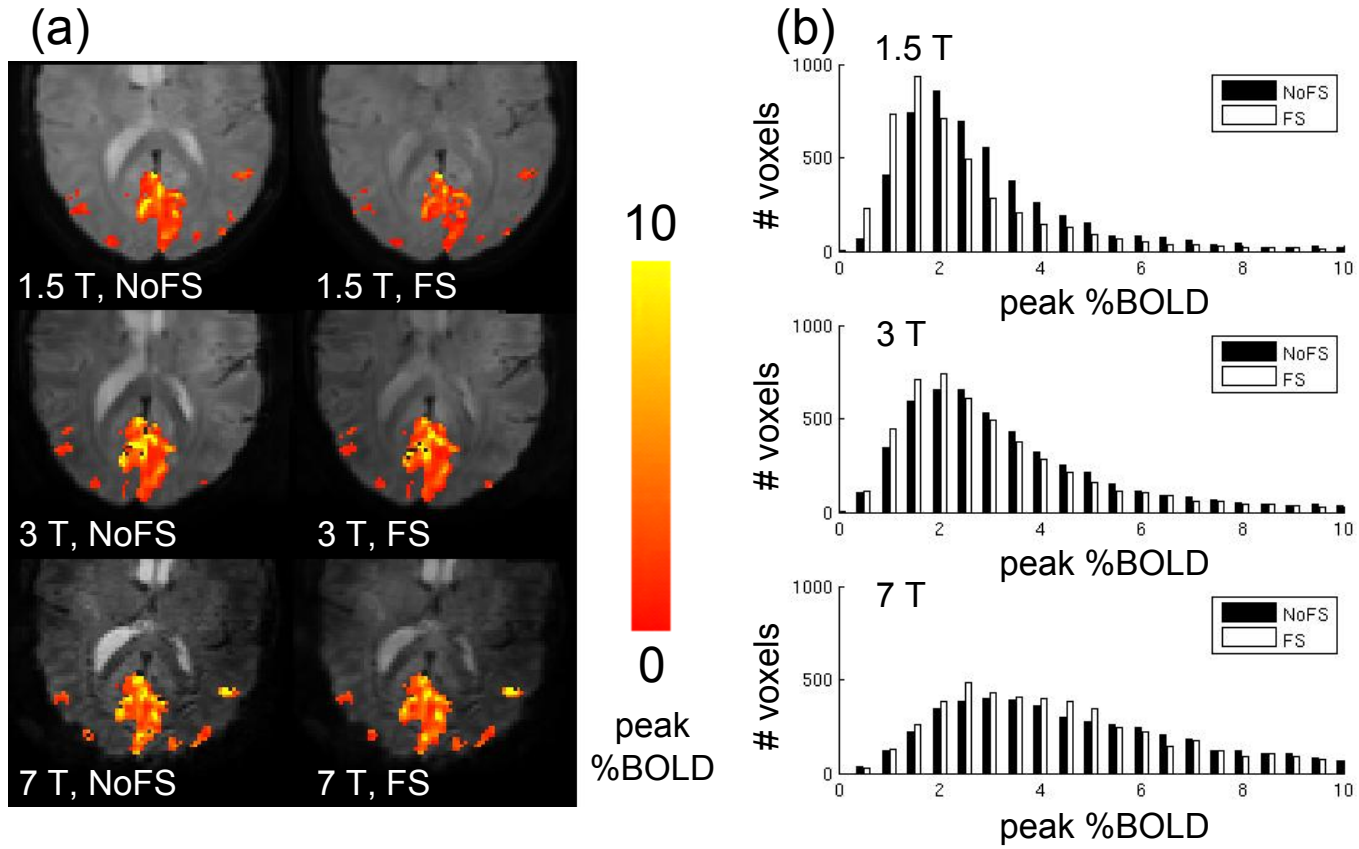


Figure 4.7: Voxelwise results for peak BOLD amplitude, the amplitude of the gaussian fit. (a) Single-subject example of the voxelwise peak BOLD maps for the NoFS and FS case at each field strength. (b) Histograms of the voxelwise peak BOLD maps, formed from common ROI voxels for all subjects.

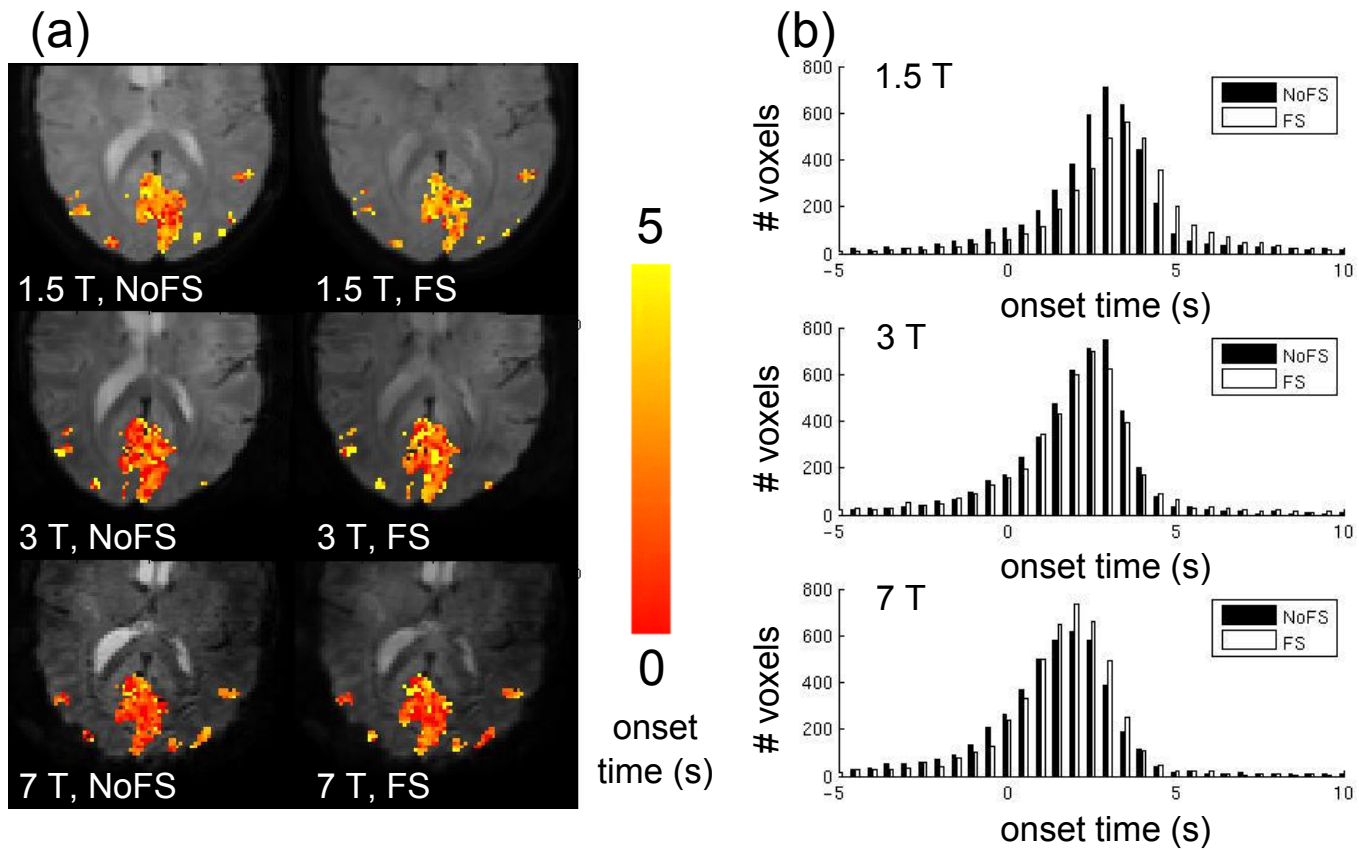


Figure 4.8: Voxelwise onset time results. (a) Single-subject example of the voxelwise onset time maps for the NoFS and FS case at each field strength. (b) Histograms of the voxelwise onset time maps, formed from common ROI voxels for all subjects.

Individual subject average trial timecourses are shown for the NoFS and FS cases and for each field strength separately in *figure 4.11*. These normalised timecourses were constructed by dividing each slice's common ROI average trial %BOLD timecourse by the gaussian-fitted peak BOLD amplitude value ( $BOLD(peak)$ ), then performing a weighted average over slices, using the number of common ROI voxels in each slice as the weighting factor. The time-axis scale was determined by a weighted average of slice timing values over slices. The horizontal lines in the top right hand corner of each plot show two weighted standard deviations of the slice timing across slices, one for each subject. A comparison of these average trial timecourses across field strength is shown in *figure 4.12*, both for the average timecourse across subjects and for a single subject example. These plots show an earlier onset time at 7 T (red lines) compared to 1.5 T (blue lines) for both NoFS and FS cases. The TTP is very similar at all field strengths in the NoFS case, but in the FS case it is later at 1.5 T compared to 3 T and 7 T. FWHM is similar across field strengths in both the NoFS and FS cases. These observations are in agreement with the histograms shown earlier.

The post-stimulus undershoot did not appear to be attenuated with the bipolar gradients, consistent with the literature [111] suggesting that it is predominantly extravascular in nature. However, a thorough analysis of the post-stimulus undershoot was not performed due to limited contrast-to-noise ratio of the feature and due to an oscillation observed in 3 out of the 6 subjects at 7 T, only in the post-stimulus undershoot, which was localised to the visual cortex (*figure 4.13*). This oscillation might be attributed to a visual rebound after-effect [112]. Further study of this oscillation was not performed due to it not being robustly repeatable across subjects or across repeated scan sessions.

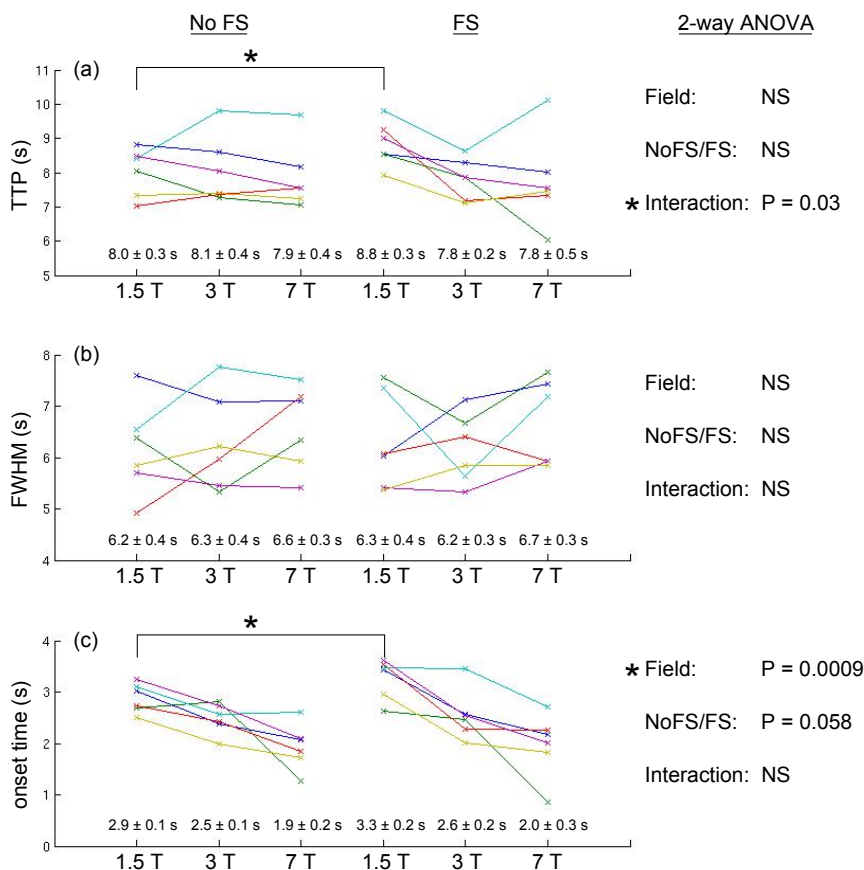


Figure 4.9: Plots showing (a) TTP, (b) FWHM and (c) onset time for each subject, taken from the voxelwise fit values averaged over the common ROI. The connecting lines demonstrate the change across field strengths for each subject. Mean  $\pm$  standard error across subjects is displayed above the x-axis for each field strength. Also shown on the right are results for the 2-way ANOVA, with significant results of  $P < 0.05$  are marked by \*. Significant differences between NoFS and FS cases at each field strength of  $P < 0.05$  (Bonferroni corrected paired t-tests) are shown by \* in the plots.

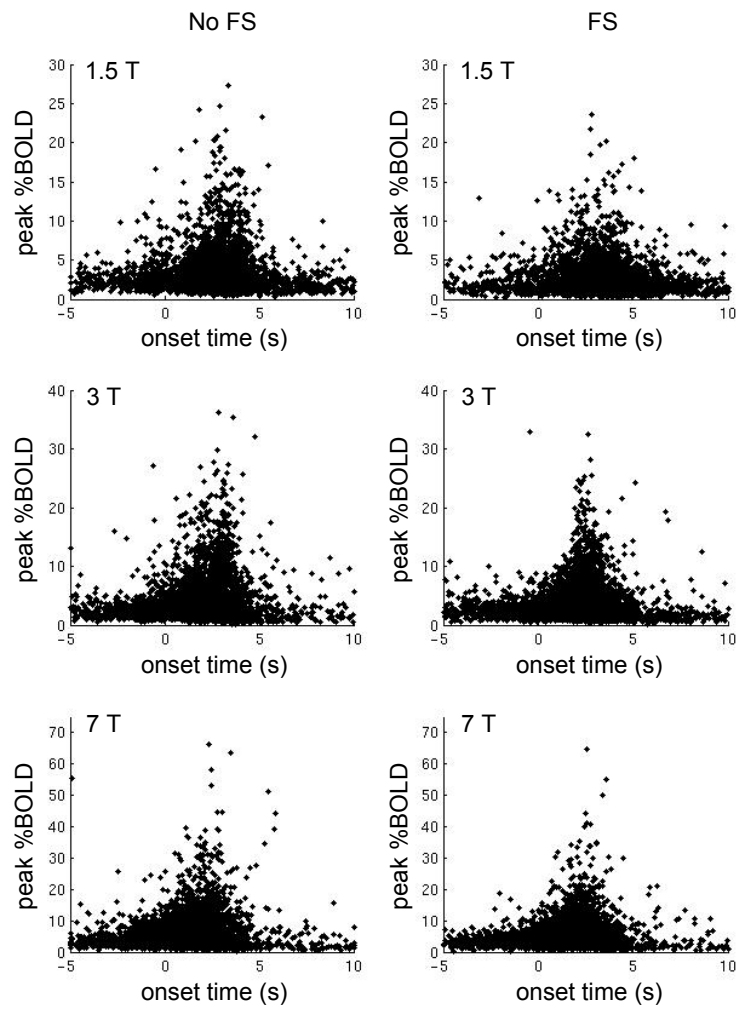


Figure 4.10: Scatter plots of peak BOLD amplitude versus onset time for every voxel in the common ROI of every subject. Note that the plots have been windowed to exclude isolated outliers for both peak BOLD amplitude and onset time.

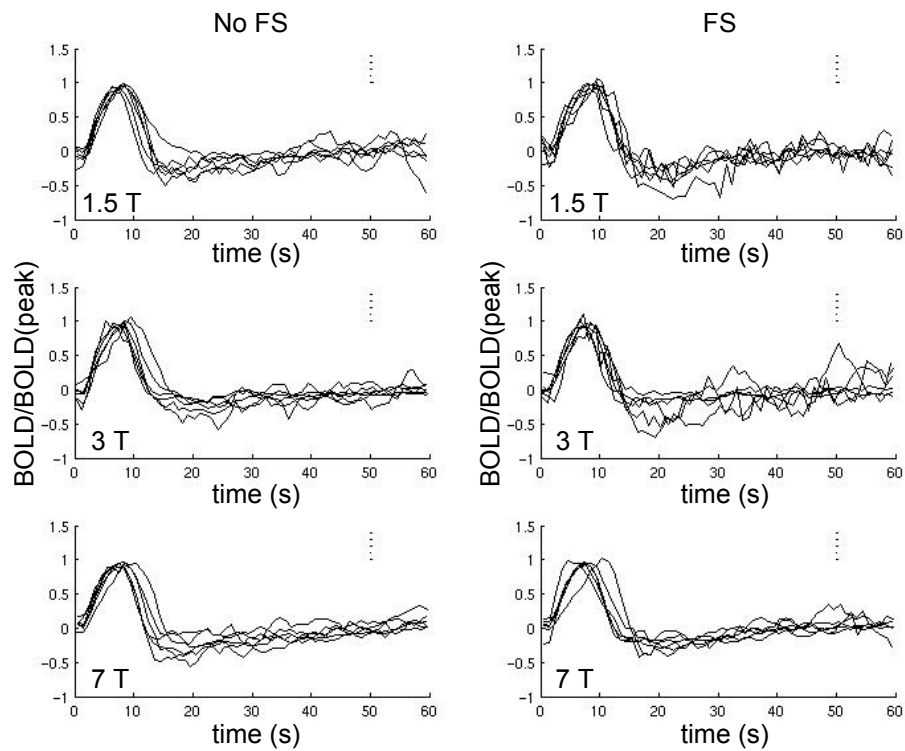


Figure 4.11: Average normalised trial timecourses for all 6 subjects, formed by the weighted average over slices. Each subject's timescale is determined by the weighted average slice timing and the horizontal lines in the top right hand corner show two weighted standard deviations of the slice timing across slices for each subject. The weighting factors were determined by the number of common ROI voxels in each slice.

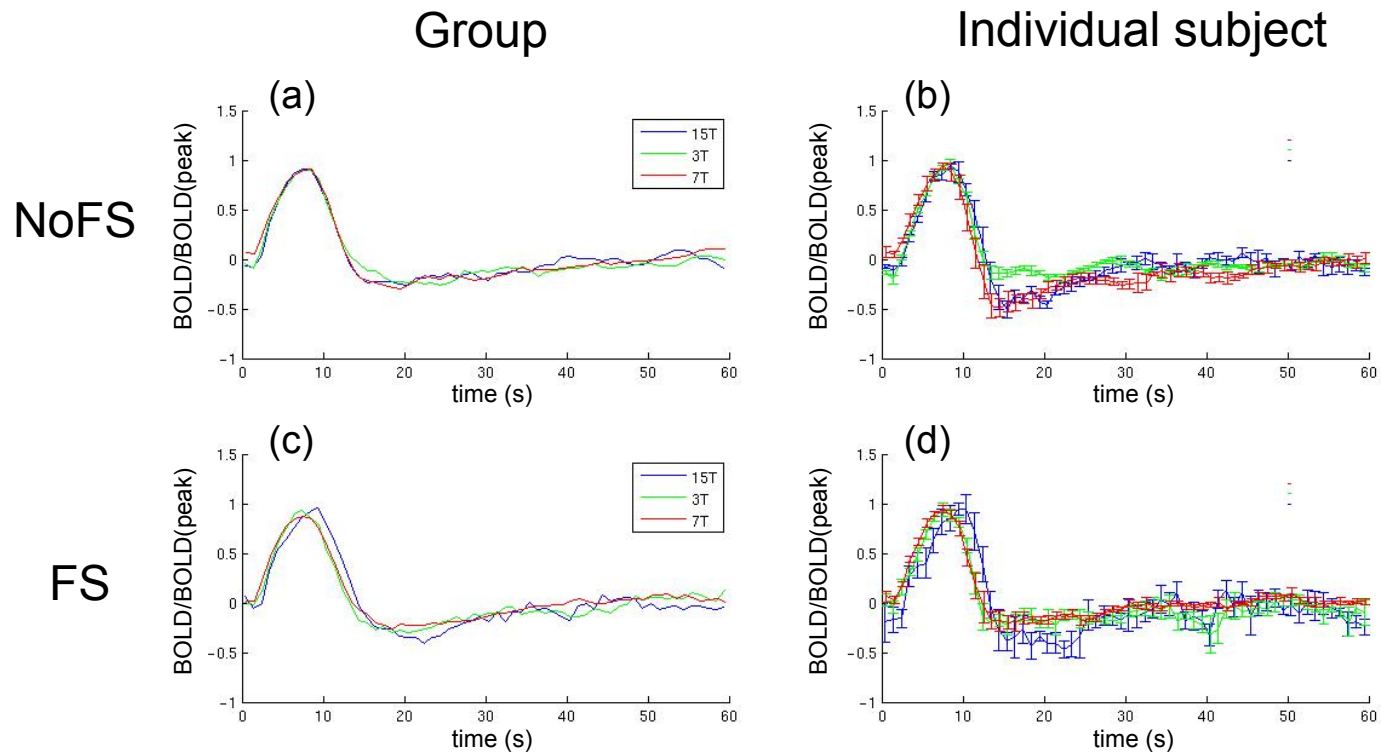


Figure 4.12: NoFS (a & b) and FS (c & d) average normalised trial timecourses compared across field strength. Timecourses (a & c) are averaged over all subjects' timecourses from *figure 4.11*, with the timescale determined from the average slice timing across subjects. Timecourses (b & d) show a single subject example average trial timecourse, where the vertical error bars show the weighted standard deviation BOLD/BOLD(peak) over slices and the horizontal lines in the top right corner show two weighted standard deviations of slice timing over slices.

## 4.4 Discussion

This study has predicted and found a significant difference in the BOLD response onset to a visual stimulus with field strength in both NoFS and FS data, higher field strength data showing a shorter onset time. This prediction was based on the BOLD signal sensitivity to vessel radius [31], being dependent on the frequency shift between the vessel and surrounding tissue, as shown in *figure 4.1*. Frequency shift is itself affected both by the susceptibility difference (dependent on haemoglobin oxygen saturation) and on field strength. At higher field strength, the BOLD signal has increased sensitivity to smaller venous vessels, which are predicted to be associated with an earlier onset of the BOLD response [97]. The results of this study demonstrate a shorter onset time in the BOLD response, relative to the start of the visual stimulus, with increasing field strength.

The statistically significant trends with field strength were inferred by voxel-wise consideration, rather than through averaging over the whole common ROI, before consideration of the temporal characteristics. The reason this method was followed is that there will be a within-subject distribution of temporal characteristics due to local differences in vascular structure. This variation may blur the BOLD dynamic response, obscuring any differences across field strength. The voxelwise consideration was used to account for this distribution, however the common ROI averaged timecourses were still able to separate out these differences, despite this within-subject variation, as shown in *figure 4.12*.

Bipolar diffusion gradients were used to suppress the signal from fast moving spins, such as in large vessels. Application of these gradients lengthened the BOLD TTP and onset time at 1.5 T (see *figure 4.9*), where the intravascular BOLD signal contribution from large veins are expected to be dominant. A possible explanation for this is that the short repetition time (1 s) could have led to inflow effects, which dominate the differences in BOLD response function and would be suppressed by the bipolar diffusion gradients. The contribution

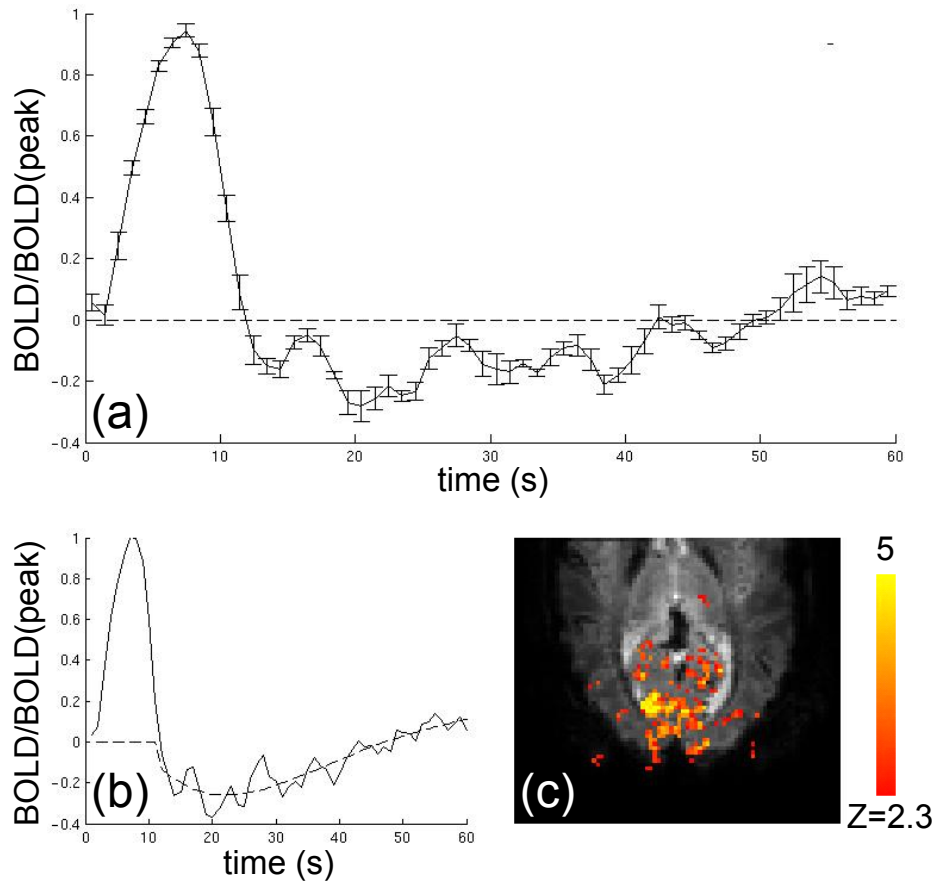


Figure 4.13: Post-stimulus oscillations, shown for the subject where they are most pronounced. (a) Average trial timecourse for the subject, at 7 T in the NoFS case, calculated in the same way as for *figure 4.12b*. (b) A 3×3 voxel ROI, centred on the voxel with maximum Z-statistic from the original FEAT analysis (FSL) was used to form the average trial timecourse shown here (solid line). To separate the oscillations from the post-stimulus undershoot, a fourth order polynomial was fit to timepoints after the average trial timecourse first becomes negative (dashed line). A correlation analysis was performed (FEAT, FSL), to identify the spatial characteristics of the oscillations, where the oscillations, post-stimulus undershoot and positive BOLD response were considered as separate components. (c) Z-statistic map of significant correlation ( $Z > 2.3$ ,  $P_{corr} < 0.05$ ) to the oscillations found in the 3×3 voxel ROI, again for the NoFS case at 7 T for this subject. Significant correlation with the oscillations is restricted to the visual cortex.

of inflow could be assessed in the future by acquiring data with a multiple echo sequence, where the fitted  $S(\text{TE} = 0)$  would show inflow effects and  $T_2^*$  would be independent of inflow effects. Assuming that these inflow effects are suppressed by the bipolar gradients, the source of the trend for later TTP at 1.5 T compared with 3 T and 7 T supports the hypothesis of an increased sensitivity in BOLD signal to large vessels at 1.5 T and reduced sensitivity to microvasculature.

As discussed in the methods section, flow suppression bipolar gradients were only applied in-plane, as through-slice gradients were found to cause large image artefacts due to eddy currents. This means that only in-plane motion is suppressed by these gradients. Bipolar gradient amplitude and duration were chosen to maximise the diffusion weighting and minimise the cut-off velocity  $v_{enc}$ , with the compromise of not making the TE too long, especially at 7 T. Here, signal from water protons moving faster than  $v_{enc}$  will be suppressed by the bipolar gradients. Due to the limitation of TE, the achieved  $v_{enc}$  of 3.26 mm/s at 1.5 T and 3 T, and 4.83 mm/s at 7 T is faster than typical blood velocities of capillaries and some of the microvasculature [110]. Thus in this study the bipolar gradients will mostly suppress the intravascular signal from veins and larger venules, however from the literature of intra-voxel incoherent motion (e.g. [113]), a diffusion weighting of  $b \geq 200 \text{ s/mm}^2$  is required to completely suppress the intravascular signal.

This paragraph aims to discuss the limitations in scan parameters for this experiment and explain the choices that were made based on these limitations. The 2 mm isotropic spatial resolution was chosen as a balance between reducing physiological noise at 7 T through smaller voxel volumes [109], whilst maintaining sufficient signal-to-noise at 1.5 T, where thermal noise dominates. This spatial resolution, combined with the use of flow suppression bipolar gradients meant that the minimum TE for a full-head acquisition would be too long for reasonable BOLD contrast. Therefore a reduced field-of-view was used, covering approximately the posterior two thirds of the brain. To prevent the remaining anterior part of the brain wrapping into the image, the

frequency encoded direction was chosen to be in the left–right direction. TE values used were chosen to be approximately equal to grey matter  $T_2^*$  [106], however due to the constraints of first applying the bipolar gradients, the TE used at 7 T was slightly longer than grey matter  $T_2^*$  (TE = 32 ms;  $T_2^* \simeq 28$  ms), but this was the minimum available without significantly reducing the diffusion weighting of the bipolar gradients. Ideally, a multi-echo acquisition would have been used, to probe the dependence of TE as well as field strength. However, a single-shot multi-echo acquisition was not used, as the shortest second echo would have been too long for a reasonable signal-to-noise ratio or BOLD contrast and would have lengthened the TR and caused the gradients to overheat. Multiple single-echo repeats, each at a different TE were ruled out due to time constraints, as the experiment already included multiple repeats with and without flow suppression bipolar gradients.

The visual paradigm consisted of flashing LED goggles which, although a crude stimulus, was chosen for repeatability between the three scanner sites. The paradigm of 5 s ON and 55 s OFF was short enough to resolve the BOLD response temporal characteristics, whilst a shorter ON period, was not used as this would lead to reduced activation, which may not be robust for temporal characterisation at 1.5 T.

This study used a common ROI across all three field strengths. The ROI selection was based on regions of common activation in the NoFS case at all three field strengths. This was to ensure that the same region (with the same vascular structure) was considered and was chosen to reduce variability, for example from the inclusion of a large draining vein in one ROI and not in another. One potential problem with this is that this method may lead to bias based on the activated region at one field strength. Although not presented here, the whole activated ROI at each field strength was considered separately and the similar trends were observed, although with increased variance expected from comparing slightly different regions. Another possible problem could be due to different image distortions at each field strength due to field inhomogeneities, particularly at 7 T. This would reduce the accuracy of the registrations between

field strengths and so the accuracy of the common ROI. However, careful consideration in checking each registration between field strengths, using an image viewer to compare the reference image and realigned image, showed that the registrations worked well, suggesting that the distortions were similar across field strengths. This was aided by the small field-of-view in the phase-encoded direction, meaning that the acquisition was of a short train length, reducing distortions. In summary, the choice of an ROI formed from the intersection of activated regions at all three field strengths ensured that the same tissue was considered across field strengths.

The temporal characteristics presented here are measured using some crude fitting techniques, which have associated errors. The gaussian fit to measure TTP and FWHM assumes that the BOLD response curve is symmetric, which is not the case. Also, fitting the rising slope to a straight line for onset time measurement assumes the leading edge of the BOLD response is fairly linear, whereas in reality it is curved. The limited number of timepoints that are used for this fit also means that it is very sensitive to noisy data points. Despite these limitations in the fitting values, structures, such as large draining veins can be seen in the voxelwise temporal characteristics maps and average values, calculated across the ROI and averaged over subjects gives values which are consistent with the timecourse averaged over subjects (*figure 4.12*). Improved fitting techniques could be used in the future, such as fitting a gamma variate function (which is not limited to being symmetrical), or a cubic splines fitting (which do not assume a shape for the BOLD response function). Monte Carlo simulations could be performed to assess the possibility of these trends arising by chance. However, despite these limitations in the fitting methods, the trends that have been observed are also seen in the timecourses formed by averaging over the common ROI.

## 4.5 Conclusion

This chapter has considered the effect of field strength on the BOLD response to a short visual stimulus, with the aim of assessing the different vascular contributions to BOLD temporal characteristics. A significant difference was found with field strength in the BOLD response onset time. This is consistent with BOLD signal Monte Carlo simulations [31], which predict a greater sensitivity to vessels with smaller radii at higher field strengths, and with the observations that smaller vessels contribute to an earlier BOLD response than larger veins [52, 97]. Future work will attempt to make use of more robust fitting techniques for measuring voxelwise temporal characteristics. Also, these results will be applied to existing dynamic BOLD models [114, 97, 106], to generate an improved model to account for these differences in sensitivity to vessel sizes and the associated change in temporal characteristics with field strength.

# Chapter 5

## Investigating cerebral haemodynamics using hypercapnia

### 5.1 Introduction

Cerebral vasculature is sensitive to changes in partial pressure of arterial carbon dioxide ( $P_aCO_2$ ). The cerebral vascular response to hypercapnia, an increase in  $P_aCO_2$ , can be a useful tool for investigating (and specifically calibrating) the BOLD signal to neuronal activity, by providing a global vascular perturbation. Through use of a hypercapnic challenge it is possible to separate oxygen consumption from the vascular components of the BOLD response [69, 77]. This is important as oxygen metabolism will be more closely correlated to the underlying neuronal activity [21, 22] than the vascular response and BOLD signal.  $CO_2$  perturbations can be used to test the capacity of local vasculature to dilate and constrict, which is important for understanding the haemodynamic response to neuronal activation and clinically for assessing the vascular reserve [115].

This chapter aims to use the measurement of cerebrovascular reactivity (*CVR*) in response to hypercapnia to improve our understanding of the BOLD signal. Here, two different *CVR* mapping paradigms are evaluated; graded hypercap-

nia and sinusoidal modulations in  $\text{CO}_2$ . The relationship between  $P_a\text{CO}_2$  and grey matter transverse relaxation rate ( $R_2^*$ ) is assessed using small, well resolved graded steps in  $P_a\text{CO}_2$ , over a normal physiological range, at 3 T and 7 T, which can be used to improve calibrated BOLD calculations [69] (see *section 2.4.5*) at field strengths above 1.5 T. A sinusoidal  $\text{CO}_2$  challenge at 7 T is used to assess CVR across brain regions, specifically the left and right hemisphere primary motor cortices, where handedness may result in a bias between hemispheres. Such changes may cause an underlying modulation in the BOLD signal, independent of the underlying neuronal activation.

## 5.2 The effect of hypercapnia on the vasculature

This section provides a literature review of the reported effects of hypercapnia on haemodynamic properties. This gives an insight into how hypercapnia can be used as a tool for assessing vascular variability in the BOLD signal, as explored in later sections of this chapter.

With the onset of hypercapnia, increased inspired  $\text{CO}_2$  diffuses into blood, leading to an increase in  $P_a\text{CO}_2$ . When a sequential gas delivery (*SGD*) breathing circuit (described in *chapter 3*) is used, it has been shown that end-tidal  $\text{PCO}_2$  ( $P_{ET}\text{CO}_2$ ) is a good approximation to  $P_a\text{CO}_2$  [116]. Arterial  $\text{CO}_2$  is dissolved in plasma, forming carbonic acid, so increasing  $P_a\text{CO}_2$  will decrease arterial pH. This decrease has been widely observed in arterial blood samples taken during hypercapnia [117, 118, 119].

Hypercapnia is a potent vasodilator [117], causing an increase in both cerebral blood volume (*CBV*) and cerebral blood flow (*CBF*). Invasive measures in rhesus monkeys have shown the change in *CBF* with  $P_a\text{CO}_2$  to be sigmoidal over the range of 5–418 mmHg  $P_a\text{CO}_2$  [118] centred on 40 mmHg (the normocapnic value), and approximately linear over a normal physiological range of  $P_a\text{CO}_2$  values. In a positron emission tomography (*PET*) study, also in rhesus monkeys [70], *CBF* and *CBV* were both shown to have approximately

linear relationships with  $P_aCO_2$ , over the  $P_aCO_2$  range of 15–76 mmHg. The average grey matter CBF response to hypercapnia has been measured using pulsed ASL (PICORe Q2TIPS) fMRI [120, 121], finding a CBF response of 4–6 %/mmHg. In another pulsed ASL study, resting CBF was found to correlate linearly (4 mL/100g/min/mmHg) with  $P_aCO_2$ , measured by blood samples in patients [122].

Perturbations of  $P_aCO_2$  have been used to investigate the coupling relationship between CBF and CBV, originally in rhesus monkeys [70] and later in humans [119] using PET. The coupling relationship between CBF and the venous component of CBV has been measured using fMRI [76], this is important as it is the venous blood volume compartment that is the predominant source of BOLD contrast. A significant increase in arterial CBV and decrease in arterial transit time has been observed under hypercapnia [123]. In the same study, the relationship between CBF and arterial CBV was measured for hypercapnia and also for a visual task. Whilst similar CBF – arterial CBV coupling was observed in the microvasculature in both cases, the larger artery contribution showed significantly different CBF – arterial CBV coupling for hypercapnia and visual activation, with a higher arterial blood volume increase relative to CBF increase on hypercapnia.

It is widely assumed that mild hypercapnia will not affect cerebral oxygen metabolism rate ( $CMRO_2$ ) and therefore oxygen demand [69]. However attempts to measure global cerebral oxygen consumption in humans [117, 124, 125] give conflicting and inconclusive results as to whether there is a significant change in cerebral oxygen consumption during mild hypercapnia.  $CMRO_2$  measured both during normocapnia and graded hypercapnia found no significant change in  $CMRO_2$  using nitrous oxide washout CBF measurements combined with oxygenation measurements of blood samples [117]. In another study, no significant change was found using both pulsed ASL and phase contrast flow measurements combined with a venous  $T_2$  measurement for blood oxygenation measurements [124]. However contrary to these findings,  $CMRO_2$  measured both during normocapnia and at a single level of hypercapnia (5

%  $\text{CO}_2$ ), using phase contrast flow measurements, combined with a venous  $T_2$  measurement for blood oxygenation measurements, found a reduction in  $\text{CMRO}_2$  [125]. Furthermore these methods do not account for potential local variations, such as a sensory response to the hypercapnia. Whether hypercapnia alters  $\text{CMRO}_2$  is an important issue, since either a global change or a local inhomogeneity in oxygen consumption in response to hypercapnia would lead to systematic errors in calibrated BOLD experiments [69].

### 5.3 Applications of hypercapnia in MRI

Hypercapnia has a wide range of applications in combination with MRI. These span from using the global nature of the hypercapnia BOLD response to test imaging techniques [126, 127], to using hypercapnia to assess local physiology [69, 128, 129]. This section provides an overview of these applications.

Small resting fluctuations in ventilation will cause fluctuations in  $P_a\text{CO}_2$  on the order of  $\pm 1$  mmHg [130], resulting in small changes in CBF, blood oxygenation and the BOLD signal. Measurements of natural  $P_{ET}\text{CO}_2$  fluctuations (as a non-invasive indicator of  $P_a\text{CO}_2$ ) have been correlated with BOLD signal fluctuations at 3 T to map BOLD CVR without the need to present a respiratory challenge [130]. This demonstrates that resting  $P_a\text{CO}_2$  fluctuations are of sufficient amplitude to have a significant contribution to the BOLD signal. Unlike respiratory noise resulting from a global field shift caused by chest motion [131],  $P_a\text{CO}_2$  related BOLD fluctuations are delayed with respect to ventilation and are not removed using typical physiological noise correction techniques, such as RETROICOR [51]. Measurements of respiratory tidal volume have been shown to account for some of these BOLD fluctuations [132] and to correlate with measured  $P_{ET}\text{CO}_2$  fluctuations [133]. Therefore,  $P_a\text{CO}_2$  related BOLD fluctuations can be partially corrected for using respiratory tidal volume measurements, which are more comfortable for the volunteer than end-tidal gas measurements.

The BOLD response to hypercapnia has been used to identify the brainstem respiratory control centres [134]. However, the measurement of these brain centres which control the neuronal response to hypercapnia is itself confounded by the global vasodilation due to hypercapnia. In that study [134] the approach that was used to account for this effect on the BOLD signal was to measure the BOLD response to resting  $P_{ET}CO_2$  fluctuations and the BOLD response to a 2–4 mmHg increase in  $P_{ET}CO_2$ , controlled using the dynamic end-tidal forcing method. Areas of neuronal activation to the hypercapnic challenge itself were determined from those voxels which had a statistically significantly higher %BOLD/mmHg response to hypercapnia than to resting  $P_{ET}CO_2$  fluctuations [134]. In an alternative approach, the neuronal response to paced breathing was mapped using isocapnic hyperventilation [135]. Isocapnia was achieved using the method proposed by Banzett *et al.* [79] (described in *chapter 3*), where freshly supplied gas is supplemented by gas with the same composition as alveolar gas to prevent the hyperventilation causing hypocapnia-related vasoconstriction.

The use of BOLD contrast as a measure of neuronal activation is known to be confounded by spatially heterogeneous vascular properties. An attempt to account for these vascular properties was proposed by Bandettini and Wong [136]. They assumed blood oxygenation changes to be spatially localised to neuronal activation, whereas the BOLD signal was also dependent on resting blood volume, which would not correspond to the site of neuronal activity. The BOLD signal due to hypercapnia was used to map this resting blood volume dependence, providing a good representation of the vascular spatial heterogeneity. Under this model, dividing the BOLD signal related to neuronal activation by the hypercapnia BOLD signal would remove the dependence on resting blood volume, with the remainder being a better representation of blood oxygenation and thus the underlying neuronal activation. Furthermore, it must be remembered that the hypercapnic BOLD response is actually dependent on vascular properties other than resting CBV, such as resting CBF and vascular responsiveness (the capacity of the local vascular tree to react). All of these properties will contribute to the BOLD signal to conceal the underlying neu-

ronal activation. Their effect will therefore be reduced by normalising by the hypercapnic BOLD signal, providing a better representation of the underlying neuronal activation, less effected by vascular variability. This normalisation method has been shown to reduce the differences of field strength and differences between  $T_2^*$ - and  $T_2$ -weighted images on activity localisation [137]. There may however be some systematic bias in this method [138], which has been attributed to a mismatch between hypercapnic and functional CBF responses.

Another approach to account for the vascular variability of the BOLD signal uses the isometabolic assumption during mild hypercapnia to calibrate the BOLD response to neuronal activity. CBF and BOLD responses to neuronal activation and hypercapnia are separately measured, from which the relative metabolic change ( $CMRO_2$ ) due to the neuronal activation is calculated. Several similar models have been proposed, relating changes in CBF, CBV and  $CMRO_2$  to BOLD signal [69, 128, 129], but the most widely accepted approach has become known as calibrated BOLD [69]. This involves using the hypercapnic CBF and BOLD responses to calculate a calibration parameter:

$$M = \frac{BOLD - 1}{1 - CBF^{\alpha-\beta}}, \quad (5.1)$$

which represents the theoretical maximum BOLD signal increase, where all the blood becomes fully oxygenated. Here,  $BOLD$  and  $CBF$  are the responses to hypercapnia, normalised to normocapnia values,  $\alpha$  is the CBV/CBF coupling relationship power law and  $\beta$  is the power law relationship for the effect of blood oxygenation on extravascular  $R_2^*$ . The method and values mentioned here are discussed in detail in *section 2.4.5*, however it is worth noting that a commonly assumed value of  $\beta = 1.5$  is used in the literature, derived for 1.5 T, whereas this value is expected to be closer to 1 at higher field strengths [31].

Hypercapnia has been used to investigate the effect of modulating CBF on the shape and size of the BOLD response to visual stimulation in humans [136, 77, 139, 140, 141, 142, 143, 144]. The effect of hypercapnia on the magnitude of the visual %BOLD response has produced conflicting results. Some studies measured an attenuation with hypercapnia [136, 142, 143, 144] and

augmentation with hypocapnia [142], other studies conclude that the visual BOLD signal is independent of hypercapnia [77, 139]. A complex relationship has been observed over a large range of  $P_{ET}CO_2$ , with the visual %BOLD response increasing with  $P_{ET}CO_2$  up to a maximum at  $\sim 50$  mmHg, then falling sharply for higher  $P_{ET}CO_2$  values. In comparison, there is much better agreement as to the effect of modulating  $P_aCO_2$  on the shape of the visual BOLD response. The delay and width of the visual BOLD response have both been shown to increase with increasing  $P_aCO_2$  [140, 142, 143]. In one study in anaesthetised monkeys [145], delivery of 6%  $CO_2$  totally suppressed the CBF and CBV responses to visual stimulus and the %BOLD signal decreased significantly. The authors interpreted this as the vasculature becoming so stressed by the hypercapnic challenge that the visual BOLD contrast was due only to increased deoxygenated haemoglobin resulting from the increased  $CMRO_2$ .

Hypercapnia has been used to assess the vascular contribution of diffusion-weighted fMRI [66]. Strongly diffusion-weighted fMRI is thought to have a close correlation with neuronal activity through cell swelling, due to increased activation leading to a decrease in diffusion coefficient. Therefore the diffusion-weighted fMRI signal should be insensitive to local vascular changes and so a purely vascular challenge, such as hypercapnia, is hypothesised to not effect the diffusion-weighted fMRI signal. Miller *et al.* [66] challenged this hypothesis by observing a strong diffusion-weighted fMRI signal increase with hypercapnia, demonstrating a significant vascular component.

Other examples of the application of hypercapnia include: Hypercapnia presented with susceptibility-weighted imaging showing that the susceptibility difference between grey and white matter cannot be explained by their different vascular densities [146]. The plausibility of spinal cord fMRI has been assessed using hypercapnia [126]. A reduction in cerebrospinal fluid (CSF) volume has been observed in response to increased CBV, using the global vasodilatory nature of hypercapnia [147]. Recently, hypercapnia has been used to test the effect of changes in blood velocity on pseudocontinuous ASL labelling efficiency, to optimise acquisition parameters [127]. Hypercapnia has

been used as a global BOLD stimulus for a novel approach to venous vessel size imaging [148]. Finally, two novel respiratory challenges have been proposed; cued deep breathing [89] and sinusoidal CO<sub>2</sub> modulation [149], which are both designed to be sensitive to measuring relative delays in BOLD CVR to changes in  $P_aCO_2$ . These methods have been proposed to add extra degree of information (delay as well as magnitude) for CVR mapping studies, which may be especially of use in studying cerebrovascular disease.

## Clinical applications

The main clinical use of hypercapnia in MRI is the assessment of cerebrovascular disease. Compared with resting CBF measurements, vascular reactivity to hypercapnia provides an extra degree of information as it assesses the capacity of the vasculature to dilate. CVR mapping highlights abnormal behaviour in the vascular bed associated with cerebrovascular disease. Feasibility of this approach was shown in healthy volunteers where a linear correlation between  $P_{ET}CO_2$  and the associated BOLD response in grey matter was shown with BOLD CVR being homogeneous across grey matter [115]. Reduced CBF CVR has been shown to correlate with higher scores in a standard vascular risk profile [150], whereas no correlation is found for resting CBF. Mandell *et al.* [67] showed that BOLD CVR is correlated to CBF CVR, even in occluded regions. CVR maps can be used to identify ischaemic regions and help to plan treatment and treatment outcome can also be assessed with hypercapnia CVR mapping [151].

Negative CVR has been observed in white matter, both using BOLD and ASL to map CVR under hypercapnia [152]. This has been attributed to a vascular steal phenomenon, where blood supply to an area is reduced to meet the demand from another area. The negative CVR regions in young, healthy volunteers were found to occur in locations vulnerable to white matter disease in elderly patients. Another study [153] found that negative CVR regions in patients exhibited an increased white matter diffusion coefficient, consistent with damage to the white matter. In this case, CVR mapping could provide an early diagnosis of white matter disease.

## 5.4 Cerebrovascular reactivity at 3 and 7 Tesla

### 5.4.1 Introduction

As discussed in *section 2.4.2*, the relationship between blood oxygenation and transverse relaxation rate ( $R_2^*$ ) is complicated, depending on the relative contributions from intravascular and extravascular compartments, and on both static and diffusing spin dephasing regimes. The BOLD response to hypercapnia, which is a tightly controlled stimulus, should provide some insight as to the dominant transverse relaxation mechanisms. A supralinear power law relationship was assumed between  $R_2^*$  and blood oxygenation in a model derived for 1.5 T [69], but this is unlikely to be appropriate at higher field strengths. Better characterisation of this power law relationship at 3 T and 7 T would improve BOLD calibration at these field strengths [69] (see *section 2.4.5*).

This study used a feed-forward, low gas flow system to target small (3 mmHg), clearly resolvable steps in  $P_{ET}CO_2$  to assess the relationship between  $R_2^*$  and  $P_{ET}CO_2$  over a normal physiological range. The  $R_2^*$  CVR measurement was assessed at both 3 T and 7 T and was used to explore the relationship between blood oxygenation, vasodilation and BOLD signal.

This study has been published (*Driver et al.* [154]). Figures which have been reproduced from the published paper have been cited as such.

### 5.4.2 Echo time optimisation

To improve the accuracy of the  $R_2^*$  calculation, simulations were performed to optimise the gradient echo (GE) EPI echo times used. If the GE EPI signal ( $S(TE)$ ) is assumed to decay monoexponentially then the natural logarithm of  $S$  has a linear relationship with TE:

$$\log_n(S) = \log_n(S_0) - TE \cdot R_2^*, \quad (5.2)$$

where  $S_0 = S(TE=0)$ . TE values that minimised the noise associated with the  $R_2^*$  calculation were found by considering noise propagation through a least

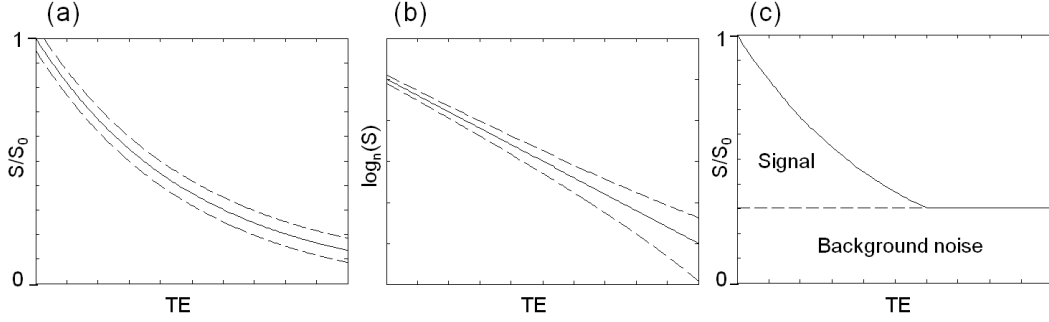


Figure 5.1: Thermal noise contribution to the simulated signal decay. Error bounds due to thermal noise are given by the dashed lines. (a) Exponential signal decay with constant thermal noise over TEs. (b) Natural logarithm of signal varies linearly with TE, whilst the effect of thermal noise increases with TE. (c) Plot illustrating a cut-off TE, where the signal drops below the level of thermal noise, causing an underestimation of  $R_2^*$ .

squares fit to a straight line [155]. Thermal noise ( $\sigma_0$ ) will cause an error in measured  $S$ , assumed to be constant with TE (*figure 5.1a*). If  $R_2^*$  is calculated from a linear fit of  $\log_n(S)$  against TE, then the thermal noise contribution to the fit error will increase with TE (*figure 5.1b*). It is then necessary to weight the noise by the inverse of the signal [156]:

$$\sigma(\log_n(S)) = \sigma(S)/S = \sigma_0/S \quad (5.3)$$

This uncertainty can be used to estimate the error propagation into the gradient ( $R_2^*$ ) of the linear fit [155]. Echo times were chosen to minimise this error. Note that the error is dependent on  $R_2^*$ , so the optimisation required a prior estimate of  $R_2^*$ , chosen as a literature value for GM average  $T_2^*$  ( $= 1/R_2^*$ ) as 66.0 ms at 3 T and 33.2 ms at 7 T [157]. These values may be slightly higher than those measured with EPI here, as the method by which they were calculated included a correction for large-scale field inhomogeneities.

There will also be a low signal limit, where the signal drops below the background noise level in the modulus images, causing the noise to dominate the linear fit (*figure 5.1c*) and  $R_2^*$  to be underestimated. This imposes an upper limit on TE. Hardware constraints also place a lower limit on TE, allowing time for the spatial encoding gradients (dependent on the gradient set, matrix

size and number of slices).

To acquire data at multiple echo times, either data can be acquired with one TE per  $T_2^*$  decay, alternating between TEs across dynamics, or multiple TEs can be acquired per shot, where there is a minimum echo spacing, approximately equal to the readout duration per echo, to fit the spatial encoding gradients. In reality, for the case of multiple TEs within a single  $T_2^*$  decay, for the matrix size ( $96 \times 96$ ) and the imaging gradient sets used only two echoes could be acquired, as further echoes would exceed the upper limit on TE mentioned in the previous paragraph. Therefore, this case will be referred to as a double echo sequence.

Optimum echo times were found by calculating the error (relative to  $\sigma_0/S_0$ ) for all combinations of two TE values (in spacings of 0.1 ms and range: scanner defined minimum TE – 100 ms) and finding the minimum error. For the double echo sequence, the optimum echo times were found to be the shortest possible TE and an echo time approximately  $T_2^*$  later than the minimum TE. This is a balance between the largest possible echo spacing and the increased error associated with a longer TE. At 7 T, the optimum value for the second echo was shorter than allowed, due to the required minimum echo spacing for image encoding with the available gradients, so the minimum allowed spacing (of 37 ms at 7 T) was used (giving the lowest estimated noise possible with this limit). Note that this method only considers thermal noise and does not account for physiological noise, which will also depend on TE [109].

### 5.4.3 Development of paradigm

This section discusses the development of the hypercapnia paradigms used in this study. All development was performed at 7 T.

Initially, single echo GE EPI data were acquired with 3 mm isotropic voxels over a  $192 \times 192$  mm<sup>2</sup> field-of-view and 10 axial slices, with no slice gap, in a 1 s TR. The GE EPI echo time alternated between TE = 20.0, 55.6, 55.6 ms, repeating every three dynamics. Thus, one  $R_2^*$  map could be acquired every 3

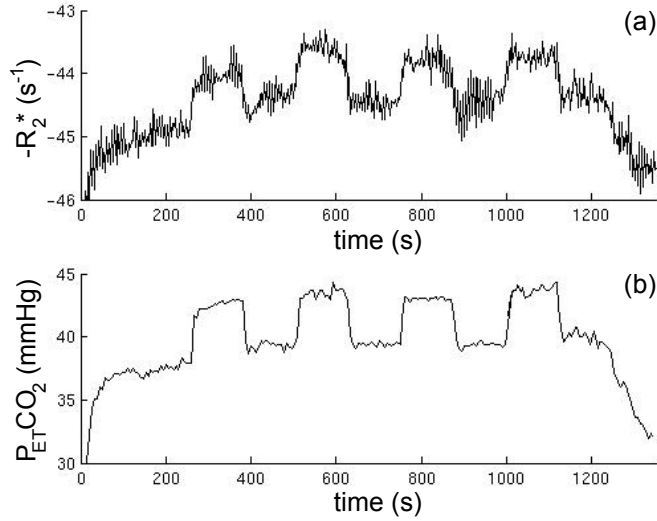


Figure 5.2: (a) Grey matter averaged  $R_2^*$  timecourse corresponding to (b) the boxcar  $P_{ETCO_2}$  paradigm.

s. The combination of one short TE and two long TE repeats was to account for the lower SNR at the long TE.  $R_2^*$  maps were formed by combining each block of three dynamics using a least squares linear fit, based on *equation 5.2*. Echo times were chosen to minimise noise in the  $R_2^*$  calculation, as described in *section 5.4.2*, using the constraint of a minimum TE = 20 ms. As each TE was acquired separately, there was no minimum spacing between echo times.

Grey matter  $R_2^*$  timecourses were formed (see *section 5.4.4* for a complete method) which showed a periodic oscillation repeating approximately every 6 seconds (*figure 5.2*), corresponding to the breathing frequency, which is thus likely to be respiratory noise [131]. The three datasets combined for  $R_2^*$  calculation will each have been acquired at a different stage in the breathing cycle, so each include a different respiratory noise contribution. Therefore a large respiratory noise contribution is associated with acquiring an  $R_2^*$  map from three single echo scans with different TEs, acquired over 3 s.

To reduce the respiratory noise contribution, a double echo acquisition was used, such that the data at the two different TEs are acquired within a single  $T_2^*$  decay, so are effectively acquired at the same stage in the breathing cycle.

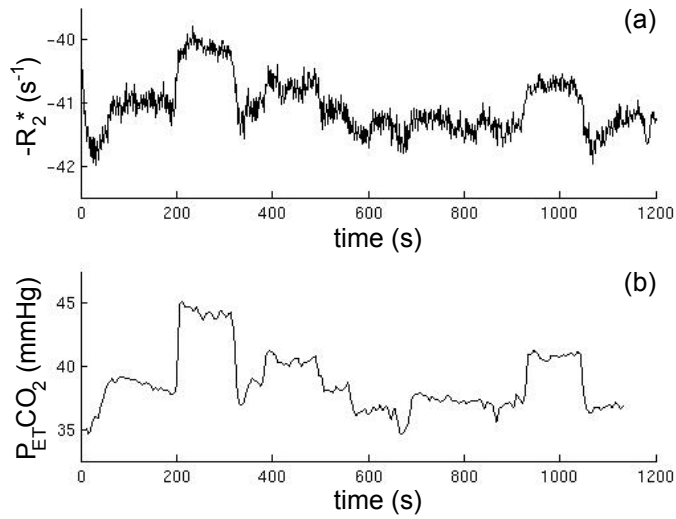


Figure 5.3: (a) Grey matter averaged  $R_2^*$  timecourse corresponding to (b) the pseudo-randomised graded  $P_{ET}CO_2$  paradigm.

The double echo dataset was acquired with TEs of 20 and 57 ms in 1.5 s. Also the in-plane voxel size was reduced to 2 mm, as this finer spatial resolution has been shown to reduce physiological noise at 7 T [109]. With these adjustments, the scan acquisition parameters are the same as used for the main study, which will be fully described in *section 5.4.4*.

The first hypercapnia paradigm attempted was a simple box-car design. This type of paradigm is popular, due to its simplicity, and it is used in the majority of hypercapnia applications in MRI (*see section 5.3*). The boxcar hypercapnia paradigm consisted of four repeats of 2 minutes of mild hypercapnia (45 mmHg  $P_{ET}CO_2$  targeted) followed by 2 minutes of normoxia (40 mmHg  $P_{ET}CO_2$  targeted). Grey matter masks were formed (*see section 5.4.4* for a complete method). The grey matter averaged  $-R_2^*$  timecourse is shown in *figure 5.2a*, and can be seen to closely follow the  $P_{ET}CO_2$  timecourse (*figure 5.2b*).

Due to the clearly resolved transitions in both  $P_{ET}CO_2$  and grey matter averaged  $R_2^*$ , a new graded respiratory paradigm was devised to provide improved dynamic range. This consisted of 5 levels of targeted  $P_{ET}CO_2$ , between 37–49 mmHg in 3 mmHg steps, with each level presented in a pseudo-randomised or-

der. The paradigm comprised two minutes at each level, followed by 1 minute at normocapnia (40 mmHg  $P_{ET}CO_2$  targeted). This respiratory paradigm is the same as used for the main study, which will be fully described in *section 5.4.4*.

The grey matter averaged  $-R_2^*$  timecourse for the pseudo-randomised graded paradigm is shown in *figure 5.3a*, which can be seen to closely follow the  $P_{ET}CO_2$  timecourse (*figure 5.3b*). The analysis to generate these timecourses will be detailed in *section 5.4.4*.

This section has described the paradigm development for this study. A double echo acquisition, with both echoes acquired in a single  $T_2^*$  decay, was preferred to multiple single-echo acquisitions over several seconds, each at a different TE, due to physiological noise across the respiratory cycle causing large oscillations in the calculated  $R_2^*$  timecourse. The resolved transitions in both  $P_{ET}CO_2$  and grey matter averaged  $R_2^*$  meant that instead of a simple boxcar design, a graded  $P_{ET}CO_2$  paradigm provided an increased dynamic range of  $P_{ET}CO_2$  transitions, suitable for studying the form of relationship between  $P_{ET}CO_2$  and  $R_2^*$ .

#### **5.4.4 Method**

Five healthy male subjects, mean age of 25 years (range 23-29 years), took part in the study. Approval for the study was obtained from the University of Nottingham Medical School Ethics Committee and all subjects gave written informed consent.

The hypercapnia challenge is described in *section 3.3*.  $P_{ET}CO_2$  was targeted at 40 mmHg (baseline) for an initial 3 minutes, followed by five repeats of 2 minutes of a target  $P_{ET}CO_2$  level, followed by one minute of baseline. The targeted  $P_{ET}CO_2$  level differed in every repeat in a pseudo-randomised order of 49, 43, 37, 40, 46 mmHg. The pseudo-randomised order is used instead of a sequential increase or decrease in  $P_{ET}CO_2$  level, as a sequential design is susceptible to bias from low order signal drift, which could be reflected in the

$R_2^*$  timecourse and as a systematic error in CVR measurements.  $P_{ET}O_2$  was targeted at 100 mmHg throughout. When not performing the challenge, the participant returned to spontaneous ventilation of medical air (21 %  $O_2$ , 79 %  $N_2$ ).

Scanning was performed on a Philips Achieva 3 T system, with a whole body volume transmit and 8 channel SENSE head receive coil, and a Philips Achieva 7 T system, with head volume transmit and 16 channel SENSE head receive coil. Axial images were acquired every 1.5 s throughout the hypercapnia challenge (800 dynamics) using a double-echo, single shot GE EPI sequence. Imaging parameters of SENSE factor=2, TE=16/81 ms with 30 ms readout per echo at 3 T, TE=20/57 ms with 37 ms readout per echo at 7 T were used. The longer readout per echo at 7 T was due to lower maximum gradient amplitude and slew rate (30  $mTm^{-1}$  and 100  $mTm^{-1}ms^{-1}$ ) compared to 3 T (40  $mTm^{-1}$  and 200  $mTm^{-1}ms^{-1}$ ). Echo times were optimised for  $R_2^*$  measurement rather than BOLD contrast (see section 5.4.2). Images consisted of  $2 \times 2 \times 3$  mm<sup>3</sup> voxels, with a  $192 \times 192$  mm field of view, over 9 slices at 3 T and 10 slices at 7 T, and no slice gap. Figure 5.4 shows the typical slice coverage at both 7 T and 3 T.

After the hypercapnia challenge, inversion-recovery (IR)-EPI datasets were acquired for tissue segmentation. This had the same geometry as the double-echo sequence, with grey matter (GM), white matter (WM) and CSF nulled (TI=600/900/1900ms at 3 T and TI=600/1100/2200 ms at 7 T). The image bandwidth was kept the same as for the double-echo sequence, to match EPI distortions. For vein segmentation, a high-resolution (0.8 mm isotropic)  $T_2^*$ -weighted fast field echo (FFE) FLASH (TR/TE=50/20 ms, EPI factor=3, bandwidth=167 Hz) image which minimises geometric distortions was also acquired at 7 T.

The double-echo data were motion corrected using MCFLIRT (FSL, fMRIB, Oxford, UK) by realigning the shorter TE images (20 ms) to the first dynamic, then applying the registrations to both sets of images. The higher

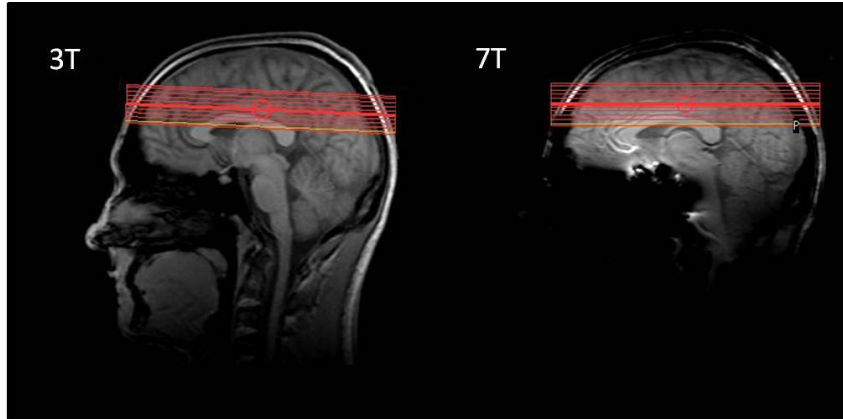


Figure 5.4: Screenshots from the 3 T and 7 T scanners, showing the survey image and typical (subject 5) slice coverage. The loss of signal below the brain at 7 T is due to a more restricted spatial sensitivity of the receive coil array at 7 T compared with 3 T. The susceptibility effects of adjacent airspaces can also be seen at 7 T, at the interface between the brain and frontal sinus.

SNR of the shorter TE images helped with the accuracy of the motion correction algorithm.  $R_2^*$  was calculated on a voxel-by-voxel basis for each timepoint by combining the signal ( $S$ ) at both echo times, assuming a monoexponential decay, using the following equation:

$$R_2^* = \frac{\log_n S(TE_1) - \log_n S(TE_2)}{TE_2 - TE_1} \quad (5.4)$$

The IR-EPI datasets were segmented, using BET (FSL) on the CSF-nulled images to remove non-brain voxels, then the FAST algorithm (FSL) was applied to generate a GM mask and GM, WM and CSF partial volume estimates. The WM mask only included voxels that were estimated to be at least 99% WM, to avoid significant partial-voluming from GM reactivity. The close correlation between  $P_{ETCO_2}$  and  $R_2^*$  meant that timepoint-by-timepoint comparison could be made to assess CVR, rather than averaging over steady state periods for each level. The  $P_{ETCO_2}$  trace was linearly interpolated (MATLAB, The MathWorks, Natick, USA) to match the sampling frequency of the double-echo data, then manually shifted to temporally align the  $P_{ETCO_2}$  timecourse with the  $R_2^*$  timecourse averaged over all GM voxels. The estimated error of

this alignment is one interpolated timepoint. This allowed the actual level of  $P_{ET}CO_2$  and  $R_2^*$  to be compared on a point-by-point basis across a range of  $P_{ET}CO_2$  levels (rather than simply comparing the signal change at prescribed  $P_{ET}CO_2$  levels). Linear regressions were performed to calculate average GM and WM  $R_2^*$  CVR to  $P_{ET}CO_2$ , defining  $R_2^*$  CVR as the absolute change in  $R_2^*$  (measured by the gradient of the linear regression) for a 1 mmHg change in  $P_{ET}CO_2$ . The fit uncertainties were used to assess the error in  $R_2^*$  CVR.

In order to consider the  $R_2^*$  CVR of tissue alone, excluding large vessels, the FLASH  $T_2^*$ -weighted image acquired at 7 T was used to identify veins, at 7 T veins have a shorter  $T_2^*$  than tissue ( $\sim 5$  ms [105] compared with 28 ms [106]) and so lower signal intensity than the surrounding tissue (*figure 5.5a*). Initially, regions outside of the brain were removed from the images using BET (FSL). The image was inverted, so that voxels dominated by veins had a high intensity and a third-order polynomial filter was applied to remove large-scale inhomogeneities (*figure 5.5b*). Nearest-neighbour smoothing was performed and the smoothed image was then subtracted from the unsmoothed image to locate voxels with a significant venous fraction [103] (*figure 5.5c*). Intensity thresholding was performed to produce a binary mask of voxels dominated by veins and cluster analysis was performed to remove any isolated voxels (*figure 5.5d*). The FLASH image was resized to  $2 \times 2 \times 3$  mm<sup>3</sup> and co-registered to both the 7 T and the 3 T double-echo datasets and these transformations were then applied to the resized binary mask. This mask was applied to the  $R_2^*$  timeseries to remove these voxels before averaging, thus allowing a comparison of GM and WM  $R_2^*$  CVR with and without the inclusion of large vessels.

Voxelwise maps of CVR were formed to confirm the global nature of the BOLD response to hypercapnia and to demonstrate the contrast in CVR between GM and WM. To do this, the linear fitting technique was performed on a voxel-by-voxel basis, rather than over an averaged timecourse. However, it was found that the  $R_2^*$  data was too noisy to calculate reasonable  $R_2^*$  CVR maps. Instead, the double echo data were combined using a weighted summation of data acquired at each echo time [16], to improve the BOLD contrast of the data, since

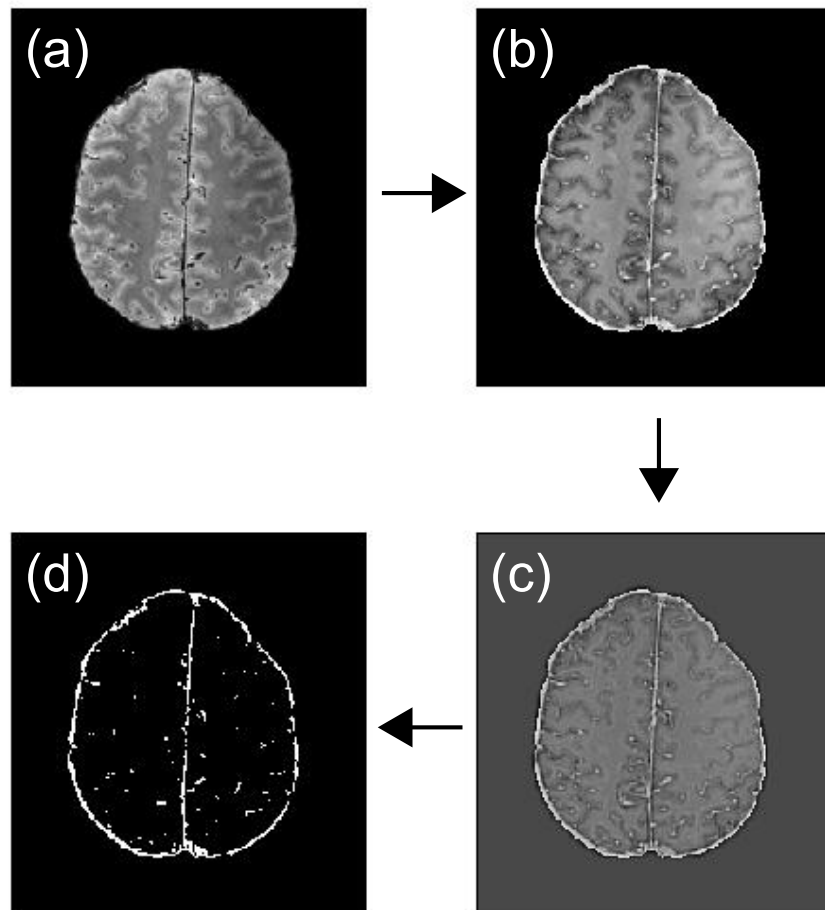


Figure 5.5: Vein segmentation method. (a) Original  $T_2^*$ -weighted image, where veins appear dark. (b) Inverted and third-order polynomial filtered image. (c) Difference image (minus nearest-neighbour smoothed image), highlighting veins. (d) Binary vein mask, generated using thresholding and cluster analysis. Note the ring around the edge of the brain is due to an imperfect brain mask and should not be mistaken for veins.

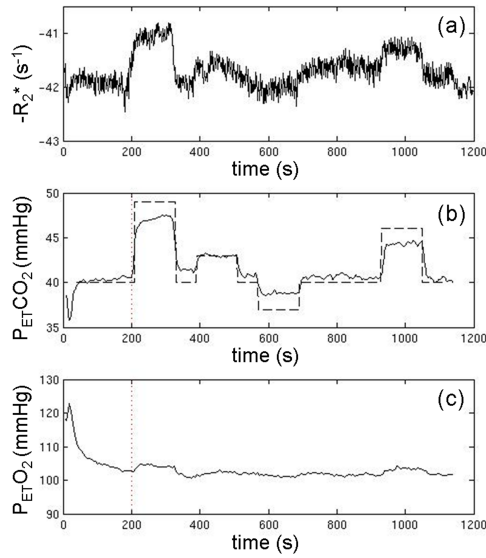


Figure 5.6: Corresponding timecourses for (a) GM averaged  $-R_2^*$  (veins excluded), (b)  $P_{ET}CO_2$  and (c)  $P_{ET}O_2$  for Subject 5 at 7 T.  $-R_2^*$  is plotted to show the tight linear correlation between  $P_{ET}CO_2$  and  $-R_2^*$ . The dotted vertical line indicates the end of the initial baseline period. The dashed trace shows targeted  $P_{ET}CO_2$  levels. This figure is reproduced from [154].

the echo times used were not optimal for BOLD contrast (as shown in *section 2.4.3*). The weighting was based on a  $T_2^*$  map calculated from the average baseline ( $P_{ET}CO_2 = 40$  mmHg) signal at both echo times. For every voxel the weighted summation signal was calculated over every timepoint, then the voxel’s timecourse was normalised to the voxel’s weighted summation average baseline signal. For each voxel, a linear fit was performed between the voxel’s normalised weighted summation timecourse and  $P_{ET}CO_2$ . The gradient of the linear fit gave a value for weighted summation % BOLD CVR.

### 5.4.5 Results

Similar changes in  $P_{ET}CO_2$  level were achieved across all subjects. *Figure 5.6* shows a representative subject at 7 T, whilst *figure 5.7* shows all subjects at both 7 and 3 T. Across all subjects, the step sizes were consistently a third

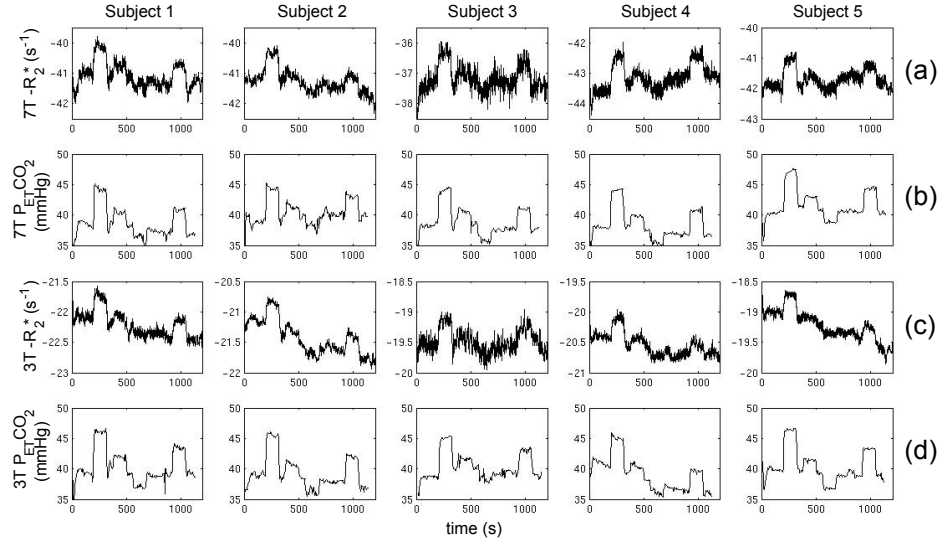


Figure 5.7: All five subject's timecourses at 7 T (a,b) and 3 T (c,d) for GM averaged  $-R_2^*$  (a,c) and  $P_{ET}CO_2$  (b,d).

less than targeted. Despite this, clearly resolvable  $P_{ET}CO_2$  transitions were achieved (figure 5.7(b & d)) whose level was well maintained over the 2 min period. The  $P_{ET}O_2$  levels reached a steady state within the initial 3 min baseline period (figure 5.6c) and then had a maximum range of 5 mmHg (across all subjects and all  $P_{ET}CO_2$  challenges).

The  $R_2^*$  timecourses closely followed the  $P_{ET}CO_2$  timecourse at both field strengths (figure 5.6a and figure 5.7(a & c)). Table 5.1 shows individual GM  $R_2^*$  reactivities both including and excluding voxels dominated by veins. Figure 5.8(a & b) plots the GM averaged  $R_2^*$  reactivity against  $P_{ET}CO_2$  at 7 and 3 T including data for each of the five subjects, also showing the linear fits. Average GM  $R_2^*$  reactivities agreed well between subjects (figure 5.8). Including voxels dominated by veins, GM  $R_2^*$  CVR was  $2.0 \pm 0.4$  times higher at 7 T than at 3 T (averaged over all subjects): GM  $R_2^*$  CVR was  $0.074 \pm 0.007$   $s^{-1}$   $mmHg^{-1}$  at 3 T and  $0.145 \pm 0.020$   $s^{-1}$   $mmHg^{-1}$  at 7 T. Excluding voxels dominated by veins GM  $R_2^*$  reactivity was  $2.1 \pm 0.5$  times higher at 7 T than at 3 T (averaged over all subjects): GM  $R_2^*$  CVR was  $0.066 \pm 0.004$   $s^{-1}$   $mmHg^{-1}$  at 3 T and  $0.141 \pm 0.008$   $s^{-1}$   $mmHg^{-1}$  at 7 T. There was a significant increase

GM average including venous voxels	$R_2^*$ CVR ( $s^{-1}$ mmHg $^{-1}$ )		
	7 T	3 T	7 T/3 T
Subject 1	$-0.173 \pm 0.005$	$-0.067 \pm 0.004$	2.6
Subject 2	$-0.146 \pm 0.009$	$-0.086 \pm 0.005$	1.7
Subject 3	$-0.163 \pm 0.008$	$-0.072 \pm 0.004$	2.3
Subject 4	$-0.133 \pm 0.010$	$-0.075 \pm 0.002$	1.8
Subject 5	$-0.109 \pm 0.006$	$-0.073 \pm 0.005$	1.5
Mean (across subjects) $\pm$ standard deviation	$-0.145 \pm 0.025$	$-0.074 \pm 0.007$	$2.0 \pm 0.4$

GM average with venous voxels excluded	$R_2^*$ CVR ( $s^{-1}$ mmHg $^{-1}$ )		
	7 T	3 T	7 T/3 T
Subject 1	$-0.168 \pm 0.005$	$-0.058 \pm 0.004$	2.9
Subject 2	$-0.134 \pm 0.009$	$-0.081 \pm 0.005$	1.7
Subject 3	$-0.163 \pm 0.008$	$-0.070 \pm 0.004$	2.4
Subject 4	$-0.128 \pm 0.009$	$-0.065 \pm 0.002$	2.0
Subject 5	$-0.109 \pm 0.006$	$-0.060 \pm 0.005$	1.8
Mean (across subjects) $\pm$ standard deviation	$0.141 \pm 0.025$	$-0.066 \pm 0.009$	$2.1 \pm 0.5$

Table 5.1: Grey matter  $R_2^*$  CVR for all subjects, calculated using a linear regression.

in the GM  $R_2^*$  CVR 7 T/3 T ratio between the case when vessels were included and when they were excluded ( $P=0.06$ , Wilcoxon paired). Contrast-to-noise ratio (CNR) was calculated for GM  $R_2^*$  CVR as  $0.88$  mmHg $^{-1}$  at 7 T and  $0.98$  mmHg $^{-1}$  at 3 T. This was calculated by dividing the GM  $R_2^*$  CVR by the variance (GM  $R_2^*$  standard deviation) of the 40 mmHg  $P_{ET}CO_2$  step, averaged over all subjects.

The paradigm provided sufficient sensitivity to detect an average WM  $R_2^*$  CVR (table 5.2) of  $0.021 \pm 0.003$  s $^{-1}$  mmHg $^{-1}$  at 3 T and  $0.040 \pm 0.007$  s $^{-1}$  mmHg $^{-1}$  at 7 T with veins removed. 7 T WM  $R_2^*$  CVR is  $1.6 \pm 0.5$  times higher than at 3 T, although interpretation of this ratio should be limited, due to the smaller

WM average with venous voxels excluded	$R_2^*$ CVR ( $s^{-1} \text{ mmHg}^{-1}$ )		
	7 T	3 T	7 T/3 T
Subject 1	$-0.035 \pm 0.006$	$-0.001 \pm 0.002$	31.7*
Subject 2	$-0.031 \pm 0.011$	$-0.020 \pm 0.002$	1.6
Subject 3	$-0.061 \pm 0.009$	$-0.028 \pm 0.004$	2.2
Subject 4	$-0.050 \pm 0.005$	$-0.036 \pm 0.003$	1.4
Subject 5	$-0.022 \pm 0.004$	$-0.020 \pm 0.002$	1.1
Mean (across subjects) $\pm$ standard deviation	$-0.040 \pm 0.015$	$-0.021 \pm 0.013$	$1.6 \pm 0.5^*$

Table 5.2: White matter  $R_2^*$  CVR for all subjects, calculated using a linear regression.

\* The 7 T/3 T ratio for Subject 1 is treated as an outlier and has been ignored in the cross-subject mean calculation.

WM contrast to noise ratio compared with GM. *Figure 5.8(c & d)* plot the WM averaged  $R_2^*$  reactivity at 7 and 3 T for each of the five subjects.

Example CVR maps from the graded hypercapnia paradigm are shown in *figure 5.9* for the same subject, acquired both at 3 T and 7 T. The CVR maps showed good grey matter contrast and clear distinction between grey and white matter.

#### 5.4.6 Discussion

This study has combined a versatile and accurate method for controlling and measuring  $P_{ET}CO_2$  and  $P_{ET}O_2$  with a quantitative  $R_2^*$  measurement to provide a new time point-by-time point approach to monitoring CVR using MRI. Small, readily tolerable steps in  $P_{ET}CO_2$  over a naturally occurring range of  $P_{ET}CO_2$  (37-49 mmHg) were used. The rapid sampling of the  $P_{ET}CO_2$  and  $R_2^*$  allowed point-by-point temporal analysis which improved sensitivity in CVR, allowing measurement of GM reactivity and detection of significant WM reactivity, at both 3 and 7 T.

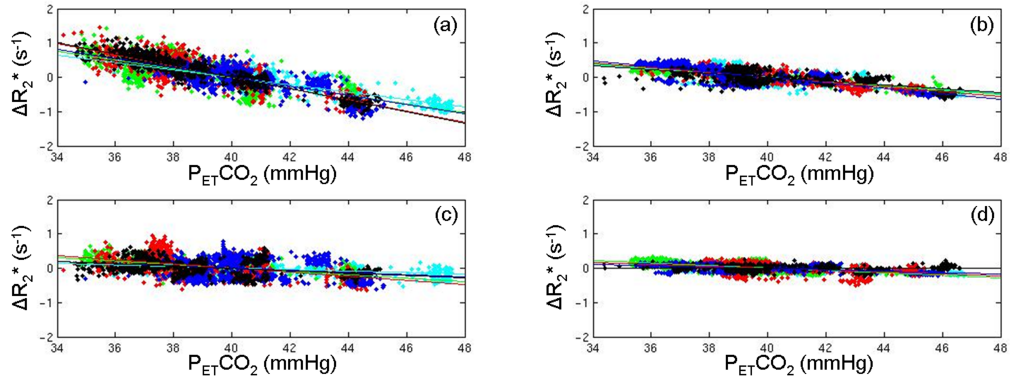


Figure 5.8: GM averaged  $R_2^*$  reactivity at (a) 7 T and (b) 3 T and WM averaged reactivity at (c) 7 T and (d) 3 T for all subjects (veins excluded). Averaged  $R_2^*$  reactivity is shown by the scatter plots and linear fits are shown as lines. Each subject is plotted in a different colour. This figure is reproduced from [154].

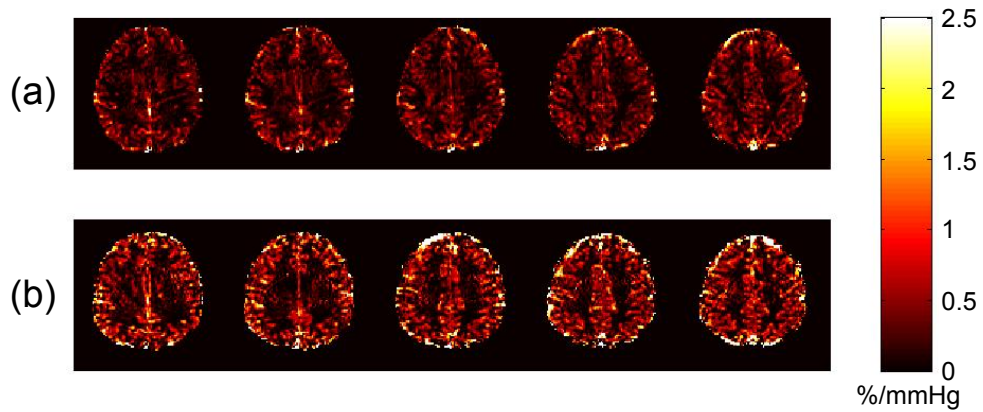


Figure 5.9: (a) 3 T and (b) 7 T weighted summation % BOLD CVR maps, calculated using a voxelwise linear fit to the  $P_{ET}CO_2$  trace.

The technique to control blood gases used in this study allowed independent control of  $P_{ET}CO_2$  and  $P_{ET}O_2$ , to provide transitions to and between stable  $P_{ET}CO_2$  levels, clearly resolvable in 3 mmHg steps, whilst maintaining  $P_{ET}O_2$  at a constant level.  $P_{ET}CO_2$  transitions were achieved within one or two breaths. Although good control over  $P_{ET}O_2$  allowed independent assessment of reactivity to changes in  $P_{ET}CO_2$  [158], the small changes in  $P_{ET}O_2$  associated with a fixed inspired  $CO_2$  challenge (of the order of  $\sim 20$  mmHg) are unlikely to have had a significant effect on venous blood oxygenation, BOLD signal and  $R_2^*$  (see section 6.4). The main advantage over a fixed inspired  $CO_2$  challenge is the reproducibility of  $\Delta P_{ET}CO_2$  across subjects [93], which for fixed inspired  $CO_2$  challenges will depend on the subject's ventilation and on their metabolism. Measured  $\Delta P_{ET}CO_2$  transitions were approximately a third less than the targeted values. This was due to the version of the Respiract<sup>TM</sup> software model at the time. CVR calculated using targeted values would therefore have been underestimated, showing the importance of measuring  $P_{ET}CO_2$ .

This study measured the change in  $R_2^*$ , rather than % BOLD signal change (except for calculating voxelwise CVR maps). The  $R_2^*$  measurement, from a double echo acquisition was based on the assumption that the voxel's transverse relaxation is monoexponential. This would not be true if there were significant contributions from different compartments, with different spin dephasing mechanisms (for example intravascular and extravascular compartments, or a mixture of static and diffusive regimes of spin dephasing [28]). Advantages of measuring  $R_2^*$  as opposed to % BOLD are that it should be less sensitive to inflow effects, as it is independent of initial magnetisation (at  $TE = 0$  ms) and  $R_2^*$  is applicable to models relating the effects of blood oxygenation on GE signal [30]. There was a low frequency temporal drift seen in some of the GM  $R_2^*$  timecourses. The pseudo-randomised paradigm was designed to minimise bias in CVR measurement from this drift, by not having a systematic increase, or decrease in  $P_{ET}CO_2$  which could be falsely matched to the drift. However, a simple temporal filter could be used to remove this drift, so long as care is taken to avoid filtering out some of the changes in  $R_2^*$  related to  $\Delta P_{ET}CO_2$ , which changes with a low temporal frequency compared with a typical fMRI

experiment.

Previously,  $T_2^*$  (not  $R_2^*$ ) CVR has been measured using a multi-echo acquisition [141], with a non-linear relationship observed over large (10 mmHg)  $P_{ET}CO_2$  steps.  $P_{ET}O_2$  was not controlled and the high gas flow rates used to achieve high (70 mmHg) and low (20 mmHg)  $P_{ET}CO_2$  target levels would have induced hyperventilation, leading to increased  $P_{ET}O_2$  (not monitored), arterial oxygenation and a further increase in  $T_2^*$ , which may have accounted for some of the non-linearity. However, a rough conversion of their results from  $T_2^*$  to  $R_2^*(=1/T_2^*)$  shows an approximately linear relationship between  $R_2^*$  and  $P_{ET}CO_2$  from 40-60 mmHg.

This study used high spatial resolution compared to previous CVR studies, and so will have reduced partial volume effects between GM and WM. In this study,  $R_2^*$  CVR was found to increase with field strength, which is consistent with a previous cross-field BOLD CVR study [137]. Removing voxels with large venous components reduced the  $R_2^*$  CVR at both field strengths, consistent with the intravascular/perivascular signal dominating the BOLD signal change. As expected this reduction in reactivity was larger at 3 T than 7 T, since the  $R_2^*$  of blood is much greater at 7 T, so the direct signal contribution from blood is reduced.

Results also suggest that the power law relating the change in  $R_2^*$  to frequency shift (due to change in relative intravascular susceptibility or field strength) (7 T:3 T  $R_2^*$  ratio of  $2.1 \pm 0.5$ ) is close to linear ( $7/3 = 2.3$ ) between 3 and 7 T, and by excluding voxels dominated by veins the 7 T:3 T  $R_2^*$  reactivity ratio was increased. Yablonskiy and Haacke [30] predicted a linear relationship for extravascular spin dephasing. A linear relationship between  $R_2^*$  and frequency offset is expected in the static dephasing regime, whereas supralinear relationships are associated with intermediate and fast dephasing regimes [31]. The effect of diffusion on transverse relaxation around a vein will depend on vessel size and frequency offset due to the vein as well as echo time. For the echo times used here, as the frequency offset increases, the vessel size at which

the static dephasing limit dominates decreases [28]. Monte Carlo simulations predict supralinear behaviour at 1.5 T [27, 69], with 3 T being the boundary between linear and supralinear behaviour [31]. It should be noted that the BOLD calibration method [69] was first developed at 1.5 T and so the power law relationship proposed in that work between intravascular oxygenation and  $R_2^*$  of 1.5 may not be appropriate at higher fields.

For WM, the power law does seem to be  $< 1$  (7 T:3 T  $R_2^*$  ratio of  $1.6 \pm 0.5$ ). WM has a different vascular structure with much smaller blood volume than GM, and also restricted extravascular water diffusion (due to myelination of the axons). This might alter the relationship between intravascular susceptibility, the microscopic field distribution in the tissue and the resulting  $R_2^*$ . This requires further investigation since WM reactivity data must be interpreted with caution due to the reduced SNR of this data.

In this study, the gas sampling data could not be electronically time locked to the scanner acquisition due to hardware limitations, so the respiratory sequence was manually synchronised with the imaging sequence ( $\sim \pm 1.5$  s). There was also a delay between gas delivery and sampling of about 5 s caused by the transit time between the mask and the gas sensors. The data signals therefore had to be aligned manually during processing, so it was not possible to estimate the absolute delay between the  $P_{ET}CO_2$  change and associated CVR. This could potentially add noise to the  $R_2^*$  CVR curves but this effect will not be significant since the  $P_{ET}CO_2$  data were resampled from  $\sim 6$  s sampling interval to 1.5 s sampling interval. Any error due to manually aligning the timecourses is small compared with the 120 s at each gas level. It is interesting to note that there was a close correlation between  $P_{ET}CO_2$  stimulus and the associated BOLD response on both the up and down transitions, with no sign of a post-stimulus undershoot, suggesting that the post-stimulus undershoot often observed in the BOLD signal evoked by neuronal activation is not vascular in origin [159], although further experiments are required to confirm this conclusion.

Hardware limitations meant that the optimal (short) echo times required at 7 T could not be reached. Therefore, although better contrast was achieved at 7 T, similar contrast-to-noise was observed at both field strengths in GM due to the non-optimal TE and increased physiological noise at 7 T. This was shown by increased  $R_2^*$  variance at 7 T over 3 T ( $p < 0.003$ ), which agrees with the findings of Triantafyllou *et al.* [109]. Respiratory noise was particularly pronounced because of pacing of the respiratory cycle and because the subjects increased their depth of breathing during the respiratory challenge. This can be seen in *figure 5.6a*, where there is a  $\sim 6$  s oscillation throughout the BOLD timecourses.

In summary, this study has demonstrated measurement of the  $R_2^*$  CVR relationship to  $P_{ET}CO_2$ . The method for gas delivery allowed small, well resolved transitions in  $P_{ET}CO_2$  to map out an approximately linear relationship between  $R_2^*$  and  $P_{ET}CO_2$ . Significant grey and white matter CVR was measured. The cross-field comparison of grey matter  $R_2^*$  CVR suggests an approximately linear relationship between grey matter  $R_2^*$  and the blood-tissue susceptibility difference, which is proportional to both venous blood oxygenation and field strength.

## 5.5 Assessing vascular asymmetry in the primary motor cortex

### 5.5.1 Introduction

The main objective of fMRI is to identify and ideally quantify the neuronal response to a particular task. However the BOLD signal results from a complex interaction between cellular oxygen metabolism (which is tightly coupled to neuronal activity [21, 22]) and local vascular structure. Although the vascular response is partially coupled to oxygen metabolism (and neuronal activity), it is also strongly dependent on local vascular state, which will confound conclusions about the underlying neuronal activity from the measured BOLD signal. The vascular contribution to the BOLD response (namely CBF and CBV

components) will depend on the relative contributions from arteries, arterioles, capillaries, venules and veins [73], the presence of a large draining vein [3], or on the resting CBF [141, 140, 142]. An important goal of fMRI is to disentangle the metabolic component from the vascular component of the BOLD signal.

BOLD fMRI has been used to investigate the functional lateralisation of handedness [160, 161, 162, 163, 164]. Studies of right-handed individuals have shown stronger BOLD signal responses to neural activity (hand motor task) in the dominant motor cortex compared to the non-dominant one [161, 164], suggesting a greater CBF response to neuronal activation in the dominant motor cortex. However, it is unclear as to whether this stronger BOLD response has a neuronal origin, or whether it is, at least in part, due to an asymmetry in vascular structure between dominant and non-dominant motor cortices.

For this work a novel CO<sub>2</sub> challenge was used that was developed in Nottingham [149], making use of the breath-by-breath  $P_{ET}CO_2$  targeting, afforded by the feed-forward, low gas flow system, to generate a sinusoidal  $P_{ET}CO_2$  waveform. In this section, such a sinusoidally varying  $P_{ET}CO_2$  respiratory challenge is used to map % BOLD CVR in the dominant and non-dominant motor cortices of right handed individuals. The aim of this experiment was to assess whether a CVR mismatch is present between the right and left motor cortex, two brain regions frequently associated with a regional mismatch in BOLD response to hand motion.

### 5.5.2 Method

Eight healthy right-handed male volunteers (aged  $26 \pm 5$  years, range 20 – 34 years) participated in this study. Approval for the study was obtained from the University of Nottingham Medical School Ethics Committee and all participants gave written informed consent. A laterality questionnaire [165] was completed by the participants prior to the MR measurements.

This experiment involved subjects completing both a motor task and a respiratory challenge. First, subjects were instructed to perform a unilateral

sequential finger tapping task, alternating between right hand and left hand motion, with four repeats of (12 s Right, 19.2 s rest, 12 s Left, 19.2 s rest). This task was visually cued with the words ‘TAP\_RIGHT’, ‘TAP\_LEFT’ and ‘REST’, shown in white on a black background, projected onto a screen at the end of the magnet bore (which the subject viewed through prism glasses). The subsequent respiratory challenge consisted of 10 cycles of sinusoidally modulated  $P_{ET}CO_2$ , targeted between 35 and 45 mmHg, with a period of 60 s per cycle. This used the feed-forward low gas flow method to target levels on a breath-by-breath basis.  $P_{ET}O_2$  was targeted at 110 mmHg throughout. Details of the respiratory challenge are described in *section 3.3*.

Scanning was performed on a Philips Achieva 7 T system, with head volume-transmit and 16-channel SENSE head receive-coil. Axial GE EPI data were acquired every 2.4 s throughout the motor task and respiratory challenge. Images were acquired with a spatial resolution of  $2 \times 2 \times 3$  mm<sup>3</sup>, with a  $192 \times 192$  mm<sup>2</sup> field-of-view and either 15 or 21 slices, with no slice gap, covering the motor cortex. Data was collected with a single-echo acquisition of TE = 25 ms using SENSE factor = 2. A whole-head MPRAGE image was acquired at  $0.5 \times 0.5 \times 1$  mm<sup>3</sup> resolution.

The motor task dataset was motion corrected using MCFLIRT (FSL) and smoothed with a 3 mm FWHM Gaussian kernel. Z-statistic maps were formed for each of the right and left hand motion using FEAT (FSL).

The respiratory challenge dataset was motion corrected using MCFLIRT (FSL) and smoothed with a 3 mm FWHM Gaussian kernel. The timecourse of each voxel was normalised to its mean value and multiplied by 100 to give the voxel’s %BOLD timecourse, linear de-trending was performed to remove any linear MR signal drift. The  $P_{ET}CO_2$  timecourse was linearly interpolated to the same temporal frequency as the MR data (2.4s). *Figure 5.10* shows an individual subject’s  $P_{ET}CO_2$  timecourse, the corresponding %BOLD signal timecourse (averaged over voxels determined to have CVR > 0.5 %/mmHg) and the fast Fourier transform (FFT) of these signals. To isolate the sinu-

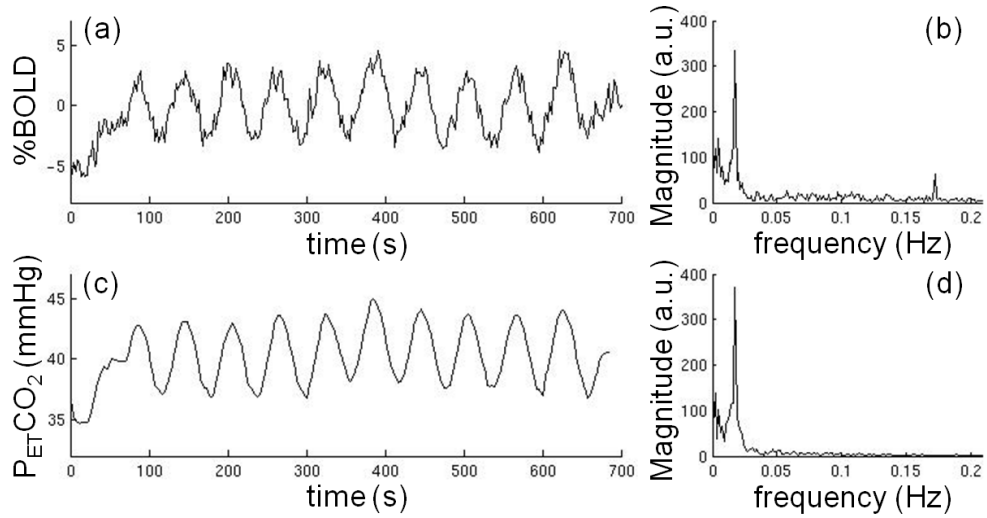


Figure 5.10: (a) CVR BOLD signal change during the sinusoidal  $CO_2$  challenge (single subject, averaged over voxels with  $CVR > 0.5$   $\%/mmHg$ ), (c) corresponding  $P_{ET}CO_2$  trace and their respective Fourier magnitude spectra (b) and (d).

soidally varying component of the signals, FFTs were calculated for both the interpolated  $P_{ET}CO_2$  timecourse and each voxel's  $\%BOLD$  timecourse. The frequency component of the FFT of the  $P_{ET}CO_2$  trace which had the greatest magnitude was determined ( $\sim 1/60$  Hz for all participants, *figure 5.10d*) and the voxel's CVR was calculated from the magnitude of the FFT of the  $\%BOLD$  signal (*figure 5.10b*) at that frequency divided by the magnitude of the FFT of the  $P_{ET}CO_2$  signal (*figure 5.10d*) at that frequency.

Two regions of interest (ROI) were selected in each hemisphere to assess the laterality in CVR (*figure 5.11*). These were taken from each individual's MPRAGE image, after this image was realigned and downsampled (FLIRT, FSL) to the same space as the EPI data. The first ROI was the precentral gyrus, manually drawn on the MPRAGE image (in EPI data space) and identified as the gyrus located between the central and precentral sulcus. The second was the whole hemisphere, segmented simply by dividing the brain along the inter-hemispheric fissure and then applying a standard brain mask (BET, FSL). The whole-hemisphere region was analysed to check for any global left-right differences in CVR not limited to the motor cortex. The investiga-

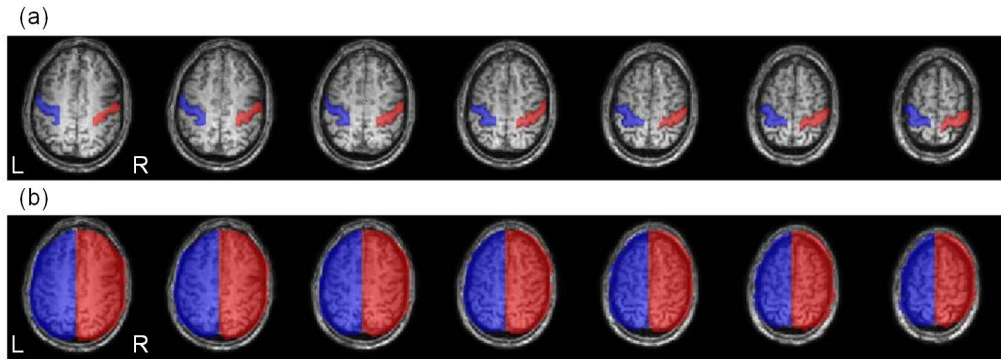


Figure 5.11: Example of (a) precentral gyrus ROIs with dominant M1 (left) shown in blue and non-dominant M1 (right) shown in red and (b) left (blue) and right (red) whole hemisphere ROIs.

tor was blind to the orientation convention (radiological or neurological) when drawing the regions. The motor task  $Z$ -statistic maps were used to manually select the 7 slices for each subject which covered the hand motor region. Only these 7 slices were used in the following analysis.

The motor BOLD response laterality was assessed within the 7 slices containing the precentral gyrus region, to assess whether the data showed similar behaviour as to those in other right-handed studies [162, 163]. The ipsilateral extent fraction ( $I$ ) [162] was calculated for each subject, for both the right and left hand tasks separately:

$$I(\text{task}) = \frac{\text{ipsilateral extent}}{\text{ipsilateral extent} + \text{contralateral extent}}. \quad (5.5)$$

The activation extent was measured by counting the number of voxels within the region which had a  $Z$ -statistic  $> 5$  for that task. The ipsilateral region for the right hand task would be the right hemisphere 7 slice precentral gyrus region, whilst the left hemisphere is the ipsilateral cortex for the left hand task. The value of  $I$  indicated the laterality of the BOLD response to the corresponding motor task. This can range between a completely contralateral response ( $I = 0$ ) to a completely ipsilateral response ( $I = 1$ ), with  $I = 0.5$  indicating a bilateral response.

For each subject, the average CVR was calculated for each region by averaging over each voxel's CVR value within the region. This meant that for each subject, four average CVR values were calculated, for the left and right hemisphere precentral gyrus ROIs and the left and right whole hemisphere ROIs.

To assess the spatial distribution of precentral gyrus CVR, group averaged CVR contour maps (*figure 5.15a*) were generated by registering each subject's MPRAGE to the MNI152 standard space 2mm-isotropic atlas image (FSL), using a non-linear registration (FNIRT, FSL). This registration was used to realign the subject's CVR map into the standard space. In this space, voxelwise averaging of CVR values was performed across all subjects to form an average CVR map, from which the CVR contour plot could be constructed.

### 5.5.3 Results

The laterality score ( $24 \pm 5$ , mean  $\pm$  standard deviation; range of sample: 18 to 31; range of test: 18 = right-handed to 90 = left-handed) confirmed that all participants were strongly right-handed. The manually drawn precentral gyrus ROIs showed no significant difference in size between left and right hemispheres ( $P=0.96$ , 2-tailed paired t-test, mean # voxels for left hemisphere =  $968 \pm 189$ , mean # voxels for right hemisphere =  $965 \pm 114$ ) The ipsilateral extent fraction ( $I$ ) for right hand motion ( $I(R) = 0.12 \pm 0.12$ ) was significantly lower ( $P=0.005$ , 1-tailed paired t-test) than for left hand motion ( $I(L) = 0.20 \pm 0.14$ ). Individual subject values are shown in *figure 5.12*. For two of the subjects, no voxels passed the threshold in either hemisphere, so their values are displayed as zero. If these subjects are discarded,  $I(R) = 0.16 \pm 0.11$  is still significantly less ( $P<0.002$ ) than  $I(L) = 0.27 \pm 0.08$ .

The  $P_{ETCO_2}$  timecourses from all subjects showed clearly resolvable sinusoidal components, with peak-to-peak amplitudes of  $5.2 \pm 0.4$  mmHg. An example CVR map is shown in *figure 5.13*, in this case without spatial smoothing to clearly demonstrate the shape of the grey matter sulci. A statistically significant ( $P<0.03$ , 1-tailed paired t-test) asymmetry in CVR was observed in the precentral gyrus (*figure 5.14a*), with the left hemisphere CVR =  $0.45 \pm 0.11$

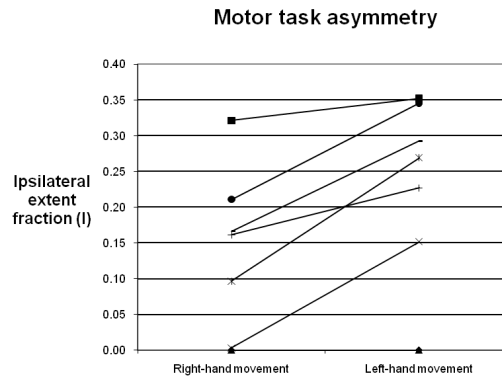


Figure 5.12: Comparison of individual subject values of  $I$  between right and left hand motor tasks. Higher values indicate a more bilateral BOLD response. Note that for two subjects no voxels passed the  $Z > 5$  threshold, so they have  $I = 0$  in this plot.

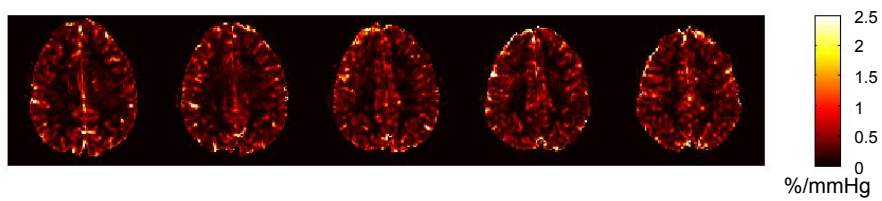


Figure 5.13: Sinusoidal hypercapnia % BOLD CVR map, calculated using the Fourier analysis method on unsmoothed data.

%/mmHg being higher than right hemisphere  $\text{CVR} = 0.37 \pm 0.06$  %/mmHg. No significant ( $P=0.25$ ) asymmetry was observed in the CVR averaged across the whole hemisphere (*figure 5.14b*), with global left hemisphere  $\text{CVR} = 0.48 \pm 0.11$  %/mmHg and right hemisphere  $\text{CVR} = 0.49 \pm 0.14$  %/mmHg.

The origin of the CVR asymmetry in the precentral gyrus appears to be due to both a general elevation of CVR values and an increase in maximal CVR values. This is demonstrated in the histogram of CVR for all voxels in the precentral gyrus ROI for all subjects (*figure 5.14c*), which shows both a decrease in the number of voxels with low CVR and an increase in the maximum CVR in the region in the left hemisphere. The histograms for each individual subject (*figure 5.14d*) all show this similar feature. This is also demonstrated on *figure 5.15*, which shows the average spatial distribution of CVR across the precentral gyri for the group and for an individual, representative subject.

#### 5.5.4 Discussion

This study has combined the advantages of precise measurement of  $P_{ET}CO_2$  and a novel, vasoactive sinusoidal respiratory challenge with the increased SNR and BOLD CNR available at 7 T for CVR mapping. CVR in the left (dominant) precentral gyrus was found to be significantly higher than in the right (non-dominant) precentral gyrus in right-handed men, the first reported evidence for a difference in vascular responsiveness between two homologous brain regions. These results appear to reflect a greater vascular compliance in the dominant (compared with non-dominant) motor cortex.

The haemodynamic origins of the BOLD signal means that it depends not only on the extent and amplitude of functional activation, but also on the structure and compliance of the local vasculature. The asymmetry observed here shows an example of two brain regions (left and right precentral gyri) with different vascular properties. Studies using fMRI that compare the neuronal activation of these regions [160, 161, 162, 163, 164] should account for the differences in underlying vascular properties (as observed here for reactivity) before using the BOLD response to assess any inter-region differences or similarities

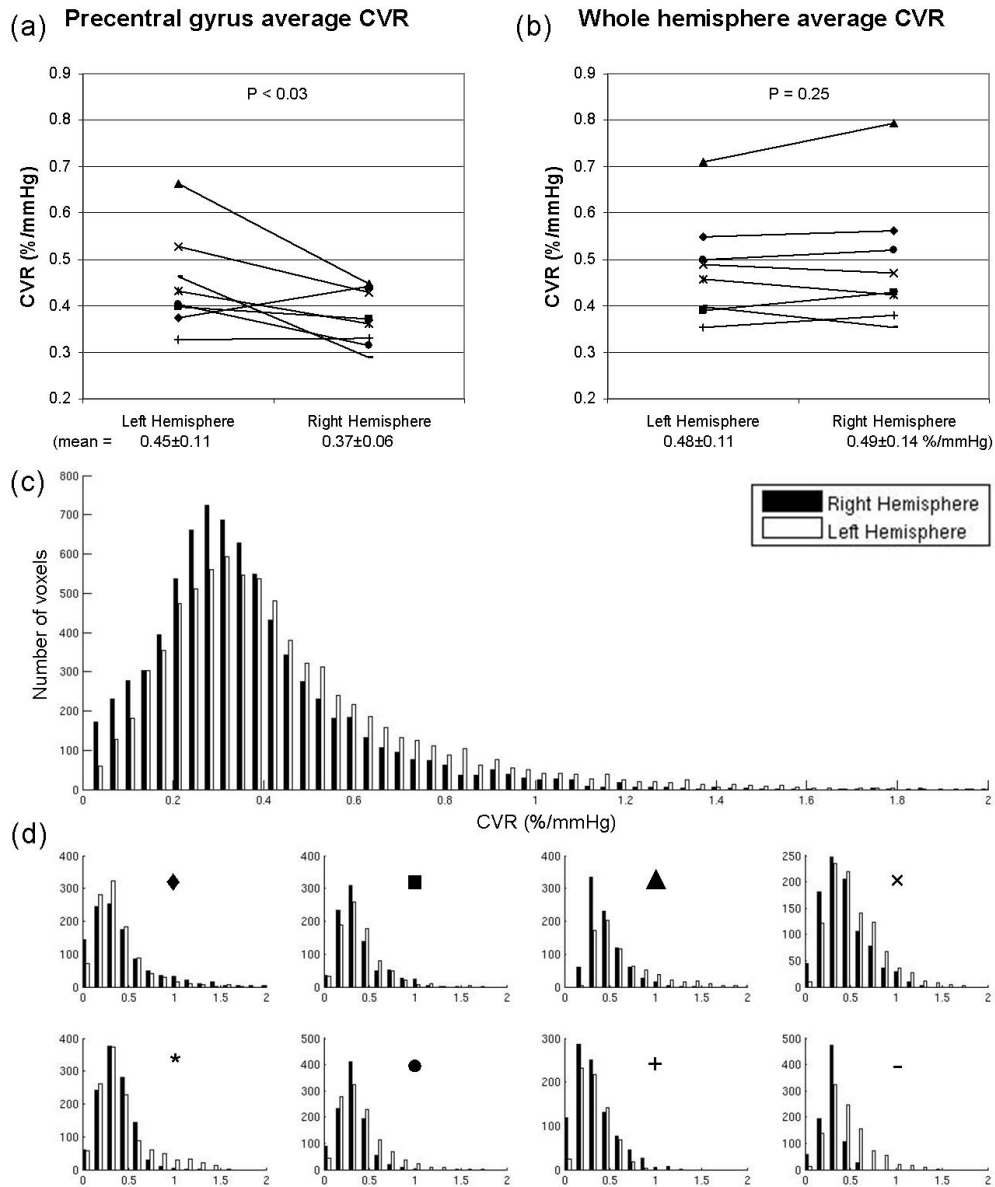


Figure 5.14: Individual subject hemisphere-averaged CVR for (a) precentral gyrus and (b) whole hemisphere regions. Mean  $\pm$  standard deviation CVR across subjects and 1-tailed paired t-test results shown on the respective plot. (c) Histogram of CVR for all precentral gyrus voxels in all subjects. (d) Individual histograms of CVR for all precentral gyrus voxels in that subject (symbols correspond to individual labels used in (a) and (b)). Black bars show the right hemisphere, white bars show the left hemisphere.

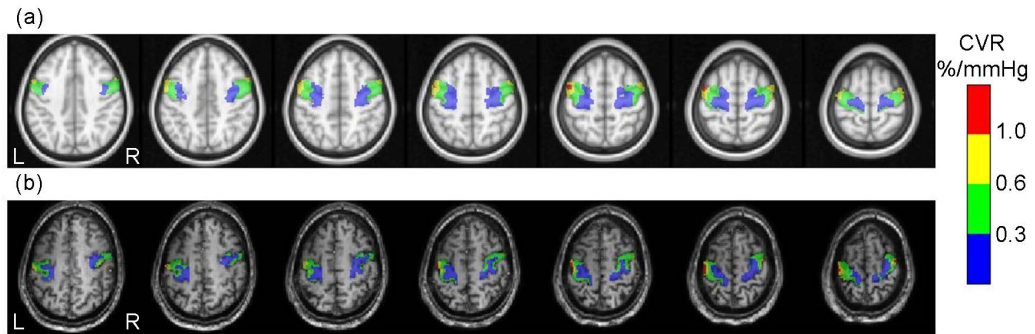


Figure 5.15: CVR contour maps of the precentral gyrus, demonstrating the spatial variation of CVR. Colours indicate CVR values: blue  $< 1/3 \leq$  green  $< 2/3 \leq$  yellow  $< 1 \leq$  red %/mmHg. (a) Average CVR over all subjects, after non-linear registration into MNI152 space. (b) Single subject CVR (• in figure 5.14).

in the size or extent of neural activation. The motor task results presented here are in agreement with other studies of BOLD laterality of right handed subjects [162, 163], where a more bilateral BOLD response is observed from a left (compared with right) hand motor task. However, in the context of the left precentral gyrus having a higher CVR than right precentral gyrus, it is possible that at least part of this difference in BOLD laterality between tasks could be due to differences in the vascular response, rather than an actual difference in the neuronal response.

The use of Fourier analysis to analyse the BOLD response to a sinusoidally varying  $P_{ET}CO_2$  stimulus provided a method of reducing the effect of physiological noise signals in the CVR maps (provided that these would not alias into the frequency selected for analysis). For example, respiratory noise, caused by chest motion during the breathing cycle, can be clearly seen in the EPI timecourse magnitude spectrum (figure 5.10b), at the frequency of 0.17 Hz. Furthermore this analysis approach requires no assumption as to the shape of the haemodynamic response function.

This sinusoidal paradigm and Fourier analysis technique can be superficially compared to the graded hypercapnia paradigm and linear regression analysis technique used in section 5.4, since one subject happened to participate in

both studies (*figures 5.9 and 5.13*). Note however that the scan parameters for both studies were different, such that a weighted summation combination of a double echo dataset was used for the graded hypercapnia paradigm, whereas a single echo dataset was acquired for the sinusoidal paradigm. The sinusoidal paradigm possibly has more finely resolved grey matter structure and less artefacts. This may reflect that the Fourier analysis approach requires no assumption as to the shape of the haemodynamic response function and is less sensitive to the effects of physiological noise. However, the approach used for the sinusoidal paradigm appears to have slightly less distinction between grey and white matter. This could be due to the sinusoidal analysis method calculating the magnitude response, independent of the sign, or the delay of the response, whereas the graded hypercapnia analysis does not account for delayed WM response. The sinusoidal approach has been used to estimate relative delays in CVR [149], showing white matter to have a delayed CVR compared with grey matter, which may partially explain this.

Due to inter-subject variability in the shape and size of the precentral gyrus, the precentral regions were manually drawn for each subject, rather than using a standard space template. Once realigned into the individual subject's space, it was found that the standard space templates did not follow the sulci closely, so the manual method was preferred. Operator bias and human error appeared to be less than the errors associated with using standard space templates.

The statistically significant regional asymmetry in CVR, with left precentral gyrus CVR being significantly higher compared to the right, shows that the vasculature in the left precentral gyrus has a greater capacity to supply increased levels of oxygen to activated tissue. Histograms (*figure 5.14c & d*) and contour maps (*figure 5.15*) of BOLD CVR show that the origin of the asymmetry corresponds to higher CVR in the left precentral gyrus close to the cortical surface as well as an increase in the maximum value of CVR in the region. This excludes the possibility of the asymmetry being due to a single large draining vein, which would cause small clusters of high CVR rather

than a general increase in CVR. The asymmetry in CVR is localised to the precentral gyrus, rather than across the whole hemisphere (*figure 5.14b*), indicating that it is not due to any global systematic bias, such as coil sensitivity.

There may be several possible explanations for the vascular asymmetry in the precentral gyrus. The asymmetry may be independent of handedness, with a natural bias to higher CVR in the left hemisphere precentral gyrus. There could be an innate asymmetry, based on handedness, but present from birth and independent of experience. Another possibility is that the vascular asymmetry is formed over time, through experience, due to an extensive preference to use the right hand for complex tasks [166, 167]. It may be that the source of the asymmetry arises from a combination of all three possibilities. A future objective could be to test these three hypotheses. The first two would involve repeating the study with a left handed group and maybe also left handed subjects who were taught to write with their right hand. For the third possibility, of an experience related cause, a different subject group would be needed, such as taxi drivers [168], bilingual subjects [169], or musicians [170], where changes in structure (plasticity) have been observed in brain regions associated with the corresponding task. An advantage of using these groups over the handedness model is that control groups can also be studied for comparison. Finding the source of this vascular asymmetry is an important goal, as it provides insight into brain development.

## 5.6 Conclusion

This chapter has investigated the use of hypercapnia as a means to measure vascular reactivity and its implications for better understanding the BOLD response to neuronal activation. A gas delivery system with the ability to target  $P_{ET}CO_2$  levels on a breath-by-breath basis and to generate transitions resolvable to within 3 mmHg has been used to develop paradigms for modulating arterial  $CO_2$  levels with novel graded and sinusoidal patterns, for accurately probing the resulting effect on BOLD signal. The boxcar is the simplest paradigm and is easiest to analyse, but it typically involves large steps, which

are not useful in characterising the relationship between the BOLD signal and  $P_{ET}CO_2$ . To test this relationship, a graded paradigm was used, which was presented in a pseudo-randomised order to prevent bias from low frequency signal drifts, such as due to a subject relaxing over the course of the experiment. The final paradigm discussed in this chapter is the sinusoidal modulation of  $P_{ET}CO_2$ . This is not appropriate where steady state periods are required, for example for calibrated BOLD experiments [69]. However, the sinusoidal approach is advantageous for measuring relative delays in response to  $CO_2$  [149]. It is also less sensitive to physiological noise than the other approaches, as the analysis only considers a narrow frequency range, not typically associated with respiratory and cardiac frequencies.

The relationship between grey matter  $R_2^*$  and  $P_{ET}CO_2$  at both 3 T and 7 T has been used to test models of the effect of blood oxygenation on  $R_2^*$ , finding an approximately linear relationship at these field strengths. This result will be useful in translating calibrated BOLD experiments [69] to field strengths above 1.5 T. A sinusoidal  $CO_2$  modulation has been used to map CVR across the primary motor cortex, finding a difference between left and right hemisphere precentral gyrus CVR. This has implications for any study which compares BOLD, or even CBF responses to a motor task to compare the neuronal response across these two regions. Comparison of the underlying neuronal activation between these regions cannot be made without first accounting for the observed differences in vascular response, which will affect both BOLD and CBF responses.

# Chapter 6

## Improved BOLD calibration using hyperoxia

### 6.1 Introduction

The observation that the gradient echo MRI signal (GE) contrast of large veins changes with hyperoxia [171] was a key step towards the discovery that the blood oxygenation level dependant (BOLD) GE signal is spatially correlated with increased neuronal activity [1]. Respiratory challenges modulate blood gases, where inspired gas mixture is changed under normobaric conditions (methods of which are described in *chapter 3*). Hyperoxia is one such challenge which refers to the state of increased lung alveolar oxygen partial pressure, caused by inhalation of a gas with oxygen composition greater than 21 %, the inspired fraction of oxygen ( $F_iO_2$ ) of room air is typically  $\sim 21$  %.

Calibration of the BOLD signal is an important goal in neuroscience, as it aims to separate neuronal from vascular components of the BOLD signal. Hyperoxia can be used to calculate a calibration parameter for BOLD imaging [172], as will be described in more detail in *section 6.2*. However, current methods of BOLD calibration require the assumption that cerebral blood flow (CBF) and cerebral blood volume (CBV) are coupled through a power law relationship:

$$CBV \propto CBF^\alpha, \quad (6.1)$$

where  $\alpha = 0.38$  is the coupling constant [70]. This coupling relationship has several limitations as it is poorly characterised in humans, does not reflect the venous CBV nature of BOLD contrast [75] and may vary with brain region and local vascular structure.

This chapter proposes and implements a new method for BOLD calibration by presenting a stimulus both at normoxia and hyperoxia. This method uses the assumption that hyperoxia does not affect CBF or oxygen metabolism to measure the relative change in venous blood oxygenation due to the stimulus. It does not require any assumption about the coupling between CBF and CBV, since the relative change in venous CBV can be calculated using hyperoxia. To support this method, the effect of hyperoxia on vascular properties is first assessed through a literature review. The magnetic properties of gaseous oxygen is considered both in the context of being dissolved in blood and of changing the magnetic properties of air spaces around the head. The results of an experiment are presented which aims to quantify the effects of increased oxygen in air spaces on field homogeneity and the associated consequences for GE EPI distortions. Finally, results from an experiment which implements the new method for BOLD calibration are presented. This approach uses hyperoxic contrast to estimate venous blood oxygenation changes associated with changes in brain activity. This provides a means to estimate changes in oxygen metabolism without the need to assume a coupling relationship between CBF and CBV.

## **6.2 Uses of hyperoxia in MRI**

This section provides an overview of the applications of hyperoxia in MRI literature. This illustrates how combination of hyperoxia with MRI provides potential for investigating vascular properties and as a tool for clinical assessment.

Hypercapnia is typically used as a method for calibrated BOLD. However, an alternative to hypercapnia-based calibration of the BOLD response has

been proposed [172], which instead makes use of the change in venous blood oxygenation due to hyperoxia to estimate the calibration constant originally proposed by Davis *et al.* [69]. A model (detailed in *section 6.4*) is used to estimate the change in global venous blood oxygenation ( $q_h$ ) due to a change in  $P_aO_2$ . This is then used, along with the GE BOLD signal change resulting from the change in  $P_aO_2$ , to estimate the calibration constant  $M$ :

$$M = \frac{\text{BOLD} - 1}{1 - q_h^\beta}, \quad (6.2)$$

where BOLD is the relative signal change in response to hyperoxia (normalised to the normoxia value) and  $\beta$  is the power law relationship for the effect of blood oxygenation on extravascular  $R_2^*$  ( $\Delta R_2^* \propto q_h^\beta$ ). Additional corrective terms are also proposed in that work, to account for changes in CBF associated with a fixed inspired fraction hyperoxia challenge, where hypocapnia occurs during hyperoxia. This method of hyperoxia calibration avoids measurement of the CBF response to hypercapnia [69], which is subject to low SNR. It does however rely on a global estimate of oxygen extraction fraction, which may vary across brain regions and across participants, especially in some patient groups.

The venous contrast provided by hyperoxia has also been identified as a means to measure cerebral blood volume. Absolute cerebral blood volume measurements have been made using the hyperoxia BOLD signal at 3 T [173]. In that study mild hyperoxia (50 %  $O_2$ ) was used to minimise hypocapnia based vasoconstriction. The venous nature of hyperoxia BOLD contrast means that this method is sensitive to venous and capillary compartments, rather than arterial CBV, since arterial blood is close to fully oxygenated. For CBV quantification, the hyperoxia BOLD signal needs to be normalised to an entirely venous voxel, which was chosen as the sagittal sinus. The major problem with this normalisation method is that the venous voxel will have a predominantly intravascular BOLD signal, whereas tissue will have both intravascular and extravascular components. As a result, the voxel's CBV content may not scale linearly with the hyperoxia BOLD signal.

At 7 T, and using the optimum TE for GE BOLD contrast (such as 25 ms), the intravascular signal component is negligible [174], except for voxels with a large venous volume fraction. This means that at 7 T the hyperoxia BOLD signal of a venous voxel cannot be compared with tissue voxels using the simple model used in [173] at 3 T. However, the dominant extravascular signal at 7 T has been combined with hyperoxia BOLD contrast to measure the relative change in venous CBV due to neuronal activation [175]. This method makes use of an analytical extravascular BOLD signal model [30], which requires the assumption that static spin dephasing is the dominant  $\Delta R_2^*$  relaxation mechanism.

Furthermore, hyperoxia has been used to test a novel method for measuring changes in cerebrospinal fluid (CSF) oxygen partial pressure ( $PO_2$ ), based on  $T_1$  [176]. Phantom results of saline with known  $PO_2$  contents found a tight linear correlation between dissolved  $PO_2$  and measured  $R_1$  relaxation rate. This observation was applied to calculating CSF  $PO_2$  in-vivo by measuring CSF  $T_1$ . Hyperoxia was used to test this model and it was found that it took the measured  $T_1$  of CSF approximately 10 minutes to decrease to a steady state after the onset of hyperoxia, suggesting that it takes up to this time for arterial dissolved oxygen to pass into CSF.

## Clinical and pre-clinical applications

There may be some potential for using normobaric hyperoxia MRI contrast to aid treatment planning in ischaemic stroke patients [177]. The theory is that the  $T_2^*$  - weighted signal response to hyperoxia is a marker for tissue metabolism. The ischaemic core of a stroke region is not metabolically active, and thus does not produce deoxygenated haemoglobin, so as haemoglobin is oxygenated, the  $T_2^*$  - weighted signal will not change with hyperoxia. The border zone, or ischaemic penumbra, which is characterised by being hypoperfused and having some recoverable neurons, is still metabolically active. The ischemic penumbra has a high oxygen extraction fraction (OEF) compared with healthy tissue, since CBF is low. This means that this region will have

a larger  $T_2^*$  - weighted signal increase due to hyperoxia than for healthy tissue. This theory has been successfully tested in an animal model [177], but initial patient results have proved less conclusive [178]. If successfully implemented, this approach would help identify recoverable tissue and inform treatment options. The advantage that this method has over the existing approach of combined perfusion and diffusion MRI to classify a lesion, is that it is related to the underlying metabolism, defining the ischemic penumbra, rather than cellular structure. It may be able to identify some recoverable tissue that the diffusion/perfusion mismatch would class as unrecoverable [177]. However, limitations of this method are the spatial blurring of the BOLD response due to its vascular nature, and the possible signal enhancement due to a decreased  $T_1$  with hyperoxia.

Normobaric hyperoxia has been suggested as a possible source of MR contrast in tumours, which are largely hypoxic. Changes in  $R_2^*$  have been used to show that blood oxygenation in meningiomas is increased during hyperoxia [179], useful as increased meningioma blood oxygenation has been linked to an improved response to radiotherapy. An interesting emerging technique focusses on angiogenesis, which is an indicator of active tumor growth [180]. Newly formed vasculature (neovasculature) can be distinguished from mature vessels, using the difference in BOLD contrast between hypercapnia and hyperoxia. Neovasculature has little vasodilatory capacity, and so only mature vasculature has an fMRI response to the vasodilator hypercapnia [181]. Both neovasculature and mature vasculature have an fMRI response to hyperoxia, which acts to increase blood oxygen content. The presence of neovasculature indicates angiogenesis, allowing identification of the parts of the tumor which are most responsive to treatment [181]. Agreement with other biomarkers of angiogenesis [180] suggest that this method could be promising as a non-invasive technique for use with antiangiogenic treatment for tumors [181]. A limitation of this technique is the fundamental limit on spatial resolution due to spatial blurring associated with GE BOLD contrast (e.g. downstream of the dilating vessel).

## 6.3 A new approach to BOLD calibration using hyperoxia

As discussed above, the hyperoxic BOLD contrast due to an increase in venous cerebral blood oxygenation ( $Y_v$ ) has been considered as a means of measuring venous CBV, both for absolute resting values [173] and to measure the relative change due to neuronal activity [175]. This is due to the assumption that hyperoxia does not affect CBF or oxygen metabolism. It should also be possible to measure the relative change in  $Y_v$  due to neuronal activity. This section proposes a model to this end. The addition of a subsequent CBF measurement also provides an estimate of the relative change in oxygen metabolism due to the motor task. Unlike previous approaches, this method does not require an assumed relationship between venous CBV and CBF.

To model the effect of hyperoxia on tissue  $R_2^*$ , an analytical model is used [30].

$$R_2^* = kV(1 - Y) + R_{2,0}^* \quad (6.3)$$

$$k = \frac{4}{3}\pi\Delta\chi[Hb_{tot}]B_0 \quad (6.4)$$

This is an extravascular signal model, based on the static dephasing regime of spin diffusion around randomly orientated blood vessels.  $R_{2,0}^*$  is the transverse relaxation rate of tissue containing only fully oxygenated blood vessels, including  $R_2$  (the spin-spin relaxation rate),  $Y$  is the blood haemoglobin oxygen saturation fraction and  $V$  is the volume fraction occupied by blood vessels. The term  $k$  is a constant, including the susceptibility of deoxygenated haemoglobin relative to oxygenated blood (similar to tissue)  $\Delta\chi$ , and the static magnetic field  $B_0$ . There is also a term for the effect of vessel geometry, which in this case is  $\frac{4}{3}\pi$  to model vessels with a random orientation.  $[Hb_{tot}]$  is the total haemoglobin concentration.

In this model,  $R_2^*$  has a linear relationship to  $V$  and  $(1-Y)$ , which is an assumption which may not be true at field strengths below 7 T, especially at 1.5 T, where there will be a significant intravascular contribution and diffusion will make a significant contribution to extravascular  $R_2^*$ . The effect of hyperoxia

is to increase venous oxygenation  $Y_v$ . The venous deoxygenated haemoglobin fraction at hyperoxia can be described by  $Q(1 - q_h)$ , where  $Q(= (1 - Y_v))$  is the normoxic resting value and  $q_h$  is the relative change due to hyperoxia (relative to the normoxic resting  $Q$ ). If the same task were performed both at normoxia and hyperoxia, the transverse relaxation rates during the related neuronal activation  $R_{2,act}^*$  and rest  $R_{2,rest}^*$  are modelled as

$$R_{2,rest}^* = kVQ(1 - q_h) + R_{2,0}^* \quad (6.5)$$

$$\begin{aligned} R_{2,act}^* &= k(V + V_{act})Q(1 - q_{act} - q_h) + R_{2,0}^* \\ &= k(V + V_{act})Q(1 - q_h) - k(V + V_{act})Qq_{act} + R_{2,0}^* \end{aligned} \quad (6.6)$$

where  $k$  is defined in *equation 6.4*;  $V$  is the resting venous CBV;  $V_{act}$  is the change in venous CBV due to the neuronal activation;  $q_{act}$  is the relative change in venous deoxygenated haemoglobin fraction due to the neuronal activation (relative to the normoxic resting  $Q$ );  $R_{2,0}^*$  is the transverse relaxation rate of tissue containing only fully oxygenated blood vessels.

Values of  $Q$  and  $q_h$  can be estimated from the model which will be presented in *section 6.4* (based on exhaled gas composition), or experimentally, either using blood  $T_2$  [182], or susceptibility-based oximetry [183] measurements, both during normoxia and hyperoxia. The gradient of the  $R_{2,rest}^*$  versus  $(1 - q_h)$  plot is  $kVQ$ , which is the calibration constant  $M$  used in previous calibrated BOLD experiments [69, 172] (see *equation 6.2* and *section 2.4.5*). The gradient of the  $R_{2,act}^*$  versus  $(1 - q_h)$  plot is  $k(V + V_{act})Q$ , which will be referred to as  $M'$ . The difference in intercepts of the rest and activation curves is  $k(V + V_{act})Qq_{act}$ , which can be divided by  $M'$  to give  $q_{act}$ . The ratio of rest and activation gradients is the relative venous CBV change on activation,

$$\frac{M'}{M} = \left(1 + \frac{V_{act}}{V}\right). \quad (6.7)$$

If the relative change in CBF on activation can be measured (e.g. using ASL), then Fick's principle [69] can be used together with the value of  $q_{act}$  to estimate the relative change in CMRO<sub>2</sub>:

$$\left(1 + \frac{\Delta\text{CMRO}_2}{\text{CMRO}_{2,rest}}\right) = (1 + q_{act})\left(1 + \frac{\Delta\text{CBF}}{\text{CBF}_{rest}}\right). \quad (6.8)$$

This method does not require the assumption of a coupling relationship between CBV and CBF [70]. However, this method assumes a linear relationship between  $R_2^*$  and deoxygenated haemoglobin fraction [30]. It also assumes that there is negligible vasoconstriction due to hyperoxia over the period of neuronal activation [184]. Finally, it is also assumed that  $q_h$  and  $q_{act}$  are independent of one another, so the change in oxygen consumption due to neuronal activation is independent of hyperoxia.

## 6.4 The effect of hyperoxia on the vasculature

In this section, the effect of hyperoxia on haemodynamic properties is considered through a literature review. This understanding is important in order to build up a model for calibrated BOLD using hyperoxia and to assess the validity of assumptions which need to be made.

The common method for inducing hyperoxia is to present 100% fixed inspired oxygen fraction ( $F_iO_2$ ). However, this method typically induces mild hypocapnia [185], which complicates the vascular response. To reduce this hypocapnic side effect, lower oxygen fractions can be presented, balanced with nitrogen, or mixed with room air. Carbogen, which is oxygen, balanced with a small fraction of  $CO_2$  (typically 95%  $O_2$ , 5%  $CO_2$ ), can also be used, but this causes both hyperoxia and hypercapnia. Two methods for minimising hypocapnia during hyperoxia are the feed-forward [158] and the dynamic end-tidal forcing [92] techniques (both previously outlined in *chapter 3*).

The effect of hyperoxia on vasoconstriction is a matter for debate, but is a vital consideration if hyperoxia is to be considered as a non-invasive contrast agent. CBF measurement techniques, including nitrous oxide washout [117] and MRI methods, such as phase-contrast angiography [186] and Gd-DTPA contrast-enhanced perfusion [187] measurements, have shown that CBF decreases upon inhalation of 100 %  $O_2$ . The CBF response to hyperoxia is slowly varying [186], taking several minutes to react significantly and up to 10 minutes to reach a steady state after the onset of a transition. Graded hyperoxia has

been investigated [188] using ASL (QUIPPSII), with statistically significant decreases in CBF (relative to room air) being shown, even for an  $F_iO_2$  of 0.4 (40 %). In that study the hypocapnic response to hyperoxia was shown at high temporal resolution and was seen to be slowly varying, possibly on a similar timescale to the CBF response, but unfortunately the CBF timecourse itself was not reported in this case. Whether the decrease in CBF is entirely due to hypocapnia associated with hyperoxia, or also in part directly a reaction to increased  $F_iO_2$  is unclear. This question has been addressed [94], by modulating inspired  $CO_2$  (0 %, 4 % and 6 %) both during hyperoxia (balanced  $O_2$ ) and normoxia (balanced air, i.e. 21 %  $O_2$ ). Using a continuous-ASL acquisition, an offset was found in CBF between the normoxia and hyperoxia response curves to  $CO_2$ , which appears to show a CBF response to increased  $F_iO_2$ , independent of  $CO_2$ . However, more recent work [184] using continuous-ASL found that the apparent decrease in CBF during 100 %  $O_2$  inhalation was mostly accounted for by a change in arterial blood  $T_1$  due to hyperoxia, rather than an actual CBF decrease. The relationship between hyperoxia and CBF, independent of hypocapnia, is still poorly understood. To draw an accurate conclusion as to how hyperoxia affects CBF and vasoconstriction, hypocapnia needs to be minimised and either arterial blood  $T_1$  changes accounted for, or phase-contrast methods used (which are less sensitive to the  $T_1$  changes).

During hyperoxic periods, arterial oxygen partial pressure ( $P_aO_2$ ) is increased, arterial haemoglobin, which is already almost fully saturated at normoxia, becomes fully saturated and the level of oxygen dissolved in arterial plasma increases. The oxygen dissociation in blood is modelled by a widely accepted model [189]. This model depends on temperature and blood pH, but for 310 K and pH of 7.4 the relationship between arterial haemoglobin oxygen saturation ( $S_aO_2$ ) and  $P_aO_2$  is

$$S_aO_2 = \left( \frac{23400}{P_aO_2^3 + 150P_aO_2} - 1 \right)^{-1}. \quad (6.9)$$

Venous haemoglobin oxygen saturation ( $S_vO_2$ ) can be estimated as follows

[172]. The total arterial blood oxygen content ( $C_aO_2$ ) is the sum of the oxygen bound to haemoglobin and dissolved in plasma

$$C_aO_2 = (\phi.[Hb].S_aO_2) + \varepsilon P_aO_2 \quad (6.10)$$

where  $\phi = 1.34 \text{ ml}_{O_2}/\text{g}$  is the oxygen carrying capacity,  $[Hb] = 15 \text{ g}/\text{dl}_{\text{blood}}$  is the concentration and  $\varepsilon = 0.0031 \text{ ml}_{O_2}/(\text{dl}_{\text{blood}}.\text{mmHg})$  is the solubility coefficient, of haemoglobin [172]. Dissolved oxygen meets part of the tissue oxygen requirement, reducing the amount of venous deoxyhaemoglobin [190]. The total venous blood oxygen content ( $C_vO_2$ ) is the remainder after oxygen is extracted from capillaries, and is given by

$$C_vO_2 = C_aO_2 - C_aO_{2,0}.OEF \quad (6.11)$$

where  $C_aO_{2,0}$  is the normoxia  $C_aO_2$  value and  $OEF$  is the oxygen extraction fraction assumed to be 0.4. Since venous haemoglobin is not close to being fully saturated under normobaric hyperoxia, an assumption can be made that a negligible amount of the total  $C_vO_2$  is dissolved oxygen. This means that the venous oxygen saturation can be calculated using

$$S_vO_2 = C_vO_2/\phi.[Hb]. \quad (6.12)$$

This model thus relates  $P_aO_2$ , which can be estimated by measuring exhaled gas oxygen fraction, to  $S_vO_2$ , as shown in *figure 6.1*. Since the change in deoxyhaemoglobin is the source of BOLD contrast the hyperoxia-perturbed BOLD signal can therefore be used to assess local venous vascular properties.

## 6.5 Magnetic Properties of $O_2$

Oxygen molecules are paramagnetic, with a molar susceptibility  $\chi_m = +3415 \times 10^{-6} \text{ cm}^3 \text{ mol}^{-1}$  at room temperature [191]. By modulating the level of inspired oxygen, the amount of oxygen both dissolved in arterial blood plasma and in air spaces around the head (such as the oral cavity and frontal sinus) will change, affecting local magnetic properties. These are important considerations in modelling the effect of hyperoxia on the BOLD signal.

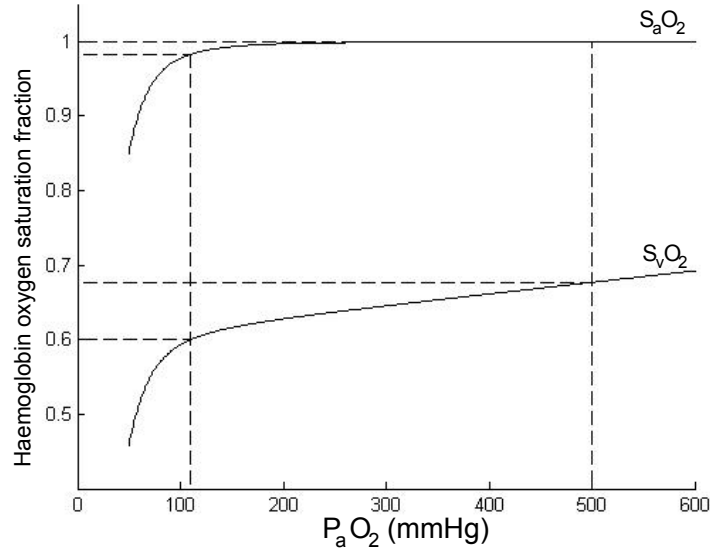


Figure 6.1: Model response of  $S_aO_2$  and  $S_vO_2$  to  $P_aO_2$ . The broken lines indicate arterial and venous oxygen saturation for 110 mmHg ( $\sim 21\%$   $O_2$ , normoxia) and 500 mmHg ( $\sim 60\%$   $O_2$ ). Model values used for this plot are  $P_aO_{2,0} = 110$  mmHg,  $OEF = 0.4$ ,  $\phi = 1.34$   $ml_{O_2}/g$ ,  $[Hb] = 15$   $g/dl_{blood}$  and  $\varepsilon = 0.0031$   $ml_{O_2}/(dl_{blood}\cdot mmHg)$ .

For this section, all magnetic susceptibility values are given in *cgs units*. The volume susceptibility of an ideal gas is given by:

$$\chi_v = \frac{\rho\chi_m}{M} = \frac{\chi_m}{10^3 \cdot V_m}, \quad (6.13)$$

where  $\rho$  is the gas density ( $g/cm^3$ ),  $M$  is the molar mass ( $g/mol$ ) and  $V_m$  is the molar volume, the volume occupied by one mole of ideal gas, which at room temperature (298 K) and atmospheric pressure (101 kPa, or 760 mmHg) is 24.5  $L/mol$ . Assuming that oxygen behaves like an ideal gas, volume susceptibility can be expressed as a function of fraction by volume ( $FO_2$ ).

$$\chi_v(FO_2) = \frac{3415 \times 10^{-6}}{24.5 \times 10^3} \cdot FO_2 \quad (6.14)$$

This gives values of  $\chi_v(100\%) = 0.139 \times 10^{-6}$ ,  $\chi_v(60\%) = 0.083 \times 10^{-6}$  and  $\chi_v(21\%) = 0.029 \times 10^{-6}$ , when balanced with nitrogen ( $N_2$ ), since for nitrogen gas,  $\chi_m = -12 \times 10^{-6} cm^3 mol^{-1}$  at room temperature [191], so nitrogen only contributes to  $\chi_v$  to the fourth decimal place in these calculations. This means that the difference in  $\chi_v$  between 100 % and 21 %  $O_2$  gas is  $\Delta\chi_v = 0.110 \times 10^{-6}$ .

The relevance of values for 60 %  $O_2$  is with reference to the experimental sections of this chapter, where an  $\sim 60$  %  $O_2$  challenge is presented.

The susceptibility contribution of dissolved oxygen in plasma can be calculated based on

$$FO_2 = \varepsilon \cdot P_a O_2 \quad (6.15)$$

where  $\varepsilon = 3.1 \times 10^{-5} L_{O_2} / (L_{blood} \cdot mmHg)$  is the solubility coefficient of oxygen in blood [172]. Normobaric dissolved oxygen makes a negligible contribution to plasma  $\chi_v$ , of  $\chi_v(FO_2) = [0.0005, 0.0022, 0.0033] \times 10^{-6}$ , for 110 mmHg ( $\cong 21$  %), 500 mmHg ( $\cong 60$  %) and 760 mmHg ( $\cong 100$  %)  $P_a O_2$  respectively.

In-vitro measurements of human blood at 1.5 T and 8.45 T [192] show a linear relationship between  $F_i O_2$  and  $T_1$ . This study also showed a similar linear relationship with plasma and saline, suggesting that the  $T_1$  dependence on  $F_i O_2$  is due to the amount of dissolved  $O_2$ , rather than blood oxygenation (the level of oxygen bound to haemoglobin). In-vivo measurements [193, 194] at 1.5 T have shown that arterial blood  $T_1$  decreases with 100 %  $O_2$  inhalation. The change in arterial  $T_1$  between an  $F_i O_2$  of 0.21 and 1.00 has been measured in-vivo at 1.5 T as  $-142 \pm 37$  ms [193] in the left ventricle or  $-226 \pm 57$  ms [194] in the femoral artery. The difference may be due to the flow rate at which hyperoxia was presented (10 L/min and 15 L/min respectively) causing different alveolar oxygen content. The arterial  $T_1$  dependence of hyperoxia has not been measured in-vivo at higher field strengths, but it has been estimated at 3 T by scaling the values based on the arterial blood  $T_1$  value at normoxia at 3 T [188], to correct for CBF measurement. Applying this scaling up to 7 T, with a normoxia arterial  $T_1$  of 2070 ms [195], arterial  $T_1$  would reduce by 350 ms between an  $F_i O_2$  of 21 % and 100 %. Venous blood  $T_1$  shows no significant change with hyperoxia [194], which can be attributed to the extra oxygen being bound to haemoglobin, rather than dissolved in plasma.

The  $T_2$  of arterial blood (femoral artery) shows no significant change on inhalation of 100 %  $O_2$ , whereas the  $T_2$  of venous blood (femoral vein) shows a significant increase of  $23 \pm 5$  ms at 1.5 T [194]. This is consistent with the

increased blood oxygenation of venous blood with hyperoxia, which is closely correlated with  $T_2$ . Increased haemoglobin oxygen saturation reduces field inhomogeneities caused by deoxyhaemoglobin, which reduces the  $T_2$  dependence on water diffusion. The fact that the arterial blood  $T_2$  shows no change with oxygenation also suggests that dissolved  $O_2$  does not have a large effect on blood  $T_2$ .

## 6.6 Image artefacts caused by hyperoxic challenges and their effect on $R_2^*$ quantification

### 6.6.1 Introduction

Hyperoxia is typically induced by increasing the oxygen volume fraction of inspired air, this will increase the oxygen fraction in the oral cavity and frontal sinus. As shown in *section 6.5*, increasing the oxygen fraction will increase the volume susceptibility of inspired air. This will act to increase the air-tissue (paramagnetic-diamagnetic) susceptibility difference and will amplify the effect of respiration-dependent noise in GE EPI images [131]. As a result, hyperoxia-induced BOLD signal artefacts have been observed close to the frontal sinus and the ventricles [196, 197]. The perturbation of hyperoxia on field homogeneity around air-tissue boundaries has been used to attempt to model the large phase shift due to the air-tissue boundary in phase imaging and subsequently filter the naturally occurring effect due to the susceptibility difference at the boundary [198].

Changes in field homogeneity will affect GE EPI magnitude data in the following ways. Field inhomogeneities will combine with the imaging spatial encoding gradients to create position encoding errors. This will cause image distortions which are dependent on the relative amplitudes of imaging gradients and the field inhomogeneity. For an EPI acquisition, the amplitude of each imaging gradient depends on the bandwidth in each respective direction (readout, phase-encode and slice directions). Intra-voxel spin dephasing is also dependent on field homogeneity, as a field inhomogeneity across a voxel will

lead to unrecoverable spin dephasing under a GE ( $T_2^*$ -weighted) acquisition, causing signal attenuation. In this section, dynamic mapping of the field shift due to hyperoxia is used to attempt to quantify the effects of hyperoxia on GE EPI data. This is crucial for an accurate model of the effects of hyperoxia on the BOLD signal, as this change in field homogeneity is time-locked to periods of hyperoxia, but will alter GE EPI magnitude data in a manner that is not related to blood oxygenation.

### 6.6.2 Method

Five healthy volunteers (3 male, 2 female; mean age =  $25 \pm 3$  years, range 22–29 years) participated in this study. All subjects gave informed written consent prior to participating and ethical approval was given by the University of Nottingham Medical School Ethics Committee.

The preparation for the respiratory challenge is described in *section 3.3*. However, unlike for the earlier hypercapnia experiments, where breathing rate was paced by visual cues, the subject was instructed to breath at a steady, but comfortable pace and asked not to hold their breath. So that the subject emptied the sample gas bag with every breath, a lower flow rate was used, compared to when breathing was paced, due to the subject being less aware of their breathing. The purpose of not pacing the breathing rate was mainly the subject's comfort, but it also reduced subject motion during scans. The low flow rate, along with the existing ventilation system in the scanner bore helped to ensure that no build-up of oxygen occurred in the magnet bore during hyperoxic periods.

The subject lay on the scanner bed, out of the bore, for approximately five minutes. This gave the subject time to become accustomed to the mask and this period was also used to estimate the flow rate at which the subject could comfortably breath the supplied gas and some of the neutral gas with every breath. The scanner bed was then positioned so the head coil lined up with the magnet iso-centre.

Targeted  $P_{ET}O_2$  was modulated between the subject's baseline value ( $\sim 110$  mmHg; normoxia) and 500 mmHg (hyperoxia), for two cycles of three minutes of normoxia followed by three minutes of hyperoxia, followed by a final three minute period of normoxia. Isocapnia was maintained at the subject's baseline ( $\sim 40$  mmHg  $P_{ET}CO_2$ ).

Scanning was performed on a Philips Achieva 7 T system, with head volume transmit and 16 channel SENSE head receive coils. GE EPI data were acquired every 2.4 s throughout the respiratory challenge. Images consisted of 2 mm isotropic voxels, with a  $192 \times 192$  mm<sup>2</sup> field-of-view, 30 axial slices were acquired (2 mm thickness, no slice gap) spanning from the ventricles to the motor cortex. Imaging parameters of TE = 25 ms, SENSE factor = 3, voxel band-width = 41.5 Hz, TR = 2.4 s and flip angle =  $75^\circ$  were used. Both magnitude and phase data were saved. An additional set of GE EPI data were acquired before the respiratory challenge to map the static  $B_0$  field component. This data had the same parameters as above, but with the echo time modulating between 25 and 28 ms for alternate dynamics, with 10 averages at each TE.

The relative change in  $B_0$  field across dynamics during the respiratory challenge was then calculated using a technique developed by Jack Harmer, based on the work of Hahn *et al.* [199]. This makes the assumption that there is a temporally invariant component of phase ( $\phi_0$ ) [200], due to radio-frequency phase inhomogeneities, which can be separated from dynamic changes. As a result,  $\phi_0$  can be subtracted from the phase data and the remaining phase change over time can be used to calculate the underlying relative changes in  $B_0$  over time.

The temporally invariant phase component ( $\phi_0$ ) was first calculated based on a static  $\Delta B_0$  map, formed using the phase difference between images taken at the two different echo times [15]. A seventh order three dimensional polynomial fit was applied to the static  $\Delta B_0$  map to reduce the effect of noise. The high order was required to accurately represent the large susceptibility effects around the frontal sinus. This polynomial fit was taken as the temporally in-

variant component of  $\Delta B_0$ , from which  $\phi_0$  was calculated. Therefore the static  $B_0$  map was used to calculate  $\phi_0$ , which was combined with the phase data acquired during the hyperoxia challenge to map the relative changes in  $B_0$  over time.

Maps of the field shift due to hyperoxia were then formed by subtracting the average normoxia from average hyperoxia periods (average over the last two minutes of each period). Comparing this map with the voxel acquisition bandwidth (41.5 Hz) indicated how much EPI distortion will result from the change in field homogeneity during hyperoxia. For this purpose, the field shift map was considered in terms of frequency shift ( $\Delta f$ , units of Hz), related to field shift by  $\Delta f = \gamma \Delta B_0 / 2\pi$ .

To assess the changes in the GE EPI signal due to this hyperoxia-related field shift, intra-voxel spin dephasing was simulated. A seventh order three dimensional polynomial fit was applied to the field shift map. Each voxel was subdivided into  $10 \times 10 \times 10$  spin isochromats, in a square grid such that the distance between isochromats is the same, even across voxels. The polynomial fit coefficients were used to estimate the change in field homogeneity ( $\Delta f$ ) at the location of each isochromat. The phase of each isochromat was allowed to evolve over the echo time by  $\phi = 2\pi \Delta f TE$ . For each voxel, the phase of all isochromats were combined by vector summation to estimate intra-voxel dephasing. This provided a measure of signal attenuation due to the hyperoxia-induced change in field homogeneity across each voxel.

### 6.6.3 Results

The frequency shift induced by hyperoxia is shown for a typical subject in *figure 6.2a*. The magnitude of this shift is largest in the frontal sinus, up to 20 Hz (50% of the voxel bandwidth) and reduces with distance from the frontal sinus, but never drops to zero. Single-subject timecourses of the frequency shift from the frontal sinus (black), motor (blue) and visual cortices (green) are shown in *figure 6.2e*. The hyperoxia-induced frequency shift in a  $5 \times 5$  voxel ROI in the motor (M1) and visual (V1) cortices (as shown in *figure 6.2d*) is  $3.1 \pm 0.2$

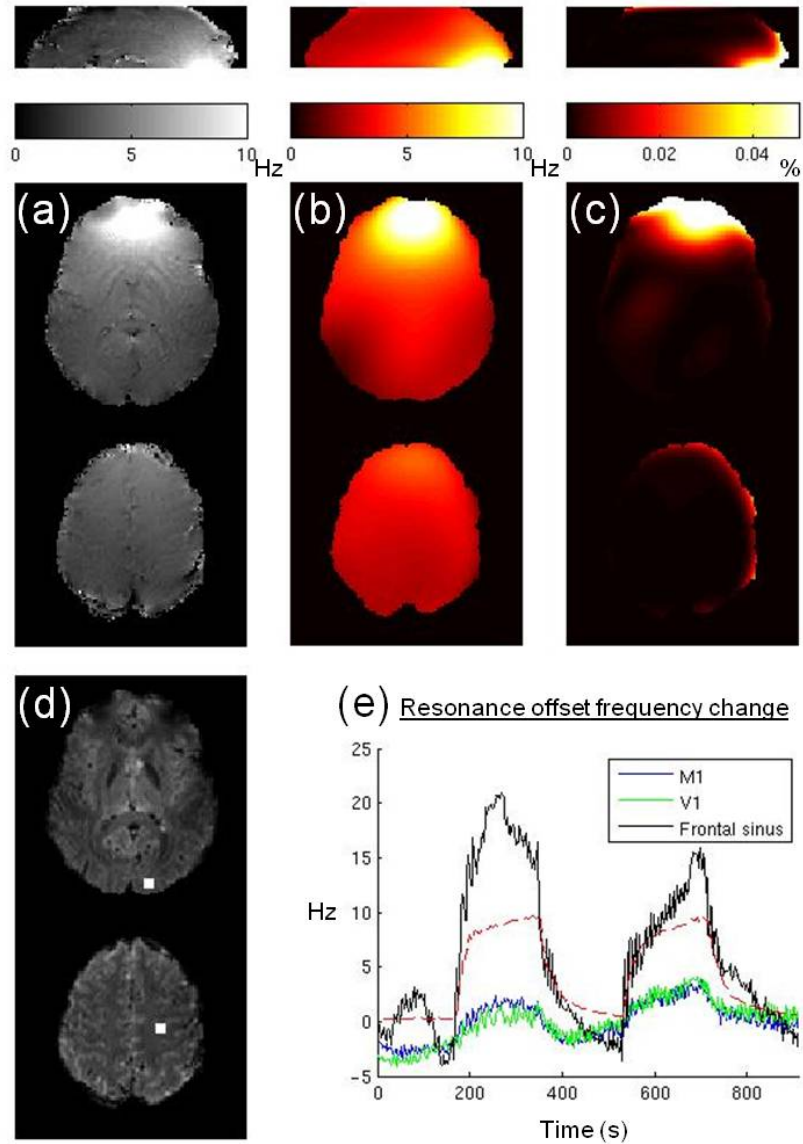


Figure 6.2: Single subject (a) Map of resonance offset change (in Hz) due to hyperoxia (1 sagittal and 2 axial slices); (b) Polynomial fit to (a); (c) Map of the simulated signal attenuation (%) due to hyperoxic changes in field homogeneity; (d) The location of the  $5 \times 5$  voxel V1 and M1 ROIs, overlaid on an average magnitude image; (e) Timecourses of frequency shift during the 15 minute hyperoxia paradigm, from the M1, V1 ROIs together with an ROI from the frontal sinus. The red dashed line shows a scaled  $P_{ET}O_2$  timecourse.

Hz in M1 and  $2.1 \pm 0.7$  Hz in V1 (mean  $\pm$  std over subjects), corresponding respectively to 7% and 5% of a voxel volume in the phase-encode direction.

The corresponding polynomial fit to *figure 6.2a*, used for the intra-voxel dephasing simulation, is shown in *figure 6.2b*. *Figure 6.2c* shows the map of simulated signal attenuation due to field inhomogeneity for this subject. Simulations indicate that the change in field homogeneity due to hyperoxia will cause a signal attenuation of only  $8 \pm 9 \times 10^{-4}$  % in M1 and  $4 \pm 4 \times 10^{-4}$  % in V1 (mean  $\pm$  std over subjects).

#### 6.6.4 Discussion

This experiment has considered the effect of changes in field homogeneity due to hyperoxia on GE EPI data. Dynamic mapping of the field shift can be calculated using phase data from a standard GE EPI fMRI experiment [199], just with the addition of a short extra scan to calculate  $\phi_0$ .

The measured hyperoxic field shift was largest over the frontal sinus, but extended over the whole head (*figure 6.2a*). The simulated intra-voxel dephasing due to the change in field homogeneity did not significantly change the transverse relaxation rate ( $< 0.05\%$  signal attenuation, as seen from *figure 6.2c*) apart from in voxels neighbouring the frontal sinus.

The measured hyperoxic field shift will cause a significant change in the EPI distortions, which will lead to the voxel composition changing under hyperoxia (by 7% in M1 and 5% in V1) in the phase-encode direction. Where the voxel lies at a boundary, such as between grey matter and white matter, a distortion could change the partial voluming in that voxel and result in a significant GE EPI signal change. Dynamic distortion correction techniques may be able to compensate for this, in the same way as static field homogeneities can be corrected [15].

The analysis assumed that the effect of oxygen in the sinuses could be modelled using a seventh order polynomial. This is based on evidence from respiration-

induced resonance field offsets [131], where the effect on  $B_0$  showed a global low frequency spatial distribution. The polynomial fit was found to be reasonable, except in some deep grey matter regions (*figure 6.2a*).

In summary, hyperoxia-induced artefacts arising due to oxygen in the sinuses or oral cavity will not significantly contaminate the results of hyperoxia BOLD measurements, although small shifts in voxel position must be considered. The change in field homogeneity due to hyperoxia has been shown to have a negligible effect on signal attenuation in M1 and V1, regions where calibrated BOLD experiments are commonly used. However, this may not be the case with anterior regions which are close to the frontal sinus, such as the orbitofrontal cortex. This technique could be used in future hyperoxia fMRI studies to monitor the temporal variations in  $B_0$  induced by hyperoxia, especially in regions close to the oral cavity and frontal sinus.

## **6.7 Venous blood oxygenation and calibrated BOLD measurements**

### **6.7.1 Introduction**

This section implements the method of measuring relative changes in venous blood oxygenation and  $CMRO_2$  proposed in *section 6.3*, by repeating the same motor task at both normoxia and hyperoxia. The addition of an ASL CBF measurement also allows an estimate of the relative change in oxygen metabolism due to the motor task. A thorough discussion is also presented outlining the assumptions and issues raised in previous sections.

### **6.7.2 Method**

Nine healthy volunteers (3 male, 6 female; mean age =  $27 \pm 3$  years, range 23–30 years) participated in this study. All subjects gave informed written consent prior to participating and ethical approval was given by the University of Nottingham Medical School Ethics Committee.

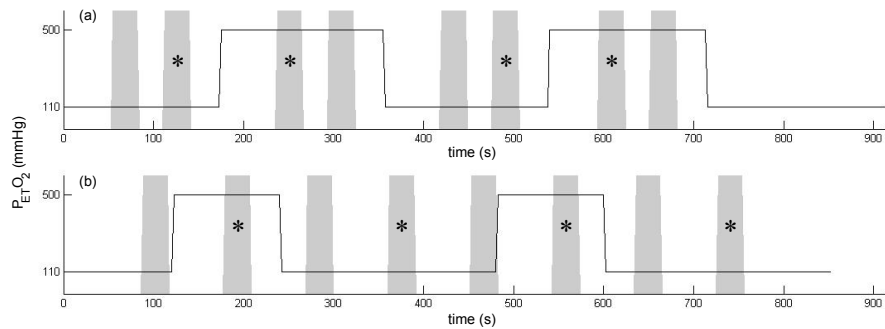


Figure 6.3: An illustration of the combined hyperoxia and motor task for (a) the 30 s ON/ 30 s OFF paradigm and (b) the 30 s ON/ 60 s OFF paradigm. The motor task is shown in grey. Trials marked with an \* were used in the analysis.

All subjects were asked to perform a motor task during a respiratory challenge, such that the same motor task was repeated both at normoxia and hyperoxia. The motor task consisted of a bilateral sequential finger tap. This was visually cued, with the word ‘TAP’ displayed in red (with a dark background) onto a projector screen at the end of the magnet bore. This was replaced by a white ‘+’ fixation point during rest periods. The motor paradigm consisted of blocks of two trials of 30 s ON/ 30 s OFF for each gas level, such that the block finishes just before the start of a transition between gas levels (see *figure 6.3*). Apart from the first four subjects, the other subjects were also asked to complete an additional motor task, for ASL acquisition. This additional motor task was performed with the subject breathing medical air, consisting of 10 trials of 30 s ON/ 30 s OFF, but was otherwise the same as the previous motor task.

The preparation for the respiratory part of the task was performed as outlined previously (*section 6.6.2*). For the first seven subjects, the respiratory challenge consisted of two repeats of three minutes of normoxia, followed by three minutes of hyperoxia, with a final three minutes of normoxia at the end. For the normoxic condition, both  $P_{ET}O_2$  and  $P_{ET}CO_2$  were maintained at the subject’s resting values ( $\sim 110$  mmHg and  $\sim 40$  mmHg, respectively). For the hyperoxic condition,  $P_{ET}O_2$  was targeted at 500 mmHg, whilst  $P_{ET}CO_2$  was

maintained at the resting value.

After reviewing the BOLD response from the first seven subjects, a signal drift was observed during the hyperoxic periods only. This would cause a systematic error, discussed later. Therefore for the final two subjects, to minimise the effect of this signal drift, the paradigm was modified such that the respiratory paradigm consisted of an initial two minutes of normoxia, followed by two repeats of two minutes hyperoxia and four minutes of normoxia. The motor paradigm was changed to 30 s ON/ 60 s OFF repeated throughout the respiratory challenge, with the two trials occurring during hyperoxia starting one minute after the transition to hyperoxia (see *figure 6.3b*). With this design, every other trial does not fall at the correct part of the respiratory paradigm to be used, but helps to maintain the subject's attention. For these two subjects, the motor task collected during ASL acquisition consisted of 8 motor trials of 30 s ON/ 60 s OFF.

Scanning was performed on a Philips Achieva 7 T system, with head volume transmit and 16 channel SENSE head receive coils. GE EPI data were acquired every 2.4 s throughout the respiratory and motor task. Images consisted of 2 mm isotropic voxels, with a  $192 \times 192 \text{mm}^2$  field-of-view, and 20 axial slices (2 mm thickness, no slice gap) spanning the motor cortex. Imaging parameters of TE = 25 ms, SENSE factor = 3, voxel band-width = 41.5 Hz, TR = 2.4 s and flip angle =  $75^\circ$  were used. ASL datasets were acquired with a FAIR labelling scheme, with TI = 1400 ms; selective thickness 10 mm wider than the imaging volume; non-selective thickness of 300 mm; background suppression pulses at 402 and 639 ms [201]; in-plane pre- and post-saturation were used. Images consisted of  $2 \times 2 \times 4 \text{mm}^3$  voxels, with a  $192 \times 192 \text{mm}^2$  field-of-view, and 8 axial slices (4 mm thickness, no slice gap) with the same orientation and centre as the GE EPI data. Imaging parameters were TE = 14 ms, SENSE factor = 3, voxel band-width = 41.5 Hz, TR = 3 s (6 s for a tag/control pair). Two base images (same parameters as for the ASL, except with no inversion and a long TR of 10 s) were acquired, one before and one after the ASL acquisition.

GE EPI datasets were motion corrected using MCFLIRT (FSL, fMRIB, Oxford, UK). Voxelwise linear detrending was then performed using a linear fit (MATLAB, The MathWorks, Natick, USA) over timepoints defined as ‘baseline’. These ‘baseline’ timepoints were during periods of normoxia and not within 30 s of a previous finger tap, so as to not include the post-stimulus undershoot. Linear detrending involved removing the linear component of the timecourse, using the linear fit coefficients. This method was chosen in preference to a high-pass temporal filter, due to the long cycle lengths of the paradigm. Each voxel’s timecourse was normalised by dividing every timepoint by the average value over all *baseline* timepoints. Maps of statistical significance of the BOLD response to the motor task were formed using the FEAT (FSL, fMRIB, Oxford, UK) general linear model. This was done on the datasets before voxelwise normalisation, but after motion correction and linear detrending. A boxcar design, representing the hyperoxia response was included in the model design as an independent regressor, so the hyperoxia-based BOLD response could be separated from the motor response in the analysis. ‘BOLD motor activation masks’ were formed of clusters of voxels with  $Z > 5$  and  $P_{cluster} < 0.05$  for the response to the motor task. The general linear model analysis contained separate regressors for the motor task and the hyperoxia challenge and although the statistical maps for the BOLD response to hyperoxia were not considered in forming the masks, significant activation was found to follow grey matter sulci and in large vessels.

To assess motion during the ASL datasets, the two base images were compared to see if there was any systematic motion between the start and end of the ASL dataset. For all subjects, the two base images appeared reasonably well aligned, when one was overlaid on the other. ASL datasets were not motion corrected, since the motion correction algorithm struggles with background suppressed data, as it removes static signal and hence key features in the images, which the registration uses for alignment. An interleaved acquisition of tag and control images meant that temporal interpolation was required before subtraction. Linear temporal interpolation (MATLAB, The MathWorks, Natick, USA) was performed to both the tag and control datasets, such that

an interpolated tag timepoint is calculated at the time of acquisition of each control timepoint and vice versa. Subtraction was then performed, between interpolated tag and control datasets, resulting in a CBF-weighted timecourse with timepoints every 3 s. Note, however that the acquisition effectively has a 6 s sampling rate, so changes on the timescale of 3s cannot be resolved. Maps of statistical significance of the CBF response to the motor task were formed using the FEAT (FSL, fMRIB, Oxford, UK) general linear model. In this analysis, the high-pass filter in FEAT was used, with a cut-off period of twice the trial length. This was 120 s for the three subjects with a 30 s ON/ 30 s OFF paradigm and 180 s for the last two subjects with a 30 s ON/ 60 s OFF paradigm. ‘CBF motor activation masks’ were formed of clusters of voxels with  $Z > 2.3$  and  $P_{cluster} < 0.05$ . The lower Z-statistic threshold was used due to the intrinsically lower SNR of ASL compared with GE EPI.

Timecourses of measured  $P_{ET}O_2$  were used to estimate the relative change in venous deoxyhaemoglobin fraction due to hyperoxia ( $q_h$ )(see section 6.4). A resting OEF of 0.4 was used and the assumptions were made that oxygen consumption is not affected by hyperoxia and hematocrit remains constant both during hyperoxia and the motor task.

Timecourses were formed for the GE EPI datasets by averaging the normalised dataset over all voxels passed by the *BOLD motor activation mask*. To minimise the error due to the hyperoxic drift, only the first motor trial during hyperoxia periods and the last trial during normoxia periods were considered. Averages of rest and active (motor task) periods were made, providing a rest and an active % change (%BOLD) for each trial relative to the normoxic *baseline* (as defined earlier). These % changes were converted to  $\Delta R_2^*$  using the approximation  $\Delta R_2^* \approx -\%BOLD/(100.TE)$ , for use in the  $q_{act}$  calculation (division by 100 is to convert from %BOLD to a fraction, for use in the approximation). Linear regressions (MATLAB, The MathWorks, Natick, USA) were performed to fit  $\Delta R_2^*$  as a linear function of  $q_h$ , separately for the rest and active conditions. The fitted parameters were then used to estimate  $q_{act}$  and  $(1 + \frac{V_{act}}{V})$ , as proposed in section 6.3.

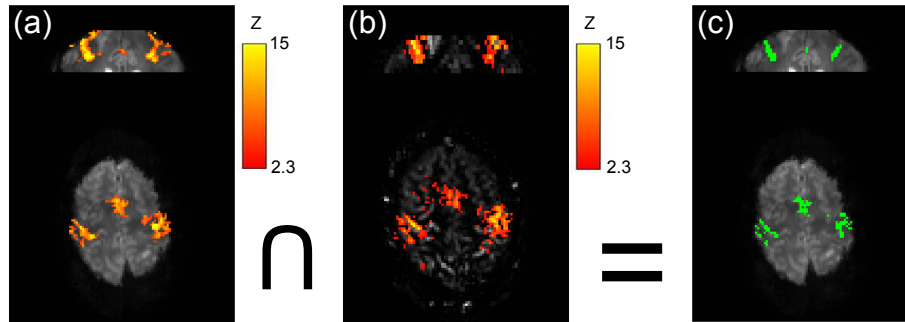


Figure 6.4: An example of the formation of the *combined mask*. (a) BOLD activation map (Z-statistic). (b) CBF activation map (Z-statistic), overlaid on the average subtraction. (c) Combined mask formed of the intersection of (a) and (b).

A new, 'combined mask' was formed for each of the five subjects for which ASL data were acquired. This involved finding the intersection of the *BOLD motor activation mask* and the *CBF motor activation mask* (see figure 6.4). The reason for this is that it was found that using the *BOLD motor activation mask* to form a CBF-weighted timecourse resulted in a dilution of the measured CBF response, underestimating the CBF change. The CBF-weighted data (after interpolation and subtraction) were normalised to the rest periods, by dividing by the average of the last half of all rest periods. For each subject, a timecourse was generated by averaging over all voxels included in the *combined mask*. The % change in CBF was calculated by averaging over the active (motor task) period of all trials, multiplied by 100. New values of  $q_{act}$  were calculated using the same method as described above, for the *combined mask* rather than the *BOLD motor activation mask*. %CBF changes and  $q_{act}$  were used to calculate %CMRO<sub>2</sub>, using equation 6.8.

### 6.7.3 Results

Transitions in  $\Delta P_{ET}O_2$  of  $330 \pm 20$  mmHg (mean $\pm$ SEM over subjects) were achieved. Using these measured  $P_{ET}O_2$  values results in a predicted increase of  $\Delta Y_v = 0.068 \pm 0.003$  during the hyperoxia periods (section 6.4), an 11% in-

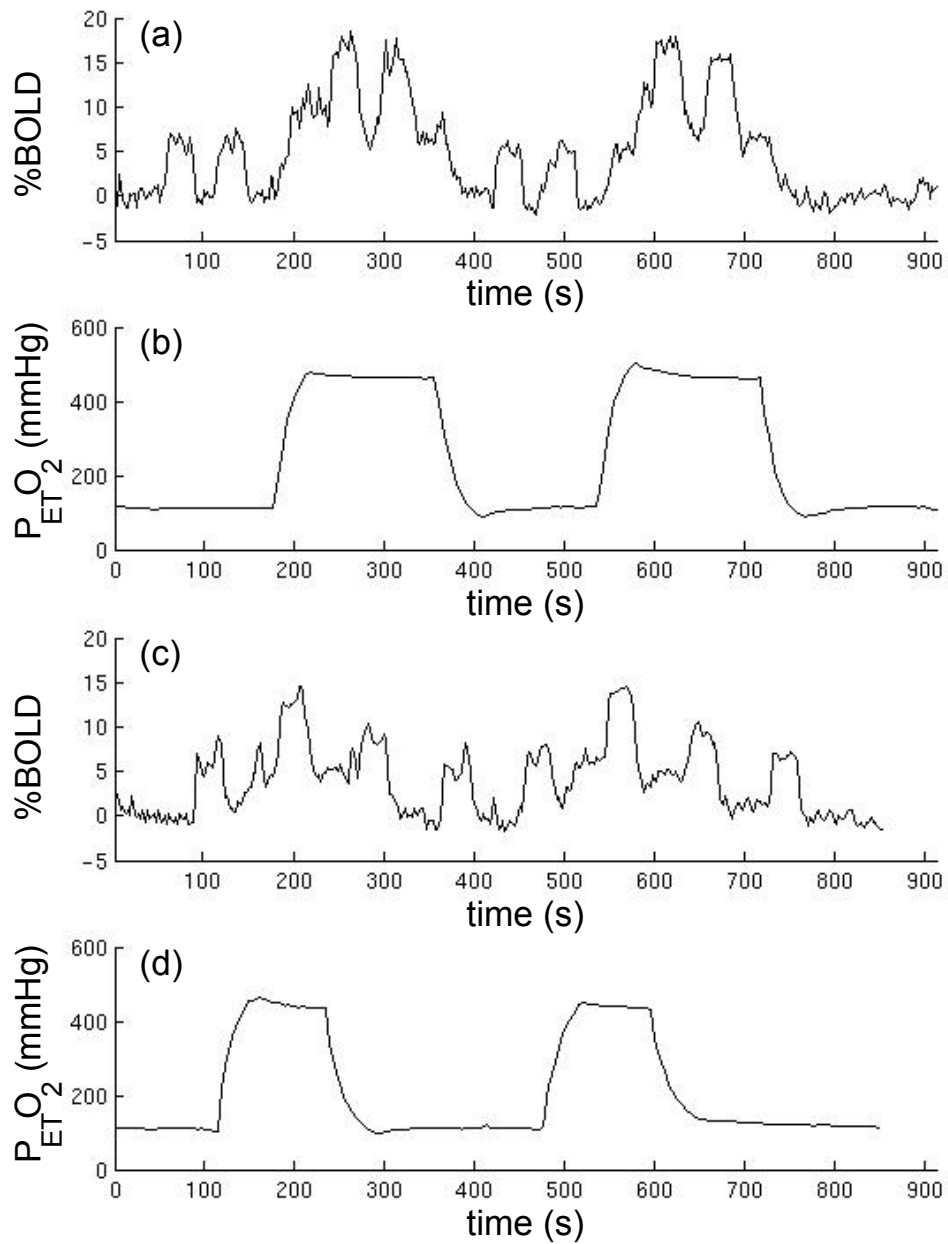


Figure 6.5: Examples of BOLD (a,c) and  $P_{ET}O_2$  (b,d) timecourses, from a single subject each for (a,b) the 30s ON/ 30s OFF paradigm and (c,d) the 30s ON/ 60s OFF paradigm.

crease over the resting normoxia value.  $\Delta P_{ET}CO_2 = -0.5 \pm 0.1$  mmHg during hyperoxia (compared with normoxia), with a range of  $-1.1 - 0$  mmHg across subjects, this was assumed too small to have a significant effect on CBF and the resulting BOLD signal.

*Figure 6.5* shows example BOLD and  $P_{ET}O_2$  timecourses for both the 30 s ON/ 30 s OFF and the 30 s ON/ 60 s OFF paradigms. The BOLD signal increased by  $6.7 \pm 0.8$  % due to hyperoxia. The BOLD response to the motor task was increased by a factor of  $39 \pm 6$  % at hyperoxia compared to normoxia. An example of the average trial of the motor task at normoxia and hyperoxia, as well as an example of the linear fits are shown in *figure 6.6*. From the linear fits, values of  $M$  and  $M'$  were calculated as  $M = 38 \pm 4$  % and  $M' = 50 \pm 5$  %. Individual subject values for the relative increase in vCBV, relative decrease in deoxyhaemoglobin fraction ( $q_{act}$ ) and corresponding absolute increase in  $\Delta Y_{act}(= 1 - Q(1 - q_{act}))$  during the motor task are reported in *table 6.1*.

For the *combined mask*, the average CBF trial timecourse is shown in *figure 6.7* (formed by averaging over all trials for each subject, and then by averaging over all subjects). From the linear fits, values of  $M$  and  $M'$  were calculated as  $M = 28 \pm 2$  % and  $M' = 34 \pm 4$  %. Results based on the *combined mask*, CBF,  $q_{act}$  and the relative increase in  $CMRO_2$  are reported in *table 6.2*.

#### 6.7.4 Discussion

This experiment has demonstrated the implementation of a new method for estimating the relative change in  $CMRO_2$  due to increased neuronal activation associated with performing a task. This method uses a simple BOLD signal model and the perturbation of venous blood oxygenation provided by hyperoxia. Performing the same task at hyperoxia in addition to normoxia provides an extra degree of contrast with which to better understand the vascular nature of the BOLD signal. As a result, this model does not require any assumption about the coupling between CBV and CBF.

The model proposed here is based on the analytical model proposed by Yablon-

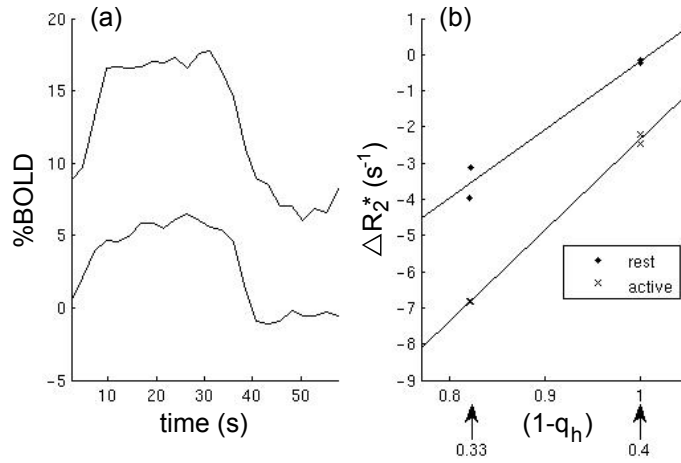


Figure 6.6: (a) Average motor trial %BOLD timecourses during hyperoxia (above) and normoxia (below). (b) Example of the linear fit between  $\Delta R_2^*$  and  $(1 - q_h)$ . Numbered arrows show the value of  $Q(1 - q_h)$  at that point. Data from (a) and (b) are from the same subject, which is the subject featured in figure 6.5(a & b).

Subject #	vCBV (%)	$q_{act}$ (%)	$\Delta Y_{act}$
1	36.8	-36.9	0.15
2	23.6	-56.1	0.22
3	33.3	-33.6	0.13
4	33.7	-39.9	0.16
5	30.5	-32.2	0.13
6	32.1	-31.0	0.12
7	30.7	-35.2	0.14
8	10.0	-17.8	0.07
9	44.6	-43.4	0.17
mean $\pm$ SEM	31 $\pm$ 3	-36 $\pm$ 3	0.14 $\pm$ 0.01

Table 6.1: Individual subject results for the *BOLD motor activation mask ROI*

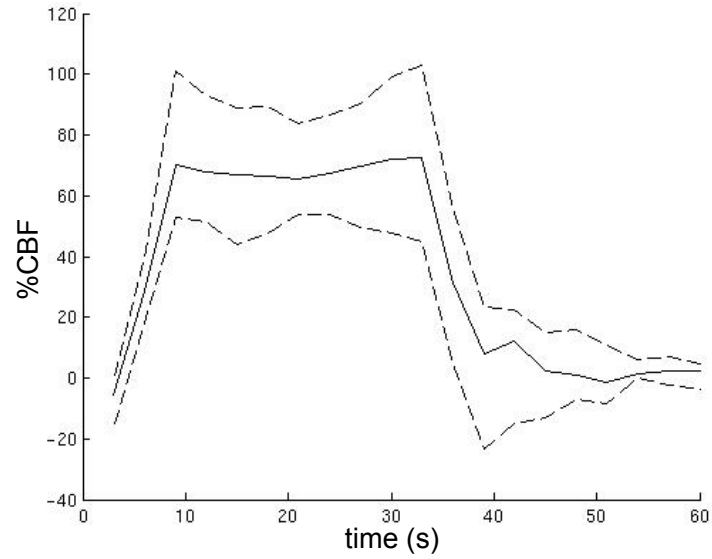


Figure 6.7: The %CBF response to the motor task, averaged over trials then across subjects. The dashed lines indicate the range of values across subjects.

Subject #	$q_{act}$ (%)	CBF (%)	CMRO <sub>2</sub> (%)
5	-35.2	58.0	2.5
6	-29.8	57.8	10.9
7	-25.8	87.2	39.0
8	-13.6	50.8	30.3
9	-40.9	87.4	10.7
mean±SEM	-29 ± 5	68 ± 8	19 ± 7

Table 6.2: Individual subject results for the *combined mask ROI*

skiy and Haacke [30]. This is an extravascular signal model, which assumes that transverse relaxation occurs in the static dephasing regime. The short  $T_2^*$  of venous blood at 7 T [105] means that the intravascular GE signal contribution is small compared to the extravascular GE signal contribution [174]. It is therefore reasonable to assume that the extravascular signal contribution dominates, except for the case of voxels which have a large vascular compartment, such as those containing a large draining vein. Field inhomogeneities cause larger frequency shifts at 7 T compared with lower fields. At 7 T the frequency shifts caused by a nearby venule are sufficient to fulfil the static dephasing condition [31, 28]. The resulting predicted linear relationship between  $R_2^*$  and blood oxygenation is consistent with the tight linear correlation between  $R_2^*$  and  $P_{ET}CO_2$  in *chapter 5*. Random vessel orientation is assumed, however the contribution of vessel orientation on transverse relaxation is included in the constant  $k$ , described in *equation 6.4*. The model proposed here does not require knowledge of this constant, so the assumption of vessel orientation could be relaxed.

The model used in this method becomes equivalent to the model proposed by Chiarelli and co workers [172] if vCBV were calculated first [175], replacing the Grubb relationship, and a linear relationship assumed between  $R_2^*$  and blood oxygenation. The values of  $M$  calculated here are the first reported human values for 7 T. Equivalent values for the motor cortex calculated using hyperoxia at 3 T are  $M \approx 5\text{--}6\%$  [172, 202], using hypercapnia at 3 T are  $M \approx 4\text{--}6\%$  [203, 202] and using hypercapnia at 1.5 T are  $M \approx 5\text{--}9\%$  [204, 37, 205, 206]. The value of  $M$  depends on field strength and TE, but the value reported here of  $M = 38 \pm 4$  (9 subjects) is a factor of 5 higher than at lower field strengths, which is consistent with increased BOLD contrast at 7 T and smaller voxel volume causing less partial voluming. With the tighter *combined mask*, the new value of  $M = 28 \pm 2$  (5 subjects) is lower than for the *BOLD motor activation mask*, this could be due to the exclusion of large draining veins. Calculated CMRO<sub>2</sub> increases agree with previous studies using a bilateral finger tap, with  $\Delta\text{CMRO}_2 = 16 \pm 9\%$  [204] and ranging from 5–45% [203], both using hypercapnia-based calibration and with a positron emis-

sion tomography (PET) study [207], using a right-handed finger tap, giving  $\Delta\text{CMRO}_2 = 11 \pm 13 \%$  in the left (contralateral) precentral gyrus.

Previous calibrated BOLD experiments [69, 172] rely on an assumed coupling relationship between total CBV and CBF (*equation 6.1*,  $\alpha = 0.38$ ), which was originally measured in rhesus monkeys, using PET and hypercapnia [70]. Due to deoxygenated haemoglobin being the source of BOLD contrast, the venous, rather than total blood volume compartment should be considered in the calibrated BOLD model. The venous compartment reacts passively to flow changes, so would be expected to have a different coupling relationship compared with the arterial compartment, which is lined with muscles for active constriction and dilatation. The vascular response to a global hypercapnia challenge may also be different to the local response to increased neuronal activity. The coupling relationship between venous CBV and CBF has recently been investigated in humans using the VERVE technique and ASL during both neuronal activation ( $\alpha = 0.23 \pm 0.05$ ) [75] and hypercapnia ( $\alpha = 0.18 \pm 0.02$ ) [76]. Although the coupling was slightly different in those two studies, the use of different ROIs makes comparison difficult. Much work is required to better characterise the coupling relationship and investigate inter-region and inter-subject variability. One possible area of variability could be that there could be a dependence of vascular size on the coupling relationship (e.g. venules might have a different relationship to veins). Despite better understanding of this coupling, it remains preferable to avoid use of an assumed coupling constant.

There is a change in arterial blood oxygenation due to hyperoxia (see *figure 6.1*), which will contribute to the hyperoxia BOLD signal. This is a problem that will effect any hyperoxia-based calibration study. *Equation 6.5* can be used to assess the scale of the arterial contribution to hyperoxia BOLD signal. For the case shown in *figure 6.1*, with arterial resting CBV assumed to be a third of venous resting CBV [73], the venous signal contribution is 14 times larger than the arterial signal contribution. The effect of this will be to cause a small underestimation of relative vCBV change and  $q_{act}$ . This change in arterial oxygenation fraction of 0.0169 (from 110 – 500 mmHg  $P_aO_2$ ) will

cause a decrease in susceptibility of  $\Delta\chi_v = -0.0018 \times 10^{-6}$ , based on a hematocrit fraction of  $\text{Hct} = 0.4$  and  $\Delta\chi_v(\text{fully deoxygenated} - \text{fully oxygenated haemoglobin}) = 0.264 \times 10^{-6}$  [25]. Another possible issue may be if small arteriolar blood oxygenation at normoxia is significantly lower (on the order of  $\sim 90\%$ ) compared to arterial blood oxygenation. On hyperoxia, these arterioles would become closer to fully oxygenated, leading to an overestimation in the BOLD response to hyperoxia at rest.

However, as shown in *section 6.5*, increased dissolved oxygen in arterial plasma will cause a small increase in arterial susceptibility. For the change in  $P_aO_2$  of 110 – 500 mmHg, there will be an increase of  $\Delta\chi_v = +0.0017 \times 10^{-6}$ . This will have an opposing effect to that of increased arterial blood oxygen saturation, as discussed in the previous paragraph, causing a small overestimation of relative vCBV change and  $q_{act}$ . These opposing effects will almost cancel each other out, leading to an insignificant change in arterial susceptibility. For a sense of scale of susceptibility changes, the estimated venous oxygenation changes of  $0.068 \pm 0.003$  due to hyperoxia and  $0.14 \pm 0.01$  due to the motor task will give susceptibility changes of  $0.0072 \times 10^{-6}$  and  $0.0148 \times 10^{-6}$  respectively. Combine this with the smaller resting arterial CBV, typically a third of venous CBV, and both the change in arterial blood oxygenation and the increased dissolved oxygen will not give a significant contribution to the hyperoxia BOLD signal (approximately two orders of magnitude smaller).

The estimation of  $q_h$  from  $P_{ET}O_2$  assumes that OEF is 0.4 (see *equation 6.11*). OEF is thought to be fairly constant across a healthy subject group, however it may vary considerably in patients. OEF does not affect the absolute venous blood oxygenation change estimation, however it will bias the relative change  $q_h$ , since this is normalised to  $Q (\equiv OEF)$ . Calculation of relative vCBV changes are independent of errors in OEF. A systematic error in  $q_{act}$  will occur, linearly proportional to the error in OEF. One way around this is to measure venous blood oxygenation in a large draining vein [182, 183], but at the moment it is not known whether the errors associated with these methods will be less than the errors associated with estimating OEF. Neither method

would account for possible local variations in OEF.

For the  $R_2^*$  model, it is assumed that  $q_h$  and  $q_{act}$  are independent of one another. This essentially means that the amount of oxygen extracted is not dependent on arterial oxygen content. This is reasonable so long as there is no metabolic response to hyperoxia and that CBF is the same in normoxic and hyperoxic periods.

Another possible source of error could be due to local increases in hematocrit during neuronal activation [208]. This possibility has been attributed to a local mismatch in plasma and red blood cell velocities during neuronal activation. This would influence *equation 6.6*, as the constant  $k$  will be different compared to in *equation 6.5*. A local increase in hematocrit would cause an overestimation of  $M'$ , so an overestimation of relative vCBV changes and an underestimation of  $q_{act}$ .

In this experiment,  $P_{ET}CO_2$  was monitored throughout and was found to decrease by  $\Delta P_{ET}CO_2 = -0.5 \pm 0.1$  mmHg during hyperoxia. This very mild hypocapnia is less than that seen with an equivalent fixed inspired hyperoxia method ( $\Delta P_{ET}CO_2 \sim -3$  mmHg during a 60 %  $O_2$  challenge) [188]. The magnitude of the decrease in  $P_{ET}CO_2$  is on the order of resting fluctuations, throughout the course of the experiment. The effect on CBF and resulting BOLD signal is expected to be insignificant (on the order of  $\sim 2\%$  and  $\sim 0.2\%$ , respectively).

A signal drift was observed in the BOLD timecourses of all subjects (see *figure 6.5a*). This drift was a slow decrease, which only occurred during hyperoxic periods. If unaccounted for, this would cause an underestimation of the hyperoxia %BOLD, underestimating  $M$ . The analysis approach attempted to minimise the effect of the drift by only considering the first motor trial of each hyperoxic period and the immediately preceding normoxic motor trial. In this case, the effect of the drift is thought to be minimal over the first minute of hyperoxia, where the motor trial takes place. For the final two subjects, a

modified paradigm with shorter hyperoxia periods was used, to try to account for the drift. The cause of the drift was unknown at the time of performing this study, however it is the subject of current work and has since arisen that the cause of the drift may be due to an overshoot in  $P_{ET}CO_2$  of 1–2 mmHg during the transition up to hyperoxia. This overshoot has recovered back to baseline values by the time of the motor task, but may be the source of the drift. The overshoot was attributed to a limitation with the Respiract™ software, which can be fixed and therefore should not be a problem in the future.

As with any experiment which combines BOLD and CBF measurements, the choice of ROI should be the subject of careful consideration. Reproducibility studies of hypercapnia calibration [209] have found that an ROI defined by significant CBF activation gives the results with least variability. It has also been observed [60] that an ROI defined by significant CBF activation will exclude large draining veins, which have a large resting CBF, but small  $\Delta$ CBF response. These large veins typically have a large BOLD response, due to draining active tissue, but do not contain active tissue. In this work, a combined ROI was formed, only including regions where both significant BOLD and CBF response to the motor task was found. As a result, large draining veins were discarded, which helps to meet the extravascular signal assumption, whilst also limiting the ROI to significant BOLD activation, helping the model for estimating  $q_{act}$ .

The paradigm used here features trials with varying time between onsets. With 30s between the end of one trial and the start of the next, it is expected that the vasculature may not recover fully. As a result, the subsequent trial's BOLD response may be attenuated, not being in the same state as for a trial with longer to recover. The original paradigm was designed without foreseeing the hyperoxia BOLD signal drift, so would have been treated as a block of two trials, repeated at normoxia and hyperoxia. To justify the analysis used here, there seems to be no significant difference in the shape or size of the two consecutive trials in each normoxia period. This is not ideal and is addressed in the last two subjects, where the trial length is fixed at 90s throughout. This

needs to be considered in the paradigm design for future studies.

The concept of comparing an event both at normoxia and hyperoxia requires the assumption that the event is identical for both repeats. This will not be the case, as the subject might relax during the course of the experiment, or experience some training through the repeats, so may perform the task differently. The design of two repeats of normoxia and hyperoxia is designed to minimise the effect of any systematic change in task performance over time. Some of the variability in task performance could be reduced by changing the task, for example to a sensory stimulus. The motor task was chosen as being simple to set up and implement in the scanner environment alongside the respiratory paradigm. The problem of task variability also applies to the subsequent ASL measurement. This can be solved through simultaneous BOLD and ASL measurement.

The method for estimating  $q_{act}$  has been designed to work at 7 T. At the clinically accessible field strengths of 1.5 T and 3 T, some modifications need to be made to the assumptions. At these field strengths, the intravascular contribution to BOLD signal becomes significant. An extra compartment is needed in the BOLD signal model to account for this, which makes it more complicated. An alternative might be to suppress the intravascular signal component using bipolar diffusion gradients. The extravascular BOLD signal at these field strengths gains a significant diffusive component. The assumption of static spin dephasing to describe transverse relaxation is no longer reasonable. This means that the relationship between  $R_2^*$  and  $Q$  is no longer linear. When not in the static dephasing regime, this relationship is complicated, but has been the subject of much investigation using Monte Carlo simulations [27, 28, 31]. The approach from the existing calibrated BOLD model [69] is to use a supralinear relationship, relating  $R_2^*$  and  $Q$  by the power  $\beta$  (*section 2.4.5*). A similar supralinear relationship could be adopted here.

## 6.8 Conclusion

This chapter has considered the use of hyperoxic BOLD contrast to assess cerebral vascular properties. A new approach was proposed and implemented, which uses hyperoxic BOLD contrast to estimate the relative changes in venous blood oxygenation and venous CBV during a motor task. By the extension of an ASL measurement, the relative change in  $CMRO_2$  was estimated. To assess the validity of this method, the effect of presenting hyperoxia on cerebral vasculature and on local magnetic properties was considered. The effect of increased oxygen in the oral cavity on field homogeneity was assessed as a possible confound to BOLD measurements. Although there was a small shift in voxel position, as long as the region of interest is not neighbouring the frontal sinus, there should not be a significant effect on the GE EPI signal. This opens the possibility for using hyperoxia as a tool for investigating the venous role in the BOLD signal. An experiment to implement the new approach resulted in measured changes in  $CMRO_2$  which agreed with other methods, but with less assumptions than those methods.

# Chapter 7

## Conclusions

This thesis has explored the haemodynamic behaviour underlying the BOLD signal, with the goal of working towards a more quantitative measurement which more closely represents the underlying neuronal activity. This chapter provides a summary of the work presented.

The field strength dependence of BOLD temporal characteristics has been investigated using a short (5 s) visual stimulus. The objective of this work was to use the relative change in sensitivity of the BOLD signal with field strength to contributions from small and large blood vessels to investigate their temporal characteristics. The main finding from this experiment is that increased field strength lead to a faster onset of the BOLD response to the visual stimulus. This is consistent with an earlier response from the small blood vessel BOLD signal component, compared to that from larger blood vessels, which are typically more distant from the region of neuronal activity. Future work will focus on using this data to test and improve existing models [114, 97, 106].

The dependence of transverse relaxation on level of hypercapnia (a global cerebral vasodilator) has been investigated at 3 Tesla and 7 Tesla, finding a tight linear relationship. An approximately linear increase in the change in transverse relaxation due to hypercapnia with field strength was found, a result which can be used to improve calibrated BOLD calculations. In another experiment, the BOLD response to hypercapnia was measured in the left and

right precentral gyri, finding a significant difference between these two regions. This suggests a vascular asymmetry, which will affect the interpretation of the BOLD response to a motor task in these regions. A future objective will be to investigate the source of this vascular asymmetry, which could provide a valuable contribution towards the understanding of brain development.

A new approach to BOLD calibration has been proposed, where a task is performed both at normoxia and hyperoxia. The main advantage of this approach over previous methods is that this approach does not assume a poorly characterised relationship between CBF and CBV. The effect of hyperoxia on haemodynamic and magnetic properties affecting the BOLD signal has been considered, in order to assess the viability of this approach. In particular, an experiment was performed to assess the effect on the EPI data of changes in field homogeneity due to changes in oxygen content in the nasal cavity and frontal sinuses. This experiment found that only the regions immediately adjacent to the nasal cavity and frontal sinuses (the orbitofrontal cortex, for example) will experience a significant change in EPI signal, whereas the effect will be negligible for the primary motor and visual cortices. The new BOLD calibration approach was implemented to assess the oxygen metabolism and venous blood oxygenation changes due to a motor task, finding values for oxygen metabolism which are consistent with the literature. Future work will focus on applications of this new approach and on a comparison with existing BOLD calibration techniques [69, 172].

Although fMRI (BOLD in particular) techniques have become widely used in the fields of psychology and neuroscience, the indirect nature of such techniques to the underlying neuronal activity restricts the conclusions that can be formed and currently limits the clinical applications of these techniques. It is hoped that the work presented here may contribute towards forming a more quantitative BOLD approach, which has a closer relationship to the underlying neuronal activity, whilst preserving the advantages of the BOLD technique, such as high SNR and spatial resolution.

# Bibliography

- [1] S. Ogawa, D. W. Tank, R. Menon, J. M. Ellermann, S. G. Kim, H. Merkle, and K. Ugurbil, “Intrinsic signal changes accompanying sensory stimulation: functional brain mapping with magnetic resonance imaging.,” *Proc Natl Acad Sci U S A*, vol. 89, pp. 5951–5955, Jul 1992.
- [2] K. K. Kwong, J. W. Belliveau, D. A. Chesler, I. E. Goldberg, R. M. Weisskoff, B. P. Poncelet, D. N. Kennedy, B. E. Hoppel, M. S. Cohen, and R. Turner, “Dynamic magnetic resonance imaging of human brain activity during primary sensory stimulation.,” *Proc Natl Acad Sci U S A*, vol. 89, pp. 5675–5679, Jun 1992.
- [3] R. Turner, “How much cortex can a vein drain? downstream dilution of activation-related cerebral blood oxygenation changes.,” *Neuroimage*, vol. 16, pp. 1062–1067, Aug 2002.
- [4] M. H. Levitt, *Spin Dynamics: Basics of Nuclear Magnetic Resonance*. Wiley: Chichester, UK, 2008.
- [5] I. Rabi, J. Zacharias, S. Millman, and P. Kusch, “A new method of measuring nuclear magnetic moments,” *Phys. Rev.*, vol. 53, p. 318, 1938.
- [6] E. M. Purcell, H. C. Torrey, and R. V. Pound, “Resonance absorption by nuclear magnetic moments in a solid,” *Phys. Rev.*, vol. 53, pp. 37–38, 1946.
- [7] F. Bloch, “Nuclear induction,” *Phys Rev*, vol. 70, pp. 460–474, 1946.

- [8] N. Bloembergen, E. M. Purcell, and R. V. Pound, “Relaxation effects in nuclear magnetic resonance absorption,” *Phys Rev*, vol. 73, pp. 679–712, 1948.
- [9] P. J. Wright, O. E. Mougin, J. J. Totman, A. M. Peters, M. J. Brookes, R. Coxon, P. E. Morris, M. Clemence, S. T. Francis, R. W. Bowtell, and P. A. Gowland, “Water proton T1 measurements in brain tissue at 7, 3, and 1.5 T using IR-EPI, IR-TSE, and MPRAGE: results and optimization.,” *MAGMA*, vol. 21, pp. 121–130, Mar 2008.
- [10] E. F. Cox and P. A. Gowland, “Simultaneous quantification of T2 and T2’ using a combined gradient echo-spin echo sequence at ultrahigh field.,” *Magn Reson Med*, vol. 64, pp. 1440–1445, Nov 2010.
- [11] P. C. Lauterbur, “Image formation by induced local interactions. Examples employing magnetic resonance,” *Nature*, vol. 243, pp. 190–191, 1973.
- [12] P. Mansfield and P. Grannell, “NMR ‘diffraction’ in solids,” *J. Phys. C: Solid State Phys.*, vol. 6, pp. L422–L426, 1973.
- [13] P. T. Callaghan, *Principles of Nuclear Magnetic Resonance Microscopy*. Oxford University Press: New York, 1991.
- [14] E. M. Haacke, R. W. Brown, M. R. Thompson, and R. Venkatesan, *Magnetic Resonance Imaging: Physical Principles and Sequence Design*. Wiley: New York, USA, 1999.
- [15] P. Jezzard and R. S. Balaban, “Correction for geometric distortion in echo planar images from B0 field variations.,” *Magn Reson Med*, vol. 34, pp. 65–73, Jul 1995.
- [16] S. Posse, S. Wiese, D. Gembris, K. Mathiak, C. Kessler, M. L. Grosse-Ruyken, B. Elghahwagi, T. Richards, S. R. Dager, and V. G. Kiselev, “Enhancement of BOLD-contrast sensitivity by single-shot multi-echo functional MR imaging.,” *Magn Reson Med*, vol. 42, pp. 87–97, Jul 1999.

- [17] H. Y. Carr and E. M. Purcell, “Effects of diffusion on free precession in nuclear magnetic resonance experiments,” *Phys Rev*, vol. 94, pp. 630–638, 1954.
- [18] S. Meiboom and D. Gill, “Modified spin echo method for measuring nuclear relaxation times,” *Rev Sci Instrum*, vol. 29, pp. 688–691, 1958.
- [19] K. P. Pruessmann, M. Weiger, M. B. Scheidegger, and P. Boesiger, “SENSE: sensitivity encoding for fast MRI,” *Magn Reson Med*, vol. 42, pp. 952–962, Nov 1999.
- [20] J. B. M. Goense and N. K. Logothetis, “Neurophysiology of the BOLD fMRI signal in awake monkeys,” *Curr Biol*, vol. 18, pp. 631–640, May 2008.
- [21] D. L. Rothman, N. R. Sibson, F. Hyder, J. Shen, K. L. Behar, and R. G. Shulman, “In vivo nuclear magnetic resonance spectroscopy studies of the relationship between the glutamate-glutamine neurotransmitter cycle and functional neuroenergetics,” *Philos Trans R Soc Lond B Biol Sci*, vol. 354, pp. 1165–1177, Jul 1999.
- [22] D. Attwell and C. Iadecola, “The neural basis of functional brain imaging signals,” *Trends Neurosci*, vol. 25, pp. 621–625, Dec 2002.
- [23] E. Rostrup, G. M. Knudsen, I. Law, S. Holm, H. B. W. Larsson, and O. B. Paulson, “The relationship between cerebral blood flow and volume in humans,” *Neuroimage*, vol. 24, pp. 1–11, Jan 2005.
- [24] P. T. Fox and M. E. Raichle, “Focal physiological uncoupling of cerebral blood flow and oxidative metabolism during somatosensory stimulation in human subjects,” *Proc Natl Acad Sci U S A*, vol. 83, pp. 1140–1144, Feb 1986.
- [25] W. M. Spees, D. A. Yablonskiy, M. C. Oswood, and J. J. Ackerman, “Water proton MR properties of human blood at 1.5 tesla: magnetic susceptibility, T1, T2, T2\*, and non-Lorentzian signal behavior,” *Magn Reson Med*, vol. 45, pp. 533–542, Apr 2001.

- [26] C. R. Fisel, J. L. Ackerman, R. B. Buxton, L. Garrido, J. W. Belliveau, B. R. Rosen, and T. J. Brady, “MR contrast due to microscopically heterogeneous magnetic susceptibility: numerical simulations and applications to cerebral physiology.,” *Magn Reson Med*, vol. 17, pp. 336–347, Feb 1991.
- [27] S. Ogawa, R. S. Menon, D. W. Tank, S. G. Kim, H. Merkle, J. M. Ellermann, and K. Ugurbil, “Functional brain mapping by blood oxygenation level-dependent contrast magnetic resonance imaging. a comparison of signal characteristics with a biophysical model.,” *Biophys J*, vol. 64, pp. 803–812, Mar 1993.
- [28] R. P. Kennan, J. Zhong, and J. C. Gore, “Intravascular susceptibility contrast mechanisms in tissues.,” *Magn Reson Med*, vol. 31, pp. 9–21, Jan 1994.
- [29] R. M. Weisskoff, C. S. Zuo, J. L. Boxerman, and B. R. Rosen, “Microscopic susceptibility variation and transverse relaxation: theory and experiment.,” *Magn Reson Med*, vol. 31, pp. 601–610, Jun 1994.
- [30] D. A. Yablonskiy and E. M. Haacke, “Theory of NMR signal behavior in magnetically inhomogeneous tissues: the static dephasing regime.,” *Magn Reson Med*, vol. 32, pp. 749–763, Dec 1994.
- [31] J. L. Boxerman, L. M. Hamberg, B. R. Rosen, and R. M. Weisskoff, “MR contrast due to intravascular magnetic susceptibility perturbations.,” *Magn Reson Med*, vol. 34, pp. 555–566, Oct 1995.
- [32] J. P. Marques and R. W. Bowtell, “Using forward calculations of the magnetic field perturbation due to a realistic vascular model to explore the BOLD effect.,” *NMR Biomed*, vol. 21, pp. 553–565, Jul 2008.
- [33] J. Martindale, A. J. Kennerley, D. Johnston, Y. Zheng, and J. E. Mayhew, “Theory and generalization of Monte Carlo models of the BOLD signal source.,” *Magn Reson Med*, vol. 59, pp. 607–618, Mar 2008.

- [34] D. Li, Y. Wang, and D. J. Waight, “Blood oxygen saturation assessment in vivo using T2\* estimation.,” *Magn Reson Med*, vol. 39, pp. 685–690, May 1998.
- [35] X. Hu, T. H. Le, and K. Ugurbil, “Evaluation of the early response in fMRI in individual subjects using short stimulus duration.,” *Magn Reson Med*, vol. 37, pp. 877–884, Jun 1997.
- [36] E. Yacoub, A. Shmuel, J. Pfeuffer, P. F. V. D. Moortele, G. Adriany, K. Ugurbil, and X. Hu, “Investigation of the initial dip in fMRI at 7 tesla.,” *NMR Biomed*, vol. 14, no. 7-8, pp. 408–412, 2001.
- [37] B. Stefanovic, J. M. Warnking, and G. B. Pike, “Hemodynamic and metabolic responses to neuronal inhibition.,” *Neuroimage*, vol. 22, pp. 771–778, Jun 2004.
- [38] J. M. Newton, A. Sunderland, and P. A. Gowland, “fMRI signal decreases in ipsilateral primary motor cortex during unilateral hand movements are related to duration and side of movement.,” *Neuroimage*, vol. 24, pp. 1080–1087, Feb 2005.
- [39] A. Shmuel, E. Yacoub, J. Pfeuffer, P. F. V. de Moortele, G. Adriany, X. Hu, and K. Ugurbil, “Sustained negative BOLD, blood flow and oxygen consumption response and its coupling to the positive response in the human brain.,” *Neuron*, vol. 36, pp. 1195–1210, Dec 2002.
- [40] J. B. Mandeville, J. J. Marota, B. E. Kosofsky, J. R. Keltner, R. Weissleder, B. R. Rosen, and R. M. Weisskoff, “Dynamic functional imaging of relative cerebral blood volume during rat forepaw stimulation.,” *Magn Reson Med*, vol. 39, pp. 615–624, Apr 1998.
- [41] J. J. Chen and G. B. Pike, “Origins of the BOLD post-stimulus undershoot.,” *Neuroimage*, vol. 46, pp. 559–568, Jul 2009.
- [42] J. Frahm, J. Baudewig, K. Kallenberg, A. Kastrup, K. D. Merboldt, and P. Dechent, “The post-stimulation undershoot in BOLD fMRI of human brain is not caused by elevated cerebral blood volume.,” *Neuroimage*, vol. 40, pp. 473–481, Apr 2008.

- [43] M. J. Donahue, R. D. Stevens, M. de Boorder, J. J. Pekar, J. Hendrikse, and P. C. M. van Zijl, “Hemodynamic changes after visual stimulation and breath holding provide evidence for an uncoupling of cerebral blood flow and volume from oxygen metabolism.,” *J Cereb Blood Flow Metab*, vol. 29, pp. 176–185, Jan 2009.
- [44] H. Lu, X. Golay, J. J. Pekar, and P. C. M. V. Zijl, “Sustained poststimulus elevation in cerebral oxygen utilization after vascular recovery.,” *J Cereb Blood Flow Metab*, vol. 24, pp. 764–770, Jul 2004.
- [45] P. Dechent, G. Schutze, G. Helms, K. D. Merboldt, and J. Frahm, “Basal cerebral blood volume during the poststimulation undershoot in BOLD MRI of the human brain.,” *J Cereb Blood Flow Metab*, vol. 31, pp. 82–89, Jan 2011.
- [46] S. Sadaghiani, K. Ugurbil, and K. Uludag, “Neural activity-induced modulation of BOLD poststimulus undershoot independent of the positive signal.,” *Magn Reson Imaging*, vol. 27, pp. 1030–1038, Oct 2009.
- [47] F. Zhao, T. Jin, P. Wang, and S.-G. Kim, “Improved spatial localization of post-stimulus BOLD undershoot relative to positive BOLD.,” *Neuroimage*, vol. 34, pp. 1084–1092, Feb 2007.
- [48] G. M. Boynton, S. A. Engel, G. H. Glover, and D. J. Heeger, “Linear systems analysis of functional magnetic resonance imaging in human v1.,” *J Neurosci*, vol. 16, pp. 4207–4221, Jul 1996.
- [49] K. J. Friston, P. Fletcher, O. Josephs, A. Holmes, M. D. Rugg, and R. Turner, “Event-related fMRI: characterizing differential responses.,” *Neuroimage*, vol. 7, pp. 30–40, Jan 1998.
- [50] G. H. Glover, “Deconvolution of impulse response in event-related BOLD fMRI.,” *Neuroimage*, vol. 9, pp. 416–429, Apr 1999.
- [51] G. H. Glover, T. Q. Li, and D. Ress, “Image-based method for retrospective correction of physiological motion effects in fMRI: RETROICOR.,” *Magn Reson Med*, vol. 44, pp. 162–167, Jul 2000.

- [52] J. Hulvershorn, L. Bloy, E. E. Gualtieri, J. S. Leigh, and M. A. Elliott, “Spatial sensitivity and temporal response of spin echo and gradient echo bold contrast at 3 T using peak hemodynamic activation time.,” *Neuroimage*, vol. 24, pp. 216–223, Jan 2005.
- [53] C. Schwarzbauer and D. A. Porter, “Single shot partial dual echo (spade) EPI—an efficient acquisition scheme for reducing susceptibility artefacts in fMRI.,” *Neuroimage*, vol. 49, pp. 2234–2237, Feb 2010.
- [54] S. G. Kim, “Quantification of relative cerebral blood flow change by flow-sensitive alternating inversion recovery (FAIR) technique: application to functional mapping.,” *Magn Reson Med*, vol. 34, pp. 293–301, Sep 1995.
- [55] J. A. Detre, J. S. Leigh, D. S. Williams, and A. P. Koretsky, “Perfusion imaging.,” *Magn Reson Med*, vol. 23, pp. 37–45, Jan 1992.
- [56] D. S. Williams, J. A. Detre, J. S. Leigh, and A. P. Koretsky, “Magnetic resonance imaging of perfusion using spin inversion of arterial water.,” *Proc Natl Acad Sci U S A*, vol. 89, pp. 212–216, Jan 1992.
- [57] R. R. Edelman, B. Siewert, D. G. Darby, V. Thangaraj, A. C. Nobre, M. M. Mesulam, and S. Warach, “Qualitative mapping of cerebral blood flow and functional localization with echo-planar mr imaging and signal targeting with alternating radio frequency.,” *Radiology*, vol. 192, pp. 513–520, Aug 1994.
- [58] E. C. Wong, R. B. Buxton, and L. R. Frank, “Implementation of quantitative perfusion imaging techniques for functional brain mapping using pulsed arterial spin labeling.,” *NMR Biomed*, vol. 10, no. 4-5, pp. 237–249, 1997.
- [59] E. C. Wong, R. B. Buxton, and L. R. Frank, “Quantitative imaging of perfusion using a single subtraction (QUIPSS and QUIPSS II).,” *Magn Reson Med*, vol. 39, pp. 702–708, May 1998.
- [60] O. Leontiev, D. J. Dubowitz, and R. B. Buxton, “CBF/CMRO<sub>2</sub> coupling measured with calibrated BOLD fMRI: sources of bias.,” *Neuroimage*, vol. 36, pp. 1110–1122, Jul 2007.

- [61] J. W. Belliveau, D. N. Kennedy, R. C. McKinstry, B. R. Buchbinder, R. M. Weisskoff, M. S. Cohen, J. M. Vevea, T. J. Brady, and B. R. Rosen, “Functional mapping of the human visual cortex by magnetic resonance imaging.,” *Science*, vol. 254, pp. 716–719, Nov 1991.
- [62] H. Lu, X. Golay, J. J. Pekar, and P. C. M. V. Zijl, “Functional magnetic resonance imaging based on changes in vascular space occupancy.,” *Magn Reson Med*, vol. 50, pp. 263–274, Aug 2003.
- [63] B. Stefanovic and G. B. Pike, “Venous refocusing for volume estimation: VERVE functional magnetic resonance imaging.,” *Magn Reson Med*, vol. 53, pp. 339–347, Feb 2005.
- [64] A. Darqui, J. B. Poline, C. Poupon, H. Saint-Jalmes, and D. L. Bihan, “Transient decrease in water diffusion observed in human occipital cortex during visual stimulation.,” *Proc Natl Acad Sci U S A*, vol. 98, pp. 9391–9395, Jul 2001.
- [65] D. L. Bihan, S. ichi Urayama, T. Aso, T. Hanakawa, and H. Fukuyama, “Direct and fast detection of neuronal activation in the human brain with diffusion MRI.,” *Proc Natl Acad Sci U S A*, vol. 103, pp. 8263–8268, May 2006.
- [66] K. L. Miller, D. P. Bulte, H. Devlin, M. D. Robson, R. G. Wise, M. W. Woolrich, P. Jezzard, and T. E. J. Behrens, “Evidence for a vascular contribution to diffusion FMRI at high b value.,” *Proc Natl Acad Sci U S A*, vol. 104, pp. 20967–20972, Dec 2007.
- [67] D. M. Mandell, J. S. Han, J. Poublanc, A. P. Crawley, J. A. Stainsby, J. A. Fisher, and D. J. Mikulis, “Mapping cerebrovascular reactivity using blood oxygen level-dependent MRI in patients with arterial stenocclusive disease: comparison with arterial spin labeling MRI.,” *Stroke*, vol. 39, pp. 2021–2028, Jul 2008.
- [68] A. I. Holodny, M. Schulder, W. C. Liu, J. Wolko, J. A. Maldjian, and A. J. Kalnin, “The effect of brain tumors on BOLD functional MR

imaging activation in the adjacent motor cortex: implications for image-guided neurosurgery.” *AJNR Am J Neuroradiol*, vol. 21, pp. 1415–1422, Sep 2000.

- [69] T. L. Davis, K. K. Kwong, R. M. Weisskoff, and B. R. Rosen, “Calibrated functional MRI: mapping the dynamics of oxidative metabolism.” *Proc Natl Acad Sci U S A*, vol. 95, pp. 1834–1839, Feb 1998.
- [70] R. L. Grubb, M. E. Raichle, J. O. Eichling, and M. M. Ter-Pogossian, “The effects of changes in PaCO<sub>2</sub> on cerebral blood volume, blood flow, and vascular mean transit time.” *Stroke*, vol. 5, no. 5, pp. 630–639, 1974.
- [71] Y. Kong, Y. Zheng, D. Johnston, J. Martindale, M. Jones, S. Billings, and J. Mayhew, “A model of the dynamic relationship between blood flow and volume changes during brain activation.” *J Cereb Blood Flow Metab*, vol. 24, pp. 1382–1392, Dec 2004.
- [72] I. Kida, D. L. Rothman, and F. Hyder, “Dynamics of changes in blood flow, volume, and oxygenation: implications for dynamic functional magnetic resonance imaging calibration.” *J Cereb Blood Flow Metab*, vol. 27, pp. 690–696, Apr 2007.
- [73] S. P. Lee, T. Q. Duong, G. Yang, C. Iadecola, and S. G. Kim, “Relative changes of cerebral arterial and venous blood volumes during increased cerebral blood flow: implications for BOLD fMRI.” *Magn Reson Med*, vol. 45, pp. 791–800, May 2001.
- [74] T. Kim, K. S. Hendrich, K. Masamoto, and S.-G. Kim, “Arterial versus total blood volume changes during neural activity-induced cerebral blood flow change: implication for BOLD fMRI.” *J Cereb Blood Flow Metab*, vol. 27, pp. 1235–1247, Jun 2007.
- [75] J. J. Chen and G. B. Pike, “BOLD-specific cerebral blood volume and blood flow changes during neuronal activation in humans.” *NMR Biomed*, vol. 22, pp. 1054–1062, Dec 2009.

- [76] J. J. Chen and G. B. Pike, "MRI measurement of the BOLD-specific flow-volume relationship during hypercapnia and hypocapnia in humans.," *Neuroimage*, vol. 53, pp. 383–391, Nov 2010.
- [77] R. D. Hoge, J. Atkinson, B. Gill, G. R. Crelier, S. Marrett, and G. B. Pike, "Investigation of BOLD signal dependence on cerebral blood flow and oxygen consumption: the deoxyhemoglobin dilution model.," *Magn Reson Med*, vol. 42, pp. 849–863, Nov 1999.
- [78] P. A. Chiarelli, D. P. Bulte, S. Piechnik, and P. Jezzard, "Sources of systematic bias in hypercapnia-calibrated functional MRI estimation of oxygen metabolism.," *Neuroimage*, vol. 34, pp. 35–43, Jan 2007.
- [79] R. B. Banzett, R. T. Garcia, and S. H. Moosavi, "Simple contrivance "clamps" end-tidal PCO<sub>2</sub> and PO<sub>2</sub> despite rapid changes in ventilation.," *J Appl Physiol*, vol. 88, pp. 1597–1600, May 2000.
- [80] R. B. Somogyi, A. E. Vesely, D. Preiss, E. Prisman, G. Volgyesi, T. Azami, S. Iscoe, J. A. Fisher, and H. Sasano, "Precise control of end-tidal carbon dioxide levels using sequential rebreathing circuits.," *Anaesth Intensive Care*, vol. 33, pp. 726–732, Dec 2005.
- [81] M. Slessarev, J. Han, A. Mardimae, E. Prisman, D. Preiss, G. Volgyesi, C. Ansel, J. Duffin, and J. A. Fisher, "Prospective targeting and control of end-tidal CO<sub>2</sub> and O<sub>2</sub> concentrations.," *J Physiol*, vol. 581, pp. 1207–1219, Jun 2007.
- [82] R. D. Dripps and J. H. Comroe, "The respiratory and circulatory response of normal man to inhalation of 7.6 and 10.4 per cent CO<sub>2</sub> with a comparison of the maximal ventilation produced by severe muscular exercise, inhalation of CO<sub>2</sub> and maximal voluntary hyperventilation.," *Am J Physiol*, vol. 149, pp. 43–51, Apr 1947.
- [83] D. R. Gitelman, I. Prohovnik, and T. K. Tatemichi, "Safety of hypercapnic challenge: cardiovascular and neurologic considerations.," *J Cereb Blood Flow Metab*, vol. 11, pp. 1036–1040, Nov 1991.

- [84] S. W. Woods, D. S. Charney, W. K. Goodman, and G. R. Heninger, "Carbon dioxide-induced anxiety. behavioral, physiologic, and biochemical effects of carbon dioxide in patients with panic disorders and healthy subjects.," *Arch Gen Psychiatry*, vol. 45, pp. 43–52, Jan 1988.
- [85] C. J. Lambertsen, R. H. Dough, D. Y. Cooper, G. L. Emmel, H. H. Loeschcke, and C. F. Schmidt, "Oxygen toxicity; effects in man of oxygen inhalation at 1 and 3.5 atmospheres upon blood gas transport, cerebral circulation and cerebral metabolism.," *J Appl Physiol*, vol. 5, pp. 471–486, Mar 1953.
- [86] H. Bitterman, "Bench-to-bedside review: oxygen as a drug.," *Crit Care*, vol. 13, no. 1, p. 205, 2009.
- [87] P. N. Ainslie, S. Ogoh, K. Burgess, L. Celi, K. McGrattan, K. Peebles, C. Murrell, P. Subedi, and K. R. Burgess, "Differential effects of acute hypoxia and high altitude on cerebral blood flow velocity and dynamic cerebral autoregulation: alterations with hyperoxia.," *J Appl Physiol*, vol. 104, pp. 490–498, Feb 2008.
- [88] S. A. Sasse, R. B. Berry, T. K. Nguyen, R. W. Light, and C. K. Mahutte, "Arterial blood gas changes during breath-holding from functional residual capacity.," *Chest*, vol. 110, pp. 958–964, Oct 1996.
- [89] M. G. Bright, D. P. Bulte, P. Jezzard, and J. H. Duyn, "Characterization of regional heterogeneity in cerebrovascular reactivity dynamics using novel hypocapnia task and BOLD fMRI.," *Neuroimage*, vol. 48, pp. 166–175, Oct 2009.
- [90] A. Kastrup, G. Krger, T. Neumann-Haefelin, and M. E. Moseley, "Assessment of cerebrovascular reactivity with functional magnetic resonance imaging: comparison of CO<sub>2</sub> and breath holding.," *Magn Reson Imaging*, vol. 19, pp. 13–20, Jan 2001.
- [91] D. P. Bulte, K. Drescher, and P. Jezzard, "Comparison of hypercapnia-based calibration techniques for measurement of cerebral oxygen

- metabolism with MRI,” *Magn Reson Med*, vol. 61, pp. 391–398, Feb 2009.
- [92] R. G. Wise, K. T. S. Pattinson, D. P. Bulte, P. A. Chiarelli, S. D. Mayhew, G. M. Balanos, D. F. O’Connor, T. R. Pragnell, P. A. Robbins, I. Tracey, and P. Jezzard, “Dynamic forcing of end-tidal carbon dioxide and oxygen applied to functional magnetic resonance imaging,” *J Cereb Blood Flow Metab*, vol. 27, pp. 1521–1532, Aug 2007.
- [93] C. I. Mark, M. Slessarev, S. Ito, J. Han, J. A. Fisher, and G. B. Pike, “Precise control of end-tidal carbon dioxide and oxygen improves BOLD and ASL cerebrovascular reactivity measures,” *Magn Reson Med*, vol. 64, pp. 749–756, Sep 2010.
- [94] T. F. Floyd, J. M. Clark, R. Gelfand, J. A. Detre, S. Ratcliffe, D. Gukavakov, C. J. Lambertsen, and R. G. Eckenhoff, “Independent cerebral vasoconstrictive effects of hyperoxia and accompanying arterial hypocapnia at 1 ATA,” *J Appl Physiol*, vol. 95, pp. 2453–2461, Dec 2003.
- [95] P. A. Robbins, G. D. Swanson, and M. G. Howson, “A prediction-correction scheme for forcing alveolar gases along certain time courses,” *J Appl Physiol*, vol. 52, pp. 1353–1357, May 1982.
- [96] P. A. Robbins, G. D. Swanson, A. J. Micco, and W. P. Schubert, “A fast gas-mixing system for breath-to-breath respiratory control studies,” *J Appl Physiol*, vol. 52, pp. 1358–1362, May 1982.
- [97] J. A. de Zwart, A. C. Silva, P. van Gelderen, P. Kellman, M. Fukunaga, R. Chu, A. P. Koretsky, J. A. Frank, and J. H. Duyn, “Temporal dynamics of the BOLD fMRI impulse response,” *Neuroimage*, vol. 24, pp. 667–677, Feb 2005.
- [98] B. Krasnow, L. Tamm, M. D. Greicius, T. T. Yang, G. H. Glover, A. L. Reiss, and V. Menon, “Comparison of fMRI activation at 3 and 1.5 T during perceptual, cognitive, and affective processing,” *Neuroimage*, vol. 18, pp. 813–826, Apr 2003.

- [99] F. Fera, M. N. Yongbi, P. van Gelderen, J. A. Frank, V. S. Mattay, and J. H. Duyn, “EPI-BOLD fMRI of human motor cortex at 1.5 T and 3.0 T: sensitivity dependence on echo time and acquisition bandwidth.,” *J Magn Reson Imaging*, vol. 19, pp. 19–26, Jan 2004.
- [100] R. Turner, P. Jezzard, H. Wen, K. K. Kwong, D. L. Bihan, T. Zeffiro, and R. S. Balaban, “Functional mapping of the human visual cortex at 4 and 1.5 tesla using deoxygenation contrast EPI.,” *Magn Reson Med*, vol. 29, pp. 277–279, Feb 1993.
- [101] J. S. Gati, R. S. Menon, K. Ugurbil, and B. K. Rutt, “Experimental determination of the BOLD field strength dependence in vessels and tissue.,” *Magn Reson Med*, vol. 38, pp. 296–302, Aug 1997.
- [102] E. Yacoub, A. Shmuel, J. Pfeuffer, P. F. V. D. Moortele, G. Adriany, P. Andersen, J. T. Vaughan, H. Merkle, K. Ugurbil, and X. Hu, “Imaging brain function in humans at 7 Tesla.,” *Magn Reson Med*, vol. 45, pp. 588–594, Apr 2001.
- [103] W. van der Zwaag, S. Francis, K. Head, A. Peters, P. Gowland, P. Morris, and R. Bowtell, “fMRI at 1.5, 3 and 7 T: characterising BOLD signal changes.,” *Neuroimage*, vol. 47, pp. 1425–1434, Oct 2009.
- [104] M. J. Donahue, H. Hoogduin, P. C. M. van Zijl, P. Jezzard, P. R. Luijten, and J. Hendrikse, “Blood oxygenation level-dependent (BOLD) total and extravascular signal changes and  $\Delta R_2^*$  in human visual cortex at 1.5, 3.0 and 7.0 T.,” *NMR Biomed*, vol. 24, pp. 25–34, Jan 2011.
- [105] N. P. Blockley, L. Jiang, A. G. Gardener, C. N. Ludman, S. T. Francis, and P. A. Gowland, “Field strength dependence of  $R_1$  and  $R_2^*$  relaxivities of human whole blood to proance, vasovist, and deoxyhemoglobin.,” *Magn Reson Med*, vol. 60, pp. 1313–1320, Dec 2008.
- [106] K. Uludag, B. Mller-Bierl, and K. Ugurbil, “An integrative model for neuronal activity-induced signal changes for gradient and spin echo functional imaging.,” *Neuroimage*, vol. 48, pp. 150–165, Oct 2009.

- [107] A. W. Song, E. C. Wong, S. G. Tan, and J. S. Hyde, “Diffusion weighted fMRI at 1.5 T.,” *Magn Reson Med*, vol. 35, pp. 155–158, Feb 1996.
- [108] J. L. Boxerman, P. A. Bandettini, K. K. Kwong, J. R. Baker, T. L. Davis, B. R. Rosen, and R. M. Weisskoff, “The intravascular contribution to fMRI signal change: Monte Carlo modeling and diffusion-weighted studies in vivo.,” *Magn Reson Med*, vol. 34, pp. 4–10, Jul 1995.
- [109] C. Triantafyllou, R. D. Hoge, G. Krueger, C. J. Wiggins, A. Potthast, G. C. Wiggins, and L. L. Wald, “Comparison of physiological noise at 1.5 T, 3 T and 7 T and optimization of fMRI acquisition parameters.,” *Neuroimage*, vol. 26, pp. 243–250, May 2005.
- [110] S. K. Piechnik, P. A. Chiarelli, and P. Jezzard, “Modelling vascular reactivity to investigate the basis of the relationship between cerebral blood volume and flow under co2 manipulation.,” *Neuroimage*, vol. 39, pp. 107–118, Jan 2008.
- [111] T. Mildner, D. G. Norris, C. Schwarzbauer, and C. J. Wiggins, “A qualitative test of the balloon model for BOLD-based MR signal changes at 3T.,” *Magn Reson Med*, vol. 46, pp. 891–899, Nov 2001.
- [112] X. Huang, S. Levine, and M. A. Paradiso, “Rebounding v1 activity and a new visual aftereffect.,” *J Vis*, vol. 8, no. 3, pp. 25.1–2510, 2008.
- [113] A. Lemke, B. Stieltjes, L. R. Schad, and F. B. Laun, “Toward an optimal distribution of b values for intravoxel incoherent motion imaging.,” *Magn Reson Imaging*, vol. 29, pp. 766–776, Jul 2011.
- [114] R. B. Buxton, E. C. Wong, and L. R. Frank, “Dynamics of blood flow and oxygenation changes during brain activation: the balloon model.,” *Magn Reson Med*, vol. 39, pp. 855–864, Jun 1998.
- [115] F. H. R. van der Zande, P. A. M. Hofman, and W. H. Backes, “Mapping hypercapnia-induced cerebrovascular reactivity using BOLD MRI.,” *Neuroradiology*, vol. 47, pp. 114–120, Feb 2005.

- [116] S. Ito, A. Mardimae, J. Han, J. Duffin, G. Wells, L. Fedorko, L. Minkovich, R. Katznelson, M. Meineri, T. Arenovich, C. Kessler, and J. A. Fisher, “Non-invasive prospective targeting of arterial p(co2) in subjects at rest.,” *J Physiol*, vol. 586, pp. 3675–3682, Aug 2008.
- [117] S. S. Kety and C. F. Schmidt, “The effects of altered arterial tensions of carbon dioxide and oxygen on cerebral blood flow and cerebral oxygen consumption of normal young men.,” *J Clin Invest*, vol. 27, pp. 484–492, Jul 1948.
- [118] M. Reivich, “Arterial PCO2 and cerebral hemodynamics.,” *Am J Physiol*, vol. 206, pp. 25–35, Jan 1964.
- [119] H. Ito, I. Kanno, M. Ibaraki, J. Hatazawa, and S. Miura, “Changes in human cerebral blood flow and cerebral blood volume during hypercapnia and hypocapnia measured by positron emission tomography.,” *J Cereb Blood Flow Metab*, vol. 23, pp. 665–670, Jun 2003.
- [120] U. Noeth, G. E. Meadows, F. Kotajima, R. Deichmann, D. R. Corfield, and R. Turner, “Cerebral vascular response to hypercapnia: determination with perfusion MRI at 1.5 and 3.0 tesla using a pulsed arterial spin labeling technique.,” *J Magn Reson Imaging*, vol. 24, pp. 1229–1235, Dec 2006.
- [121] U. Noeth, F. Kotajima, R. Deichmann, R. Turner, and D. R. Corfield, “Mapping of the cerebral vascular response to hypoxia and hypercapnia using quantitative perfusion MRI at 3 T.,” *NMR Biomed*, vol. 21, pp. 464–472, Jun 2008.
- [122] J. M. Pollock, A. R. Deibler, C. T. Whitlow, H. Tan, R. A. Kraft, J. H. Burdette, and J. A. Maldjian, “Hypercapnia-induced cerebral hyperperfusion: an underrecognized clinical entity.,” *AJNR Am J Neuroradiol*, vol. 30, pp. 378–385, Feb 2009.
- [123] Y.-C. L. Ho, E. T. Petersen, I. Zimine, and X. Golay, “Similarities and differences in arterial responses to hypercapnia and visual stimulation.,” *J Cereb Blood Flow Metab*, vol. 31, pp. 560–571, Feb 2011.

- [124] J. J. Chen and G. B. Pike, “Global cerebral oxidative metabolism during hypercapnia and hypocapnia in humans: implications for BOLD fMRI,” *J Cereb Blood Flow Metab*, vol. 30, pp. 1094–1099, Jun 2010.
- [125] F. Xu, J. Uh, M. R. Brier, J. Hart, U. S. Yezhuvath, H. Gu, Y. Yang, and H. Lu, “The influence of carbon dioxide on brain activity and metabolism in conscious humans.,” *J Cereb Blood Flow Metab*, vol. 31, pp. 58–67, Jan 2011.
- [126] J. Cohen-Adad, C. J. Gauthier, J. C. W. Brooks, M. Slessarev, J. Han, J. A. Fisher, S. Rossignol, and R. D. Hoge, “BOLD signal responses to controlled hypercapnia in human spinal cord.,” *Neuroimage*, vol. 50, pp. 1074–1084, Apr 2010.
- [127] S. Aslan, F. Xu, P. L. Wang, J. Uh, U. S. Yezhuvath, M. van Osch, and H. Lu, “Estimation of labeling efficiency in pseudocontinuous arterial spin labeling.,” *Magn Reson Med*, vol. 63, pp. 765–771, Mar 2010.
- [128] S. G. Kim, E. Rostrup, H. B. Larsson, S. Ogawa, and O. B. Paulson, “Determination of relative CMRO<sub>2</sub> from CBF and BOLD changes: significant increase of oxygen consumption rate during visual stimulation.,” *Magn Reson Med*, vol. 41, pp. 1152–1161, Jun 1999.
- [129] C. Schwarzbauer and W. Heinke, “Investigating the dependence of bold contrast on oxidative metabolism.,” *Magn Reson Med*, vol. 41, pp. 537–543, Mar 1999.
- [130] R. G. Wise, K. Ide, M. J. Poulin, and I. Tracey, “Resting fluctuations in arterial carbon dioxide induce significant low frequency variations in BOLD signal.,” *Neuroimage*, vol. 21, pp. 1652–1664, Apr 2004.
- [131] P.-F. V. de Moortele, J. Pfeuffer, G. H. Glover, K. Ugurbil, and X. Hu, “Respiration-induced B<sub>0</sub> fluctuations and their spatial distribution in the human brain at 7 tesla.,” *Magn Reson Med*, vol. 47, pp. 888–895, May 2002.

- [132] R. M. Birn, J. B. Diamond, M. A. Smith, and P. A. Bandettini, “Separating respiratory-variation-related fluctuations from neuronal-activity-related fluctuations in fMRI,” *Neuroimage*, vol. 31, pp. 1536–1548, Jul 2006.
- [133] C. Chang and G. H. Glover, “Relationship between respiration, end-tidal CO<sub>2</sub>, and BOLD signals in resting-state fMRI,” *Neuroimage*, vol. 47, pp. 1381–1393, Oct 2009.
- [134] K. T. S. Pattinson, G. D. Mitsis, A. K. Harvey, S. Jbabdi, S. Dirckx, S. D. Mayhew, R. Rogers, I. Tracey, and R. G. Wise, “Determination of the human brainstem respiratory control network and its cortical connections in vivo using functional and structural imaging,” *Neuroimage*, vol. 44, pp. 295–305, Jan 2009.
- [135] L. C. McKay, K. C. Evans, R. S. J. Frackowiak, and D. R. Corfield, “Neural correlates of voluntary breathing in humans,” *J Appl Physiol*, vol. 95, pp. 1170–1178, Sep 2003.
- [136] P. A. Bandettini and E. C. Wong, “A hypercapnia-based normalization method for improved spatial localization of human brain activation with fMRI,” *NMR Biomed*, vol. 10, no. 4-5, pp. 197–203, 1997.
- [137] E. R. Cohen, E. Rostrup, K. Sidaros, T. E. Lund, O. B. Paulson, K. Ugurbil, and S.-G. Kim, “Hypercapnic normalization of BOLD fMRI: comparison across field strengths and pulse sequences,” *Neuroimage*, vol. 23, pp. 613–624, Oct 2004.
- [138] J. Liau and T. T. Liu, “Inter-subject variability in hypercapnic normalization of the BOLD fMRI response,” *Neuroimage*, vol. 45, pp. 420–430, Apr 2009.
- [139] D. R. Corfield, K. Murphy, O. Josephs, L. Adams, and R. Turner, “Does hypercapnia-induced cerebral vasodilation modulate the hemodynamic response to neural activation?,” *Neuroimage*, vol. 13, pp. 1207–1211, Jun 2001.

- [140] L. J. Kemna and S. Posse, “Effect of respiratory CO<sub>2</sub> changes on the temporal dynamics of the hemodynamic response in functional MR imaging,” *Neuroimage*, vol. 14, pp. 642–649, Sep 2001.
- [141] S. Posse, L. J. Kemna, B. Elghahwagi, S. Wiese, and V. G. Kiselev, “Effect of graded hypo- and hypercapnia on fMRI contrast in visual cortex: quantification of T<sub>2</sub>\* changes by multiecho EPI,” *Magn Reson Med*, vol. 46, pp. 264–271, Aug 2001.
- [142] E. R. Cohen, K. Ugurbil, and S.-G. Kim, “Effect of basal conditions on the magnitude and dynamics of the blood oxygenation level-dependent fMRI response,” *J Cereb Blood Flow Metab*, vol. 22, pp. 1042–1053, Sep 2002.
- [143] A. L. Vazquez, E. R. Cohen, V. Gulani, L. Hernandez-Garcia, Y. Zheng, G. R. Lee, S.-G. Kim, J. B. Grotberg, and D. C. Noll, “Vascular dynamics and BOLD fMRI: CBF level effects and analysis considerations,” *Neuroimage*, vol. 32, pp. 1642–1655, Oct 2006.
- [144] Y. J. Liu, C. J. Juan, C. Y. Chen, C. Y. Wang, M. L. Wu, C. P. Lo, M. C. Chou, T. Y. Huang, H. Chang, C. H. Chu, and M. H. Li, “Are the local blood oxygen level-dependent (BOLD) signals caused by neural stimulation response dependent on global BOLD signals induced by hypercapnia in the functional MR imaging experiment? experiments of long-duration hypercapnia and multilevel carbon dioxide concentration,” *AJNR Am J Neuroradiol*, vol. 28, no. 6, pp. 1009–1014, 2007.
- [145] A. C. Zappe, K. Uludag, and N. K. Logothetis, “Direct measurement of oxygen extraction with fMRI using 6vol. 26, pp. 961–967, Sep 2008.
- [146] J. Sedlacik, C. Kutschbach, A. Rauscher, A. Deistung, and J. R. Reichenbach, “Investigation of the influence of carbon dioxide concentrations on cerebral physiology by susceptibility-weighted magnetic resonance imaging (SWI).,” *Neuroimage*, vol. 43, pp. 36–43, Oct 2008.

- [147] S. K. Piechnik, J. Evans, L. H. Bary, R. G. Wise, and P. Jezzard, "Functional changes in CSF volume estimated using measurement of water T2 relaxation.," *Magn Reson Med*, vol. 61, pp. 579–586, Mar 2009.
- [148] T. H. Jochimsen, D. Ivanov, D. V. M. Ott, W. Heinke, R. Turner, H. E. Mller, and J. R. Reichenbach, "Whole-brain mapping of venous vessel size in humans using the hypercapnia-induced BOLD effect.," *Neuroimage*, vol. 51, pp. 765–774, Jun 2010.
- [149] N. P. Blockley, I. D. Driver, S. T. Francis, J. A. Fisher, and P. A. Gowland, "An improved method for acquiring cerebrovascular reactivity maps.," *Magn Reson Med*, vol. 65, pp. 1278–1286, May 2011.
- [150] L. Glodzik, H. Rusinek, M. Brys, W. H. Tsui, R. Switalski, L. Mosconi, R. Mistur, E. Pirraglia, S. de Santi, Y. Li, A. Goldowsky, and M. J. de Leon, "Framingham cardiovascular risk profile correlates with impaired hippocampal and cortical vasoreactivity to hypercapnia.," *J Cereb Blood Flow Metab*, vol. 31, pp. 671–679, Feb 2011.
- [151] S. D. Goode, N. Altaf, D. P. Auer, and S. T. R. MacSweeney, "Carotid endarterectomy improves cerebrovascular reserve capacity preferentially in patients with preoperative impairment as indicated by asymmetric BOLD response to hypercapnia.," *Eur J Vasc Endovasc Surg*, vol. 38, pp. 546–551, Nov 2009.
- [152] D. M. Mandell, J. S. Han, J. Poublanc, A. P. Crawley, A. Kassner, J. A. Fisher, and D. J. Mikulis, "Selective reduction of blood flow to white matter during hypercapnia corresponds with leukoaraiosis.," *Stroke*, vol. 39, pp. 1993–1998, Jul 2008.
- [153] J. Conklin, J. Fierstra, A. P. Crawley, J. S. Han, J. Poublanc, D. M. Mandell, F. L. Silver, M. Tymianski, J. A. Fisher, and D. J. Mikulis, "Impaired cerebrovascular reactivity with steal phenomenon is associated with increased diffusion in white matter of patients with Moyamoya disease.," *Stroke*, vol. 41, pp. 1610–1616, Aug 2010.

- [154] I. Driver, N. Blockley, J. Fisher, S. Francis, and P. Gowland, “The change in cerebrovascular reactivity between 3 T and 7 T measured using graded hypercapnia,” *Neuroimage*, vol. 51, pp. 274–279, May 2010.
- [155] P. Bevington, *Data Reduction and Error Analysis for the Physical Sciences*. McGraw-Hill: New York, 1969.
- [156] P. A. Gowland and R. Bowtell, “Theoretical optimization of multi-echo fMRI data acquisition,” *Phys Med Biol*, vol. 52, pp. 1801–1813, Apr 2007.
- [157] A. M. Peters, M. J. Brookes, F. G. Hoogenraad, P. A. Gowland, S. T. Francis, P. G. Morris, and R. Bowtell, “T2\* measurements in human brain at 1.5, 3 and 7 T.,” *Magn Reson Imaging*, vol. 25, pp. 748–753, Jul 2007.
- [158] E. Prisman, M. Slessarev, J. Han, J. Poublanc, A. Mardimae, A. Crawley, J. Fisher, and D. Mikulis, “Comparison of the effects of independently-controlled end-tidal PCO(2) and PO(2) on blood oxygen level-dependent (BOLD) MRI.,” *J Magn Reson Imaging*, vol. 27, pp. 185–191, Jan 2008.
- [159] J. B. Mandeville, J. J. Marota, C. Ayata, G. Zaharchuk, M. A. Moskowitz, B. R. Rosen, and R. M. Weisskoff, “Evidence of a cerebrovascular postarteriole windkessel with delayed compliance.,” *J Cereb Blood Flow Metab*, vol. 19, pp. 679–689, Jun 1999.
- [160] A. Bertolino, G. Blasi, G. Caforio, V. Latorre, M. D. Candia, V. Rubino, J. H. Callicott, V. S. Mattay, A. Bellomo, T. Scarabino, D. R. Weinberger, and M. Nardini, “Functional lateralization of the sensorimotor cortex in patients with schizophrenia: effects of treatment with olanzapine.,” *Biol Psychiatry*, vol. 56, pp. 190–197, Aug 2004.
- [161] K. Y. Haaland, C. L. Elsinger, A. R. Mayer, S. Durgerian, and S. M. Rao, “Motor sequence complexity and performing hand produce differential patterns of hemispheric lateralization.,” *J Cogn Neurosci*, vol. 16, pp. 621–636, May 2004.

- [162] T. Verstynen, J. Diedrichsen, N. Albert, P. Aparicio, and R. B. Ivry, “Ipsilateral motor cortex activity during unimanual hand movements relates to task complexity.,” *J Neurophysiol*, vol. 93, pp. 1209–1222, Mar 2005.
- [163] M. Gut, A. Urbanik, L. Forsberg, M. Binder, K. Rymarczyk, B. Sobiecka, J. Kozub, and A. Grabowska, “Brain correlates of right-handedness.,” *Acta Neurobiol Exp (Wars)*, vol. 67, no. 1, pp. 43–51, 2007.
- [164] L. Zeng, H. Chen, L. Ouyang, D. Yao, and J.-H. Gao, “Quantitative analysis of asymmetrical cortical activity in motor areas during sequential finger movement.,” *Magn Reson Imaging*, vol. 25, pp. 1370–1375, Dec 2007.
- [165] H. F. Crovitz and K. Zener, “A group-test for assessing hand- and eye-dominance.,” *Am J Psychol*, vol. 75, pp. 271–276, Jun 1962.
- [166] J. E. Black, K. R. Isaacs, B. J. Anderson, A. A. Alcantara, and W. T. Greenough, “Learning causes synaptogenesis, whereas motor activity causes angiogenesis, in cerebellar cortex of adult rats.,” *Proc Natl Acad Sci U S A*, vol. 87, pp. 5568–5572, Jul 1990.
- [167] R. A. Swain, A. B. Harris, E. C. Wiener, M. V. Dutka, H. D. Morris, B. E. Theien, S. Konda, K. Engberg, P. C. Lauterbur, and W. T. Greenough, “Prolonged exercise induces angiogenesis and increases cerebral blood volume in primary motor cortex of the rat.,” *Neuroscience*, vol. 117, no. 4, pp. 1037–1046, 2003.
- [168] E. A. Maguire, D. G. Gadian, I. S. Johnsrude, C. D. Good, J. Ashburner, R. S. Frackowiak, and C. D. Frith, “Navigation-related structural change in the hippocampi of taxi drivers.,” *Proc Natl Acad Sci U S A*, vol. 97, pp. 4398–4403, Apr 2000.
- [169] A. Mechelli, J. T. Crinion, U. Noppeney, J. O’Doherty, J. Ashburner, R. S. Frackowiak, and C. J. Price, “Neurolinguistics: structural plasticity in the bilingual brain.,” *Nature*, vol. 431, p. 757, Oct 2004.

- [170] G. Schlaug, L. Jäncke, Y. Huang, and H. Steinmetz, “In vivo evidence of structural brain asymmetry in musicians,” *Science*, vol. 267, pp. 699–701, Feb 1995.
- [171] S. Ogawa, T. M. Lee, A. S. Nayak, and P. Glynn, “Oxygenation-sensitive contrast in magnetic resonance image of rodent brain at high magnetic fields,” *Magn Reson Med*, vol. 14, pp. 68–78, Apr 1990.
- [172] P. A. Chiarelli, D. P. Bulte, R. Wise, D. Gallichan, and P. Jezzard, “A calibration method for quantitative BOLD fMRI based on hyperoxia,” *Neuroimage*, vol. 37, pp. 808–820, Sep 2007.
- [173] D. Bulte, P. Chiarelli, R. Wise, and P. Jezzard, “Measurement of cerebral blood volume in humans using hyperoxic MRI contrast,” *J Magn Reson Imaging*, vol. 26, pp. 894–899, Oct 2007.
- [174] T. Q. Duong, E. Yacoub, G. Adriany, X. Hu, K. Ugurbil, and S.-G. Kim, “Microvascular BOLD contribution at 4 and 7 T in the human brain: gradient-echo and spin-echo fMRI with suppression of blood effects,” *Magn Reson Med*, vol. 49, pp. 1019–1027, Jun 2003.
- [175] N. P. Blockley, I. D. Driver, S. T. Francis, and P. A. Gowland, “A new method for measuring changes in venous cerebral blood volume using hyperoxia,” in *Proc. Intl. Soc. Mag. Reson. Med. 18, Stockholm, Sweden*, no. 3476, 2010.
- [176] G. Zaharchuk, A. J. Martin, G. Rosenthal, G. T. Manley, and W. P. Dillon, “Measurement of cerebrospinal fluid oxygen partial pressure in humans using mri,” *Magn Reson Med*, vol. 54, pp. 113–121, Jul 2005.
- [177] C. Santosh, D. Brennan, C. McCabe, I. M. Macrae, W. M. Holmes, D. I. Graham, L. Gallagher, B. Condon, D. M. Hadley, K. W. Muir, and W. Gsell, “Potential use of oxygen as a metabolic biosensor in combination with T2\*-weighted MRI to define the ischemic penumbra,” *J Cereb Blood Flow Metab*, vol. 28, pp. 1742–1753, Oct 2008.

- [178] K. A. Dani, C. Santosh, D. Brennan, C. McCabe, W. M. Holmes, B. Condon, D. M. Hadley, I. M. Macrae, M. Shaw, and K. W. Muir, "T2\*-weighted magnetic resonance imaging with hyperoxia in acute ischemic stroke.," *Ann Neurol*, vol. 68, pp. 37–47, Jul 2010.
- [179] J. Schuurings, M. Rijpkema, H. Bernsen, P. Bernsen, R. van der Maazen, J. Kaanders, A. van der Kogel, and A. Heerschap, "Effect of breathing a hyperoxic hypercapnic gas mixture on the oxygenation of meningiomas; preliminary results.," *J Neurooncol*, vol. 57, pp. 127–132, Apr 2002.
- [180] S. P. Robinson, C. Ludwig, J. Paulsson, and A. Ostman, "The effects of tumor-derived platelet-derived growth factor on vascular morphology and function in vivo revealed by susceptibility MRI.," *Int J Cancer*, vol. 122, pp. 1548–1556, Apr 2008.
- [181] M. Neeman, H. Dafni, O. Bukhari, R. D. Braun, and M. W. Dewhirst, "In vivo BOLD contrast MRI mapping of subcutaneous vascular function and maturation: validation by intravital microscopy.," *Magn Reson Med*, vol. 45, pp. 887–898, May 2001.
- [182] H. Lu and Y. Ge, "Quantitative evaluation of oxygenation in venous vessels using T2-relaxation-under-spin-tagging MRI.," *Magn Reson Med*, vol. 60, pp. 357–363, Aug 2008.
- [183] V. Jain, M. C. Langham, and F. W. Wehrli, "MRI estimation of global brain oxygen consumption rate.," *J Cereb Blood Flow Metab*, vol. 30, pp. 1598–1607, Sep 2010.
- [184] G. Zaharchuk, A. J. Martin, and W. P. Dillon, "Noninvasive imaging of quantitative cerebral blood flow changes during 100% oxygen inhalation using arterial spin-labeling MR imaging.," *AJNR Am J Neuroradiol*, vol. 29, pp. 663–667, Apr 2008.
- [185] S. Iscoe and J. A. Fisher, "Hyperoxia-induced hypocapnia: an underappreciated risk.," *Chest*, vol. 128, pp. 430–433, Jul 2005.

- [186] N. A. Watson, S. C. Beards, N. Altaf, A. Kassner, and A. Jackson, “The effect of hyperoxia on cerebral blood flow: a study in healthy volunteers using magnetic resonance phase-contrast angiography,” *Eur J Anaesthesiol*, vol. 17, pp. 152–159, Mar 2000.
- [187] C. Kolbitsch, I. H. Lorenz, C. Hrmann, M. Hinteregger, A. Lckinger, P. L. Moser, C. Kremser, M. Schocke, S. Felber, K. P. Pfeiffer, and A. Benzer, “The influence of hyperoxia on regional cerebral blood flow (rCBF), regional cerebral blood volume (rCBV) and cerebral blood flow velocity in the middle cerebral artery (CBFVMCA) in human volunteers.,” *Magn Reson Imaging*, vol. 20, pp. 535–541, Sep 2002.
- [188] D. P. Bulte, P. A. Chiarelli, R. G. Wise, and P. Jezzard, “Cerebral perfusion response to hyperoxia.,” *J Cereb Blood Flow Metab*, vol. 27, pp. 69–75, Jan 2007.
- [189] J. W. Severinghaus, “Simple, accurate equations for human blood O<sub>2</sub> dissociation computations.,” *J Appl Physiol*, vol. 46, pp. 599–602, Mar 1979.
- [190] E. Rostrup, H. B. Larsson, P. B. Toft, K. Garde, and O. Henriksen, “Signal changes in gradient echo images of human brain induced by hypo- and hyperoxia.,” *NMR Biomed*, vol. 8, pp. 41–47, Feb 1995.
- [191] *CRC Handbook of chemistry and physics*. Boca Raton, FL, USA: CRC Press, 91st ed., 2010.
- [192] B. J. d’Othe, G. Rachmuth, J. Munasinghe, and E. V. Lang, “The effect of hyperoxygenation on T1 relaxation time in vitro.,” *Acad Radiol*, vol. 10, pp. 854–860, Aug 2003.
- [193] E. Tadamura, H. Hatabu, W. Li, P. V. Prasad, and R. R. Edelman, “Effect of oxygen inhalation on relaxation times in various tissues.,” *J Magn Reson Imaging*, vol. 7, no. 1, pp. 220–225, 1997.
- [194] M. D. Noseworthy, J. K. Kim, J. A. Stainsby, G. J. Stanisiz, and G. A. Wright, “Tracking oxygen effects on MR signal in blood and skeletal mus-

- cle during hyperoxia exposure.,” *J Magn Reson Imaging*, vol. 9, pp. 814–820, Jun 1999.
- [195] M. C. Dobre, K. Ugurbil, and M. Marjanska, “Determination of blood longitudinal relaxation time (T1) at high magnetic field strengths.,” *Magn Reson Imaging*, vol. 25, pp. 733–735, Jun 2007.
- [196] N. P. Blockley, I. D. Driver, S. T. Francis, J. A. Fisher, and P. A. Gowland, “Susceptibility artefacts in experiments involving changes in inspired oxygen level,” in *Proc. Intl. Soc. Mag. Reson. Med. 17, Honolulu, Hawaii*, no. 1618, 2009.
- [197] D. T. Pilkington, S. Gaddam, M. A. Elliott, and R. Reddy, “Negative contrast enhancement in T2\*-weighted images of the human brain during hyperoxia,” in *Proc. Intl. Soc. Mag. Reson. Med. 18, Stockholm, Sweden*, no. 3482, 2010.
- [198] J. P. Marques and R. Gruetter, “Removing air-tissue artifacts in phase images by modulating the air susceptibility,” in *Proc. Intl. Soc. Mag. Reson. Med. 18, Stockholm, Sweden*, no. 3015, 2010.
- [199] A. D. Hahn, A. S. Nencka, and D. B. Rowe, “Improving robustness and reliability of phase-sensitive fMRI analysis using temporal off-resonance alignment of single-echo timeseries (TOAST).,” *Neuroimage*, vol. 44, pp. 742–752, Feb 2009.
- [200] F. Lamberton, N. Delcroix, D. Grenier, B. Mazoyer, and M. Joliot, “A new epi-based dynamic field mapping method: application to retrospective geometrical distortion corrections.,” *J Magn Reson Imaging*, vol. 26, pp. 747–755, Sep 2007.
- [201] D. M. Garcia, G. Duhamel, and D. C. Alsop, “Efficiency of inversion pulses for background suppressed arterial spin labeling.,” *Magn Reson Med*, vol. 54, pp. 366–372, Aug 2005.
- [202] C. I. Mark, J. A. Fisher, and G. B. Pike, “Improved fmri calibration: precisely controlled hyperoxic versus hypercapnic stimuli.,” *Neuroimage*, vol. 54, pp. 1102–1111, Jan 2011.

- [203] P. A. Chiarelli, D. P. Bulte, D. Gallichan, S. K. Piechnik, R. Wise, and P. Jezzard, “Flow-metabolism coupling in human visual, motor, and supplementary motor areas assessed by magnetic resonance imaging.,” *Magn Reson Med*, vol. 57, pp. 538–547, Mar 2007.
- [204] A. Kastrup, G. Krger, T. Neumann-Haefelin, G. H. Glover, and M. E. Moseley, “Changes of cerebral blood flow, oxygenation, and oxidative metabolism during graded motor activation.,” *Neuroimage*, vol. 15, pp. 74–82, Jan 2002.
- [205] B. Stefanovic, J. M. Warnking, E. Kobayashi, A. P. Bagshaw, C. Hawco, F. Dubeau, J. Gotman, and G. B. Pike, “Hemodynamic and metabolic responses to activation, deactivation and epileptic discharges.,” *Neuroimage*, vol. 28, pp. 205–215, Oct 2005.
- [206] B. Stefanovic, J. M. Warnking, K. M. Rylander, and G. B. Pike, “The effect of global cerebral vasodilation on focal activation hemodynamics.,” *Neuroimage*, vol. 30, pp. 726–734, Apr 2006.
- [207] H. Ito, M. Ibaraki, I. Kanno, H. Fukuda, and S. Miura, “Changes in cerebral blood flow and cerebral oxygen metabolism during neural activation measured by positron emission tomography: comparison with blood oxygenation level-dependent contrast measured by functional magnetic resonance imaging.,” *J Cereb Blood Flow Metab*, vol. 25, pp. 371–377, Mar 2005.
- [208] P. Herman, B. G. Sanganahalli, D. Coman, and F. Hyder, “Impact of tube hematocrit on calibrated fMRI,” in *Proc. Intl. Soc. Mag. Reson. Med. 18, Stockholm, Sweden*, no. 3549, 2010.
- [209] O. Leontiev and R. B. Buxton, “Reproducibility of BOLD, perfusion, and CMRO<sub>2</sub> measurements with calibrated-BOLD fMRI.,” *Neuroimage*, vol. 35, pp. 175–184, Mar 2007.